Polymer fouling in tubular reactors for radical polymerizations

A thesis accepted by the Faculty of Energy-, Process- and Bio-Engineering

of the University of Stuttgart to fulfil the requirements

for the degree of Doctor of Engineering Sciences (Dr.-Ing.)

by

Stefan Welzel

born in Rheinfelden (Baden)

Main examiner:	Prof. Dr.-Ing. Ulrich Nieken
Co-examiner:	Prof. Dr. rer. nat. Klaus-Dieter Hungenberg
Chairperson of the examination:	Prof. Dr.-Ing. Joachim Groß

Date of the oral examination:	10th October 2024

Institute of Chemical Process Engineering
of the University of Stuttgart

Stuttgart 2024

Danksagung

Die vorliegende Dissertation entstand während meiner Zeit als wissenschaftlicher Mitarbeiter am Institut für Chemische Verfahrenstechnik der Universität Stuttgart.

Für das mir entgegengebrachte Vertrauen und die Freiheit, meine Ideen einzubringen und umzusetzen, möchte ich mich bei Prof. Ulrich Nieken herzlich bedanken. Die Diskussionen und Anregungen haben wesentlich zum Gelingen dieser Arbeit beigetragen. Des Weiteren möchte ich Herrn Prof. Klaus-Dieter Hungenberg für die vielen Diskussionen und Hinweise zu dieser Arbeit danken sowie für die Anfertigung des Zweitgutachtens. Des Weiteren möchte ich Herrn Prof. Joachim Groß und den Kollegen vom ITT danken für die Hilfe bei thermodynamischen Fragestellungen sowie die Anwendung derer.

Bei den experimentellen Arbeiten gilt ein besonderer Dank an Dörthe Schiewe und Robert Fettig, ohne die der Umfang dieser Arbeiten sicherlich nicht so gut zu bewältigen gewesen wäre. Auch die vielen studentischen Arbeiten wie beispielsweise die von Jule Burmeister haben zum Gelingen dieser Arbeit beigetragen.

Allen Kollegen am ICVT, besonders den beiden Jungstars Giuliano und Daniel, meinem langjährigen Zimmerkollegen Lukas Maier und der besten Verwaltungsfachangestellten Katrin Hungerbühler, möchte ich für die gemeinsame Zeit und den vielen Aktivitäten neben der Arbeit danken.

Für die finanzielle Unterstützung im Rahmen der ENPRO-Initiative danke ich dem Bundesministerium für Wirtschaft und Energie („KoPPonA 2.0“, FKZ 03EN2004F).

Zuletzt möchte ich mich bei meiner Familie bedanken, welche es mir ermöglicht hat, den Weg der Promotion zu gehen und meiner langjährigen Freundin Rahel für ihre Unterstützung und Geduld beim Anfertigen dieser Arbeit.

Contents

Zusammenfassung

Die Produktion von Spezialpolymeren wie beispielsweise Polyvinylpyrrolidone wird derzeit hauptsächlich in batch oder semi-batch Fahrweise von Tankreaktoren aufgrund deren hoher Flexibilität realisiert. Im Sinne der Prozessintensivierung stehen vermehrt kontinuierliche Reaktoren aufgrund der besseren Energieeffizienz im Fokus der derzeitigen Forschung. Um den Wärmeeintrag in das Reaktionsmedium zu gewährleisten, werden Reaktoren mit statischen Mischelementen eingesetzt. Das Problem, welches während der Polymerisation in Rohrreaktoren auftritt, ist die Bildung bzw. Ablagerung von hochviskosem Polymer an Reaktorwänden bis zu einem hochvernetzten Polymergel. Dies führt zu Verblocken bzw. dem Abschalten der kontinuierlichen Reaktoren. Für die Industrie ist daher eine Umstellung zu einem kontinuierlichen Betrieb momentan nicht tragbar. Um die Belagsbildung und damit das Abschalten des Reaktors zu verhindern, gilt es, Einflussfaktoren für Fouling in kontinuierlichen Reaktoren zu erforschen, um geeignete Maßnahmen ergreifen zu können.

In dieser Arbeit wird als Beispiel die Belagsbildung bei der radikalischen Polymerisation von N-Vinylpyrrolidone (NVP) zu Polyvinylpyrrolidone (PVP) erforscht. Dabei wird die Arbeit in einen experimentellen und einen simulativen Anteil gegliedert, wobei die experimentellen Erfahrungen direkt in die Modellierungsarbeiten einfließen. Das Ziel ist es hierbei ein mechanistisches Verständnis der Belagsbildung abzuleiten und geeignete Maßnahmen zu ergreifen, um Fouling in kontinuierlichen Reaktoren zu verhindern bzw. zu beherrschen.

Zuerst werden die experimentellen Arbeiten, welche in unterschiedlichen kontinuierlichen Rohrreaktoren durchgeführt worden sind, vorgestellt. Im Fokus liegt hierbei die Detektion der Belagsbildung, die zum einen in Kapillarreaktoren durch eine Verweilzeitmessung mittels Salztracer und zum anderen in statischen Mischerreaktoren durch eine UV/VIS Sonde erzielt wurde. Unterschiedliche Prozessbedingungen konnten in den jeweiligen Reaktoren getestet werden. Eine erhöhte Monomer- sowie Initiatorkonzentration führt daher mit gleichzeitig steigendem Polymergehalt zu früherem und stärkerem Fouling. Geometrieveränderungen des Kapillarreaktors haben große Auswirkungen auf das Verhalten. Besonders im Drucksignal wird deutlich, dass sowohl ein längerer Reaktor als auch ein größerer Reaktordurchmesser bei gleicher Verweilzeit einen positiven Einfluss auf das Foulingverhalten zeigen. Wichtig ist, dass sowohl die Verweilzeitmessung als auch die optische UV/VIS

Spektroskopie frühzeitig das Signal zur Belagsbildung liefern können. Weiter wurden unterschiedliche Beschichtungen auf Edelstahlmischelemente getestet. Besonders dünnwandige Beschichtungen mit niedriger Oberflächenenergie sind geeignet, um die Belagsbildung bei der radikalischen Polymerisation von NVP zu reduzieren. Letztlich lässt sich jedoch durch eine Beschichtung das Polymerfouling nicht umfassend verhindern. Sollte Fouling entstehen, kann dies chemisch mithilfe von Natriumhypochlorit bei hohen Temperaturen (T= 80 °C) gut gereinigt werden.

Die komplementären Modellierungs- bzw. Simulationsarbeiten gliedern sich in drei Hauptbausteine: die Reaktionskinetik, der Transport der Polymere und die umfassende CFD-Simulation. Um Informationen über die Struktur der Polymere zu erhalten, wurde ein kinetisches Modell für die Verzweigungsverteilung entwickelt. Einflussfaktoren wie Verweilzeit im Reaktor bzw. Monomerkonzentration konnten hierdurch evaluiert werden. Dieses Modell konnte im nächsten Schritt durch experimentelle Befunde hinsichtlich der Molekulargewichtsverteilung, dem Umsatz und der Verzweigungsverteilung mittels Gelpermeationschromatographie, Hochdruckflüssigkeitschromatographie und Feldflussfraktionierung validiert werden.

Polymere werden mathematisch häufig durch ihre Momente (Mittelwerte einer Verteilung) beschrieben. Um den Transport von Polymeren bzw. deren Momente korrekt beschreiben zu können, wird die Maxwell-Stefan Diffusionsgleichung verwendet. Für zwei Grenzfälle (niedriger und hoher Polymergehalt) kann eine mathematische Schließung der Transportgleichung für die Momente erfolgen. Thermodynamisch kann dieses Modell durch die Verwendung der PC-SAFT Zustandsgleichung ergänzt werden. Zusätzlich konnten mittels dynamischer Lichtstreu-Versuche Diffusionskoeffizienten zwischen Polymer und Lösungsmittel abhängig von Temperatur, Zusammensetzung und Molekulargewicht des Polymers ermittelt werden.

Eine gesamtheitliche Betrachtung des Systems kann abschließend durch das Zusammenspiel der Hydrodynamik, der Kinetik und des Transports der Polymermomente in der CFD-Simulation mit der zusätzlichen Implementierung eines eigens parametrierten Viskositätsmodell erreicht werden. Hierbei wird das CFD-Modell für unterschiedliche Prozessbedingungen durch die experimentellen Befunde aus dem Kapillarreaktor validiert. Anschließend werden unterschiedliche Einflussfaktoren wie die Wahl des Transportmodells der Polymere, das Viskositätsmodell, Nebenreaktionen und die Beschreibung des Diffusionskoeffizienten untersucht. Ergänzt wird das Modell schließlich durch die PC-SAFT Zustandsgleichung, welche mittels neuronaler Netze zur Beschreibung der Triebkraft in der Maxwell-Stefan Diffusionsgleichung approximiert wurde.

Durch dieses Modell ist es möglich qualifizierte Voraussagen für die Belagsbildung für unterschiedliche Prozess- und Geometriebedingungen zu treffen und daraus geeignete Maßnahmen abzuleiten.

Abstract

The production of specialty polymers such as polyvinylpyrrolidones is currently mainly realized in batch or semi-batch operation of tank reactors due to their high flexibility. In terms of process intensification, current research is increasingly focusing on continuous reactors due to their improved energy efficiency. Microreactors with static mixing elements are used to ensure heat input into the reaction medium. The problem that occurs during polymerization in tubular reactors is the formation or deposition of highly viscous polymer on the reactor walls until it forms a highly cross-linked polymer gel. This leads to blocking or shutdown of the continuous reactor. For the industry, a switch to continuous operation is therefore currently not viable. To prevent fouling and thus the shutdown of the reactor, factors influencing fouling in continuous reactors need to be investigated to be able to take appropriate measures.

In this work, the formation of deposits during the radical polymerization of N-vinylpyrrolidone (NVP) to polyvinylpyrrolidone (PVP) is considered as an example. The work is divided into an experimental and a simulative part, whereby the experimental experience flows directly into the modeling work. The aim is to derive a mechanistic understanding of fouling formation and to take suitable measures to prevent or control fouling in continuous reactors.

First, the experimental work carried out in various continuous tubular reactors is presented. The focus here is on the detection of deposit formation, which was achieved on the one hand in capillary reactors by measuring the residence time using a salt tracer and on the other hand in static mixer reactors using a UV/VIS probe. Different process conditions were tested in the respective reactors. An increased monomer and initiator concentration therefore leads to earlier and stronger fouling with a simultaneous increase in polymer content. Changes in the geometry of the capillary reactor have a major impact on the behavior. The pressure signal in particular shows that both a longer reactor and a larger diameter have a positive effect on the fouling behavior for the same residence time. It is important that both the residence time measurement and the optical UV/VIS spectroscopy can provide the signal for fouling formation at an early stage. Different coatings were also tested on stainless steel mixer. Thin film coatings with low surface energy are particularly suitable for reducing the formation of deposits during the radical polymerization of NVP. Ultimately, however, polymer fouling cannot be comprehensively prevented by a coating. If fouling does occur, it can be easily chemically cleaned using sodium hypochlorite at high temperatures (T= 80 °C).

The modeling and simulation work is divided into three main components: the reaction kinetics, the transport of the polymers and the comprehensive CFD simulation. In order to obtain information about the structure of the polymers, a kinetic model for the branching distribution was developed. Influencing factors such as residence time in the reactor and monomer concentration were evaluated. In the next step, this model was validated by experimental findings regarding molecular weight distribution, conversion and branching distribution using gel permeation chromatography, high performance liquid chromatography and field flow fractionation.

Polymers are often described mathematically by their moments (mean values of a distribution). The Maxwell-Stefan diffusion equation is used to describe the transport of polymers or their moments. For two limiting cases (low and high polymer content), the transport equation for the moments can be mathematically closed. This model can be supplemented thermodynamically by using the PC-SAFT equation of state. In addition, dynamic light scattering experiments were used to determine diffusion coefficients between polymer and solvent as a function of temperature, composition and molecular weight of the polymer.

A holistic view of the system can be achieved through the interaction of hydrodynamics, kinetics and transport of the polymer moments in the CFD simulation with the additional implementation of a specially parameterized viscosity model. The CFD model is validated for different process conditions using the experimental findings from the capillary reactor. Subsequently, different influencing factors such as the choice of the transport model of the polymers, the viscosity model, side reactions and the description of the diffusion coefficient are investigated. Finally, the model is complemented by supplementing the PC-SAFT equation of state by approximation using a neural network to describe the driving force in the Maxwell-Stefan diffusion equation.

This model makes it possible to make qualified predictions for the formation of deposits for different process and geometry conditions and to derive suitable measures from this.

Nomenclature

Abbreviations

1D	One-dimensional
AFM	Atomic force microscope
BP	Branching points
const	constant
CFD	Computational Fluid Dynamics
CPM	Customized Photo Multipliers
CSTR	Continuous stirred-tank reactor
CVD	Chemical vapor deposition
DLC	Diamond like carbon
DLS	Dynamic light scattering
dyn	dynamic
FeOs	Framework for Equations of State
FE-SEM	Field-emission scanning electron microscopy
FFF	Field flow fractionation
Fluitec	Fluitec mixing + reaction solutions AG
FOTS	Perfluorinated organosilane
FTIR	Fourier transform infrared spectroscopy
GC	Group contribution
GPC/SEC	Gel permeation chromatography/ Size exclusion chromatography
HPLC	High-performance liquid chromatography
Inj.	Injection
K12, K25, K30, K90	Kollidon 12, 25, 30, 90
MALS	Multi-angle light scattering
MWD	Molecular weight distribution

NN	Neural Network
nps	Non-polished stainless steel
NVP	N-Vinylpyrrolidone
PACVD	Plasma-assisted chemical vapor deposition
PCS	Photon correlation spectroscopy
PC-SAFT	Pertubed Chain - Statistical Associating Fluid Theory
pent	Pentene
PI	Proportional-Integral
ps	Polished stainless steel
PVP	Polyvinylpyrrolidone
QELS	Quasi-elastic light scattering
RI	Refractive index
RTD	Residence time distribution
RU	Repeating units
TDB	Terminal double bonds
UPB	University of Paderborn
UV	Ultraviolet
VIS	Visible
WCA	Water contact angle
ZrOx	Zirkoniumoxide

Latin letters

A, B	Coefficients for the correlation to calculate the number of TDB
A_2, B_2	Coefficients for the correlation to calculate the number of BP
A_i, B_i	Association sites
B_{ij}	Elements of the Maxwell-Stefan diffusion matrix
c	Molar concentration

$c^{(m)}$	Mass concentration
C	Carbon
C_η	Constant for viscosity correlation
D'	Dispersity in closure relation for modeling the reaction mechanism
d_i	Inner diameter
d_i	Driving force in Maxwell-Stefan equation
d_w	Winding diameter
$\mathfrak{D}_{ij}$	Maxwell-Stefan Diffusion coefficient between species i and j
$\frac{dn}{dc^{(m)}}$	Refractive index increment
E_λ	Extinction to the wavelength λ
E_{out}	Area-normalized response signal
f_d	Kinetic parameter for the initiator efficiency
g	Branching ratio
g^1	Field-time correlation function (DLS)
g^2	Autocorrelation function (DLS)
H	Hydrogen
H^{TDB}	Reaction counter variable for number of terminal double bonds
I	Intensity
I_Θ	Intensity of the scattered light
J_i^N	Molar flux of component i
K^*	Detector constant of MALS detector
k_B	Boltzmann constant
k_d	Kinetic rate coefficient for the initiator dissociation
k_{ij}	Binary-interaction parameter
k_p	Kinetic rate coefficient for the monomer propagation
$k_{p,max}$	Kinetic rate coefficient for the maximum rate of monomer propagation

$k_{p,TDB}$	Kinetic rate coefficient for the propagation of TDB
k_{RD}	Kinetic rate coefficient for reaction diffusion in termination reaction
K_{RI}	Detector constant of the RI detector
k_{SD}	Kinetic rate coefficient for segmental diffusion in termination reaction
$k_{t,c}$	Kinetic rate coefficient for the termination by recombination
k_{TD}	Kinetic rate coefficient for translational diffusion in termination reaction
$k_{tr,M}$	Kinetic rate coefficient for the transfer to monomer reaction
l	Length
M	Monomer
m_i	segment number
$\dot{m}_F$	Mass flow rate
M_i	Molecular weight of species i
M_n	Number average molecular weight
M_{seg}	Molar mass of a segment
$M_w, \overline{M}_w$	Weight average molecular weight
n	Number of contributions
n	Solvent refractive index (DLS)
N	Allowed confirmations
N	Molar
n_0	Refractive index of the solvent
N_A	Avogadro number
$N^{assoc}.$	Number of association sites
N_n	Number average chain length
N_w	Weight average chain length
O	Oxygen
p	Pressure
p_0	Initial pressure

$P1, P2$	Polymer 1,2
$P1, P2, P3, P4$	HPLC piston pump 1,2,3,4
$p(m)$	Correlation for average number of terminal double bonds
P_s	Polymer with chain length s
p^{sat}	Vapor pressure at saturation
q	Wave vector (DLS)
$q(m)$	Average number of branching points per chain length m
R	Distance between measuring volume and detector (MALS)
R	Ideal gas constant
Re_{in}	Reynolds number inlet
R_n	Living Species with chain length n
R_Θ	Rayleigh ratio
$\vec{r}_i$	Bond vectors
R_g	Radius of gyration
R_n	Living polymer species with chain length n
$\vec{R}_n$	End-to-end vector
s	Chain length
S	Solvent
S_{RI}	Signal of the RI detector
t	Time
T	Temperature
u_i/k_B	Dispersion energy parameter
v	Velocity
V_0	Measuring volume
$\dot{V}^+$	Volume flow influx to reactor
V_i^{elu}	Elution volume
V_R	Reactor volume

w	Weight fraction
W	Fraction for a respective distribution
x_i	Molar fraction of species i
X_M	Monomer conversion
Z	Compressibility factor

Greek letters

β	Correction factor (DLS)
γ_i	Activity coefficient of species i
Γ	Decay rate (DLS)
δ_{ij}	Kronecker delta
$\epsilon^{A_iB_i}/k_B$	Association energy
η	Shear viscosity
θ	Scattering angle
$\kappa^{A_iB_i}$	Effective association volume
λ_L	Specific wavelength of the laser beam (MALS detector)
μ_P^k, μ_R^k	Kth chain length moment for dead resp. living polymers
μ_i	Chemical potential of species i
ξ^k	Polymer moment
ρ_i	Mass density of component i
σ_i	Segment diameter
τ	Residence time
τ	Lag time (DLS)
τ	Viscous stress tensor
φ_i	Fugacity coefficient of species i
ϕ_n^K	Kth branching moment for living polymer chains

Ψ_m^L	L^{th} branching moment for dead polymer chains

Subscripts

0	Initial value
br	Branched polymer chain
cm	Center of mass
i	species
I	Initiator
k	K^{th} moment
k,l	Branching point
lin	Linear polymer chain
low	Low molecular species
M	Monomer
n	Number
N	Molar
n,m	Chain length index
Out	Outlet
P	Polymer
PVP	Polyvinylpyrrolidone
ref	Reference value
SEC	Size exclusion chromatography
seg	Segment
T	Tracer
w	Weight

Superscripts

+	feed
assoc	Association term
BP	Branching points
disp	Dispersive term
hc	Hard-chain term
id	Ideal Gas
k	Kth moment
P	Polymer
R	Living Polymer
TDB	Terminal double bond

1 Introduction

Tank reactors, which are operated in batch or semi-batch mode, are the main technique used to produce specialty polymers like Polyvinylpyrrolidone (PVP) [1]. This type of process is characterized by a very high degree of flexibility, while continuously operating reactor systems are considered for process intensification due to improved controllability, energy efficiency, and heat transfer. The production of low-volume products like PVP necessitates the use of tubular reactors with mixing elements to ensure the heat input into the reaction medium. The problem of the operation in such reactors is the formation of an insoluble polymer gel, known as fouling, on surfaces. Polymer fouling is a complex phenomenon that arises from the deposition of polymers on the reactor surfaces, leading to reduced heat transfer efficiency, changed flow dynamics, and ultimately compromising the reactor's performance and eventually cause total blocking, leading to unavoidable reactor shutdowns [2]–[4]. Figure 1 illustrates a mixing element completely covered with fouling deposits after the polymerization of N-Vinylpyrrolidone (NVP) to PVP in a tubular reactor with mixing elements. Side reactions that produce large molecular weight, branched, or crosslinked polymer chains are a prerequisite for fouling [5], [6]. The presence of dead zones with sluggish flow and increased local residence time intensifies the formation of a polymer network [7].

Figure 1: Static mixing element filled with fouling deposits after the polymerization of N-Vinylpyrrolidone in a Fluitec ContiPlant reactor.

In order to anticipate fouling during reactor scale-up and to choose appropriate process conditions, this thesis aims to comprehend the factors that lead to deposit formation and develop a model that can be used to enlighten the process of deposit formation in polymer reactors. This chapter will give an overview of the state of the literature on work in polymer fouling and then presents the aim and outline of this thesis.

1.1 Fouling in continuous reactors

Fouling, a common occurrence in many industrial processes, is the build-up of undesired deposits on surfaces that reduce the performance of a certain system. A wide variety of materials such as Minerals, sediments, biological materials on ships [8], and other inorganic or organic materials can be found in these deposits. Fouling causes higher energy consumption, decreased heat transfer, and operational inefficiencies in heat exchangers [9], [10], pipelines [11], membranes [12], and other equipment and therefore provide huge challenges for industry and research. Developing successful solutions that include preventive measures, state-of-the-art materials and cleaning methods requires an understanding of the mechanisms of fouling. So far, however, the problem of polymer fouling has been systematically addressed by only a few people. Very good examples of this are works in the field of emulsion polymerization [2], [4] and LDPE synthesis [3], [13], [14]. In the field of solution polymerization, the works of Hellmund [15] and Zander [7] were carried out previously and form the basis of this thesis.

In a recent work [16], the fouling process was described in 5 successive steps: i) The polymer chains are formed in the bulk of the reaction fluid; ii) The chains are transported to the reactor wall by turbulent eddies and diffusion across the boundary layer; iii) Polymer chains attach or adsorb to the wall surface (i.e. on the reactor walls or mixing elements); iv) Detachment from the deposited polymer chains; v) Transportation to the core fluid. This is particularly favored by dead water zones, as the residence times are particularly high at these points, and the polymer can therefore grow to a very large molecule if side reactions are likely [1], [7]. This situation is further reinforced by particularly high-molecular polymer molecules. Other factors influencing polymer fouling are the process conditions, such as the flow rate in a tubular reactor or the feed conditions, as high initiator concentrations generally lead to high conversion. A high monomer to initiator ratio also ensures long-chain polymer compounds [7].

Different strategies for tracking fouling have already been investigated. Deposit formation in polymer reactors is often accompanied by strong temperature gradients [17], [18]. Therefore, in the work of Hohlen et al. [17] the influence of the reactor wall temperature of cooled and heated surfaces was investigated. The temperature gradient between the wall and the bulk plays an important role, especially in the structure of the fouling layer. By using a digital microscope, the deposition process was quantified by the mass-based fouling resistance, fouling layer height, and surface coverage [17]. Furthermore, a single channel ultrasound echo measurement was used to trace the fouling process of an emulsion polymerization in real time, while the reaction and substance properties in the process are monitored [19]. In another work, the early development of membrane surface fouling was measured on the surface of electrically conductive membranes (ECMs) using electrical impedance spectroscopy (EIS) [20]. In [21], a fiber-optic rod probe was used to monitor in-situ membrane fouling with reflectance UV/VIS spectrophotometry.

Several strategies for reducing or avoiding fouling or polymer fouling can be found in the literature. The most widely used method is certainly to coat the surfaces which are in contact with the reaction medium [8], [22]–[25]. Depending on the reaction medium (hydrophobic or hydrophilic), a surface treatment to high or low surface energies is selected. However, the problem is that these coatings can only reduce the amount of fouling and cannot prevent it completely. This can have various reasons, e.g. the coating is not durable enough or that the polymer adsorbs anyway [26]. A relatively new method for preventing or eliminating fouling is the use of ultrasound. In [27] it could be shown that a direct coupling of a sonotrode in a microstructured heat exchanger has a significant positive influence on the fouling tendency of a solution of calcium nitrate/sodium hydrogen carbonate. In a further study, two decalcification scenarios in pipelines were investigated and showed that contamination can be effectively removed with ultrasound [11]. In [28], Nonlinear Control was used to address the fouling concern by a neural Wiener model predictive control. Therefore, LDPE reactors can be cleaned online by pressure cleaning or thermal shock. If fouling has already occurred, a suitable cleaning strategy is required, which can be a physical, chemical, or combined process. In [29], the factors affecting chemical cleaning performance such as concentration, cleaning time and temperature were discussed in detail on microfiltration membranes.

The modeling of fouling processes is possible using different methods. Kinetic models for polymerization and their correct parameterization are important [7]. By describing the reaction kinetics, structural properties of the polymer such as the branching distribution can be modeled [30]. Compartment models [31] or Computational Fluid Dynamics (CFD) simulations [7] can then be used to describe the hydrodynamics of the system, whereby the accuracy of the former can be significantly lower than with a CFD simulation, as some important areas are lumped into a single compartment.

1.2 Aim and outline of this work

After a detailed presentation of current research on polymer fouling, the structure and aim of this thesis are described below. Figure 2 shows a graphical illustration of the outline of this thesis.

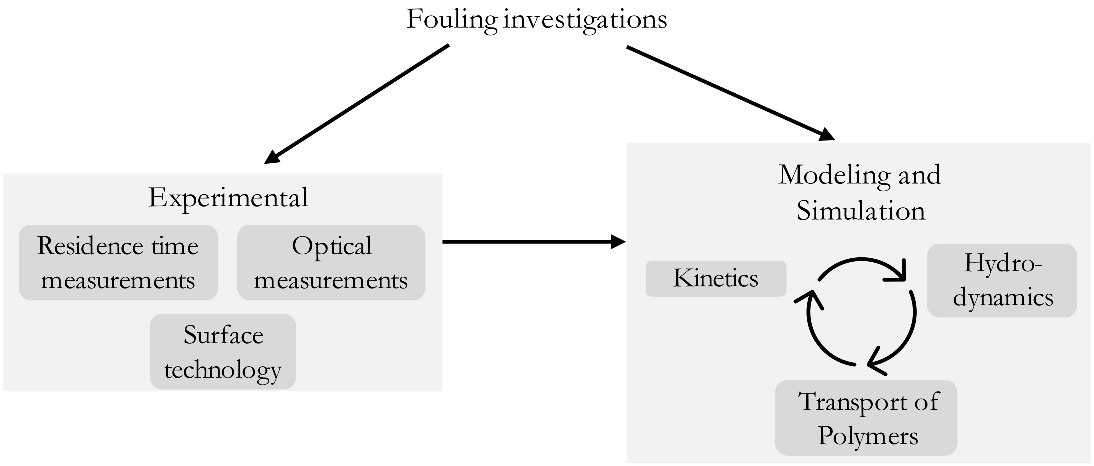

Figure 2: Graphical illustration of the outline of this thesis.

The aim of this work is to investigate the phenomenon of fouling using the example of the free radical solution polymerization of N-vinylpyrrolidone to polyvinylpyrrolidone. The work is divided into experimental and simulative investigations, whereby the experimental findings have a direct influence on the modeling and the simulations.

To acquire an empirical understanding of the fouling mechanisms and to identify the influencing factors, polymerization reactions will be initially conducted within a geometrically straightforward capillary reactor, employing diverse process conditions and reactor geometries. The reactor's behavior will be investigated through residence time measurements. Subsequent examinations will be performed in a tubular reactor with mixing elements, aided by an optical measurement rod probe with UV/VIS to validate the influencing factors identified in the capillary reactor. In accordance with present methodologies, hydrophobic coatings represent the preferred approach for mitigating polymer fouling. This study will cover the evaluation of diverse coatings to determine their efficiency in this regard.

The outcomes derived from experimental runs will be seamlessly integrated into the modeling framework, serving to validate the simulation model. As illustrated in Figure 2, the modeling of the system contains three essential components. Consequently, this thesis will be initiated by presenting the kinetics and formulating a capable model to dynamically compute the branching distribution. The polymer transport is then investigated using the Maxwell-Stefan approach, from which limiting cases are derived and validated for a respective application. For an enhanced thermodynamic representation of the polymer system, the PC-SAFT equation of state will be applied. The description of the transport of the polymers is complemented by an improved calculation of the diffusion coefficients between polymer and solvent by means of parameterization through dynamic light scattering experiments. These methods are then combined in a CFD simulation and coupled with a suitable viscosity model, parameterized with independent viscosity measurements. The validity of the CFD simulation will be approved through comparisons with experimental results from the capillary reactor under varying process conditions. To further achieve a thermodynamically accurate depiction, the PC-SAFT equation of state will be applied to construct a specific mapping of thermodynamic states, subsequently approximated by a neural network. This neural network will then be incorporated into the CFD simulation.

In the conclusion, the findings will be summarized, and the exhaustive investigations will provide a comprehension of the fouling tendency within tubular reactors for radical polymerizations. This acquired knowledge will be used to provide sound guidance on strategies to prevent or mitigate fouling in such systems.

2 Literature review

This Chapter is intended to provide the reader with an overview of the available theory in the literature and methods that are used in this thesis. First, Chapter 2.1 summarizes the basics of polymers and their physical characterization. Subsequently, polymer reactions and their modeling will be discussed. This is followed by the analytical methods used to determine the characteristics of the polymer. Finally, the thermodynamic properties of polymers are explained, and different modeling methods are described.

2.1 Polymers and their physical characterization

Polymers are macromolecules in which a large number of atoms are linked together by covalent bonds. The structure can be linear, branched, or three-dimensional networks. If the building blocks are the same, the molecule is a homopolymer. The characteristics of repeating units, end groups, potential branches and cross links, and the kind of structural sequence defects make up a polymer's chemical structure [32]. However, the properties of the polymers are primarily revealed in the end application, where the structural properties come into play [30]. One of the most important structural properties is the molar mass and normally, synthetic polymers have a distribution of molar masses. This can be expressed in different ways as a differential or integral distribution.

2.1.1 Molecular weight distributions and averages

The simplest representation of a distribution of molar masses is the frequency distribution. Here, the number of polymers P_S with the chain length s is plotted against the corresponding molecular weight or chain length. The mass of the polymer can ultimately be described by a weighted sum of the monomer units. Therefore, the weight distribution of a polymer can be expressed as [30]

$$W_w^P(t) = P_s(t) \cdot s \cdot M_{seg} \tag{1}$$

with the molar mass of the repeating unit resp. monomer M_{seg}. It should be noted here that a polymer distribution can only have discrete values (1,2,3,...,s). The last important distribution to be mentioned is the GPC resp. SEC distribution for which the measurement method is described in Chapter 2.3.2. Data obtained by this measurement method is proportional to the distribution [30]

$$W_{SEC}^{P}(t) = P_s(t) \cdot s^2 \cdot M_{seg}^2. \tag{2}$$

In addition to the molar mass distributions, any type of property of a polymer can be represented as a distribution, such as the branching distribution. The procedure for another property is the same as mentioned here for the chain length and is therefore not described in more detail.

In most cases, a description of the polymer distribution using statistical moments representing mean values is sufficient. Such a moment (e.g. the chain length moments) of the distribution P of the type/order k at time t can be represented by [30]

$$\mu_P^k(t) = \sum_{s=1}^{\infty} s^k \, P_s(t). \tag{3}$$

Therefore, the meaning of the zeroth (chain length) moment μ_P^0 is the total polymer concentration of the chains P_S, whereas the first (chain length) moment μ_P^1 can be interpreted as the total concentration of all repeating units which are polymerized in P_S. With these polymer moments, important mean values like the average chain length or molar mass to characterize a polymer distribution can be calculated. Two different averages, the number and mass/weight averages, are presented here. While the number average describes the average number of repeating units per polymer chain and the mass average leads to averages weighted with mass fractions. The number average chain length is defined as [30]

$$\bar{N}_n^P(t) = \frac{\mu_P^1(t)}{\mu_P^0(t)} \tag{4}$$

while the weight average chain length is

$$\bar{N}_w^P(t) = \frac{\mu_P^2(t)}{\mu_P^1(t)}. \tag{5}$$

The corresponding averages of the molar mass are usually of particular interest and are defined for homopolymers as

$$\overline{M}_n^P(t) = \frac{\mu_P^1(t)}{\mu_P^0(t)} M_{seg} = N_n^P(t) M_{seg}, \tag{6}$$

$$\overline{M}_w^P(t) = \frac{\mu_P^2(t)}{\mu_P^1(t)} M_{seg} = N_w^P(t) M_{seg} \tag{7}$$

with the number average molar mass $\overline{M}_n^P$ and the weight average molar mass $\overline{M}_w^P$.

2.1.2 Branched polymers

The conformation of polymer molecules can be determined by the end-to-end vector [33]. This is calculated by the sum of all n bond vectors $\vec{r}_i$ in the chain

$$\vec{R}_n = \sum_{i=1}^{n} \vec{r}_i. \tag{8}$$

Different polymer molecules therefore have different bond vectors and thus different end-to-end vectors. The average end-to-end vector (average over all possible states of the system) is specified as mean-square end-to-end distance to [33]

$$\langle \vec{R}_n \rangle^2 = \langle \vec{R}_n \cdot \vec{R}_n \rangle = \sum_{i=1}^{n} \sum_{j=1}^{n} \langle \vec{r}_i \cdot \vec{r}_j \rangle. \tag{9}$$

In radical polymerization in particular, branching is likely and difficult to regulate. A polymer's characteristics both in solution and in a molten state are impacted by branching [32]. Because branched polymers either have too many ends or none at all, their mean-square end-to-end distance is not well characterized. As every object has a gyration radius, it may be used to describe the size of polymers in any design [33]. Figure 3 illustrates the confirmation of a random branched polymer with position vectors ($\vec{R}_i$, $\vec{R}_{cm}$) and the center of mass (cm).

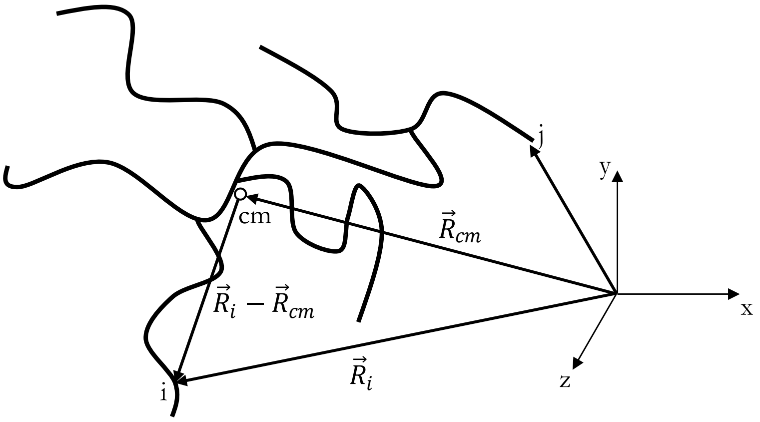

Figure 3: Conformation of a branched polymer with position vectors and center of mass (cm). Adapted from [33].

The definition of the radius of gyration is an average distance between monomer molecules and the polymers center of mass and is usually averaged over all monomer position vectors N, which leads to the equation [33]

$$\langle R_g^2 \rangle = \frac{1}{N} \sum_{i=1}^{N} \langle \left(\vec{R}_i - \vec{R}_{cm} \right)^2 \rangle \tag{10}$$

with the position vector for the center of mass

$$\vec{R}_{cm} = \frac{1}{N} \sum_{i=1}^{N} \vec{R}_i . \tag{11}$$

The radius of gyration can be determined with a suitable measurement system, which will be explained in Chapter 2.3. The number of branching points can be calculated afterwards with the branching ratio

$$g = \frac{\langle R_g^2 \rangle_{br}}{\langle R_g^2 \rangle_{lin}}, \tag{12}$$

in which the index br and lin denote a branched resp. a linear chain with the same molecular weight [34].

2.2 Polymer reactions and modeling

The polymer reactions that take place when modeling a polymer system are often described using predefined reaction schemes or modules [30]. One example is the propagation or chain growth reaction, which can be described in a radical polymerization to $R_n + M \xrightarrow{k_p} R_{n+1}$. In addition to propagation, there are of course many other reactions that need to be identified. These schemes are then described using balance equations for the individual species. Within the balance equations, the rate coefficients of the individual reactions are necessary for the description. They can usually be taken from literature. If this is not the case, rate coefficients can be derived from experimental data by parameter estimation. For a kinetic approach, a distinction can be made between step-growth and chain-growth polymerization. In the latter case, elementary reactions such as the initiation and chain growth reaction must take place.

2.2.1 Radical solution polymerization

Radical polymerizations belong to the group of chain-growth polymerizations. In addition to initiation, which describes the start of the chain, and propagation, which describes chain growth, radical polymerization also involves termination reactions such as disproportionation and termination by combination. For example, the balance equations for a propagation reaction for the monomer (M) and living polymer (R_1, R_s) are [30]:

$$\begin{aligned} \frac{dM}{dt} &+= k_p M \sum_{s=1}^{\infty} P_s \\ \frac{dR_1}{dt} &+= -k_p M R_1 \\ \frac{dR_s}{dt} &+= -k_p M (R_s - R_{s-1}) \end{aligned} \tag{13}$$

The $+=$ term describes the contribution of a certain reaction, which is commonly used in c code. In addition to the main reactions, side reactions such as transfer reactions to polymer, monomer and solvent also take place, which are accompanied by subsequent reactions such as their propagation. The complete set of reactions for radical polymerizations and the associated balance equations can be found in [30].

The reaction schemes to be investigated for the polymer system under consideration is shown in Chapter 4.

As already stated, it is often of interest to consider more than one property coordinate of a polymer system. In addition to the chain length, these properties can also represent the number of terminal double bonds, branching points or similar. Multidimensional simulations are usually not solvable with the available computing power. Therefore, the problem has to be reduced to 1D problems along a single property coordinate. Two ways of reducing a system are generally presented below.

2.2.2 Classes approach

In this approach, one property is usually treated as a continuous variable (often the chain length), while the second property coordinate is treated as a discrete variable. For each number of this second property coordinate, a balance equation is required, which is referred to as a "class" [35]. This is only possible if the distribution of the discrete variable falls off sufficiently quick and the number of classes can be kept low. For practical reasons, the number of classes is less than 10. $R_{1,2}$ denotes for example a living polymer with the chain length 1 as the first property coordinate and the second property coordinate is 2. In Chapter 4.2.3 this approach is used on the number of branching points for the NVP polymerization.

2.2.3 Moment approach

The second approach to reduce the calculated properties is the method of moment or pseudo-distributions [36]. Compared to the classes model, the number of equations and therefore the numerical costs can be reduced drastically. Statistical moments have been introduced in Chapter 2.1.1. These moments can now be applied to a specific property coordinate like the chain length in Equation (3). The balance equation for the moment directly follows from the definition (for living polymer moments)

$$\frac{d\mu_R^k}{dt} = \frac{d\left(\sum_{s=1}^{\infty} s^k \, R_s(t)\right)}{dt} \tag{14}$$

and can be applied on the propagation reaction for example

$$\frac{d\mu_R^k}{dt} += -k_p M \sum_{s=1}^{\infty} s^k R_s + k_p M \sum_{s=2}^{\infty} s^k R_{s-1} = -k_p M \mu_R^k + k_p M \sum_{s=1}^{\infty} (s+1)^k R_s. \tag{15}$$

Normally, moments for $k = 0{,}1{,}2$ are required and develop to

$$\frac{d\mu_R^0}{dt} += -k_p M \mu_R^0 + k_p M \sum_{s=1}^{\infty} R_s = -\, k_p M \mu_R^0 + k_p M \mu_R^0 = 0$$

$$\frac{d\mu_R^1}{dt} += -k_p M \mu_R^1 + k_p M \sum_{s=1}^{\infty} (s+1) R_s = -\, k_p M \mu_R^0 + k_p M (\mu_R^1 + \mu_R^0) = k_p M \mu_R^0 \tag{16}$$

$$\frac{d\mu_R^2}{dt} += -k_p M \mu_R^2 + k_p M \sum_{s=1}^{\infty} (s+1)^2 R_s = k_p M (2\mu_R^1 + \mu_R^0).$$

The same procedure can be applied for all other reactions and all other species. The moment approach was used here for 1D moments, but it can also be used for higher-dimensional moments. A detailed description of the investigated polymer system can be found in Chapter 4.2.2 or Appendix A.3.

2.3 Analytics

There are various methods that are suitable for the characterization of polymers. The aim of this work is to obtain information about the molecular weight distribution, the monomer conversion, and the branching distribution. The most commonly used method for polymer analysis is size exclusion chromatography (SEC) or gel permeation chromatography (GPC). However, this leads to errors for large molecular weights, which is why another method, the field flow fractionation (FFF), was used additionally for separation. After separation via GPC or FFF, the polymers are detected using an RI (refractive index) or MALS (multi-angle light scattering) detector for example. The monomer conversion was determined using high-performance liquid chromatography (HPLC). The individual methods of polymer analysis are briefly presented below.

2.3.1 High-performance liquid chromatography (HPLC)

By using high-performance liquid chromatography (HPLC), it is possible to determine the monomer conversion at the time of sampling. HPLC is usually based on the different polarities of the stationary and mobile phases of the used separation column [37]. A polar stationary phase is referred to as normal-phase chromatography and a non-polar stationary phase as reversed-phase chromatography [37]. When choosing normal phase chromatography, the sample components, that are non-polar, pass through the column more quickly as they do not interact with the mobile phase. Polar components interact, which is why they elute later. Solvent gradients are often used to avoid broad peaks, which can be lost in the background noise of the detector. This means that the polarity of the solvent is changed over time by mixing two or more components. An UV detector can be used to detect the desired sample proportion. With this, the sample material is irradiated with a specific wavelength in the UV range. The wavelength should be selected so that it is absorbed by the sample component to be examined. The extent to which the light is absorbed can be measured using a photo measuring cell, from which the concentration of a component can be determined [37]. If necessary, this concentration must be corrected for the proportion of intensity losses due to the vessel used or, as in the case for NVP, for the stopper solution used [37]. The conversion can then be calculated from the amount of monomer used and the concentration still present in the sample. The evaluation of the HPLC data is discussed in more detail in Chapter 2.3.5.

2.3.2 Gel permeation chromatography (GPC)

Size Exclusion Chromatography (SEC), also known as Gel Permeation Chromatography (GPC), is one of the most common methods for the experimental analysis of polymers. With the help of suitable sensors, it can provide information about the molecular weight distribution and the radius of gyration (Chapter 2.1.2). In this method, the polymer is first separated according to the hydrodynamic volume, where a column filled with porous gel is used for the separation process [32]. There is a mobile phase in the interstices and pores of the gel. The diluted sample is then injected into the separation system. Depending on the size of the molecule, the molecules can diffuse into the pores of the porous gel and thus be separated according to their hydrodynamic volume. As larger molecules do not or hardly diffuse into the pores, they elute first. Smaller molecules, on the other hand, diffuse more frequently into the pores of the gel and can therefore only pass through the column slowly [34].

In order to achieve a higher separation efficiency, various separation columns can be used [38]. The respective eluent can be analyzed with different concentration- and molar mass-sensitive detectors. These will be discussed in more detail in Chapter 2.3.4.

A disadvantage of the use of SEC systems is that the measurement results can be distorted due to the separation principle. On the one hand, van der Waals interactions can occur between large molecules and the gel, on the other hand, molecules with a molecular weight $>10^6$ g mol^{-1} can lead to shear degradation [34].

2.3.3 Field flow fractionation (FFF)

Like SEC, field-flow fractionation is based on the separation of polymer molecules according to their hydrodynamic volume. Compared to SEC, however, FFF has the advantage that there is no stationary phase and therefore no interactions or shear degradation take place [38]. A schematic representation of the separation process with FFF is shown in Figure 4. The separation of the molecules takes place in a horizontal channel, which consists of a semi-permeable membrane on the lower side. This membrane is only permeable to the solvent, but not to the polymer molecules. The channel is traversed by a main fluid flow into which the sample is injected. In addition, a cross flow is created on the upper side of the channel. The laminar flow of the main flow creates a parabolic flow profile in the channel. As a result, molecules in the wall area have a lower velocity than those in the center of the flow. Due to main fluid flow, for which the membrane is permeable, the polymer molecules are displaced towards the underside of the channel. This is counteracted by diffusive effects, whereby smaller molecules with a higher diffusion coefficient are closer to the center of flow. As the flow velocities are greater in this area, smaller molecules elute first in the FFF. Compared to SEC, the elution sequence is reversed in the FFF [34].

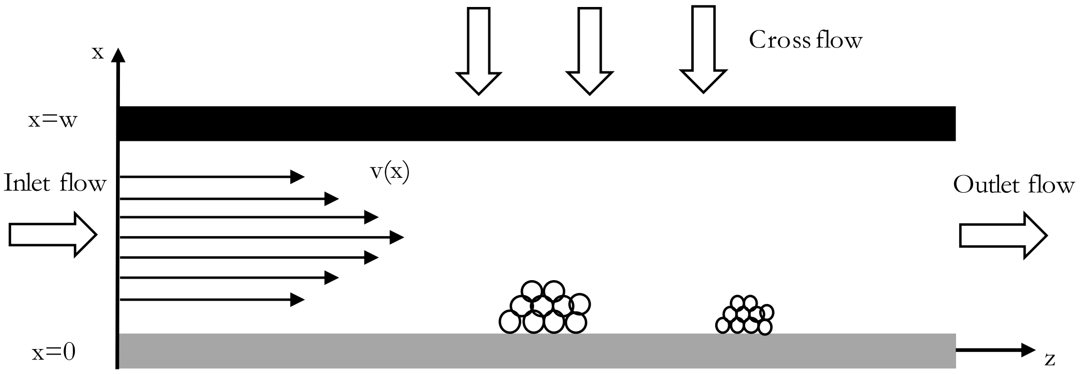

Figure 4: Schematic illustration of the separation process in FFF according to [34].

2.3.4 Detectors for polymer analysis

For polymers that have been separated by SEC or FFF according to their hydrodynamic volume, the combination of a concentration detector with a molar mass sensitive detector such as a multi-angle light scattering detector (MALS) or a viscosity detector is necessary to accurately determine the molecular weight [34]. In the following, the detectors will be discussed in more detail.

Concentration-sensitive detectors include the refractive index (RI) and the ultraviolet (UV) detector. RI detectors are widely used in SEC and FFF systems [34]. They have the advantage over UV detectors that they also provide a result for non-UV-absorbing samples [34]. The following formula results for the measured signal of the RI detector:

$$S_{RI} = K_{RI} \frac{dn}{dc^{(m)}} \, c^{(m)} \tag{17}$$

K_{RI} is the detector constant and $dn/dc^{(m)}$ is the change in the refractive index with increasing mass concentration $c^{(m)}$ (unit: kg/m^3) [34]. For clarification, the index (m) stands for mass. It is therefore possible to determine the respective mass concentration if the change in the refractive index with increasing mass concentration and the detector constant are known. Furthermore, the absolute or actual molecular weight distribution (MWD) can be determined for standards with a known molecular weight. For this purpose, with measurements of the standards, a calibration curve is created. If no standards are available, a combination with a molecular weight sensitive detector is required [34].

Multi-angle light scattering detectors (static light scattering) are among the molar mass-sensitive detectors. Static light scattering is an experimental method that can be used to determine absolute molar masses and the gyration radius (Chapter 2.1.2). The method is based on elastic light scattering on particles. If a laser beam with the specific wavelength λ_L is directed at the sample material, the light scatters with different scattering intensities. The intensities and the associated light scattering angles are detected and averaged over time. As the scattering intensities are indirectly related to the refractive index n, polymers with a diameter smaller than $\frac{\lambda_L}{20}$ behave like point scatterers [38]. This means that there is no dependence of the intensities on the angle for these sizes [34]. If the particle diameter is greater than $1/20$ of the light wavelength, scattering is increased to small angles [38]. This is shown in Figure 5.

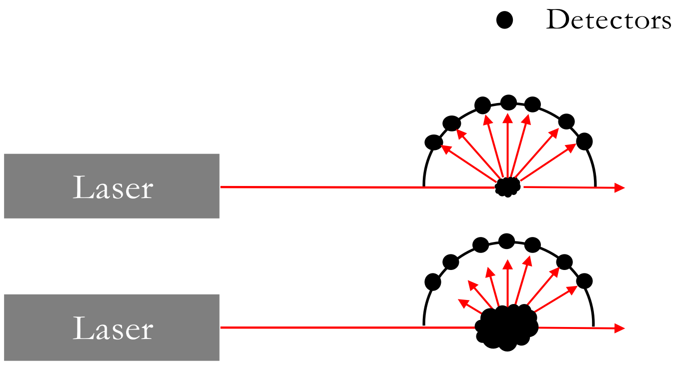

Figure 5: Schematic representation of the scattering intensities at different angles for molecules smaller than $\frac{\lambda_L}{20}$ (top) and for molecules larger than $\frac{\lambda_L}{20}$ (bottom). Adapted from [38].

By using the 'Rayleigh ratio', see Equation (18), the light scattering intensities can be characterized independently of the system with

$$R_\Theta = \frac{(I_\Theta - I_{\Theta,s})r^2}{I_0 V_0}. \tag{18}$$

Here, I_Θ and $I_{\Theta,s}$ are the intensities of the scattered light for the sample and the solvent at the respective scattering angle θ. I_0 is the irradiated light intensity of the laser, r is the distance between the measuring volume and the detector and V_0 is the measuring volume, i.e. the volume of the sample [34]. In addition, a general relationship can be established for the 'Rayleigh ratio'

$$R_\Theta = K^* \sum_i c_i^{(m)} M_i. \tag{19}$$

This applies to diluted, polydisperse samples. With

$$\sum_i c_i^{(m)} M_i = c^{(m)} \overline{M}_w, \tag{20}$$

Equation (19) can be developed [34] to

$$\frac{K^* c^{(m)}}{R_\Theta} = \frac{1}{\bar{M}_w}. \tag{21}$$

In Equations (19) to (21), $c_i^{(m)}$ is the mass concentration of a polymer with chain length i and M_i is the corresponding molar mass. $\bar{M}_w$ describes the weight-average molecular weight and K^* is the optical constant of the detector, which is defined as

$$K^* = \frac{4\pi^2 n_0^2}{\lambda_L^4 N_A}\left(\frac{dn}{dc^{(m)}}\right)^2. \tag{22}$$

with n_0 the refractive index of the solvent, λ_L the wavelength of the irradiated light, N_A the Avogadro constant and $\frac{dn}{dc^{(m)}}$ the refractive index increment of the sample in the solvent [34].

In contrast to smaller molecules, the intensity of molecules larger than $\frac{\lambda_L}{20}$ depends on the scattering angle. The reason for this is the existence of several scattering centers, which lead to interference [34]. A schematic representation can be found in Figure 5. In order to include the angular dependence for large molecules, Equation (21) was extended by a shape factor [34] to the Zimm plot

$$\frac{K^* c^{(m)}}{R_\Theta} = \frac{1}{\bar{M}_w} + \frac{16\pi^2 \langle R_g^2 \rangle}{3\bar{M}_w \lambda_L^2} \sin^2\left(\frac{\Theta}{2}\right). \tag{23}$$

θ is the scattering angle and $\langle R_g^2 \rangle$ is the mean square radius of gyration. The Zimm plot can be used to determine the weight-average molecular weight and the mean square radius of gyration from the measured data. For this purpose, Equation (23) is plotted against $sin^2\left(\frac{\theta}{2}\right)$ and fitted by a polynomial relationship (usually linear). $\bar{M}_w$ results from extrapolation to the zero angle, i.e. from the point of intersection with the ordinate axis. The mean square radius of gyration can be determined from the gradient. For polydisperse samples with broad molecular weight distributions and large molecules, the angular dependence is not always linear. Therefore, in contrast to the Zimm plot, where $\bar{M}_w$ resp. the slope especially for branched polymers is overestimated, the Berry plot (Equation (24)) provides better results for high molecular weights. For this reason, the Berry plot

$$\sqrt{\frac{K^{*}c^{(m)}}{R_{\Theta}}} = \frac{1}{\overline{M}_w} + \frac{16\pi^2\langle R_g^2\rangle}{3\overline{M}_w\lambda_L^2}\sin^2\left(\frac{\Theta}{2}\right) \tag{24}$$

should preferably be used for random coils with high molecular weights [34].

2.3.5 Evaluation of experimental data[1]

By using high performance liquid chromatography (HPLC) monomer conversion is monitored along reaction time. The sample material is separated according to the polarity of the components and then analyzed with a UV detector. Thereby, the concentration of the sample component, in this case the monomer concentration, can be determined. From the feed monomer weight fraction w_M^+ and the monomer weight fraction of the sample w_M, the conversion in a CSTR can be calculated by

$$X_M = \frac{w_M^+ - w_M}{w_M^+}. \tag{25}$$

Measurements with concentration and molar mass sensitive detectors can determine the mass concentration $c^{(m)}$ and the weight-average molecular weight $\overline{M}_w$ as a function of time or the elution volume V_i^{elu}. The molecular weight averages can be calculated using

$$\overline{M}_w = \frac{\sum_i c^{(m)} M_i}{\sum_i c^{(m)}} \tag{26}$$

with the mass concentration $c^{(m)}$ and corresponding molecular weights M_i, while i indicates the i^th^ elution volume slice [34]. The weight fractions w_i at the corresponding elution volumes [34] are

$$w\left(V_i^{elu}\right) = \frac{c^{(m)}}{\sum_i c^{(m)}} \tag{27}$$

Since the data provided by the detectors are dependent on the selected separation system (GPC or FFF), Equation (27) needs to be converted to a molecular weight-dependent function $w(M_i)$ or

---

[1] The majority of this chapter has been published in advance of this thesis under the terms of the Creative Commons Attribution License (CC BY 4.0) in [81]. Minor changes have been made and passages have been added for better comprehensibility and embedding in the context of this thesis.

$w(logM_i)$. At this point, the usual logarithmic calibration curve $\log M(V_i^{elu})$ is used and the relationship

$$w(logM_i) = \pm w(V_i^{elu}) \frac{dV_i^{elu}}{dlogM_i} \tag{28}$$

is obtained [33], [34]. The choice of sign depends on the chosen separation method. For GPC, the sign must be chosen negative, since molecular weights decrease with increasing elution volume [33]. For FFF, the sign must be positive, as the molecular weight increases with increasing elution volume.

For the characterization of polymers, the radius of gyration R_g is often used, since this can provide information about the polymer size, independent of the molecular structures [33]. With the Berry plot (Equation (24) in Chapter 2.3.4), the radius of gyration can be calculated from the slope. To calculate the branching points of a polymer, the branching ratio from Equation (12) is used.

To determine the gyration radius for linear PVP molecules, the conformation plots of samples from CSTR experiments were analyzed with FFF for different average residence times (shown in Figure 6). Samples were taken at early operating times with polymer contents around 5 wt.-% and monomer conversions less than 50%. The plots coincide for all residence times. Therefore, the molecular structure of the polymers of the samples should be identical, which means short and unbranched chains. A relation can be approximated with a power law [34] by Equation (29). This correlation for the linear polymer chains was used for all further calculation of branching points.

$$\langle R_g^2 \rangle_{lin} = 10^{-2.01314} \cdot M^{0.615} \tag{29}$$

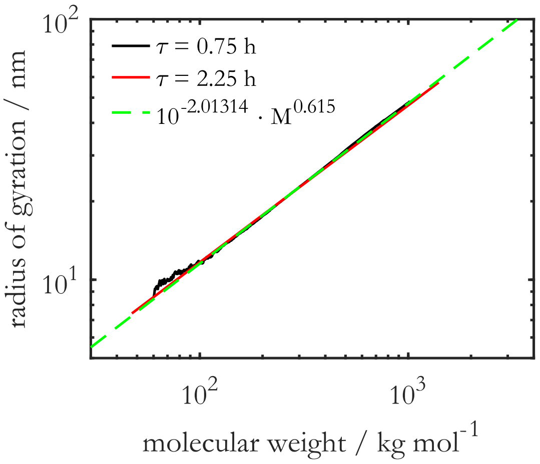

Figure 6: Comparison of the conformation plots from CSTR experiments with different average residence times at early operating times. The green dashed line is the power law fit, which is used as a linear reference.

The number of branches BP can be calculated assuming trifunctional branches, as depicted in Figure 3, (since during polymerization a monomer can form three bonds to further monomers [34], [39]) by

$$g = \left[\left(1 + \frac{BP}{7}\right)^{0.5} + \frac{4BP}{9\pi}\right]^{-0.5}. \tag{30}$$

2.3.6 Dynamic light scattering (DLS) to determine the diffusion coefficient between solvent and polymer

Dynamic light scattering (DLS), also known as photon correlation spectroscopy (PCS) or quasi-elastic light scattering (QELS), can be used to examine the diffusion behavior or diffusion coefficients of polymer solutions. DLS is therefore a technique that primarily measures the Brownian motion of macromolecules in solution and relates this to the size of particles. The size and form of macromolecules cause light to disperse in all directions when a monochromatic light beam comes into contact. When scattering static light, the intensity of the scattered light is analyzed as time-averaged intensity. This yields valuable details on the molecular weight and gyration radius of macromolecules. However, the translational diffusion coefficient $\mathfrak{D}_\tau$, which is connected to the hydrodynamic size of macromolecules, may be found by analyzing the intensity variations of the scattered light. Small particles mean rapid fluctuations in the intensity signal. Detailed information about the measurement system as well as the theory and application can be found in [40].

For DLS measurements, the intensity-time autocorrelation function

$$g^2(q;\tau) = \frac{< I(t)I(t+\tau) >}{< I(t) >^2} \tag{31}$$

is recorded, which may be represented as a normalized integral over the product of intensities I at time t and delayed time $(t + \tau)$ and depicts the migration of macromolecules [41]. For small molecules, the autocorrelation function therefore decays rapidly. g^2 is a function of the wave vector q and lag time τ. The autocorrelation function g^2 can be related to the field-time correlation function g^1 via the Siegert relation to

$$g^2(q;\tau) = 1 + \beta[g^1(q;\tau)]^2 \tag{32}$$

with the correction factor β. For monodisperse particles g^1 decays exponentially and is reliant on Γ, the decay constant, to

$$g^1\,(q;\tau) = exp(-\Gamma\tau). \tag{33}$$

For a polydisperse system g^1 can be represented as an intensity weighed integral over a distribution of decay rates $G(\Gamma)$

$$g^1(q;\tau) = \int_0^\infty G(\Gamma)\,exp(-\Gamma dT) \tag{34}$$

The decay rate can then be used to calculate the translational diffusion coefficient $\mathfrak{D}_\tau$ to

$$\Gamma = \mathfrak{D}_\tau q^2. \tag{35}$$

Different wave vectors q can be calculated with

$$q = \frac{4\pi n}{\lambda} \cdot sin\left(\frac{\theta}{2}\right), \tag{36}$$

where n is the solvent refractive index and λ the laser wavelength. Since DLS investigates the particle diffusion in a solvent, the obtained particle size is the hydrodynamic radius R_h, which can be determined from the Stokes-Einstein equation [33]

$$\mathfrak{D} = \frac{k_B T}{6\pi\eta R_h}. \tag{37}$$

Here k_B is the Boltzman constant, T the temperature, η the viscosity of the medium in which it is suspended and R the radius of the sphere.

2.4 Thermodynamics of polymers

The phase behavior of polymer solutions is crucial in the production and processing of polymers. Polymer solutions are complex solutions from a thermodynamic perspective. But still, the most common and at the same time simplest approach to describing polymers is that of the ideal mixture. A polymer is a composite of many components distinguished by its molecular weight distribution rather than a single component. For this reason, this chapter introduces a more complex type of thermodynamic description of polymer systems, the PC-SAFT (Pertubed Chain - Statistical Associating Fluid Theory) equation of state.

2.4.1 PC-SAFT equation of state

The PC-SAFT theory, developed by [42], [43], is a further development of the SAFT equation of state by adding the dispersion term. While the SAFT theory was only valid for spherical molecules, the new theory is extended to chain molecules, as each segment in the chain under consideration is again of spherical shape. Still, a hard-chain fluid serves as a reference for the perturbation theory. The equation of state is expressed as the total of the ideal gas contribution ($Z^{id} = 1$), the hard-chain term (hc) for repulsion, the dispersive part (disp), and the contribution owing to association (assoc) for the formation of hydrogen bonds, in terms of the compressibility factor Z to

$$Z = 1 + Z^{hc} + Z^{disp} + Z^{assoc}. \tag{38}$$

The newly added contribution of dispersion (disp) describes the van der Waals attractions. The individual contributions to the equation of state can be found in [42], [43]. The following five expressions are required for the complete parameterization of the model: the segment diameter σ_i, the segment number m_i, the dispersion energy parameter u_i/k_B, where k_B denotes the Boltzmann constant and the associating interactions between the association site A_i and B_i of a pure component i are determined by two pure-component parameters: the association energy $\epsilon^{A_iB_i}/k_B$ and the effective association volume $\kappa^{A_iB_i}$. However, the last two parameters are only necessary if the molecules of the substance under consideration can form hydrogen bonds. Moreover, a molecule's chemical structure influences the number of association sites N^{assoc}. In the case of a polymer, the number of these sites therefore increases with the chain length.

The PC-SAFT equation of state is already implemented in the FeOs framework [44] and only needs to be parameterized for the polymer system under investigation. The framework can be integrated into the programming language ‘python’ as a library.

2.4.2 Group contribution (GC) method for PC-SAFT parameters

As already mentioned, if PC-SAFT parameters are not known, they can be approximated using experimental data. Another possibility to determine parameters for a pure substance is the group-contribution (GC) method. In particular, the number of segments for a given molecule $m_{molecule}$ can be determined using this method according to [45] as

$$m_{molecule} = \sum_i n_i m_i, \tag{39}$$

where n_i denotes the number of contributions with the associated segment number m_i. This method is then applied schematically for the number of segments of N-vinylpyrrolidone. Figure 7 shows the applied GC-method to the molecular structure of NVP with the number of contributions of the respective end groups.

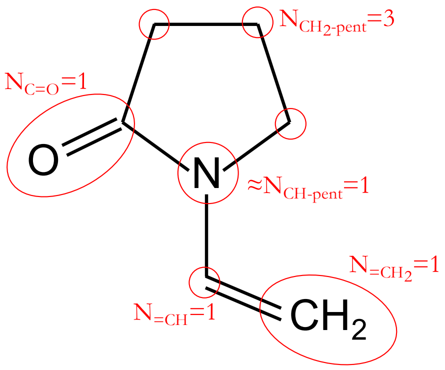

Figure 7: GC method applied to the molecular structure of NVP with number of contributions of the respective end groups (red circle).

The end group with the nitrogen is currently not implemented in the GC method of the FeOs framework and is therefore approximated via a CH-pent group. The segment number is calculated as follows

$$\begin{aligned} m_{NVP} &= N_{CH_2-pent} \cdot m_{CH_2-pent} + N_{C=O} \cdot m_{C=O} + N_{CH-pent} \cdot m_{CH-pent} + N_{=CH} \\ &\quad \cdot m_{=CH} + N_{=CH_2} \cdot m_{=CH_2} \\ &= 3 \cdot 0.467 + 1 \cdot 1.223 + 1 \cdot 0.033 + 1 \cdot 0.564 + 1 \cdot 0.369 \\ &= 3.591 \end{aligned} \tag{40}$$

The remaining required parameters are approximated resp. fitted using experimental data from saturated vapor pressures of [46], [47] and densities of [48], and are shown in Table 1.

2.4.3 Modeling of mixtures with PC-SAFT

In the case of solution polymerization, the polymer system consists of a total of four components: the solvent, the monomer, the polymer and the initiator. As the latter is very small in relation to the other species, only a tertiary mixture is considered thermodynamically. A tertiary mixture can be modeled by means of the binary interactions of subsystems using PC-SAFT.

In [49], PC-SAFT parameters for polyvinylpyrrolidone (Kollidone 25, M_W=25700 g/mol) were determined and are displayed in Table 1. Furthermore, parameters for water were taken from the literature [50] and those for NVP were approximated in this work.

Table 1: PC-SAFT pure component parameter for PVP [49], Water [50] and NVP (this work).

	M_W g/mol	m^{seg}/M_W mol/g	σ	u/k_B K	$\epsilon^{A_iB_i}/k_B$ K	$\kappa^{A_iB_i}$ -	N^{assoc} -
PVP	25700	0.0407	2.710	205.599	0	0.02	231/231
Water	18.015	0.0555	2.938	272.028	3125.320	0.044	1/1
NVP	111.14	0.0316	3.481	322.857	0	0	1/1

Segment diameter σ and dispersion-energy u are the pure-component characteristics that are subject to mixing rules when modeling mixtures using PC-SAFT, as demonstrated by Equation (41) from [49]

$$\sigma_{ij} = \frac{1}{2}(\sigma_i + \sigma_j),$$
$$u_{ij} = \sqrt{u_i \cdot u_j}(1 - k_{ij}). \tag{41}$$

Deviations from the geometric mean of the dispersion-energy parameters of two distinct components are corrected by the binary-interaction parameter k_{ij}. By fitting this parameter to experimental data, PC-SAFT modeling's quantitative performance can be enhanced. The interaction parameter k_{ij} between PVP and water has been determined resp. fitted in [49] to experimentally conducted water-sorption isotherms to $k_{PVP,Water} = -0.1483$.

The interaction parameter $k_{PVP,NVP}$ between NVP and PVP can be determined with the vapor pressure of the binary system at $T = 85\ °C$, which was determined to be $p^{sat}(w_{NVP} = 0.57) = 2120\ Pa$. For vapor-liquid equilibrium the thermodynamic $\varphi - \varphi$-approach can be used [51]

$$x_i'\varphi_i' \ = \ x_i''\varphi_i'' \tag{42}$$

with the fugacity coefficient φ_i and the molar fraction x_i. The superscripts ' and " denote the first and second equilibrium phases, respectively. For the experimentally determined vapor (phase ") pressure, the Equation (42) applied to NVP is simplified to

$$ln(x'_{NVP}) + ln(\varphi'_{NVP}) - ln\,\varphi_{NVP}'' \ = \ 0, \tag{43}$$

because only NVP and no PVP can be in the vapor phase. The equation of state is now evaluated with different values for $k_{PVP,NVP}$ and Equation (43) is minimized by varying the system pressure. For each $k_{PVP,NVP}$, a system pressure can be obtained which can then be compared with the measured value to minimize

$$ln(p_{model}) - ln\,(p_{exp}) \ = \ 0. \tag{44}$$

This procedure is necessary because otherwise FeOs does not converge for the phase equilibrium. The interaction parameter therefore can be approximated to $k_{PVP,NVP} = 0.2061$. Due to the fact that only one value was used to determine the interaction parameter, this value is not very reliable. It is rather qualitatively about the procedure.

Further, it is assumed that the interaction between water and NVP is very small compared to the interaction between polymer and solvent or monomer. The interaction parameter is therefore set to $k_{NVP,Water} = 0$.

2.4.4 Neural networks as a machine learning tool for the approximation of characteristic maps

Neural networks (NN) were developed by modelling the networking of neurons in the nervous system of a living being. An NN is an abstract model for information processing and is trained using a very large amount of data (machine learning) [52]. The structure of an NN can be interpreted as a "map" with different layers as depicted in Figure 8 with a layer size of 2.

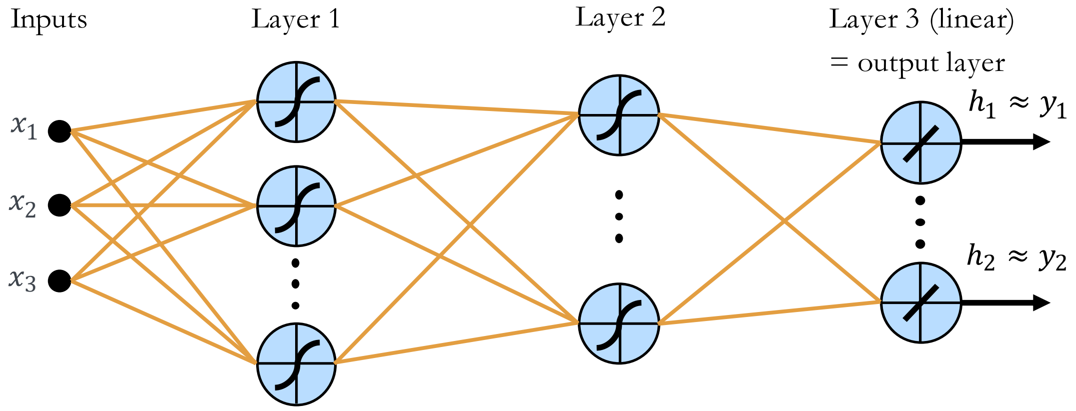

Figure 8: Schematic structure of a neural network.

Several inputs and outputs are possible. After the construction of the neural network, which determines the number of layers and neurons, the training takes place. This involves training the individual weights and biases of the inputs and layers. The output of the layer 1 can mathematically be described as:

$$h_{1,1}(\overline{x}, \overline{w}) = \sum_{j=0}^{M} w_{1j}^{(2)}\, tanh\left(\sum_{i=0}^{D} w_{ji}^{(1)} x_i\right) \tag{45}$$

with the input x and the weights/bias w. For the output of the output layer an activation function is no longer used

$$h_1(\overline{x},\overline{w}) = \sum_{j=0}^{M} w_{1j}^{(3)} h_{j,2}. \tag{46}$$

The following optimization problem arises

$$res = min\ (||h(x,w) - y)||_2) \tag{47}$$

with the value to be approximated y. Numerical methods like Levenberg-Marquardt can be used to solve the optimization problem.

3 Experimental findings

Understanding and mitigating fouling in continuous reactors is a huge challenge in industrial chemical processes, particularly where efficiency and longevity of the reactors are of specific importance. As stated in the introduction, fouling can significantly impact reactor performance, leading to increased pressure drops, reduced heat transfer efficiency, and ultimately, reactor shutdown. Addressing this issue requires a thorough examination of the mechanisms driving fouling and the effectiveness of various mitigation strategies.

In this chapter, a comprehensive experimental exploration of fouling in continuous tubular reactors, including capillary reactors and a half-shell reactor with static mixing elements, is provided. The intricacies of the various measuring technologies, process conditions and reactor geometries are explained. This chapter therefore includes residence time measurements, optical assessments using UV/VIS technology, the evaluation of hydrophobic coatings and cleaning methods. This offers a multi-faceted understanding of how fouling manifests and can be controlled.

The findings presented in this chapter provide a depiction of fouling phenomena, revealing the formation of highly viscous wall layers at reactor surfaces that eventually lead to gelation and polymer fouling. The impact of modifying process conditions, such as reducing monomer or initiator concentrations, and the benefits of increased flow velocity and larger reactor cross-sections are highlighted. Additionally, the efficiency of hydrophobic coatings in reducing fouling is discussed, alongside the potential for chemical cleaning as a last resort.

Building on these experimental insights, the subsequent aim is to develop a model that accurately describes and predicts fouling in continuous reactors. This model will integrate the knowledge gained from the experimental investigations, paving the way for more efficient reactor design and operation, enhancing process reliability and performance in industry.

3.1 Residence time distribution measurements in a capillary tubular reactor

In contrast to the pressure signal, residence time measurements can provide a significantly earlier indication of deposit formation. In this chapter, residence time measurements using a salt tracer and a conductivity cell are used to identify not only differences in viscosity but also the buildup of a wall layer. The method is applied to geometrically particularly simple reactors, the capillary reactors. Besides different process conditions, different geometric variations of the capillary reactor and their effect will also be tested.

3.1.1 Experimental setup[2]

A reaction system with capillary tubular reactors has been set up, where the residence time distributions at different times of the reaction can be recorded. In Figure 9 the simplified flow sheet for the reaction system is shown. Two storage containers were prepared, one containing a mixture of monomer and solvent, the other containing initiator dissolved in the solvent. Both containers were degassed under vacuum. The feed streams were pumped by two Knauer Smartline 1050 HPLC piston pumps equipped with 50 ml pump heads and controlled by employing Bronkhorst Coriolis mass flow meters and PI controllers. The feed streams from both tanks were mixed in a 1:1 ratio by using a dynamic mixing chamber (Knauer Wissenschaftliche Geräte GmbH) at room temperature to ensure good mixing quality before entering the reactor. A HPLC switching valve (two position microelectric valve actuator (8 ports) by VICI Valco Instruments Co. Inc.) is used to pulse a tracer solution in the reaction medium. 1 molar NaCl (Sodium chlorite) solution was used as a tracer. The capillary tubular reactor (stainless steel 1.4435 by Swagelok Company) is then placed in a tempered oil bath (VWR) to conduct polymerizations at a temperature of T=85 °C. At the end of the reactor a conductivity measurement with a flow-thru conductivity electrode (ET908 with 93 µl of eDAQ Pty Ltd) is conducted. With this setup the formation of a wall layer can be observed by measuring the residence time distribution.

---

[2] The majority of this chapter has been published in advance of this thesis under the terms of the Creative Commons Attribution License (CC BY 4.0) in [82]. Minor changes have been made and passages have been added for better comprehensibility and embedding in the context of this thesis.

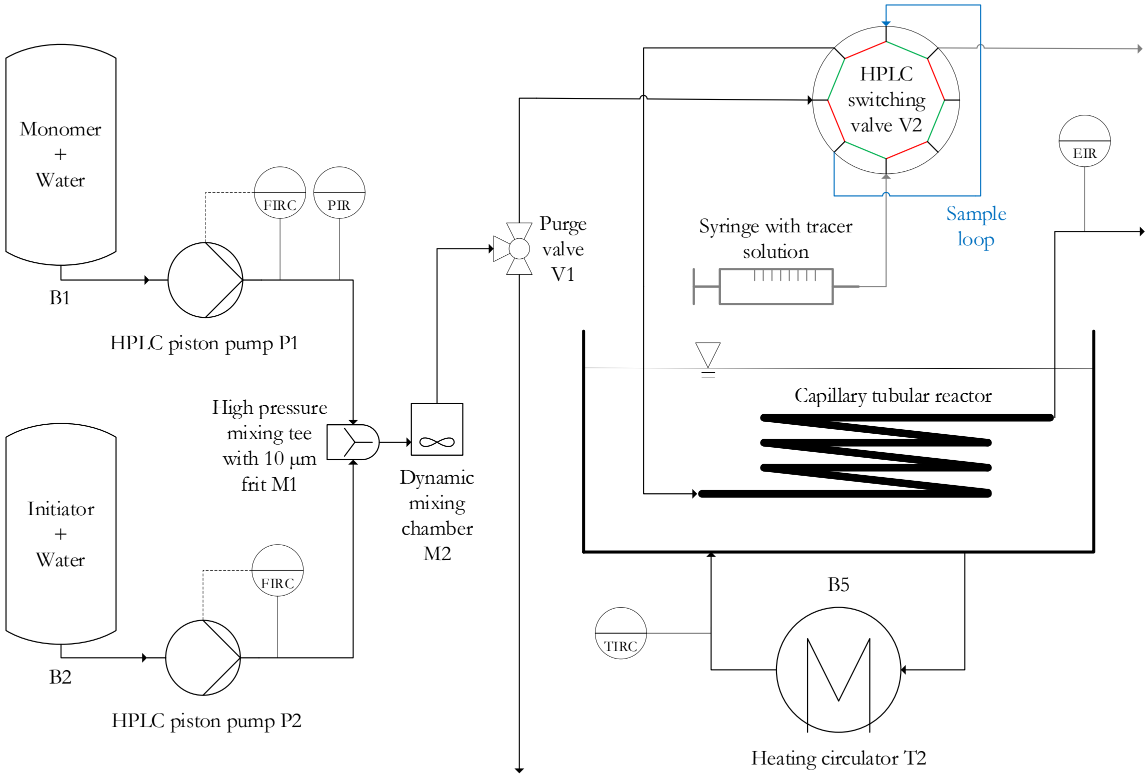

Figure 9: Simplified flow sheet for the reaction system for the polymerization of N-Vinylpyrrolidone. Adapted from [7].

3.1.2 Residence time distributions for different feed conditions

In Table 2 the reactor and process conditions are presented. The winding diameter was chosen to be higher as 400 mm so that low dean numbers are achieved, and secondary flows are prevented. The flow velocity of v=12 mm/s corresponds to a mean residence time of approx. 250 s in the reactor.

Table 2: Reactor and process conditions for experimental residence time distributions for different feed conditions.

Reactor geometry	**Process conditions**
Length: $l = 3000\ mm$	Monomer feed concentration:
	$w_M = 5 - 20\ wt.-\%$
Inner diameter: $d_i = 1.76\ mm$	Initiator feed concentration:
	$w_I = 0.002 - 0.02\ wt.-\%$
Winding diameter: $d_w > 400\ mm$	Mean flow velocity:
	$v = 12\ mm/s$
	Reactor temperature: $T = 85\ °C$

Figure 10 shows the idealized input signal and the response signal. The input signal was idealized as a Dirac function, since only a qualitative comparison of the growth of the deposit formation was aimed at. For the comparison over time, the measured signal at the output of the reactor (response signal) is considered. In the output signal in Figure 10 for a feed concentration of w_M=20 wt.-% and w_I=0.02 wt.-%, it can be seen, that the baseline of the current signal rises shortly after the start of the experiment. This increase is due to the reaction medium breaking through since the initiator has a higher conductivity than water (initial filling). The signal height of the peaks decreases with time.

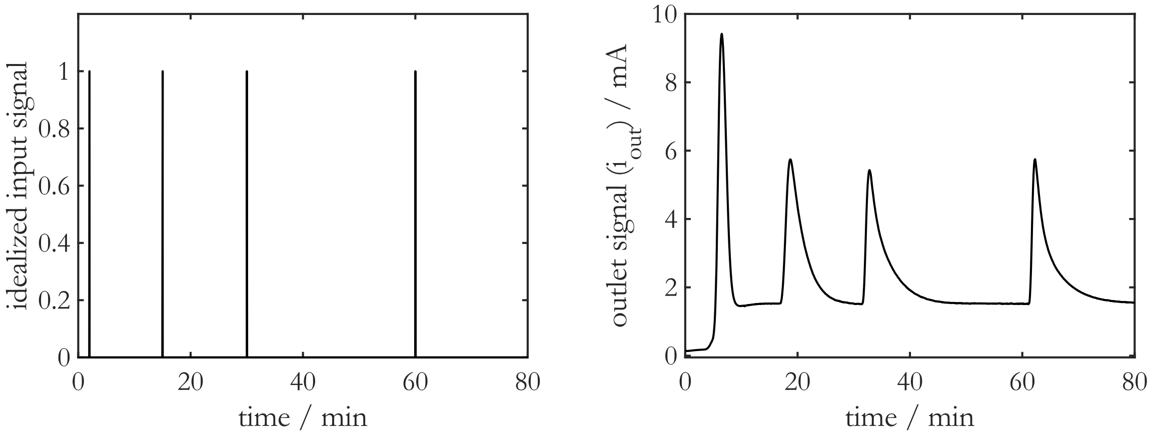

Figure 10: Idealized input and measured output signal of the conductivity measurement cell.

To be able to make a comparison between the different injection times, the baseline, which takes the increase in conductivity due to the addition of the initiator into account, was subtracted from the output signal. Further, all signals are area-normalized with the water signal, which is recorded prior each experiment. Figure 11 shows the area normalized response signal of the conductivity cell multiplied by the average residence time at different injection times for a feed concentration of w_M=20 wt.-% and w_I=0.02 wt.-%. As the operation time progresses (2-60 min), the signal breaks through earlier and overall, a longer signal tailing occurs. At the same time, the height of the signal peak becomes smaller. This is due the fact that, because of the layer formation on the wall the cross-section decreases, and a faster channel flow occurs, which consequently breaks through earlier. In contrast, a certain amount of the tracer diffuses into this wall layer and thus creates the tailing in the signal. From an operating time of 60 min, the residence time behavior changes slightly. After 24 h, a part of the wall layer has been torn off, allowing the signal to break through earlier. At the outlet of the reactor, this can be visually observed by extremely long non-solvable polymer. After a one-hour water flush with increased flow rate, a signal was again recorded with water. The distribution of the initial state couldn't be restored, which means that there is still a polymer layer on the reactor surface.

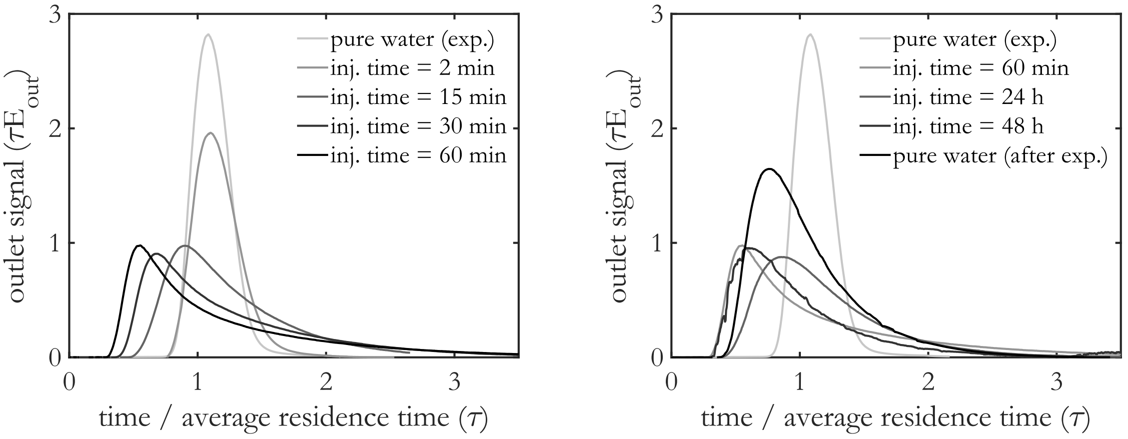

Figure 11: Evolution of the area-normalized response signal E_{out} at different times for w_M=20 wt.-% and w_I=0.02 wt.-%.

Figure 12 shows the area-normalized response signal of the conductivity measuring cell at different times for a feed concentration of w_M=5 wt.-% and w_I=0.02 wt.-%. The trend is also clear in this figure towards longer tailing and slightly earlier breakthrough as the operating time progresses. Compared to Figure 11, however, it should be noted that the flattening of the signal occurs much more slowly, and the tailing is not very pronounced. This suggests that at a lower monomer content, gelation or fouling occurs later than at higher monomer contents. From an operating time of 60 min, it can be observed that the geometry and the formation of the wall layer no longer change. However, the residence time distribution after 72 h is somewhat unsteady due to the viscous layer and gel formation. After the 1 h water rinse, a signal was again recorded with water. However, the initial condition could not be restored.

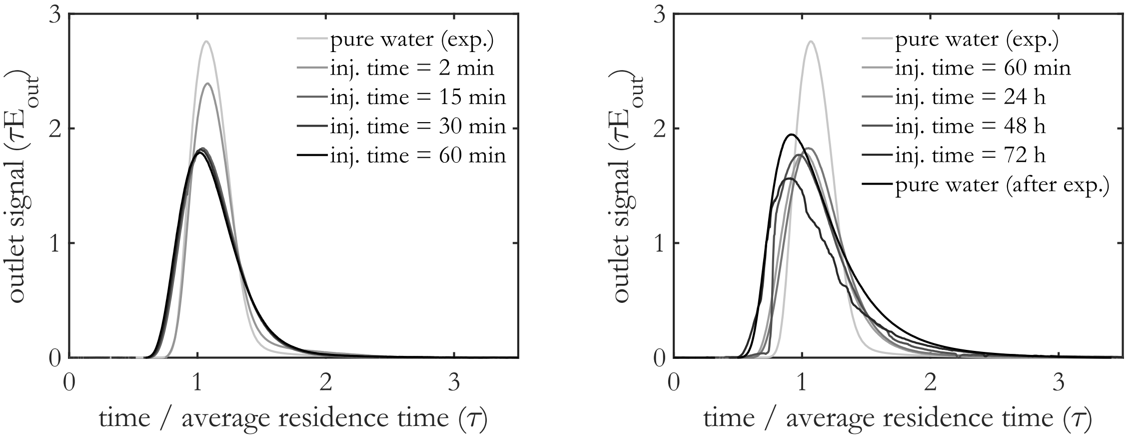

Figure 12: Evolution of the area-normalized response signal E_{out} at different times for w_M=5 wt.-% and w_I=0.02 wt.-%.

Figure 13 shows the area normalized response signal of the conductivity cell at different time points for a feed concentration of w_M=20 wt.-% and w_I=0.002 wt.-%. Even for such a low initiator concentration, the trend is visible that the peak of the tracer becomes smaller for progressing operating times (2-60 min) and the tailing is increased. However, compared to Figure 11, this behavior is much less visible. This means that the formation of the wall layer is much smaller. After an operating time of 60 min or more, no change in the wall layer can be observed (Figure 13 right). After a water rinse following 72 hours of operation, the original behavior can even be restored. This means that no volume-changing or macroscopically no wall layer is present after flushing.

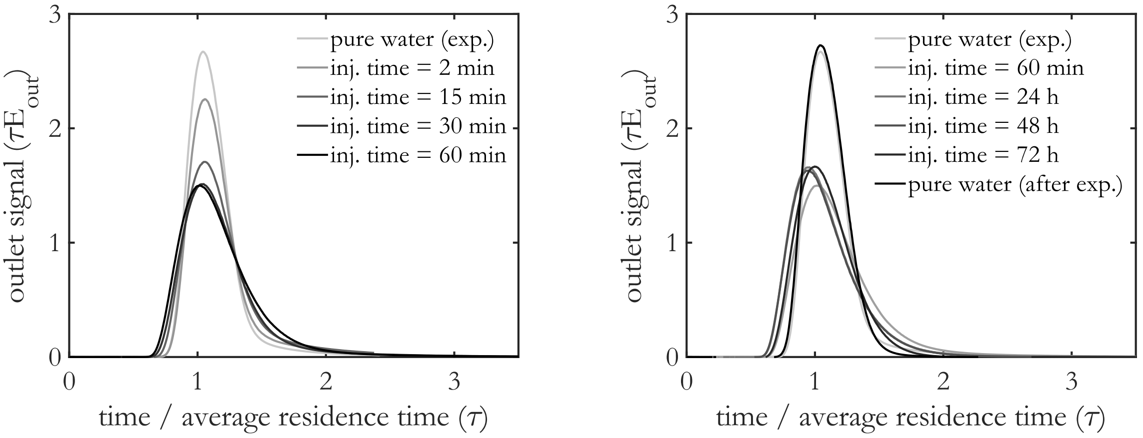

Figure 13: Evolution of the area-normalized response signal E_{out} at different times for w_M=20 wt.-% and w_I=0.002 wt.-%.

To achieve a better comparison of the different process conditions, the distributions of the different process conditions are shown in Figure 14 for an operating time of 60 min. A greater wall layer formation occurs earlier at process conditions of feed concentrations of w_M=20 wt.-% and w_I=0.02 wt.-%. Lower monomer and initiator concentration therefore mean a less pronounced wall layer.

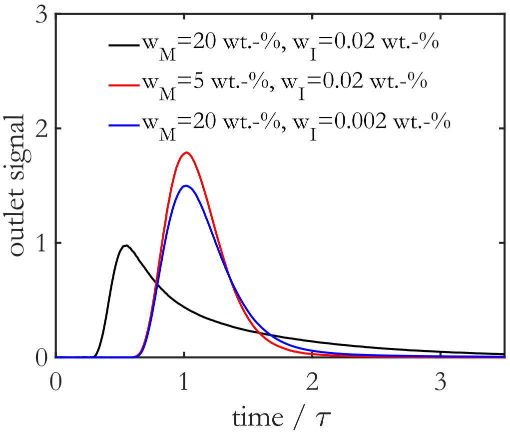

Figure 14: Evolution of the area-normalized response signal E_{out} at 60 min reaction time for different process conditions.

Figure 122 and 123 in the appendix complete the residence time measurements of this series with different process conditions and confirm the trend that with higher monomer and initiator feed concentrations a more predicted wall layer is formed, and stronger fouling occurs. These are therefore not listed here in detail.

For a direct comparison of the process conditions, the pressure curves for the different tests are also shown. Figure 15 shows the pressure curve for the monomer feed concentrations w_M=5 wt.-%, w_M=10 wt.-% and w_M=20 wt.-% with an initiator content of w_I=0.02 wt.-%. The pressure increases somewhat at the beginning of the tests due to the viscosity change. At the same time, with w_M=20 wt.-% a strong pressure increase occurs significantly approx. 24 h, whereas with w_M=10 wt.-% the pressure increase occurs after approx. 35 h and for w_M=5 wt.-% after approx. 45 h. The pressure peak for the highest monomer concentration is followed by a pressure drop and stronger fluctuations of the pressure signal until a strong increase of the signal occurs again. This progression suggests that the gel formed closes the reactors cross-section after a certain time. Due to a certain pressure, the gel is entrained, and the reactor is flushed free. The experiment with w_M=20 wt.-% was stopped after 48 h of operation due to the strong pressure increase.

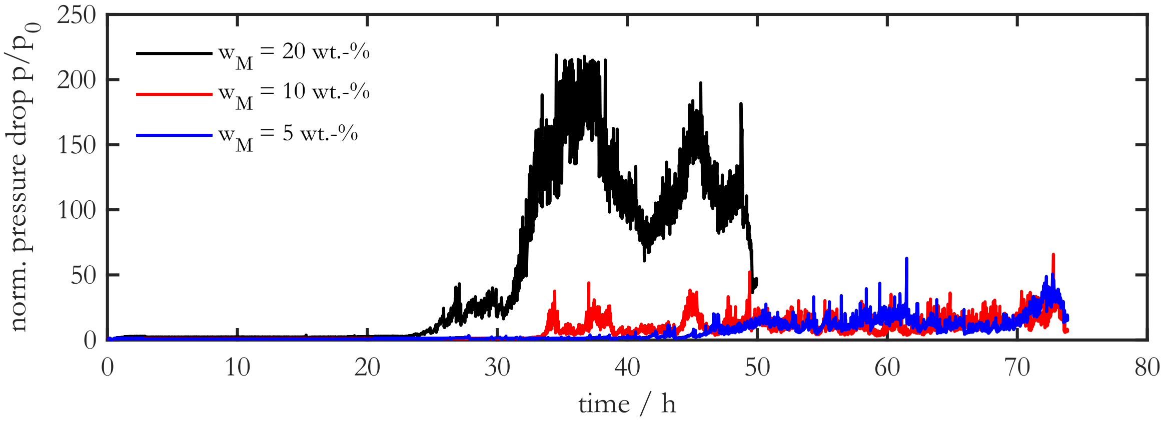

Figure 15: Pressure curve over the entire operating time for different monomer concentrations at an initiator content of w_I=0.02 wt.-%.

Figure 16 shows the corresponding monomer conversion curve for the individual monomer concentrations over the operating time. In both cases, the narrowing of the cross-section due to the formation of the wall layer leads to a slight decrease in conversion. At a monomer concentration of w_M=20 wt.-%, however, this decrease takes place much earlier. At a monomer content of 20 wt.-%, the polymer content in the solution is the highest compared to the other feed concentrations and it can be concluded that a high polymer content has a negative effect on the fouling behavior.

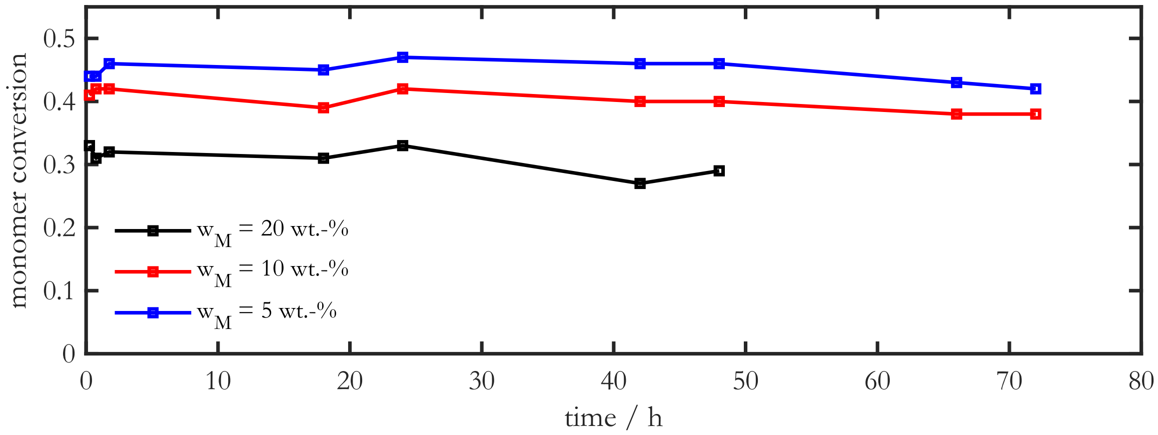

Figure 16: Conversion curve over the entire operating time for different monomer concentrations at an initiator content of w_I=0.02 wt.-%.

The pressure signal for the initiator variation is then presented in Figure 17. As in the previous figure, there is initially an increase in pressure due to the viscosity increase caused by the reaction. A lower initiator content (w_I=0.007 wt.-%.) shifts the point in time for the strong pressure increase whereas a very low initiator content (w_I=0.002 wt.-%.) does not result in a pressure peak at all, which suggests that reactor blocking does not occur.

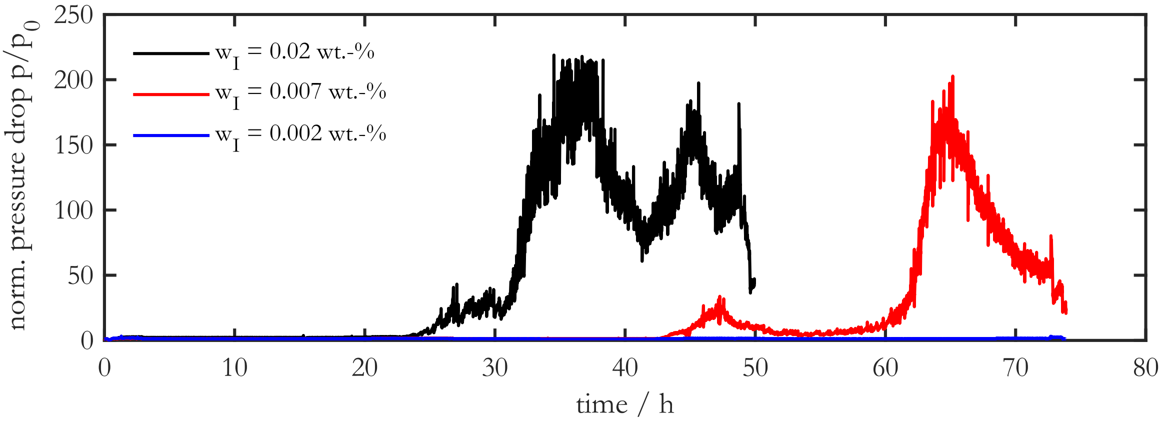

Figure 17: Pressure curve over the entire operating time for different initiator concentrations at a monomer content of w_M=20 wt.-%.

Figure 18 also shows the conversion curve for the initiator variation. It can be seen, that at an initiator concentration of w_I=0.002 wt.-%, the conversion fluctuates between 4-8 %, because fewer monomer radicals are formed. In general, however, the chains of the polymers are longer. Due to this low conversion, there is no gel formation and thus no pressure increase. When varying the initiator concentration, the polymer content is directly dependent on the conversion while the monomer concentration remains constant. It can therefore be said that the polymer content is highest with a high initiator content and therefore fouling occurs most strongly.

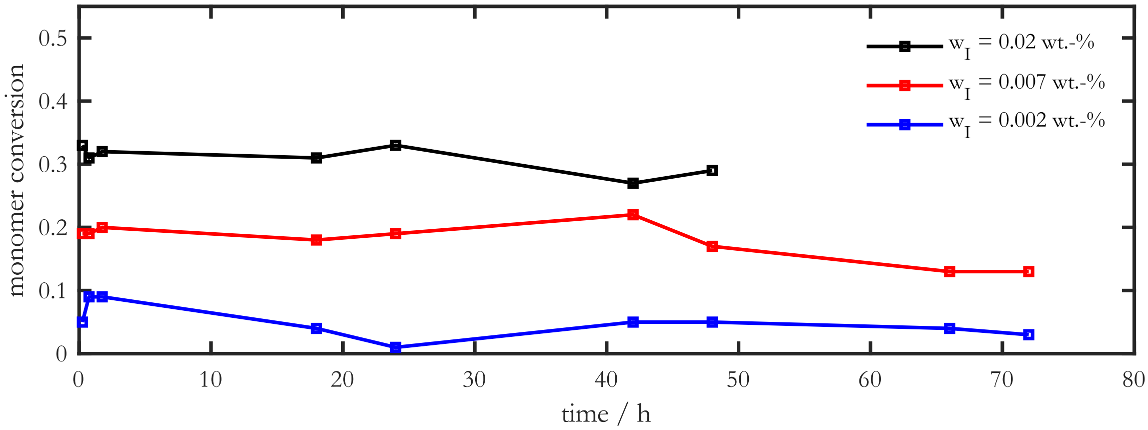

Figure 18: Conversion curve over the entire operating time for different monomer concentrations at an initiator content of w_M=20 wt.-%.

In summary, at a standard feed concentration of w_M=20 wt.-% and w_I=0.02 wt.-%, a highly viscous wall layer is formed, and pressure increase takes place due to gelation with increasing operating time. At a lower monomer concentration of w_M=5 wt.-%, a later and significantly lower formation of the wall layer takes place. The pressure increase due to fouling is much lower, resulting in significantly longer operating time. At a lower initiator concentration of w_I=0.002 wt.-%, the buildup of a viscous wall layer is visible, but no gelation occurs due to the low conversion. The pressure therefore remains at the initial level.

In addition to the determination of the conversion, the molecular weight distribution, the mass average molecular weight and the branching point distribution could be determined using GPC analysis. Figure 19 shows the average molecular weight for different monomer and initiator feed concentrations. The molecular weight increases with increasing monomer content. Nevertheless, the measured values fluctuate significantly more. As the initiator concentration increases, the molecular weight is also higher in some cases, which is actually contradictory. However, it was found that at higher initiator concentrations the wall layer formation starts much earlier and more strongly and it can be assumed that therefore long polymer chains accumulate at the reactor wall and shorter chains are found at the outlet.

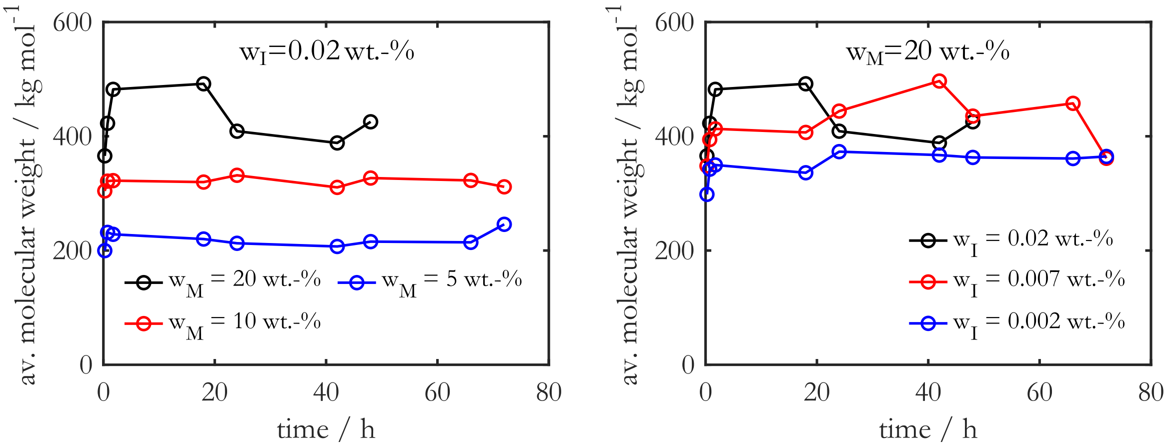

Figure 19: Comparison of the evolution of the weight average molecular weight from experiments at different monomer feed concentrations with w_I=0.02 wt.-% (left) and different initiator feed concentrations with w_M=20 wt.-% (right).

In Figure 20 the molecular weight distribution after 48 h reaction time for different feed conditions is illustrated. For higher monomer and initiator concentrations, the distribution becomes significantly broader, whereby $\overline{M}_W$ is almost identical for w_I=0.02 wt.-% and w_I=0.007 wt.-%. This underlines that short but also long polymers (presumably from the wall layer) are flushed to the reactor outlet.

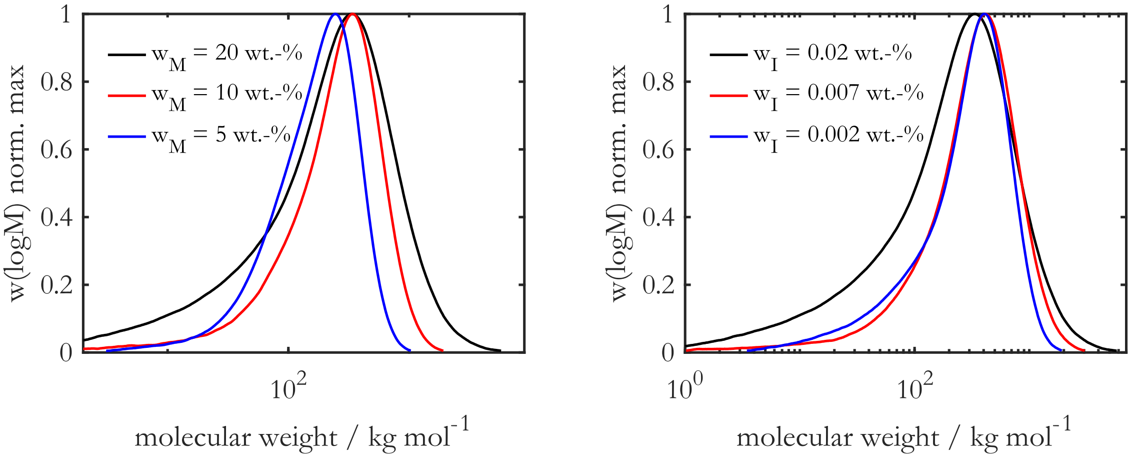

Figure 20: Comparison of the normalized GPC distribution from experiments for different monomer feed concentrations with w_I=0.02 wt.-% (left) and different initiator feed concentrations with w_M=20 wt.-% (right) at t=48 h.

The branching points were calculated according to Chapter 2.3.5 and are displayed in Figure 21. As the monomer concentration decreases, even small polymer molecules carry more branching points. However, at higher monomer concentrations, longer chains are formed overall, which ultimately carry more branches. Increasing initiator concentration in the feed stream, results in an increase in the average number of branching points in Figure 21 (right). A higher initiator concentration, results in a higher monomer conversion, resulting in lower monomer concentration in the system. Due to the dependence of the side reactions on the monomer concentration, the number of BPs increases with increasing initiator concentration in the feed.

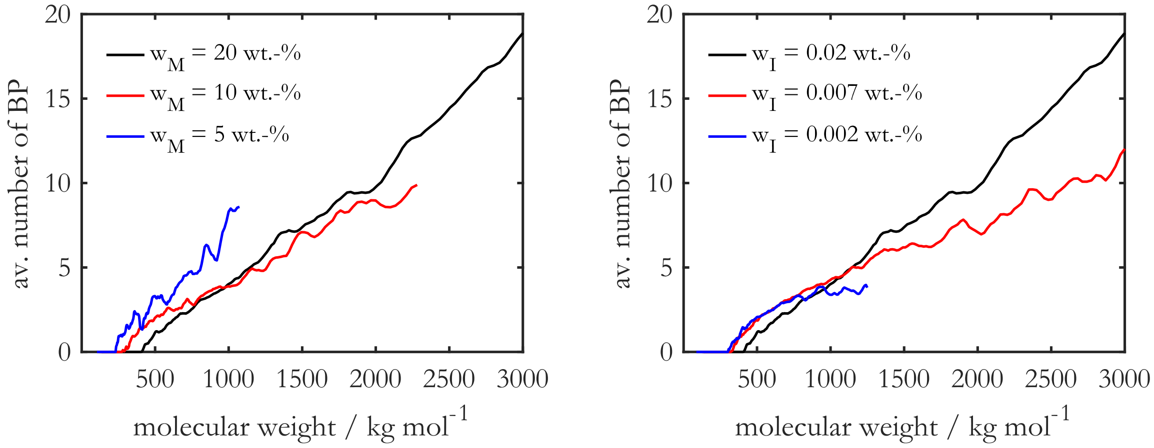

Figure 21: Comparison of the av. number of branches from experiments for different monomer feed concentrations with w_I=0.02 wt.-% (left) and different initiator feed concentrations with w_M=20 wt.-% (right) at t=48 h.

Therefore, from a reaction kinetics point of view, it is understandable that fouling occurs earlier and more strongly when a higher monomer and initiator feed concentration is used. This is discussed in more detail in Chapter 4. Figure 22 shows the GPC distribution and the branching points for different reaction times for a feed condition of w_M=20 wt.-% and w_I=0.02 wt.-%. As the reaction time increases, the GPC distribution becomes broader. The number of branches only increases after 24 h for very long molecules.

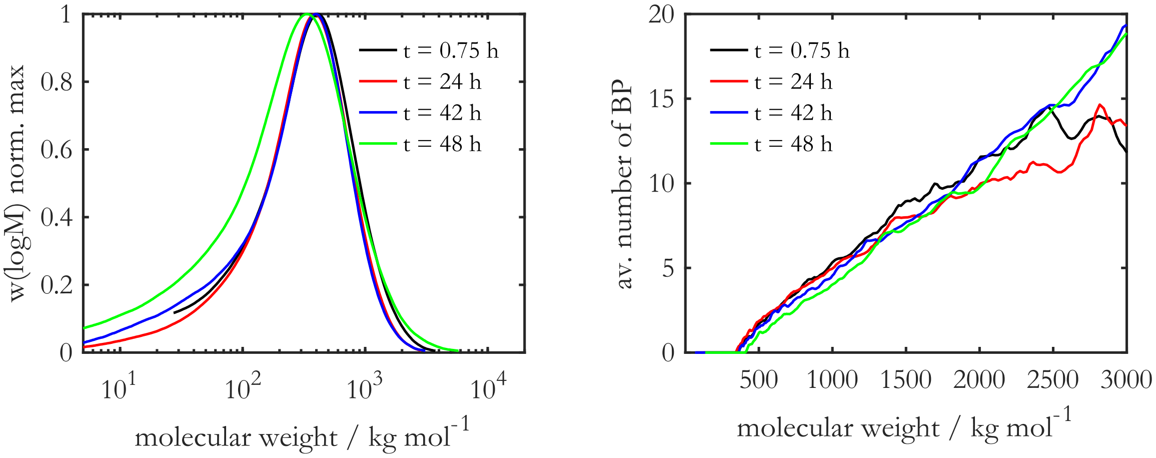

Figure 22: Comparison of the normalized GPC distribution (left) and av. number of branches (right) from experiments for different operating times at w_M=20 wt.-% and w_I=0.02 wt.-%.

3.1.3 Residence time distributions for different geometric reactor variations[3]

Different capillary reactors were used under constant process conditions to investigate the influence of different geometry factors on wall layer formation. The process conditions were selected according to Table 2 with a monomer feed content of w_M=20 wt.-% and an initiator feed concentration of w_I=0.02 wt.-%.

To check the influence of flow velocity on wall layer formation, the flow velocity was increased while the average residence time kept constant by adjusting the reactor length accordingly. First, a flow velocity of v=24 mm/s and a reactor length of l=6 m is presented. Therefore, in Figure 23 the development of the residence time distribution is shown. Compared to Figure 11 (v=12 mm/s and

---

[3] The majority of this chapter has been published in advance of this thesis under the terms of the Creative Commons Attribution License (CC BY 4.0) in [85]. Minor changes have been made and passages have been added for better comprehensibility and embedding in the context of this thesis.

l=3 m), the breakthrough of the tracer happens later for operating times up to 60 min. This means that the cross section of the reactor is reduced less and therefore the main flow is faster in relation to the shorter reactor with lower flow velocity.

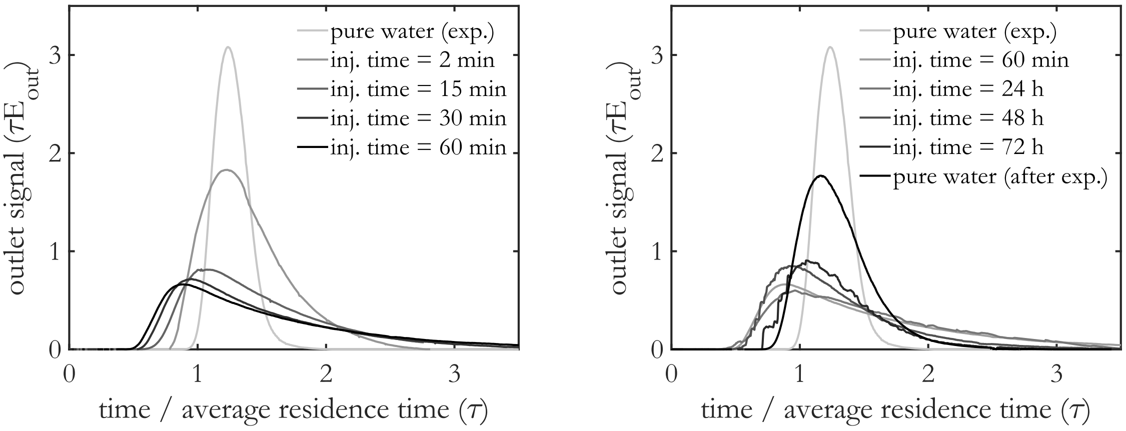

Figure 23: Evolution of the area-normalized response signal Eout at different times for v=24 mm/s, l=6 m and d_i = 1.76 mm.

In addition to an extended reactor with double the flow rate, a reactor with a larger diameter but with a higher mass flow rate was tested for comparison, so that the residence time was kept constant. The inner diameter was chosen to d_i=3.05 mm instead of 1.76 mm and the reactor's length of l=3 m at a flow velocity of v=12 mm/s. Figure 24 shows the residence curves for different operating times. Compared to Figure 11, the formation of the wall layer takes place in a similar time frame. The tailing of the distributions (especially for times less than 60 min) is much more pronounced than in Figure 11. This can be explained by the fact that the wall layer in the reactor is significantly thicker and therefore diffusion processes of the tracer become more dominant. Furthermore, the distributions become very unsteady after 48 h of operation, which also indicates a thick wall layer. After operation, this wall layer can only be rinsed off very moderately and a certain PVP layer remains.

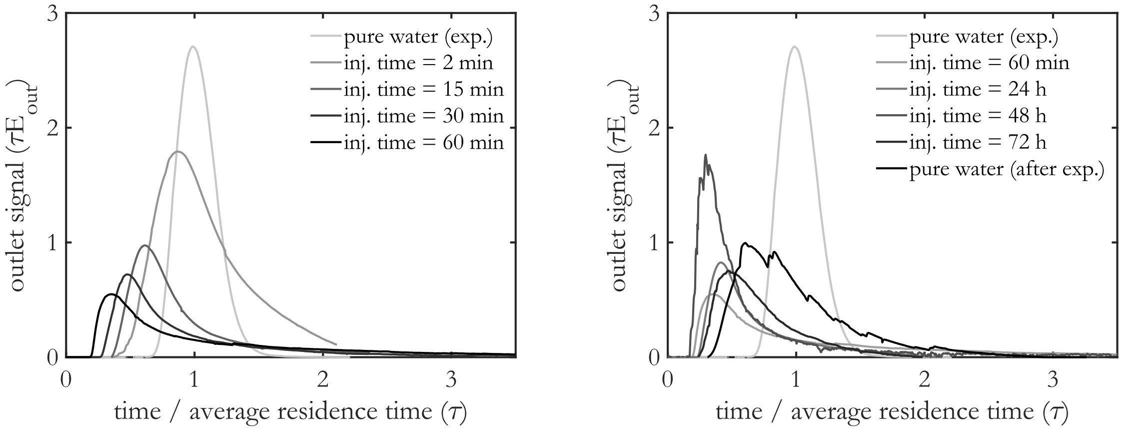

Figure 24: Evolution of the area-normalized response signal Eout at different times for v = 12 mm/s, l=3 m and d_i = 3.05 mm.

Figure 25 shows a comparison at an operating time of 60 min for the different geometries. A larger reactor cross-section therefore means a more pronounced wall layer, whereas a longer reactor shows better residence time behavior after 60 min, which means that the wall layer is less pronounced.

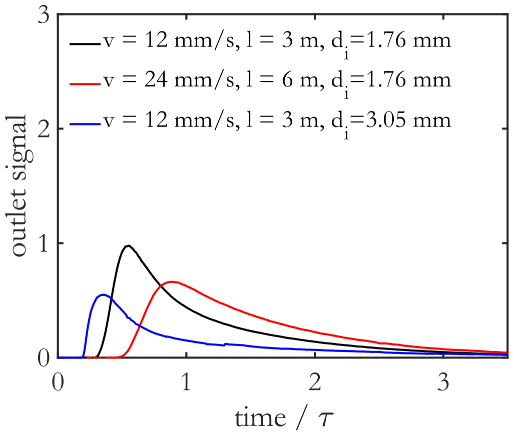

Figure 25: Evolution of area-normalized response signal E_{out} at 60 min reaction time for different reactor geometries. Signals are area-normalized with the pure water signal.

The pressure signal in Figure 26 shows that blockages, which lead to an increase in pressure, occur much later at increased flow velocity (from approx. 30 h operating time). At the same time, blockages are flushed out much faster due to the increased flow velocity and thus increase the pressure drop only moderately. Therefore, an operating time of 72 h could be tested, whereas the shorter reactor with lower flow velocity was operated for only 48 h. The same phenomenon can be seen with larger reactor diameters. The pressure starts to rise much later and at the same time less strong than in the standard reactor.

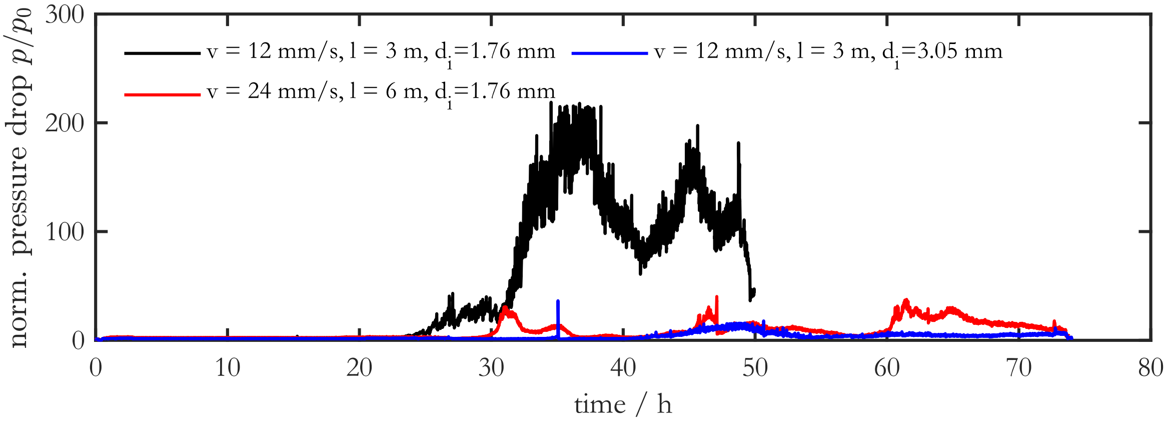

Figure 26: Pressure curve over the entire operating time for different geometric reactor conditions at a monomer content of w_M=20 wt.-% and an initiator concentration of w_I=0.02 wt.-%.

In addition to the residence time and pressure measurements, the monomer conversion has been determined. This is shown in Figure 27. The same average residence time results in similar conversions. Only the conversion curve of the reactor with the larger diameter experiences very strong fluctuations.

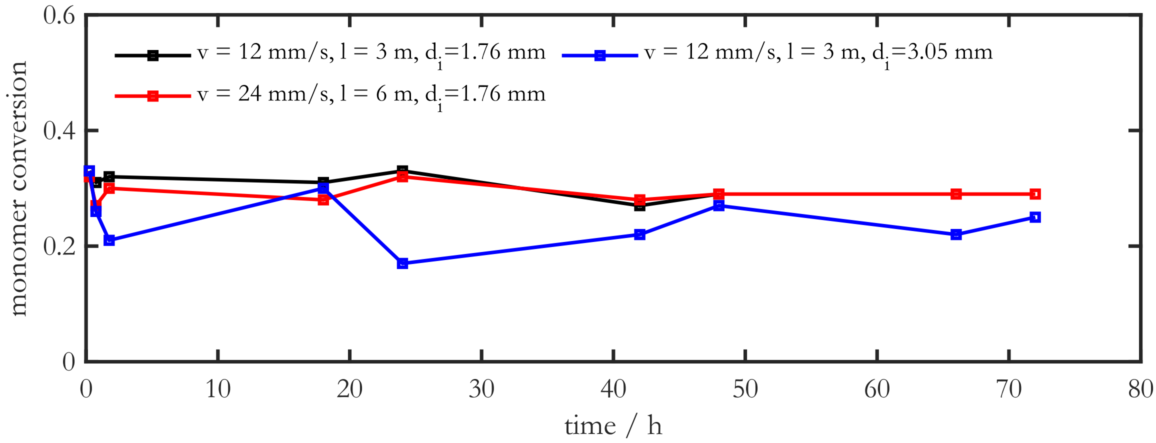

Figure 27: Conversion curve over the entire operation for different geometric reactor conditions at a monomer content of w_M=20 wt.-% and an initiator concentration of w_I=0.02 wt.-%.

A polymer analysis could also be carried out for the different geometric conditions of the reactor. Figure 28 and 29 clearly show that the reactor geometry has very little influence on the polymer structure. The average molecular weight of the reactor with a length of l=6 m fluctuates less and is slightly lower.

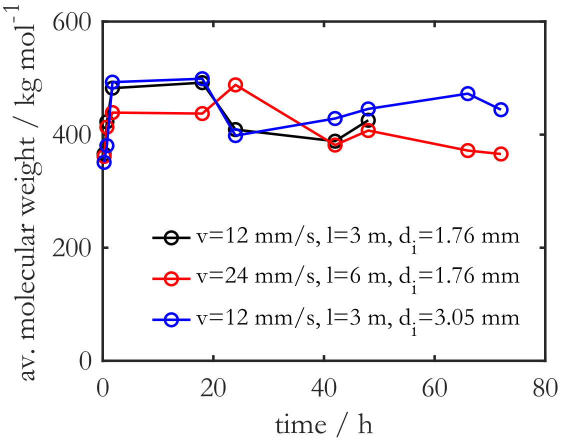

Figure 28: Comparison of the evolution of the weight average molecular weight from experiments at different geometric conditions at a monomer content of w_M=20 wt.-% and an initiator concentration of w_I=0.02 wt.-%.

The same applies to the GPC distribution and the branches, which are displayed at an operating time of t=48 h in Figure 29. Both a narrower distribution and fewer branches can be found for the reactor with l=6 m and increased flow velocity. The reactor with the largest cross-section showed most branching points.

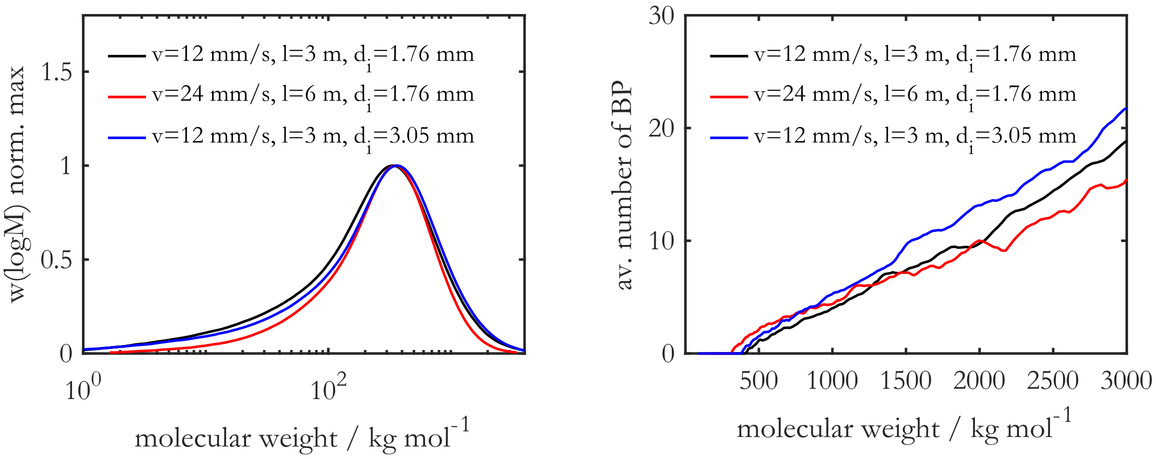

Figure 29: Comparison of the normalized GPC distribution (left) and av. number of branches (right) from experiments for different geometric conditions with w_M=20 wt.-% and w_I=0.02 wt.-% at t=48 h.

3.1.4 Conclusions

In this Chapter residence time distributions for different feed conditions and reactor geometries were presented. These investigations reveal that a highly viscous wall layer forms in the capillary reactor during operation. This is indicated by the earlier break-through of the tracer and the prolonged tailing with increasing run time. The wall layer grows until an equilibrium between the viscosity and the shear force is reached caused by the convective flow, eventually leading to gelation and polymer fouling. Fouling and the resulting cross-sectional constriction or even blocking cause an increase in pressure, potentially leading to reactor shut down.

Feed conditions have a major influence on the development and thickness of this wall layer. Higher monomer concentrations result in longer polymer chains, increased branching, polymer content and viscosity. With increased initiator content, the monomer conversion raises, further increasing viscosity. Both lead to increased and earlier fouling.

A change in geometry can positively affect reactor control without modifying the process conditions and therefore the polymer structure. With increased flow velocity, while maintaining residence time, the viscous wall layer builds up similarly in time to the reference case. However, the cross-sectional constriction is less severe, due to increased shear, which entrain polymers more effectively. The wall layer exhibits similar behavior as soon as gelation sets in. Due to the higher shear force, branched polymers are torn off and transported away by the main flow, making the reactor less prone to blockages and easier to flush out. The experiment with an increased reactor inner diameter shows a similar behavior. Once again, a wall layer builds up similar to the reference case, but it is significantly thicker due to the larger cross-section of the reactor resp. higher mass flow as evidenced by higher tailing of the residence time curves. However, due to the lower surface area to volume ratio, the formation of this wall layer is not as noticeable in the pressure signal, as the channel flow has sufficient free volume available. Because of the larger free volume, attached polymers can also be removed better when fouling occurs.

Overall, fouling can be reduced but not avoided by a suitable choice of process and geometry conditions.

3.2 Optical measurement with UV/VIS in a half shell reactor[4]

As already stated, the primary drawback of employing continuous reactors for PVP polymerization is the formation of gel deposits. The state of the art for fouling measurements in reactors has not yet been established. However, a number of methods are currently being developed, including the use of ultrasonic sensors in the study by Osenberg et al. [19], quartz crystal microbalance in the study by Böttcher et al. [18]. In [21], a fiber-optic rod probe was used to monitor in-situ membrane fouling. However, there were no documented examples in the literature of spectroscopic inline measurements of polymer fouling. For the inline measurements, a special measuring system and optical arrangement was developed at the Center for Mass Spectrometry and Optical Spectroscopy of the University of Applied Sciences in Mannheim, tested, and evaluated at the University of Stuttgart. The development of this measurement technology as well as inline measurements are described in detail in the appendix to this thesis and in [53]. However, only a brief overview is provided here.

The set of experiments aimed to assess the formation of fouling deposits during the reaction of NVP to PVP in a half-shell reactor using the developed UV rod probe. Installed against the direction of flow, the rod probe designed for this purpose continuously records the spectral change of the NVP- and PVP-peak in the 320 nm wavelength range. The 450 nm wavelength range functions as baseline reference. Measurements of concentration series were made during the initial research to demonstrate the impact of the various components on the spectrum. To appropriately interpret the signal progression throughout reaction processes, the influence of the change in conversion was also determined in a preliminary study. It is evident from examining the entire spectrum that rising extinction signals are associated with rising product deposition (fouling) and rising conversion.

Using UV spectroscopy, multiple series of measurements with varying feed conditions for radical polymerizations were carried out in a half-shell reactor. For the standard case (w_M=20 wt.-% and w_I=0.02 wt.-%), an increase in extinction over an 8-hour operation is indicative of a layer build-up during the first three hours, confirmed by opening the reactor. After this time (3 h) a fouling layer forms at the tip of the rod probe. The signal diminishes after five hours reaction time due to the decrease of the reactor volume and conversion as confirmed via HPLC analysis.

---

[4] A detailed version of this chapter has been published in advance of this thesis under the terms of the Creative Commons Attribution License (CC BY 4.0) in [53]. In order not to impair the flow of reading, only a summary has been chosen in this thesis.

Since less product is formed at lower monomer feed concentrations, the extinction signal rises less at the beginning of the experiment and conversion is falling less sharply at the same time, indicating reduced fouling tendency. Decreasing initiator concentrations show a similar trend. Polymer analysis demonstrates that with increasing monomer and decreasing initiator concentration longer polymers are formed, as expected. The number of branches increases with increasing chain length, especially for high monomer concentrations.

In conclusion, the results of the preliminary tests and the manual tracing of the fouling layer on the probe provided an interpretation of the signal course regarding the layer expansion and the conversion decrease. However, a direct correlation between the measurement signal and the layer thickness is only partially possible because the extinction signal is both influenced by layer growth and conversion decrease. Further, a direct correlation between the extinction signal and the conversion curve is unachievable due to strong fluctuations. Additional measurements rule out a change in conversion for the first three hours, but after that, the overlapping signal from both effects obscure any representative statement regarding layer thickness. Nevertheless, UV spectroscopy can identify product deposits earlier as pressure measurements to optimize process control and prevent a total reactor clog. Due to the sensitivity, fouling signals are even generated at low concentrations. Further applications of the measurement technology optimized for fouling detection can delve deeper into the process control of current processes and ultimately lead to their optimization. Optimized process control can, in the simplest scenario, result in batches being stopped in good time prior to the need for extensive deposit cleaning or, in the worst scenario, before the reactor being clogged.

3.3 Surface properties[5]

As presented in the past chapter, deposit formation and fouling in polymer reactors especially microreactors is a well-known phenomenon. Despite the flow and pressure loss optimized static mixers, fouling occurs on the surfaces of the mixer elements. Past studies [7] have shown that the mechanical and chemical stability of the coating is of particular relevance, as otherwise the coating will be infil-

---

[5] The majority of this chapter has been published in advance of this thesis under the terms of the Creative Commons Attribution License (CC BY 4.0) in [54]. Minor changes have been made and passages have been added for better comprehensibility and embedding in the context of this thesis.

trated and blistering or flaking will occur, as can be seen in Figure 30. Mechanical stability is important, as otherwise the coating will be damaged during installation. To improve the performance of such parts even further, stainless steel substrates were coated at the university of Paderborn (UPB) with ultra-thin films which have a low surface energy, low adhesion, and high durability. Furthermore, an extremely hard and stable (diamond-like carbon, DLC) coating has been developed by Fluitec. In the following, these coatings are described in detail and results will be presented subsequently.

Figure 30: Coated stainless-steel mixer with a teflon coating after multiple studies in a Fluitec ContiPlant reactor.

3.3.1 Coatings

3.3.1.1 Coating applications by university of Paderborn

The ability of perfluorinated organosilane (FOTS) films to prevent deposit formation and fouling during polymerization processes in microreactors was compared to that of sol-gel films containing zirconium oxide and FOTS. The anti-adhesive characteristics of micro-reactor component surfaces during the aqueous polymerization were created by both film structures.

Using chemical vapor deposition (CVD), the hydrophobic FOTS layer was applied to the substrates. ZrOx films containing FOTS were applied using the sol-gel technique. In [54], the fabrication is explained in detail.

Surface morphology

FE-SEM and AFM imaging were used to examine the surface morphology. Figure 31 displays high-resolution AFM images of the 1.4404 polished (ps) substrate both before and after modification with the FOTS or ZrOx/FOTS coatings. To characterize the surface topography, roughness parameters were calculated, such as the root-mean square roughness (rms(sq)) values.

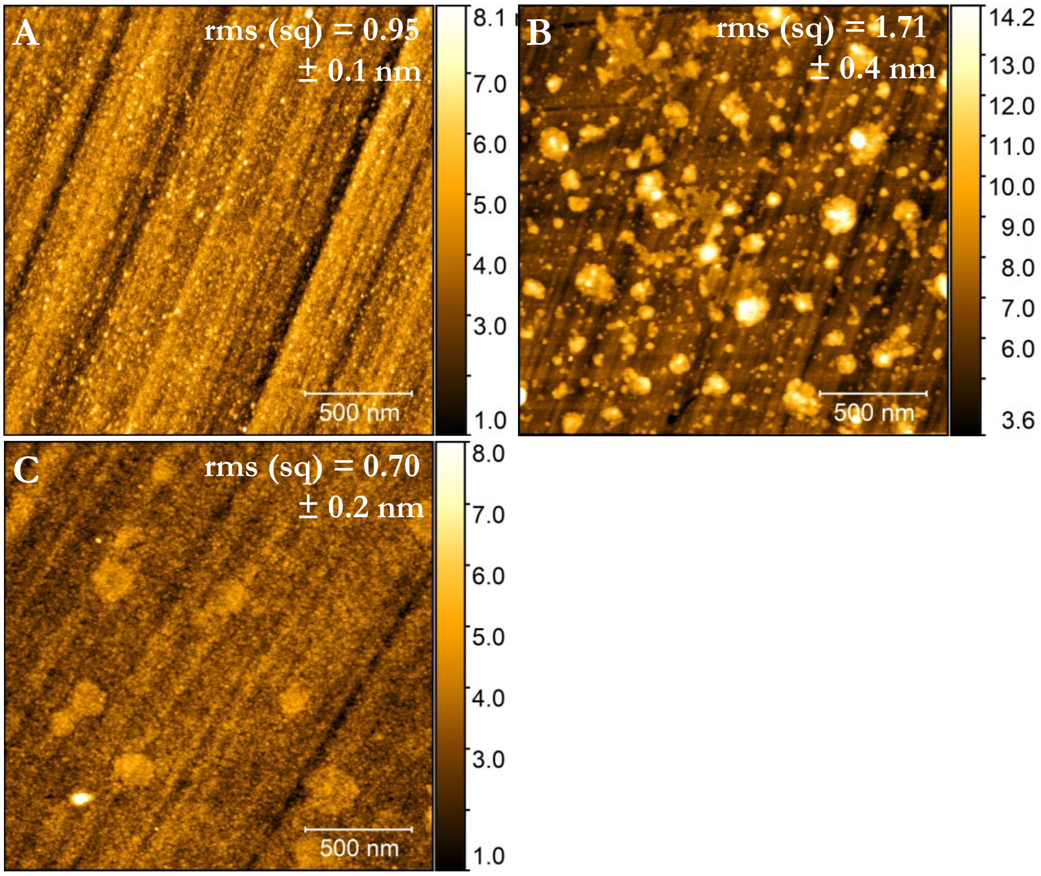

Figure 31: (2x2) μm^2 AFM images of bare 1.4404 ps substrate (A), the latter after FOTS-deposition (B) and after ZrOx/FOTS coating (C). The rms-value given is the root-mean square roughness of the respective surface. Applied from [54].

The AFM image of the FOTS-coated 1.4404 ps surface (Figure 31 B) suggests a multilayer film with defects up to about 14 nm in height. The surface roughness of the FOTS-modified surface increases due to the island-like film structure. On the other hand, following the application of the ZrOx/FOTS film, the substrate's surface roughness (Figure 31 C) is marginally less than it was before. The film is evenly applied to the surface. FE-SEM images of the bare 1.4404 nps surface and those taken after the ZrOx/FOTS hybrid film was deposited, as displayed in Figure 32, corroborate this.

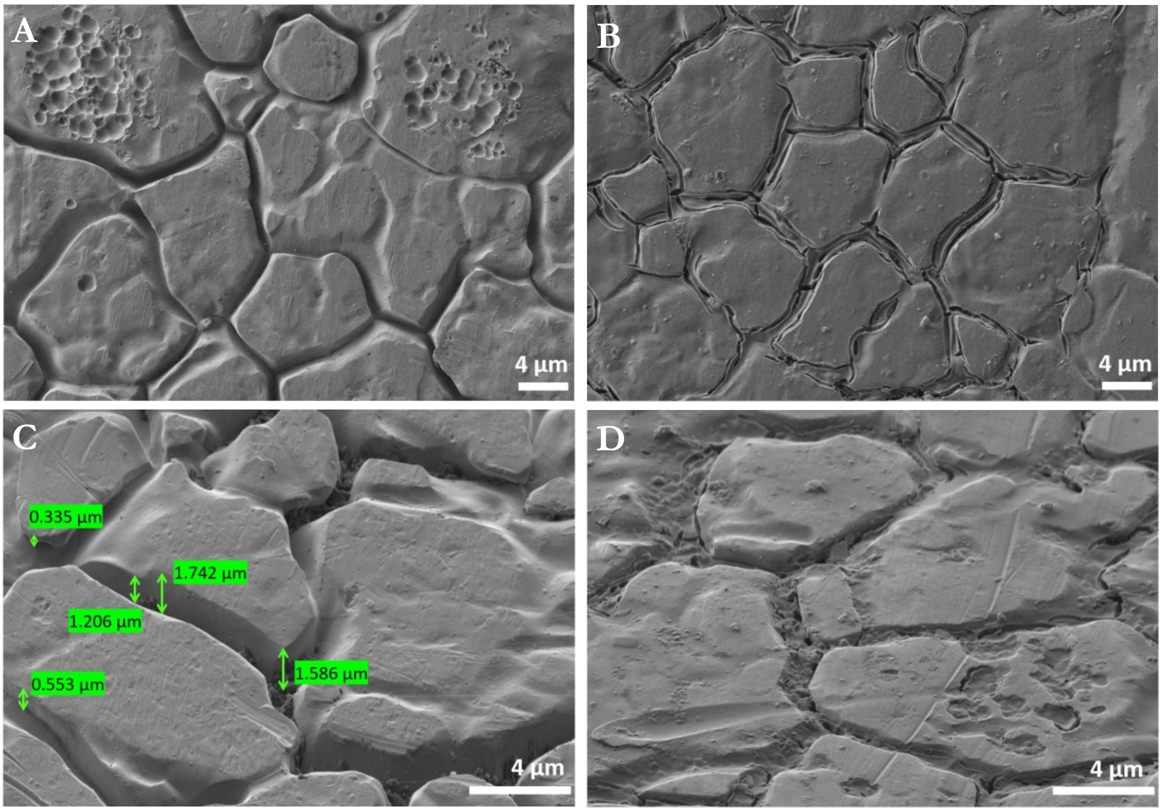

Figure 32: FE-SEM images of solvent cleaned 1.4404 nonpolished (nps) surface with a magnification of 2500 x magnification (A) and 5000 x magnification with 36° tilt (C) as well as comparable surfaces after applying the ZrOx/FOTS film by sol-gel method (B, D). Applied from [54].

It is clear from the pictures in Figure 32 that the ZrOx/FOTS film fills the small trenches. A smaller quantity of the film is applied to the surface. This results in a reduced surface roughness and partial smoothing, which validates the observation from AFM-images and is a feature resp. benefit of a coating applied using the sol-gel method [54].

Water contact angles

Water contact angle (WCA) measurements of the pure surface states and after the ZrOx/FOTS and FOTS coatings, respectively, were used to assess the surface hydrophobicity. Table 3 displays the outcomes for the two types of 1.4404 stainless steel substrates that were used.

Table 3: Water repellency of the pure, CVD and dip-coated 1.4404 stainless steel surfaces, respectively. Applied from [54].

Substrate	Applied coating	Water contact angle / °
Non-polished stainless steel (nps)	-	81 ± 3.8
	FOTS	128 ± 3.1
	ZrO_x/FOTS	117 ± 2.4
Polished stainless steel (ps)	-	73 ± 2.1
	FOTS	107 ± 3.9
	ZrO_x/FOTS	104 ± 1.3

When the FOTS-containing films were applied, the hydrophilic characteristics of the 1.4404 ps and nps substrates (water contact angle <90°) became evidently hydrophobic. The water contact angles of both the coatings are nearly the same for applying to the 1.4404 ps substrate, when considering the mentioned errors. On the other hand, when comparing the hybrid ZrOx-coating to the FOTS-film onto the 1.4404 nps substrate, the measured contact angle is reduced by 11°. This difference may be due to the sol-gel films' ability to reduce surface roughness. It is also evident that, regardless of surface roughness, the water contact angle for the ZrOx/FOTS-coating constantly displays lower values than for the pure FOTS-coating.

3.3.1.2 Coatings from Fluitec

A large number of Fluitec coatings were tested. A promising alternative to the UPB coatings is a diamond like carbon (DLC) application from Fluitec. The coating is applied using plasma-assisted chemical vapor deposition (PACVD) with a layer thickness approx. 2 µm. Due to the carbon, this coating is black as displayed in Figure 33, which has the advantage that even the smallest defects in the surface application can be seen by eye.

Figure 33: Diamond like carbon (DLC) coating from Fluitec applied by PACVD.

3.3.2 Experimental setup

The reactor setup with the Fluitec ContiPlant half-shell reactor is shown in Figure 129 in the Appendix A.2.3.2 of this thesis. For this set of experiments, the optical measurement was not used. The mass flow rates are given in Table 4 for the reference conditions, which results in a superficial velocity of 5 mm s^{-1} due to a different mixing geometry used in this set of experiments.

Table 4: Mass fluxes and composition for the reference case conditions and a superficial velocity of 5 mm/s in the Fluitec ContiPlant half-shell reactor.

Feed pump	Mass flux / g/min	Weight fractions (NVP / water / initiator)
P1	6.2	1 / 0 / 0
P2	9.3	0 / 1 / 0
P3	9.3	0 / 1 / 0
P4	6.2	0 / 0.999 / 0.001

The tested geometry of the static mixing elements in this study is the flow and pressure-loss optimized Fluitec CSE-XD6 (Figure 34).

Figure 34: Single static mixing element with the Fluitec CSE-XD6 geometry. Applied from [54].

In each experiment 7 coated or uncoated static mixer elements were placed in the reactor, respectively. In the reactor outlet a small flat plate with the same surface composition as the static mixers was mounted for offline characterization. The operation time of each run was 10.25 h. As deposits only occur after a certain time in factory-fresh, uncoated mixers, each test was carried out several times.

3.3.3 Results for thin film applications

3.3.3.1 Evolution of the pressure drop

Figure 35 shows a comparison of the pressure drop evolution during operation time using coated and uncoated mixer elements. After startup of the polymerization the pressure drop increases in all experiments due to an increase of viscosity (first 30 min). Then the pressure stays constant for roughly 8 h in all cases. The small recurring peaks in the pressure signal are due to sampling extraction from the reactor.

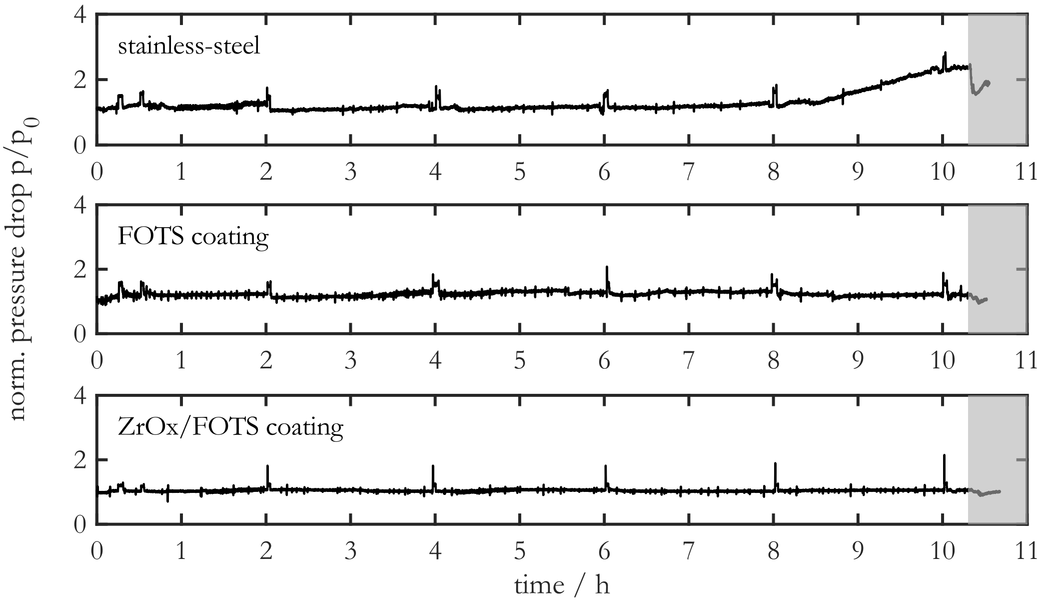

Figure 35: Comparison of the normalized entry pressure evolution in experiments with and without the hydrophobic coating. p_0=p(0 h). Applied from [54].

Uncoated mixers: After eight hours of operation, the pressure drop starts to increase for the uncoated stainless steel mixing elements and becomes more and more volatile (Figure 35). This can be attributed to accumulation of an insoluble polymer gel, which adheres to the casted steel mixer elements and blocks the free volume in the reactor. The pressure increases continuously until the end of the experiment, where the absolute pressure loss is approx. 150 mbar compared to the reactor inlet. Then the reactor is rinsed with water (Figure 35, grayed area). Part of the clogging is removed by water flushing, however, the pressure does not return to the initial value. This indicates persistent adherence of gel on the uncoated mixers.

FOTS coated mixers: The operation of the reactor over 10 h using FOTS coated mixers does not lead to an increase of pressure drop (Figure 35). Thus, employing FOTS-coated mixing elements lead to a significant increase of operation time in radical polymerization of PVP. Small fluctuations in the pressure profile (for instance after 4 h) may be due to locally increased viscosity in the outlet of the reactor, which is an uncoated stainless-steel element. After the end of the polymerization experiment the reactor is rinsed with water. Contrary to the uncoated mixers, the pressure signal returns to the initial state (Figure 35, colored gray). This clearly indicates, that either no gel deposits are formed, or they are weakly bound to the surface and can be removed easily.

ZrO_x/FOTS coated mixers: The second hydrophobic coating is the ZrO_x/FOTS coating on factory fresh stainless steel mixing elements. Figure 35 shows the pressure drop for the coated mixing elements. The pressure profile increases initially due to viscosity changes and then stays constant. After flushing with water (Figure 35, colored gray), the initial pressure is reached again. Compared to uncoated mixing elements, the operation time can be significantly increased.

The measured monomer conversion for all runs is in the range of 7-15 % (Figure 36). At the beginning of the operating period, the monomer conversion of the ZrOx/FOTS coating is slightly higher. However, it is unknown where this increased conversion comes from. No further significant differences in the conversion rate were found between uncoated and coated mixers. It can be observed that conversion decreases with increasing operating time for all tests. In the case of the uncoated mixer, this is certainly due to the formation of the fouling, which is shown below. In the case of the coatings, on the other hand, the decreasing conversion can possibly be explained by deactivation of the initiator or the radicals by the coating.

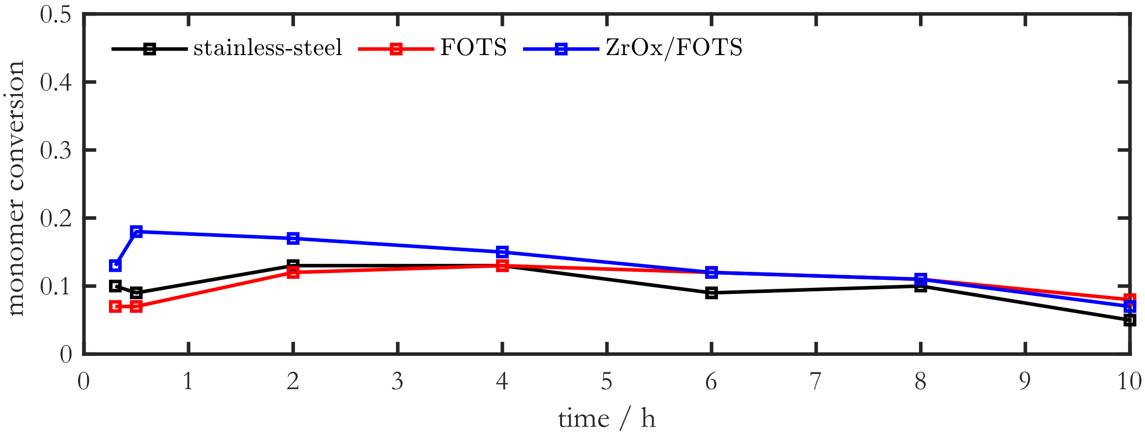

Figure 36: Conversion over operating time for stainless-steel mixer, FOTS and ZrOx/FOTS coating.

3.3.3.2 Gel formation on dismounted mixing elements

After completion of the experiments the mixing elements are dismounted. To visualize the residual gel, the dismounted mixing elements are placed in deionized water over night. In a second step the mixers are cleaned with a water jet until all visible polymer is removed. Then they are placed in a

0.1 N iodine-water solution for 5 min, which allows to detect residual gel deposition on the surface. The PVP-Iodine complex formation results in a red-brown coloration of the polymer [55]–[57].

Uncoated mixers: An uncoated mixer element is shown in Figure 37 A. The polymer gel has accumulated and blocked most of the free volume in the reactor.

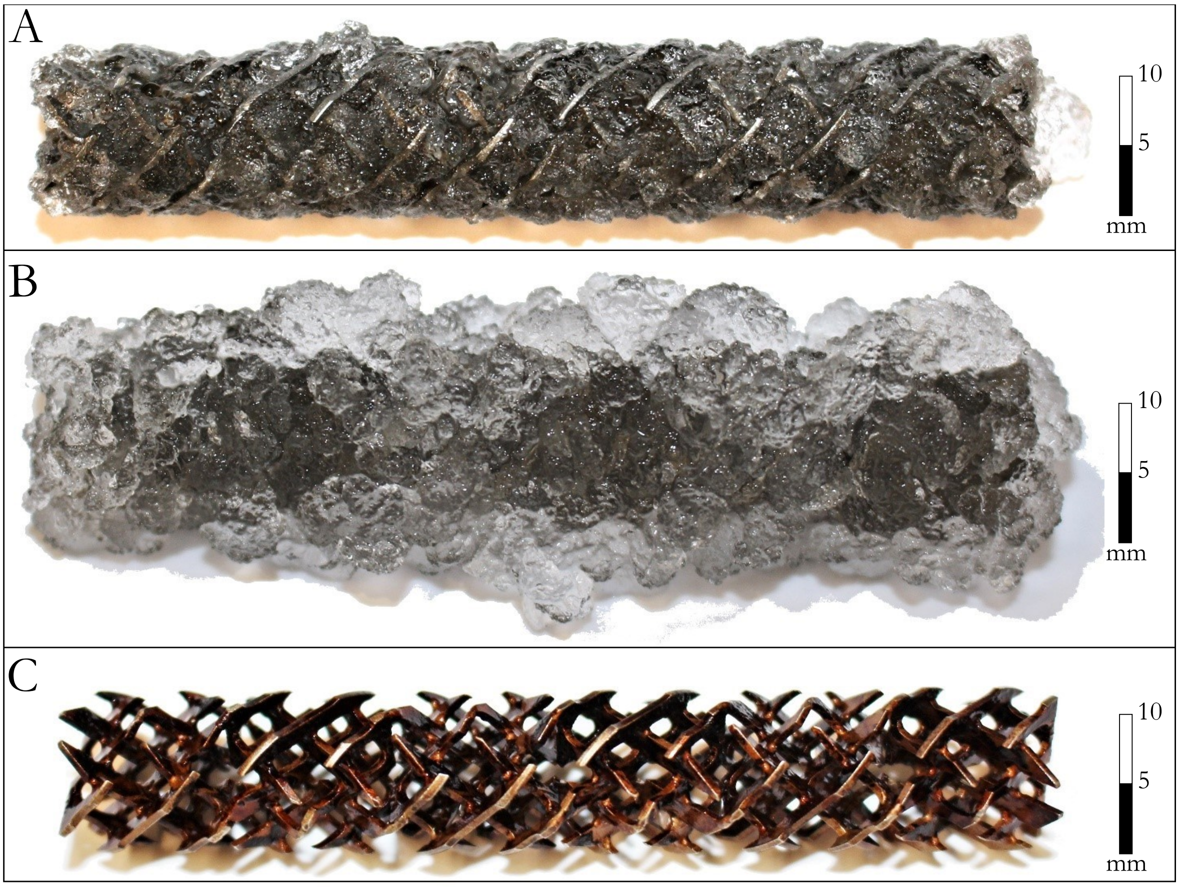

Figure 37: PVP gel fouling on a casted steel static mixer element (A) and swollen PVP gel on a casted steel static mixer element (B) as well as a cleaned uncoated mixing element with a water jet and additionally placed in an iodine-water solution (C). Applied from [54].

By placing the dismounted mixer elements in deionized water over night, the accumulated gel could be swollen. The result is a mixer, shown in Figure 37 B, which is no longer visible due to the swollen gel. While only small amounts of polymer gel accumulated in beginning of the run with factory-fresh mixer elements, the amounts increased to the state that is shown in Figure 37 A over time.

Whereas in the entrance region of the reactor only small amounts of fouling occurs, the amount increases along the reactor length. This insight can be explained by the initial heating distance in the reactor. After the experiment, the mixer elements are cleaned with a water jet. Figure 37 C shows the uncoated mixing element after the cleaning procedure and exposition to the iodine-water solution. Even after cleaning with a water jet the whole surface of the mixing element is coated with a PVP layer.

Initial state with applied thin films

Since the adhesion of macromolecules seems to be an important part of the fouling mechanism, experiments with different surface modifications have been carried out.

FOTS coated mixers: A mixer element from the experiment described above is shown in Figure 38 A. Minor fouling can be observed in regions close to the metal reactor walls. These fouling deposits could easily be removed by rinsing with water.

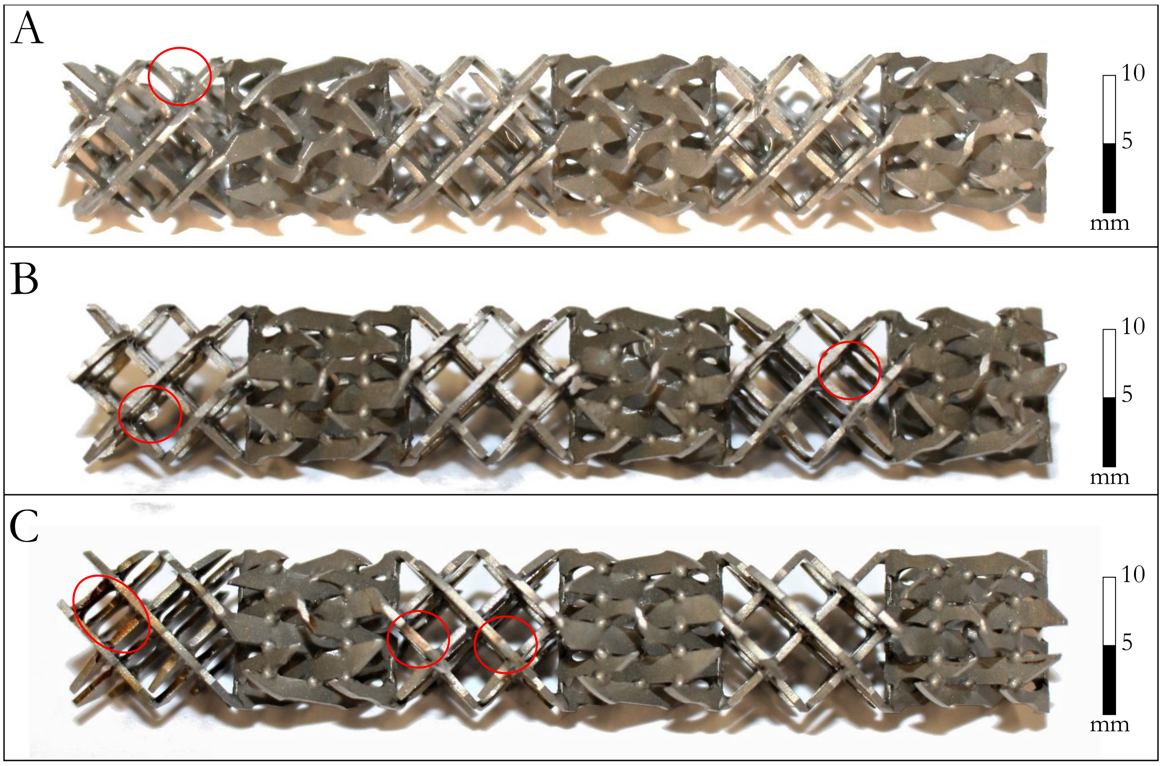

Figure 38: Minor fouling due to hydrophobic coatings (FOTS) on casted steel static mixer element (A) and small amounts of swollen PVP gel on hydrophobic coatings (FOTS) on casted steel static mixer element (B) as well as the cleaned coated (FOTS) mixing element with a water jet and additionally placed in an iodine-water solution (C). Applied from [54].

By placing the dismounted mixer elements in water over night, accumulated gel becomes visible. Figure 38 B shows that only small amounts of swollen PVP gel are attached on the coated mixing element.

Figure 38 C shows the FOTS-coated static mixer element after the cleaning procedure and complexing reaction with iodine. Clearly on the most part of the surface no PVP can be seen.

It can therefore be concluded that a FOTS-coated surface not only significantly reduces the amount of fouling, but also enhances the cleaning process drastically.

ZrO_x/FOTS coated mixers: Figure 39 A shows the coated mixing element after the operation time with a small amount of gel deposits.

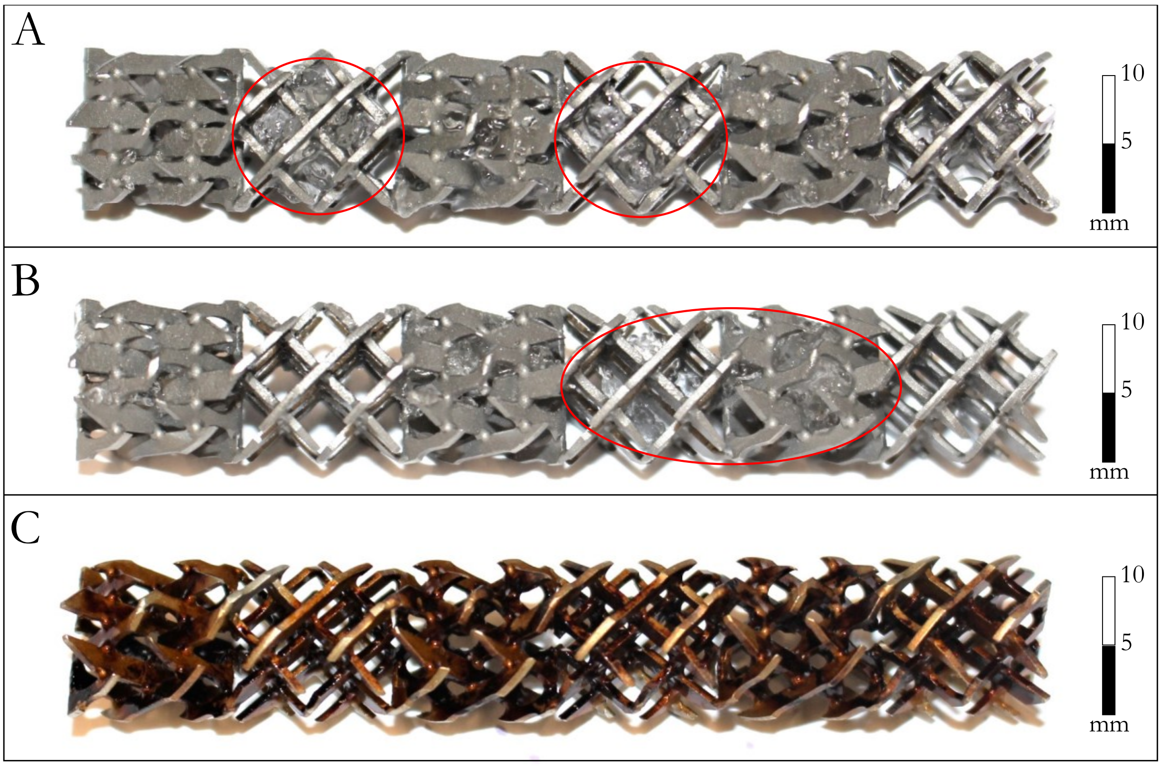

Figure 39: Minor fouling due to hydrophobic coatings (ZrOx/FOTS) on casted steel static mixer element (A) and small amounts of swollen PVP gel on hydrophobic coatings (ZrOx/FOTS) on casted steel static mixer element (B) as well as the cleaned coated (ZrOx/FOTS) mixing element with a water jet and additionally placed in a iodine-water solution (C). Applied from [54].

The mixer elements are again dismounted and placed in water over night to make accumulated gel better visible. Figure 39 B shows that only small amounts of swollen PVP gel have been attached on the coated mixing element.

Figure 39 C shows the ZrO_x/FOTS-coated mixing element after the cleaning procedure and complexing reaction with iodine. It is clearly visible that the surface is colored brown-red by iodine, so PVP deposits on the surface of the mixing element are clearly visible. Nevertheless, it should be mentioned that much less gel forms on the mixers due to the coating compared to the uncoated mixers.

3.3.3.3 Polymer analytics

Figure 40 shows the GPC distribution for both the thin film coatings for an operating time of t=0.25 h (left) and t=10 h (right). It can be seen that after a short period of operation, the molecular weight distributions of the uncoated mixers and the two coatings match relatively well. After an operating time of 10 h, it can be seen that all distributions are significantly broader and shifted to higher molecular weights. Furthermore, it is clear that the distributions now deviate significantly from each other. The distribution of the ZrOx/FOTS coating in particular has broadened towards high molecular weights. This shows that in the case of the uncoated mixer, long-chain polymers are formed and fouling occurs, but in the coated mixers these long-chain polymers do not begin to gel.

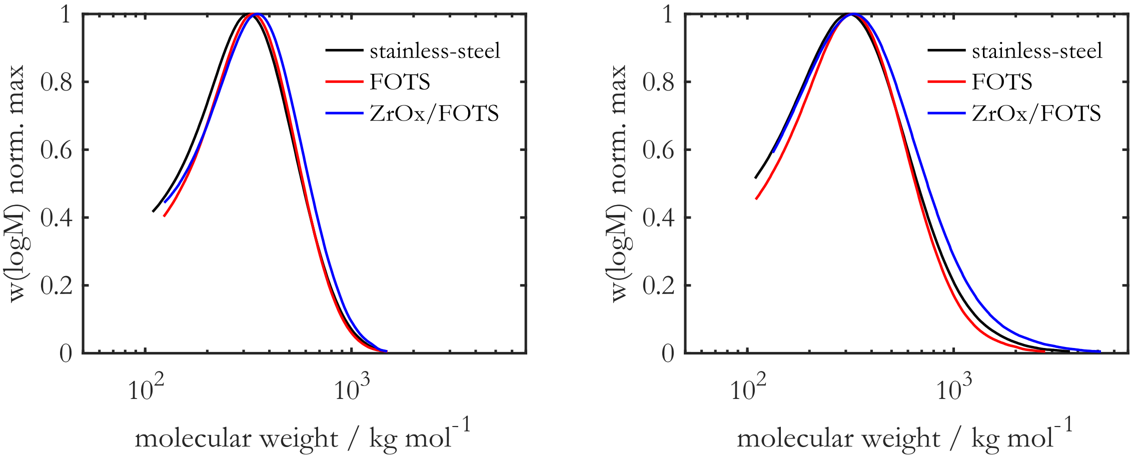

Figure 40: Comparison of the normalized GPC distribution for coatings at an operating time t=0.25 h (left) and t=10 h (right).

The increase in molecular weight for the ZrOx/FOTS coating can be seen particularly in Figure 41, whereas only a small increase in molecular weight can be seen for stainless-steel and FOTS coatings. This is supported by Figure 42, which shows the GPC distribution of different operating times for the ZrOx/FOTS coating. As time progresses, a broadening of the distribution and a shift towards higher molecular weights can be seen. A FOTS coating therefore has no influence on the polymer, whereas a hybrid coating of ZrOx and FOTS has an influence on the structural properties of the polymer, presumably by deactivating the initiator.

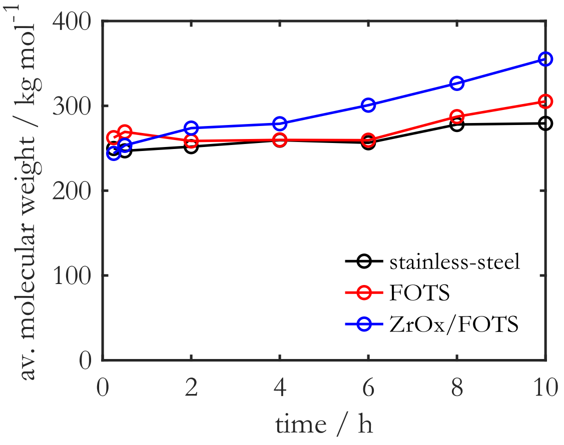

Figure 41: Comparison of the evolution of the weight average molecular weight for different coatings.

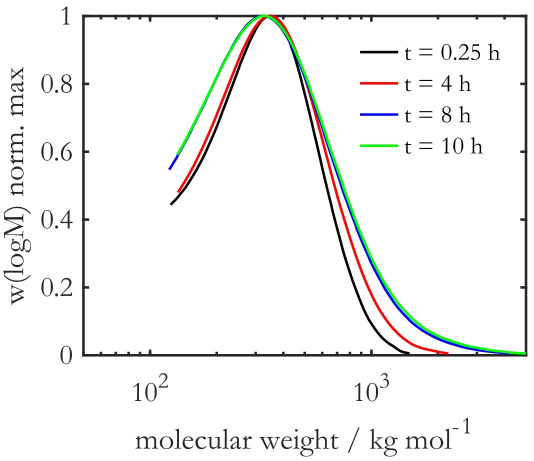

Figure 42: Comparison of the normalized GPC distribution for ZrOx/FOTS coating for different operating times.

3.3.3.4 Post-reaction surface characterization

To further analyze the microscopic effectiveness of the described FOTS and ZrOx/FOTS films bare and modified 1.4404 nps substrates with flat geometry were placed at the reactor outlet during one reaction cycle. This was followed by a 24-hour water bath treatment and subsequent recording of the FTIR spectra at the University of Paderborn [54]. The obtained spectra are displayed in Figure 43 together with as-prepared ZrOx/FOTS and FOTS hybrid films, as well as the spectra recorded of the bare 1.4404 nps substrate following contact with polymer solution and a subsequent water bath treatment. A solvent-cleaned 1.4404 nps substrate was used as the standard in each instance.

Using Figure 43A as a reference, the FOTS-modified substrate exhibits typical infrared signals for a perfluorinated organosilane film. The ZrOx/FOTS coated 1.4404 nps substrate as a reference can be identified at Figure 43B. Following contact with the polymeric media, the unmodified stainless-steel substrate (Figure 43E) shows characteristic stretching bands at 1645 cm^{-1} and 1416 cm^{-1} in the FTIR spectrum. These bands correspond to the pyrrolidone C=O group and the hydrocarbon absorption of PVP [54]. Furthermore, distinct local peak maxima are produced at 2949 cm^{-1} and 2980 cm^{-1} (asymmetric) as well as 2880 cm^{-1} and 2918 cm^{-1} (symmetric) by the CH_2 stretching vibrations of the pyrrole ring and chain. Overall, the peaks indicated above unequivocally show that PVP is present on the substrate. Furthermore, the OH-stretching of adsorbed water, which denotes the formation of hydrogel, is correlated with the strong absorption band at wavenumbers above 3400 cm^{-1}. On the other hand, following contact with the polymer, the PVP characteristic bands on the FOTS-modified surface are only marginally developed (Figure 43C), highlighting the thin film's potent anti-fouling qualities. In contrast to the uncoated nps reference substrate (Figure 43E), the ZrOx/FOTS coated 1.4404 nps substrate exhibits slightly PVP-characteristic signals following contact with the polymeric media (Figure 43D). While the peaks associated with the CH_2-stretching vibrations of the pyrrole ring and chain (2800-3000 cm^{-1}) can still be identified, there is a noticeable reduction in the distinctive band of the C=O-group, which validates the findings from earlier research on the hybrid film's anti-adhesive properties.

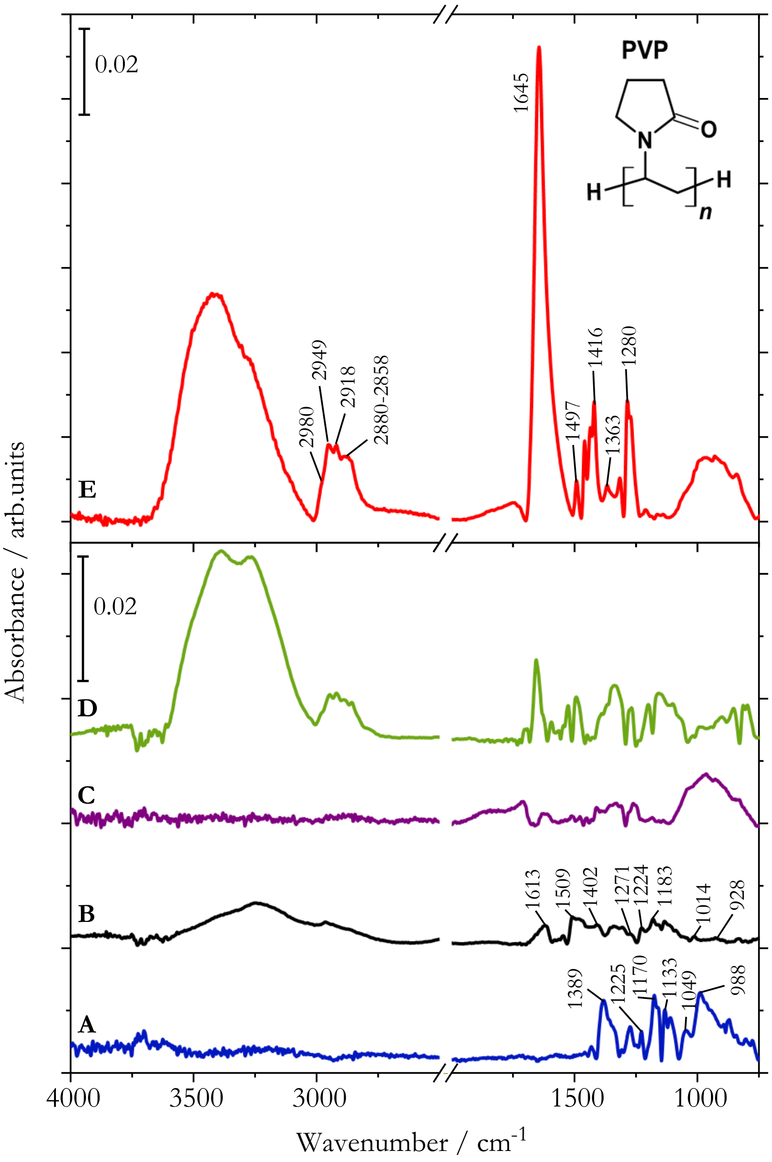

Figure 43: FTIR spectra of the FOTS (C) and ZrOx/FOTS (D) film coated 1.4404 nps surfaces after contact with PVP in the microreactor for one reaction cycle and subsequent water cleaning process in comparison to analogously treated bare nps surface (E) and as-prepared FOTS (A) and ZrOx/FOTS surface (B). A solvent cleaned nps substrate served as reference. Applied from [54].

3.3.4 Long term polymerizations with selected coatings

Following the exceptionally good results of the FOTS coating, it is being examined in a long-term test together with uncoated mixers. The operation time was therefore increased to 26 h. The mass flows were throttled to reduce monomer consumption. The mass fluxes for a superficial velocity of 2.5 mm s^{-1} are shown in Table 5 for the long-term polymerizations.

Table 5: Mass fluxes and composition for the reference case conditions and a superficial velocity of 2.5 mm/s in the Fluitec ContiPlant half-shell reactor.

Feed pump	Mass flux / g/min	Weight fractions (NVP / water / initiator)
P1	3.1	1 / 0 / 0
P2	4.65	0 / 1 / 0
P3	4.65	0 / 1 / 0
P4	3.1	0 / 0.999 / 0.001

Monomer conversion ranges are from 33 % at the beginning of operation to 4 % at the end. Figure 44 shows the normalized pressure drop for the long-term polymerizations of factory fresh stainless-steel and FOTS coated mixing elements. A pressure increase for the uncoated mixers occurs after 13 h operating time, whereas for the coated FOTS mixer is only observed after approx. 16 h.

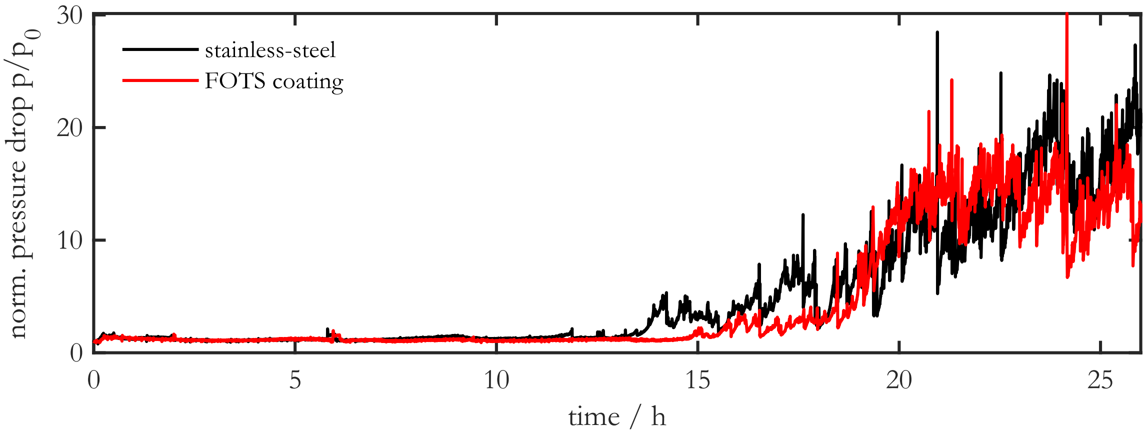

Figure 44: Norm. pressure drop for stainless-steel and FOTS coated mixing elements for long term polymerizations with a reduced flow velocity (Table 5).

However, the pressure of a mixer coated with FOTS increases to a similar extent as the pressure curve of the uncoated mixer. Therefore, only a minor influence on the operating time of the FOTS coating in terms of long-term polymerization can be observed. For this reason, the DLC coating presented above and tested in preliminary trials as well as an improved FOTS coating were tested in long-term trials. An improved FOTS coating is described as a double-layer FOTS coating, where a second FOTS layer is applied on top of the existing layer. Figure 45 shows the pressure drop for all coatings compared to stainless-steel. The pressure increase of the DLC coating and the improved FOTS layer occur significantly later, i.e. with progressing operating time. The pressure increase of the two new coatings is also not as steep as with the stainless-steel or FOTS coated mixers. At the end of the operating time of 26 h, the pressure loss is significantly lower for the improved FOTS and the DLC coating and the reactor can be operated notably longer with these coatings.

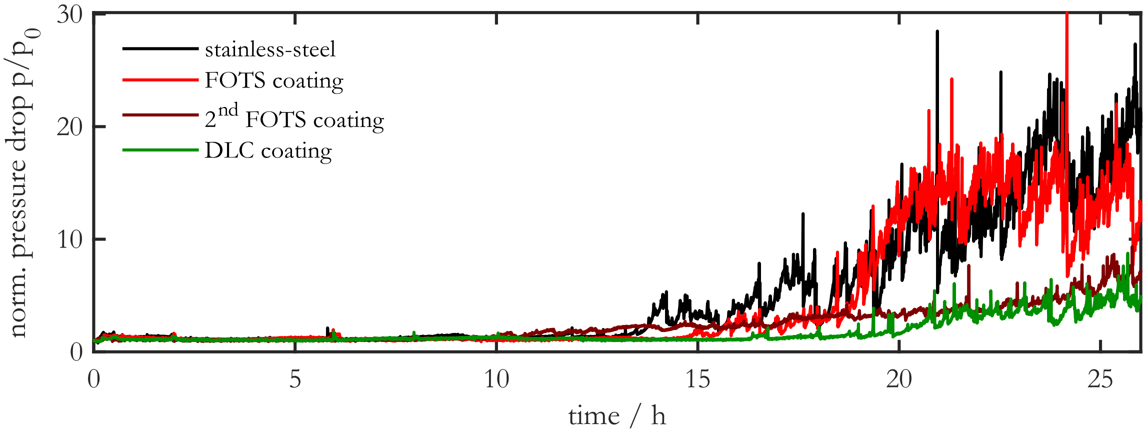

Figure 45: Norm. pressure drop for stainless-steel and different coatings applied on mixing elements for long term polymerizations with a reduced flow velocity (Table 5).

However, it should be mentioned that after this long operating time and the longer residence time in the reactor, gelation occurs for all the coatings considered. For this reason, Figure 46 shows a dismantled DLC mixer after 26 hours of operation. The cavities of the mixer are filled with cross-linked polymer deposits and lead to an increase in pressure. The different pressure curves can be explained by an increased chemical stability of the 2-fold FOTS and the DLC coating or a lower adsorption energy of the polymers on the coatings.

Figure 46: Dismounted DLC-coated mixing element after an operation time of 26 h.

3.3.5 Thin film applications in capillary reactors[6]

After the successful application of the coatings from Paderborn on the static mixing elements, the ZrOx/FOTS hybrid coating was applied internally in a capillary. Coating the inside of a 3 m long component with an internal diameter of 1.76 mm is not possible with every coating process. However, UPB's hybrid coating is suitable for this geometry due to its simple application. The reactor setup and the reaction conditions have already been presented in Figure 9 resp. Table 2. For comparison a feed concentration of w_M=20 wt.-% and w_I=0.02 wt.-% is tested. Figure 47 shows the evolution of the response signal for the coated capillary reactor and can be compared to Figure 11, where the response signal for a stainless-steel capillary with the same process conditions is shown. Compared to the stainless-steel capillary, the first distribution (2 min reaction time) shows a higher peak. This is due to the fact, that the adsorption forces of the polymer on the coating are not as high as on a stainless-steel surface and therefore a viscous flow cannot adhere as well as on an uncoated surface or the adsorption of the tracer is smaller on coated surfaces. As the operating time progresses (≤ 60 min), a wall layer build-up also occurs in the coated capillary. However, it is less pronounced.

The signal becomes very unstable after an operating time of 48 hours. Furthermore, the breakthrough times of a stainless-steel capillary after 48 h of operation are significantly earlier than those of a coated capillary. This indicates a much more pronounced wall layer in the uncoated capillary. Furthermore, the test with the coated capillary could be carried out as planned with an operating time of 72 h, whereas the test with the uncoated capillary had to be terminated after 48 h because the wall layer formation or fouling was so strong that the pressure increased extremely.

---

[6] The majority of this chapter has been published in advance of this thesis under the terms of the Creative Commons Attribution License (CC BY 4.0) in [85]. Minor changes have been made and passages have been added for better comprehensibility and embedding in the context of this thesis.

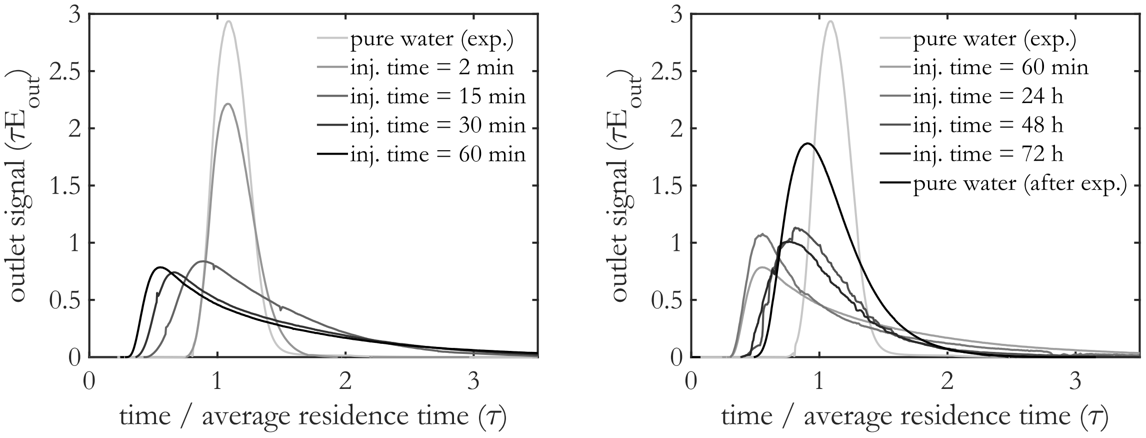

Figure 47: Evolution of the area-normalized response signal Eout at different times for a ZrOx/FOTS coated capillary reactor at w_M=20 wt.-% and w_I=0.02 wt.-%.

Figure 48 shows therefore the pressure drop over the operating time for both reactors. The pressure curve of the stainless-steel capillary begins to rise after just 24 hours. The pressure drop fluctuates quite strongly from this time onwards, which means that the wall layer is repeatedly torn off. Between 30 and 40 hours of operation, the pressure rises extremely quick and sharp and reaches a peak, which means an absolute pressure of 40 bar. The pressure curve of the coated reactor behaves differently. A slight increase in pressure can be observed after approx. 27 hours. This increase remains quite moderate over the entire operating time of 72 hours. The fluctuations in the pressure signal are also very small compared to the uncoated reactor. After an operating time of 48 h or 72 h, the reactor was rinsed for 1 h at an increased flow rate (28 mm/s), which means that the pressure dropped in each case. For both reactors, the initial state could not be restored.

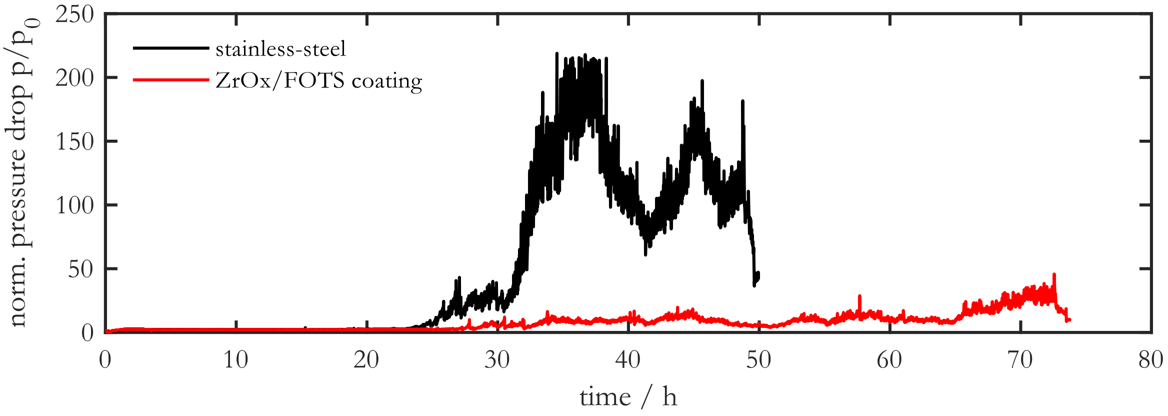

Figure 48: Comparison of the development of the normalized pressure drop in experiments without and with hydrophobic coating in a capillary reactor.

In summary, it can be said that once again the importance of coatings for polymer fouling could be demonstrated using the example of NVP polymerization. Even capillary reactors with a diameter $d<2$ mm can be provided with a hydrophobic coating on the inside and can therefore be able to reduce fouling, but not completely prevent it.

3.3.6 Conclusions

This chapter demonstrates the relevance of coatings for avoiding or reducing fouling in continuous tubular reactors. Preliminary investigations have shown that both mechanical and chemical stability are crucial for the coatings effectiveness [7], as otherwise it does not represent a long-term option for preventing deposits. Hydrophobic coatings (high water contact angle) like ZrOx/FOTS, FOTS, 2-fold FOTS and DLC, can reduce fouling to a minimum. The 2-fold FOTS and the DLC coating show the best behavior for all coatings.

The investigation reveals that the conversion decreases with increasing operating time in all tests. For the uncoated mixer, this is certainly due to the formation of the fouling, whereas in the case of the coatings this may be due to the deactivation of the initiator or the radicals by the coating. Molecular weight distributions significantly broaden the distribution at the end of the operation, both for coated and uncoated mixers. Long-chain polymers begin to gel in uncoated mixing elements, whereas this is not the case in coated ones. The possibility of deactivation of the initiator is confirmed by a broadening of the molecular weight distribution, especially for the ZrOx/FOTS coating. FTIR results clearly show different polymer quantities of uncoated and coated surfaces. Whereas hardly any PVP residues are found on a FOTS-coated surface, high quantities can be detected on an uncoated surface. Furthermore, in long-term tests (>26 h), the FOTS and the ZrOx/FOTS coatings cannot prevent fouling and only minor influence on the length of the operating time in long-term polymerization can be observed. The 2-fold FOTS coating and the DLC coating stood out in particular for long-term tests but gelation occurs for all coatings.

The hybrid coating of ZrOx/FOTS is suitable for inner tube coating in a capillary reactor, resulting in a less pronounced wall layer than in an uncoated reactor. However, it should be emphasized that a coating can only reduce the formation of deposits but not completely prevent it.

3.4 Cleaning procedures

As described in the previous chapter, polymer fouling during the radical polymerization of N-Vinylpyrrolidone leaves a polymer film on the surface after mechanical cleaning using a high-pressure water jet, which is not visible. Only after staining with iodine according to Figure 37 this residue appears on the surface. To restore this surface, chemical cleaning using sodium hypochlorite (NaClO) can be carried out. According to [58], two different mechanisms for chain scission of PVP are relevant. On the one hand, the disproportionation of the radical leads to chain scission and, on the other hand, oxidative degradation leads to the formation of aldehyde groups. To investigate the influencing factors of the cleaning agent, a serie of tests was carried out according to Figure 49 at different concentrations of NaClO solution, different pH values and different temperatures of the solution.

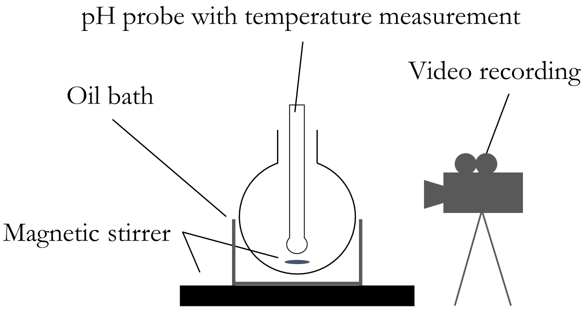

Figure 49: Experimental setup for the preliminary chemical cleaning tests with NaClO.

For this purpose, a defined amount of polymer gel (0.5 g gel and 4.5 g water) was dissolved in NaClO solution (95 g) under different conditions. From preliminary tests it became clear that the pH value has almost no influence on the cleaning result. This should ideally not be increased or reduced by acid or base. For pH values below 8, a white polymer precipitates, which can only be dissolved by increasing the pH value again. Table 6 shows a few further test conditions and the associated cleaning times.

Table 6: Experimental conditions and the associated cleaning times for the experiments on chemical cleaning using NaClO.

NaClO concentration / wt.-%	Temperature / °C	Time until dissolving of gel deposits / h
4	25	20
12	25	9.5
4	40	5
4	80	0.5

An increased chlorine concentration in the cleaning solution has a positive effect on the cleaning speed. A proportional relationship between concentration and cleaning time can be seen here. However, temperature has the greatest influence on cleaning. A significant increase in cleaning performance can be observed with increased temperature. The best result was achieved at temperatures of T=80 °C.

After successful preliminary tests, entire mixer rods can then be cleaned using the cleaning process. Figure 50 shows on the left side the mixer cleaned with a water jet and subsequent iodine staining and on the right side a mixer cleaned with NaClO. After chemical cleaning, there may be occasional traces of rust (especially at the welding points). These were cleaned in an oxalic acid bath.

Figure 50: Cleaning procedure for static mixing elements with NaClO solution.

In addition to the process-related measures to reduce fouling, chemical cleaning is therefore another way of eliminating fouling in systems once it has occurred.

3.5 Concluding remarks

In this chapter, a comprehensive experimental exploration of fouling in continuous reactors was undertaken through the investigation of various measurement techniques, process conditions, and reactor geometries, including capillary and half-shell reactors.

The experimental findings paint a nuanced picture of fouling phenomena. Using residence time measurements reveals that a highly viscous wall layer forms on reactor surfaces during operation until viscosity and shear forces equalize each other. This wall layer eventually leads to gelation resp. polymer fouling resulting in blockage and reactor shutdown.

Notably, modifying process conditions, such as reducing monomer or initiator concentration, exhibited a positive impact on fouling behavior in tubular reactors. This conclusion was substantiated through a second approach: the optical measurements in UV/VIS utilizing glass fiber technology in a half-shell reactor with static mixing elements. Moreover, a higher flow velocity or a larger reactor cross-section while maintaining the residence time, positively influences pressure loss and, consequently, fouling behavior. Increased flow velocity therefore facilitates more effective polymer detachment, transported away by the primary flow, while a lower surface-to-volume area benefits channel flow by providing ample free volume.

Mechanically and chemically stable hydrophobic coatings were identified as effective in significantly reducing fouling; however, complete prevention remained elusive. These coatings proved to mitigate adhesion forces, making polymer removal more manageable while acknowledging that a residual adhesion persists.

If it is not possible to prevent polymer fouling by means of process engineering measures or coatings, the polymer residues can be removed by chemical cleaning with sodium hypochlorite.

The aim of the following work is to incorporate the previously gained knowledge into a model that is able to describe fouling in continuous reactors.

4 Kinetic modeling and simulation[7]

Side reactions which produce high molecular weight, branched, or even crosslinked polymer chains are considered as a prerequisite for fouling. Local back-mixing and stagnant flow in dead zones increase the local residence time and enhance the formation of a polymer network [1], [4], [13]. To predict the onset of fouling in continuous reactors, kinetic models, which provide information about the microstructure of the polymers, are essential.

The reaction mechanism of the NVP polymerization has been studied extensively. The propagation rate coefficient [59], [60] as well as the termination rate coefficient [61] in aqueous solution were determined using pulsed-laser polymerization in conjunction with polymer analysis by size-exclusion chromatography. Transfer to monomer has been studied in [4] and [62]. Transfer reactions to the solvent seem to be the dominant termination reaction in organic solutions while termination by combination dominates the termination in aqueous solution [63]. In previous work [5] the formation of terminal double bonds (TDBs) by transfer to monomer and subsequent propagation of the TDBs was identified as the main reason for long chain branching in the aqueous NVP polymerization. In a recent publication, a model for the number of terminal double bonds has been developed, which was successfully validated against experimental data from CSTR experiments [6].

The full scheme of kinetic reactions for aqueous radical polymerization of NVP (Table 7) characterizes a PVP chain by three discrete property coordinates: the chain length, the number of terminal double bonds (TDB) and the number of branching points (BP). Rigorous treatment is practically impossible, and model reduction is required. In this work the approach of Zander et al. [6] is extended and a one-dimensional model for the chain length and the number of branching points as a function of chain length is derived. Parameters, which are required for model reduction, are now updated dynamically, which improves predictions during transient reactor operation. To validate the modelling approach, results are compared to a computationally expensive classes model. Afterwards,

---

[7] The majority of this chapter has been published in advance of this thesis under the terms of the Creative Commons Attribution License (CC BY 4.0) in [86] and [81]. Minor changes have been made and passages have been added for better comprehensibility and embedding in the context of this thesis.

the impact of residence times and monomer concentrations on the branching point distribution in a CSTR reactor is shown. In the last part, experimental data will be compared to simulative results to test the correctness and the applicability of the model. From this the number of branching points can be calculated using a zero-dimensional approach.

4.1 Reaction scheme

The set of reactions for the polymerization of N-Vinylpyrrolidone in aqueous solution, which was identified in [5], is summarized in Table 7. The dead species are defined as P and the living species as R respectively. Three different property coordinates are taken into account: the chain length (n, m), the number of terminal double bonds (i, j) and the number of branching points (k, l). In addition to classical reactions for a radical polymerization such as initiation, propagation and termination, there are important side reactions (Figures 51-53), which are the reason for the formation of branching points.

Table 7: Set of reactions for the polymerization of N-Vinylpyrrolidone in aqueous solution with the chain length (*n,m*), the number of terminal double bonds (*i,j*) and the number of branching points (*k,l*). [5]

Initiator dissociation/ Initiation	$I_2 \overset{k_d}{\rightarrow} 2f_d I \;/\; I + M \overset{k_p}{\rightarrow} R_{1,0,0}$
Propagation	$R_{n,i,k} + M \overset{k_p}{\rightarrow} R_{n+1,i,k}$
Termination by recombination	$R_{n,i,k} + R_{m,j,l} \xrightarrow{k_{t,c}} P_{n+m,i+j,k+l}$
Transfer to monomer	$R_{n,i,k} + M \xrightarrow{k_{tr,M}} P_{n,i,k} + R_{1,1,0}$
Propagation of terminal double bonds	$R_{n,i,k} + P_{m,j,l} \xrightarrow{j \cdot k_{p,TDB}} R_{n+m,i+j-1,k+l+1}$

The transfer to monomer reaction generates a terminal double bond (TDB) due to transfer of the radical (red) to a monomer molecule by H-abstraction as illustrated in Figure 51.

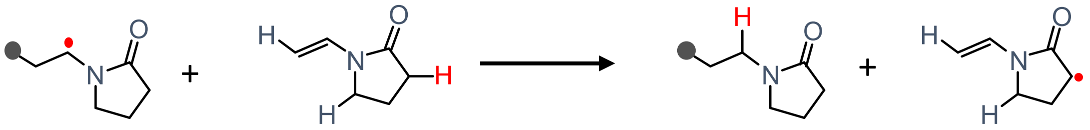

Figure 51: Transfer to monomer reaction scheme. The radical center (red dot) is transferred to a monomer molecule. Adapted from [5].

Figure 52 shows the propagation of terminal double bonds, which consumes one TDB and produces one branching point (BP).

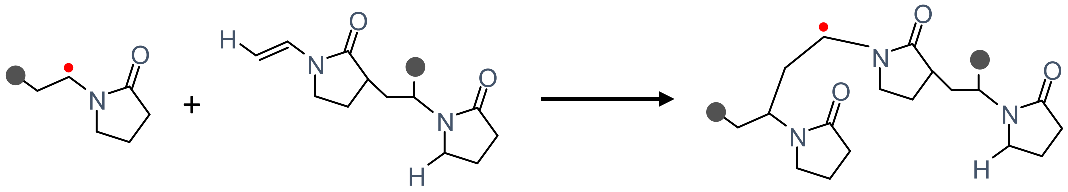

Figure 52: Propagation of terminal double bonds (TDB) for polymer chains with one TDB. Adapted and simplified from [5].

By formation and propagation of terminal double bonds, highly branched molecules are generated as sketched in Figure 53.

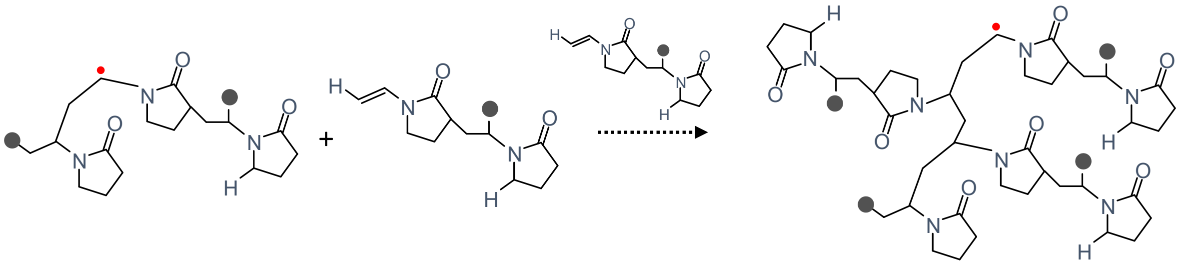

Figure 53: Propagation reaction of terminal double bonds allows formation of highly branched molecules.

While propagation of monomer units does not affect the number of terminal double bonds and branching points, termination by combination reaction adds up the number of TDB, BP as well as the chain length. The rate of propagation of terminal double bonds is proportional to the number of TDB in a polymer molecule. This makes the reaction scheme nonlinear. Thus, moment equations do not close, and a closure condition is required. To avoid further increase in complexity, the formation of multiradicals has been neglected. The kinetic coefficients for all reactions are listed in Table 8.

Table 8: Kinetic coefficients for the reaction system of N-Vinylpyrrolidone

---

$$k_d/s^{-1} = 9.17 \times 10^{14}\exp\left(\frac{-1.49\times10^4}{(T/K)}\right)$$ [62]

$$\frac{k_p}{k_{p,max}} = 0.36 + 0.64\exp(-9.2w_{NVP}) - 0.31w_{NVP}$$ [59]

with $k_{p,max}/(L \cdot mol^{-1} \cdot s^{-1}) = 2.57 \times 10^7\exp\left(\frac{2.12\times10^3}{(T/K)}\right)$

$$\frac{k_t}{L \cdot mol^{-1} \cdot s^{-1}} = \left(\frac{1}{k_{SD}} + \frac{\eta}{k_{TD}}\right)^{-1} + k_{RD}$$ [64]

with

$$\frac{k_{SD}(p)}{L \cdot mol^{-1} \cdot s^{-1}} = \left(4.87 \times 10^7 \exp\left(-\frac{w_{NVP}}{0.29}\right) + 5.47 \times 10^6\right) \cdot \exp\left(-5.61 \times 10^{-4}\left(\frac{p}{bar} - 2000\right)\right)$$

$$k_{TD} = 31\, k_{SD}$$

$$\eta = \exp(14.75\, w_{PVP})$$

$$k_{RD} = 140\, w_{NVP} k_p$$

with the mass fraction w_{NVP} for NVP resp. w_{PVP} for PVP and the viscosity η.

$$\frac{k_{tr,m}}{k_p} = 6 \cdot 10^{-4}$$ [62]

$$\frac{k_{p,TDB}}{L\, mol^{-1}\, s^{-1}} = 3300$$ [6]

$$f_d = 0.7$$ [62]

4.2 Model development

Rigorous simulations with three property coordinates (chain length, terminal double bonds, branching points) are practically infeasible. Therefore, the problem needs to be reduced into 1D problems along one single property coordinate, which can be solved for example by Predici®.

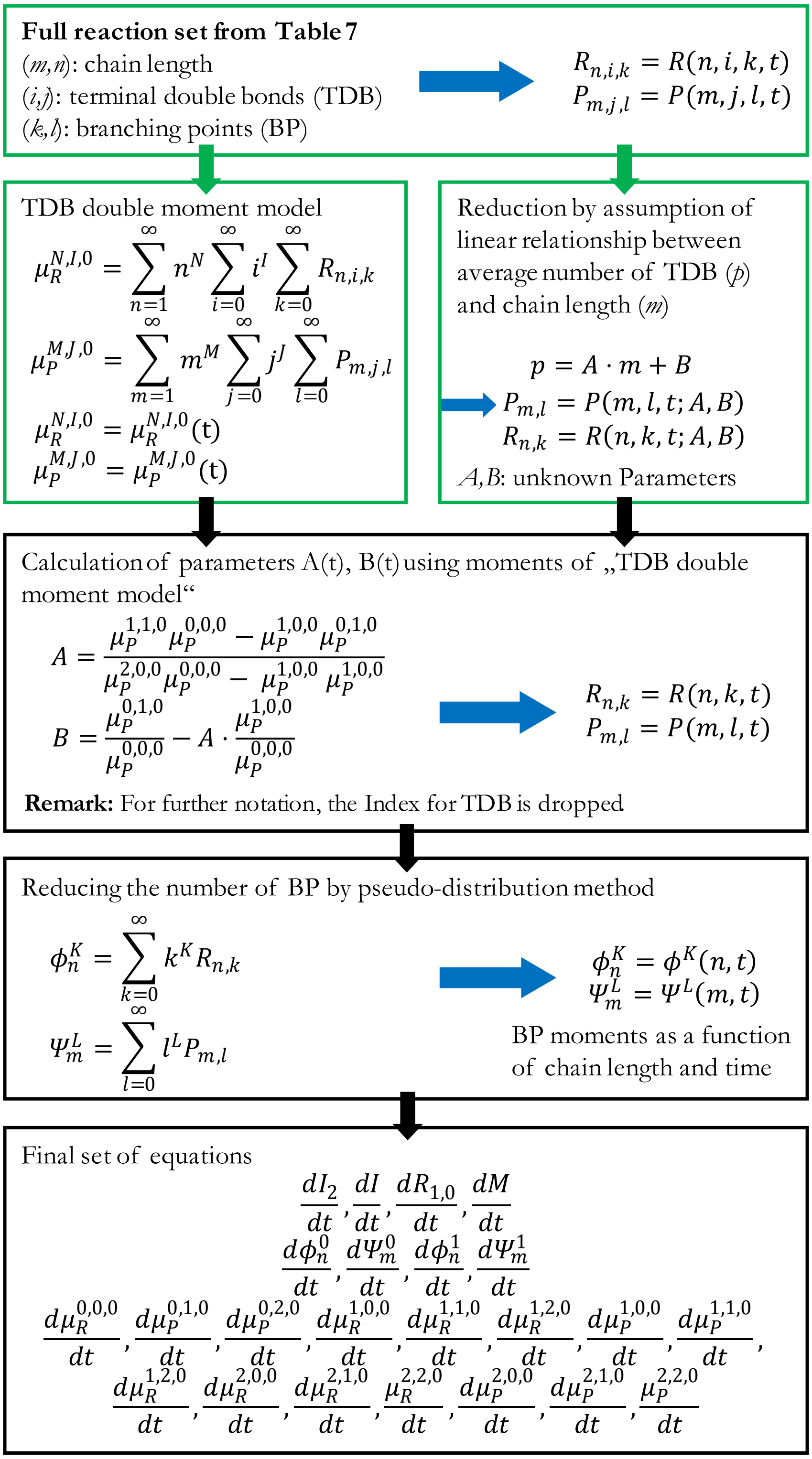

Figure 54: Overview of the different model reduction steps of a full three-dimensional property distribution to 1D model.

Here, the work of Zander [6] is extended and a model that allows to calculate the full chain length distribution and the average number of branching points as a function of chain length is developed. The model developed in [6] is briefly summarized in Chapter 4.2.1. As shown in [6], there is a linear correlation between the average number of TDB's and the chain length. This allows to eliminate the number of terminal double bonds as an independent property coordinate by calculating the moments of this property coordinate and using the linear correlation as a closure relation. Parameters of this closure relation (slope (A) and axis intercept (B)) can be calculated from a computationally cheap moment model, which is termed "TDB double moment model" in [6]. Model designation is kept for convenience. The two-dimensional model (chain length, branching points) can be further reduced by calculation of the moments of the branching points. This step is detailed in Chapter 4.2.2. Finally, one gets a set of one-dimensional models: the chain length distribution of dead and living polymers and the moments of the branching point distribution as a function of chain length. Since the parameters of the linear correlation between chain length and average number of terminal double bonds (TDB) are propagated during model reduction, source terms of the reduced model are functions thereof. By simultaneous calculation of the "TDB double moment model" and the one-dimensional models, the parameters of the linear correlation (A, B) are updated dynamically and the model can be used for transient simulations without any adaption. Figure 54 shows an overview of the model reduction.

To validate the reduced model a comparison with a two-dimensional model (classes model) is conducted. The classes model is briefly introduced in Chapter 4.2.3 and a comparison of simulation results are discussed in 4.2.4. Parameters of a reference case for simulations are given in Table 9. These conditions are typical for a polymerization of NVP in aqueous solution. An isothermal CSTR is used as reactor setup.

Table 9: Parameter for the reference case which is used for all simulations if not stated otherwise.

Feed	
Monomer weight fraction w_{NVP}^{+}	0.2
Initiator weight fraction $w_{I_2}^{+}$	0.0002
Solvent weight fraction $w_{H_2O}^{+}$	1-w_{NVP}^{+}-$w_{I_2}^{+}$
Feed rate $\dot{m}_F$ [g min^{-1}]	10.38 (resp. 1.038 in Chapter 4.2.5)
Initial conditions in reactor	
Solvent weight fraction $w_{H_2O}^{0}$	1
Reactor temperature T_R [°C]	85
Reactor volume V_R [ml]	650
ρ_{H_2O} (85°C) [kg m^{-3}]	959 [62]
ρ_{NVP}(85°C) [kg m^{-3}]	989 [62]

4.2.1 Reduction of the property coordinate "Terminal Double Bonds"

The full set of reactions listed in Table 7 spans three dimensions in property space, with coordinates chain length, terminal double bonds (TDB), and branching points (BP). As already mentioned, the propagation rate of TDBs depends on the number of TDB, while the number of branching points does not enter the rate expressions. Zander [6] therefore investigated the kinetic model with the property coordinates chain length and TDB's only and found that the average number of TDB's and the chain length are linearly correlated. Polymer chains of length (m) thus exhibit an average number of TDB's, $p(m)$, according to Equation (48):

$$p(m) = A \cdot m + B \tag{48}$$

with parameters A and B. Making use of this relation as a closing condition and forming the moments on the number of TDB allows to remove the property coordinate "terminal double bonds". To determine the parameters A and B, a (zero-dimensional) moment model was formulated [6]. This approach is summarized in the following.

To get averaged information on the number of terminal double bonds, a moment model is derived by taking the moments of all property coordinates. This results in a set of differential equations for the moments and can be solved with minimal computational effort.

The moments $\mu_R^{N,I,0}$ for the living chains and $\mu_P^{M,J,0}$ for the dead chains resp. with the Nth, Mth moment on the chain length, Ith, Jth moment on the number of TDB and the 0th moment on the branching points are calculated by Equation (49) resp (50):

$$\mu_R^{N,I,0} = \sum_{n=1}^{\infty} n^N \sum_{i=0}^{\infty} i^I \sum_{k=0}^{\infty} R_{n,i,k} \tag{49}$$

$$\mu_P^{M,J,0} = \sum_{m=1}^{\infty} m^M \sum_{j=0}^{\infty} j^J \sum_{l=0}^{\infty} P_{m,j,l} \tag{50}$$

A complete derivation was made in [6], where the model is called "TDB double moment model". The complete resulting set of equations is compiled in the Appendix A.3. As can be seen from Equation (51) and (52), closure relations are necessary due to the TDB propagation reaction.

$$\begin{aligned}\frac{\mu_R^{2,2,0}}{dt} = {} & k_p M\left(2\mu_R^{1,2,0} + \mu_R^{0,2,0}\right) - k_{t,c}\mu_R^{2,2,0}\mu_R^{0,0,0} - k_{tr,m}M\left(\mu_R^{2,2,0} + \mu_R^{0,0,0}\right) \\ & + k_{p,TDB}\left(2\mu_R^{2,1,0}\mu_P^{0,2,0} - 2\mu_R^{2,1,0}\mu_P^{0,1,0} + \mu_R^{2,0,0}\mu_P^{0,3,0} - 2\mu_R^{2,0,0}\mu_P^{0,2,0}\right. \\ & + \mu_R^{2,0,0}\mu_P^{0,1,0} \\ & + 2\left(\mu_R^{1,2,0}\mu_P^{1,1,0} + 2\mu_R^{1,1,0}\mu_P^{1,2,0} - 2\mu_R^{1,1,0}\mu_P^{1,1,0} + \mu_R^{1,0,0}\mu_P^{1,3,0}\right. \\ & \left. - 2\mu_R^{1,0,0}\mu_P^{1,2,0} + \mu_R^{1,0,0}\mu_P^{1,1,0}\right) + \mu_R^{0,2,0}\mu_P^{2,1,0} + 2\mu_R^{0,1,0}\mu_P^{2,2,0} \\ & \left. - 2\mu_R^{0,1,0}\mu_P^{2,1,0} + \mu_R^{0,0,0}\mu_P^{2,3,0} - 2\mu_R^{0,0,0}\mu_P^{2,2,0} + \mu_R^{0,0,0}\mu_P^{2,1,0}\right)\end{aligned} \tag{51}$$

$$\begin{aligned}\frac{\mu_P^{2,2,0}}{dt} = {} & k_{t,c}\left(\mu_R^{2,0,0}\mu_R^{0,2,0} + 2\mu_R^{2,1,0}\mu_R^{0,1,0} + \mu_R^{2,2,0}\mu_R^{0,0,0} + \mu_R^{1,0,0}\mu_R^{1,2,0} + 2\mu_R^{1,1,0}\mu_R^{1,1,0}\right. \\ & \left. + \mu_R^{1,2,0}\mu_R^{1,0,0}\right) + k_{tr,m}M\,\mu_R^{2,2,0} - k_{p,TDB}\,\mu_R^{0,0,0}\mu_P^{2,3,0}\end{aligned} \tag{52}$$

The moments $\mu_P^{M,3,0}$ with M=1,2,3 are the chain length averaged moments and can be estimated by the closure relation [6]

$$\mu_P^{M,3,0} = D'_M \frac{\mu_P^{M,2,0}\mu_P^{M,2,0}}{\mu_P^{M,1,0}} \tag{53}$$

and the dispersity D'_M, which was determined in [6] to $D'_M = 1$. Using the moments calculated by the "TDB double moment model" allows to calculate the parameters A and B as follows. B can be determined from the average TDB concentration c^{TDB} per chain calculated from the moments by Equation (54) as demonstrated in [6]:

$$\begin{aligned} c^{TDB} &= \sum_{m=1}^{\infty} \mu_P^{(M),1,0} = A \sum_{m=1}^{\infty} m \cdot \mu_P^{(M),0,0} + B \sum_{m=1}^{\infty} \mu_P^{(M),0,0} = A \cdot \mu_P^{1,0,0} + B \cdot \mu_p^{0,0,0} \\ &= \mu_P^{0,1,0} \end{aligned} \tag{54}$$

with the 0th and 1st moment on the number of the terminal double bonds $\mu_P^{M,0,0}$ resp. $\mu_P^{M,1,0}$ for dead chains. Inserting Equation (54) in Equation (48) results in Equation (55):

$$p(m) = A \cdot \left(m - \frac{\mu_P^{1,0,0}}{\mu_P^{0,0,0}} \right) + \frac{c^{TDB}}{\mu_P^{0,0,0}} = A \cdot \left(m - \frac{\mu_P^{1,0,0}}{\mu_P^{0,0,0}} \right) + \frac{\mu_P^{0,1,0}}{\mu_P^{0,0,0}} \tag{55}$$

The parameter A can be calculated from Equation (56):

$$A = \frac{\mu_P^{1,1,0}\mu_P^{0,0,0} - \mu_P^{1,0,0}\mu_P^{0,1,0}}{\mu_P^{2,0,0}\mu_P^{0,0,0} - \mu_P^{1,0,0}\mu_P^{1,0,0}} \tag{56}$$

Details of the derivation can be seen in [6]. In [6] the parameter was calculated once and treated as a constant. In Section 4.2.5 will be demonstrated that the parameter changes during transient operation and will be proposed to calculate the parameter dynamically.

Summarizing, the full model can be reduced by a linear relation between chain length and average number of TDB's per molecule. The parameters of this relation can be calculated from a zero-dimensional moment model. The elimination of the property coordinate "terminal double bonds" leads to a set of reactions, with two property coordinates: chain length and number of branching points (BP). The corresponding reaction scheme is shown in Table 10.

Table 10: Set of reactions after elimination of the TDB property coordinate. Chain length *(n,m)* and the number of branching points *(k,l)* are the remaining property coordinates.

Initiator dissociation/ Initiation	$I_2 \overset{k_d}{\rightarrow} 2f_d I \;/\; I + M \overset{k_p}{\rightarrow} R_{1,0}$
Propagation	$R_{n,k} + M \overset{k_p}{\rightarrow} R_{n+1,k}$
Termination by recombination	$R_{n,k} + R_{m,l} \overset{k_{t,c}}{\rightarrow} P_{n+m,k+l}$
Transfer to monomer	$R_{n,k} + M \xrightarrow{k_{tr,M}} P_{n,k} + R_{1,0}$
Propagation of terminal double bonds	$R_{n,k} + P_{m,l} \xrightarrow{p(m)\cdot k_{p,TDB}} R_{n+m,k+l+1}$

Next, the moments of the branching points are calculated, thus only the chain length is left as an independent coordinate. The moments of the branching points are determined along the chain length as well. To validate the model, simulation results are compared to a classes model, which can be seen as a solution to the two-dimensional case (chain length, branching points) if the number of classes is sufficiently high.

Remark: To simplify notation in the following sections the first index in subscript or superscripts refers to the chain length (m, n), the second to the number of branching points (k, l). The Index for TDB is dropped in subsequent notation.

4.2.2 Moment model

The property coordinate "branching points" (BP) is reduced by taking the moments of the distribution along the BP's, often denoted as pseudo-distribution method [65].

The K^{th} resp. L^{th} branching moments are defined in Equation (57) for living chains and in Equation (58) for dead chains respectively:

$$\phi_n^K = \sum_{k=0}^{\infty} k^K R_{n,k} \tag{57}$$

$$\Psi_m^L = \sum_{l=0}^{\infty} l^L P_{m,l} \tag{58}$$

The first moments, ϕ_n^1 and Ψ_m^1 are the concentrations of BP in living or dead chains of length (n,m). The chain length moments for living chains are defined by Equation (59) resp. for dead chain in Equation (60):

$$\mu_R^{N,K=0} = \sum_{n=0}^{\infty} n^N \phi_n^0 = \sum_{n=0}^{\infty} n^N \sum_{k=0}^{\infty} R_{n,k} \tag{59}$$

$$\mu_P^{M,L=0} = \sum_{m=0}^{\infty} m^M \Psi_m^0 = \sum_{m=0}^{\infty} m^M \sum_{l=0}^{\infty} P_{m,l} \tag{60}$$

Application of the weighted summation over branching points for propagation and transfer to monomer reaction is straight forward while termination by combination reaction needs more consideration due the occurrence of a double sum due to the combination of two molecules. The propagation of terminal double bonds needs to be considered in more detail as well. The complete derivation of moment equations is lengthy and detailed in the Appendix A.3. Exemplary the contribution to the overall balance for the propagation of TDB is subsequently shown in Equation (61) for living chains and for dead chains in Equation (62), respectively. The moment equations for the living chains should be understood as follows: The terms with a negative sign are the consumption of living chains, whereas a positive sign indicates formation of a living chain with the formation of a BP. It is important to note here, that the reaction rate is multiplied by the linear correlation between the average number of TDB's per molecule and the chain length. The moment equations for dead chains only describes the consumption of dead chains and can be calculated straight forward.

$$\begin{aligned}\frac{d\phi_n^K}{dt} += {} & k_{p,TDB}\sum_{k=0}^{\infty}k^K\left(-R_{n,k}\sum_{m=1}^{\infty}\sum_{l=0}^{\infty}p(m)\,P_{m,l}\right.\\ & \left.+\sum_{m=1}^{n-1}\sum_{l=0}^{k-1}p(m)\,P_{m,l}\,R_{n-m,k-l-1}\right)\\ & = k_{p,TDB}\left(-\phi_n^K\sum_{m=1}^{\infty}p(m)\,\Psi_m^0\right.\\ & \left.+\sum_{m=1}^{n-1}\sum_{l=0}^{\infty}p(m)\,P_{m,l}\left(\sum_{k=l+1}^{\infty}k^K R_{n-m,k-l-1}\right)\right)\\ & = k_{p,TDB}\left(-\phi_n^K\sum_{m=1}^{\infty}p(m)\,\Psi_m^0\right.\\ & \left.+\sum_{m=1}^{n-1}\sum_{l=0}^{\infty}p(m)\,P_{m,l}\left(\sum_{k=0}^{\infty}(k+l+1)^K R_{n-m,k}\right)\right)\end{aligned} \tag{61}$$

$$\frac{d\Psi_m^L}{dt} += -k_{p,TDB}\,p(m)\sum_{l=0}^{\infty}l^L\,P_{m,l}\sum_{n=1}^{\infty}\sum_{k=0}^{\infty}R_{n,k} = -k_{p,TDB}\,p(m)\,\Psi_m^L\mu_R^{0,K=0} \tag{62}$$

To evaluate the number of branching points as a function of chain length, the zeroth and the first moments of the dead and living chains must be considered in the model. The contribution to the dynamics of the zeroth moments for the propagation of TDB reaction is evaluated in Equation (63) for living chains and for dead chains in Equation (64), respectively. The zeroth moments are obtained straight forward by inserting zero for K resp. L and the transformation to moments.

$$\begin{aligned}\frac{d\phi_n^0}{dt} += k_{p,TDB} &\left(-\phi_n^0 \sum_{m=1}^{\infty} p(m)\, \Psi_m^0 \right.\\ &\left. + \sum_{m=1}^{n-1} \sum_{l=0}^{\infty} p(m)\, P_{m,l} \left(\sum_{k=0}^{\infty} (k+l+1)^0 R_{n-m,k} \right) \right) \\ &= k_{p,TDB} \left(-\phi_n^0 \sum_{m=1}^{\infty} p(m)\, \Psi_m^0 + \sum_{m=1}^{n-1} p(m) \Psi_m^0 \phi_{n-m}^0 \right)\end{aligned} \tag{63}$$

$$\frac{d\Psi_m^0}{dt} += -k_{p,TDB}\, p(m)\, \Psi_m^0 \mu_R^{0,K=0} \tag{64}$$

The contribution of this reaction to the first moments is shown in Equation (65) for living chains and for dead chains in Equation (66), respectively. To obtain the first moments, K and L are set to one, respectively. The first moment then reads:

$$\begin{aligned}\frac{d\phi_n^1}{dt} += k_{p,TDB} &\left(-\phi_n^1 \sum_{m=1}^{\infty} p(m)\, \Psi_m^0 \right.\\ &\left. + \sum_{m=1}^{n-1} \sum_{l=0}^{\infty} p(m)\, P_{m,l} \sum_{k=0}^{\infty} (k+l+1)^1 R_{n-m,k} \right)\\ &= k_{p,TDB} \left(-\phi_n^1 \sum_{m=1}^{\infty} p(m)\, \Psi_m^0 \right.\\ &\left. + \sum_{m=1}^{n-1} p(m) \left(\sum_{l=0}^{\infty} l\, P_{m,l} \phi_{n-m}^0 + \sum_{k=0}^{\infty} k\, \Psi_m^0\, R_{n-m,k} + \Psi_m^0 \phi_{n-m}^0 \right) \right)\\ &= k_{p,TDB} \left(-\phi_n^1 \sum_{m=1}^{\infty} p(m)\, \Psi_m^0 \right.\\ &\left. + \sum_{m=1}^{n-1} p(m)\, (\Psi_m^1 \phi_{n-m}^0 + \Psi_m^0 \phi_{n-m}^1 + \Psi_m^0 \phi_{n-m}^0) \right)\end{aligned} \tag{65}$$

$$\frac{d\Psi_m^1}{dt} += -k_{p,TDB}\, p(m)\, \Psi_m^1 \mu_R^{0,K=0} \tag{66}$$

The overall zeroth and first moments of branching points for a CSTR reads as follows

$$\begin{aligned}\frac{d\phi_n^0}{dt} &= k_p M\left(-\phi_{n-1}^0 + \phi_n^0\right) - k_{t,c}\mu_R^{0,K=0}\phi_n^0 - k_{tr,M}M\phi_n^0 \\ &\quad + k_{p,TDB}\left(-\phi_n^0 \sum_{m=1}^{\infty} p(m)\,\Psi_m^0 + \sum_{m=1}^{n-1} p(m)\Psi_m^0\phi_{n-m}^0\right) - \frac{\dot{V}^+}{V_R}\phi_n^0\end{aligned} \tag{67}$$

$$\frac{d\Psi_m^0}{dt} = \frac{1}{2}k_{t,c}\sum_{n=1}^{m-1}\phi_n^0\phi_{m-n}^0 + k_{tr,M}M\phi_m^0 - k_{p,TDB}\,p(m)\,\Psi_m^0\mu_R^{0,K=0} - \frac{\dot{V}^+}{V_R}\Psi_m^0 \tag{68}$$

$$\begin{aligned}\frac{d\phi_n^1}{dt} &= k_p M\left(-\phi_{n-1}^1 + \phi_n^1\right) - k_{t,c}\mu_R^{0,K=0}\phi_n^1 - k_{tr,M}M\phi_n^1 \\ &\quad + k_{p,TDB}\left(-\phi_n^1 \sum_{m=1}^{\infty} p(m)\,\Psi_m^0\right. \\ &\quad \left. + \sum_{m=1}^{n-1} p(m)\left(\Psi_m^1\phi_{n-m}^0 + \Psi_m^0\phi_{n-m}^1 + \Psi_m^0\phi_{n-m}^0\right)\right) - \frac{\dot{V}^+}{V_R}\phi_n^1\end{aligned} \tag{69}$$

$$\frac{d\Psi_m^1}{dt} = k_{t,c}\sum_{n=1}^{m-1}\phi_n^1\phi_{m-n}^0 + k_{tr,M}M\phi_m^1 - k_{p,TDB}\,p(m)\,\Psi_m^1\mu_R^{0,K=0} - \frac{\dot{V}^+}{V_R}\Psi_m^1 \tag{70}$$

$\dot{V}^+$ describes the influx and V_R the volume of the reactor. The model is linear in the property coordinate of the number of branching points. Therefore, no closure relation for the branching point property coordinate is needed and only the zeroth and first branching point moments are evaluated, because higher moments do not provide additional information. In what follows this model is referred as the "BP moment model".

4.2.3 Classes model

The classes approach allows to calculate two-dimensional distributions. Usually, one property is treated like a continuous variable (here: chain length), while the second property coordinate is treated as a discrete variable (here: branching points). For each number of branching points a balance equation is required, which is called a "class" [35]. This is only feasible if the distribution of the discrete variable decays sufficiently fast and the number of classes can be kept low.

For example, $R_{n,1}$ is a living polymer of the chain length (n) carrying one branching point and $P_{m,2}$ is a dead polymer of the chain length (m) carrying two branching points and so on. The whole reaction scheme presented in Table 10 can be derived by assigning numbers to the second property coordinate. To describe the propagation of terminal double bonds, for example, the number of branching points is summed up and added by one, since one branching point is additionally created during the reaction, which is shown in Equation (71):

$$R_{n,1} + P_{m,2} \xrightarrow{p(m)\cdot k_{p,TDB}} R_{n+m,4} \tag{71}$$

The BP classes model yields exact solutions if the number of branching points (k, l) is unlimited. For practical reasons, however, a cut-off value is used, which limits the number of BP to values typically lower than 10 to reduce the computational effort. If a reaction results in higher numbers of BP than 10, they are combined in the cut-off value of 10.

A classes model with a cut-off value of 10 is applied here, which will be referred to as the "BP classes model". However, this model only works satisfactorily if less than 10 branching points are relevant. Still the computational effort is very high. For these reasons, the classes model will only serve to validate the "BP moment model".

4.2.4 Comparison of the moment model and classes model

To validate the derivation and implementation of the BP moment and BP classes models, both models are compared for the reference case defined in Table 9. The most important information that can be extracted from both models is the average number of branching points per chain $q(m)$ calculated by Equation (72):

$$q(m) = \frac{\Psi_m^1}{\Psi_m^0} \tag{72}$$

as well as the average number of branching points per molecule defined in Equation (73), which is the corresponding ratio of the integrals over all chain lengths:

$$\frac{\sum_m \Psi_m^1}{\sum_m \Psi_m^0} = \frac{c^{BP}}{\mu_P^{0,L=0}} \tag{73}$$

Figure 55 shows the average number of BP per chains of length (m). After an initial delay the number of branching points correlated linearly with chain length. Figure 56 shows the average number of branching points after start-up of the CSTR. During the first hours the number of branching points rises and levels off when approaching the steady-state.

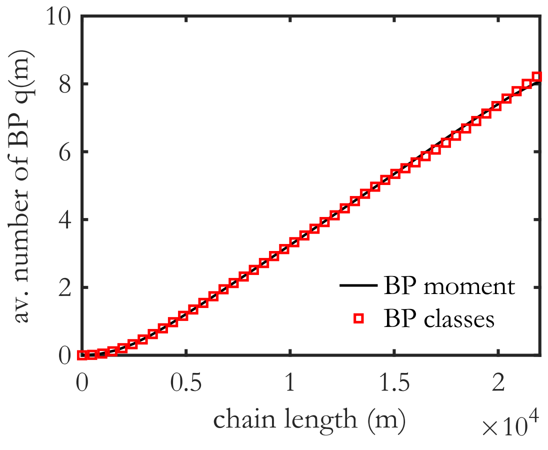

Figure 55: Comparison of the average number of branching points q(m) as a function of the chain length for the BP moment and classes model for the stationary reference case.

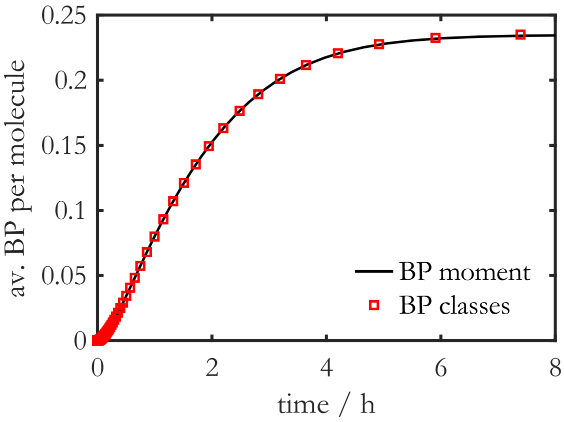

Figure 56: Comparison of the average branching points per molecule for the BP moment and classes model for the reference case.

To validate the BP moment model a comparison of the normalized Gel Permeation Chromatography (GPC) distribution for both models has been made, which is shown in Figure 57. Both models show indistinguishable results for the GPC distribution as well as the evolution of monomer conversion, which is shown in Figure 58.

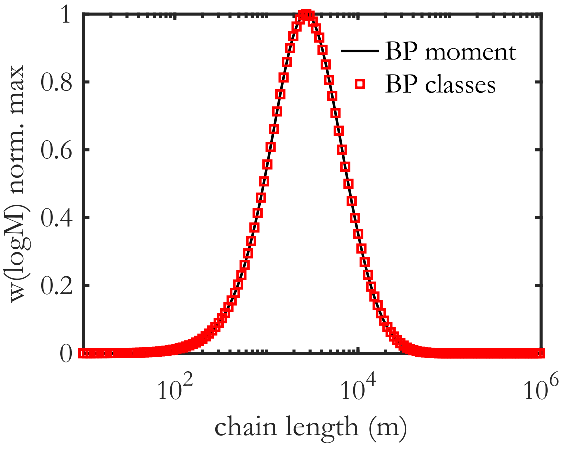

Figure 57: Comparison of the normalized GPC distribution for the BP moment and classes model for the stationary reference case.

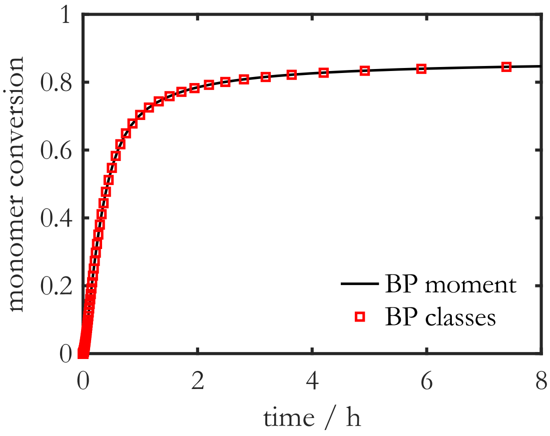

Figure 58: Comparison of the evolution of monomer conversion for the BP moment and classes model for the reference case.

The two different models for calculation of the branching point distribution were compared and show excellent agreement.

4.2.5 Dynamic calculation of branching points and terminal double bonds

In Chapter 4.2.1 was shown that the parameters of the linear relation between chain length and number of terminal double bonds can be calculated from a zero-dimensional moment model. In [6] the parameter A was calculated for the steady-state and the parameter B by using a massless counter variable to track the total number of terminal double bonds c^{TDB}.

Thus, a constant A provides correct results for the stationary case but is not a good approximation during transient operation like the startup and shutdown of a reactor. Therefore, it is proposed to continuously adapt the parameter A by calculating the moment model ("TDB double moment model") and the BP moment model in parallel.

An additional advantage of combining the two models is the ability of changing the recipe without reparameterization of A. To demonstrate the advantage of continuous adaption of parameter A (and B) a start-up of a CSTR is calculated with very low feed rate ($\dot{m}_F$=1.038 g min^{-1}), thus a high residence time of τ=10 h. Figure 59 shows the evolution of A during transition to steady-state operation and Figure 60 the mass averaged polymer weight for a constant (stationary value A=5.62·10^{-5} from Figure 59) and a continuously adapted value of A.

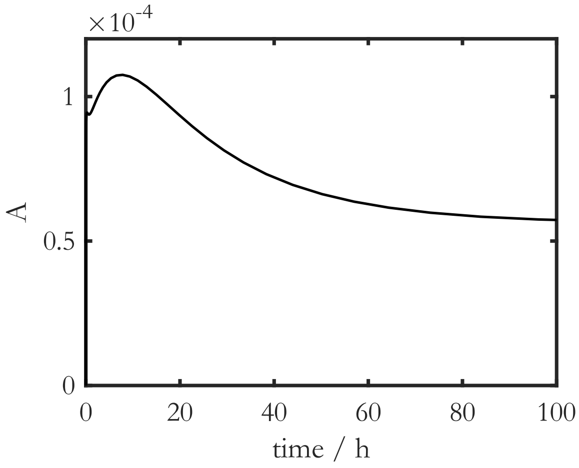

Figure 59: Time dependence of the parameter A for the modified reference case calculated with the TDB double moment model.

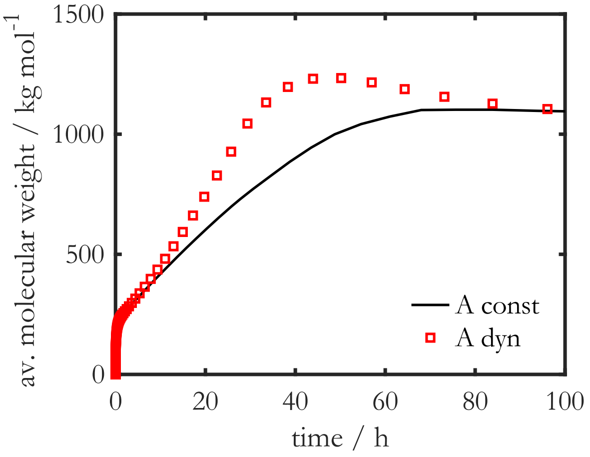

Figure 60: Comparison of the average molecular weight as a function of time for a constant A and the dynamically calculated A calculated with the BP moment model acc. to Equation (48) for the modified reference case.

The molecular weight with a constant value for A is underestimated because the steady state value for A is lower than the dynamically calculated one. The stationary state of the reaction system is reached after 100 h reaction time. A dynamically calculated A depends on the state of the reaction system and therefore it takes even longer to reach a steady state.

Additionally, the normalized GPC distribution at different times is shown in Figure 61a-c to demonstrate the dynamic behavior of the CSTR and the benefit of calculating distributions like the GPC distribution simultaneously. The previously mentioned finding that the steady state for a dynamically calculated A takes longer, can also be seen in Figure 61b. The GPC distribution between a dynamically calculated A and fixed value for A still deviates after 60 h, while after 100 h both distributions agree. Clearly, a constant value of A introduces some error during transition to the steady-state.

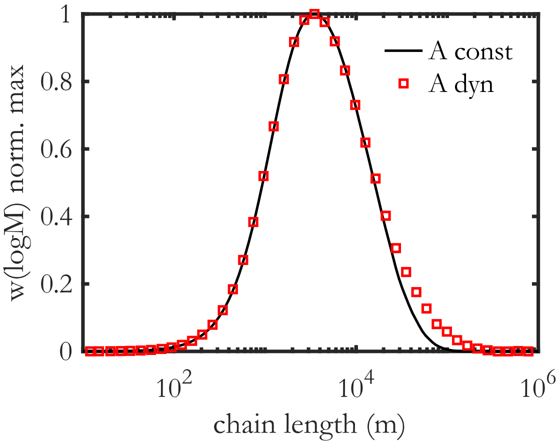

Figure 61a: Results after 30 h of reaction time.

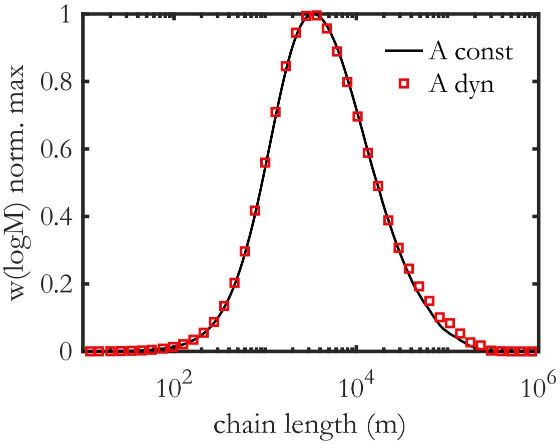

Figure 61b: Results after 60 h of reaction time.

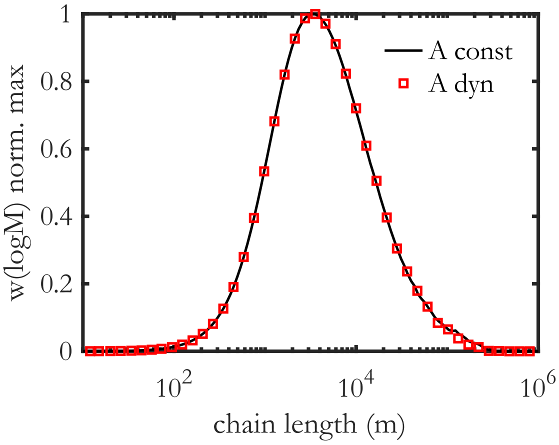

Figure 61c: Results after 100 h of reaction time.

Figure 61: Comparison of the normalized GPC distribution for the BP moment calculated with a constant and a dynamically calculated A for the modified reference case.

4.3 Results

Using the zero-dimensional "TDB double moment model" (Eqn. (49)-(52)) together with the "BP moment model" (Eqn. (67)-(70)) allows to calculate the molecular weight distribution together with the moments of the branching points. Figure 62 shows the stationary average number of branching points as a function of chain length for different residence times in a CSTR. The number of branches increases approximately linearly with the chain length. Long polymers react more often with polymers containing terminal double bonds and consequently have more branching points. With increasing residence time, the number of branching points per molecule also increases. This can be explained by lower monomer and initiator concentration, which favors the propagation of TDB's and more branching points are formed. Figure 63 shows the time-depending average BP per molecule. The stationary number of branching points increases with residence times, while the initial slope decreases slightly.

The increase of the average number of branching points is directly related to the formation of long polymer chains with increasing residence time. Then, side reactions like the transfer to monomer and subsequent propagation of TDB become more important.

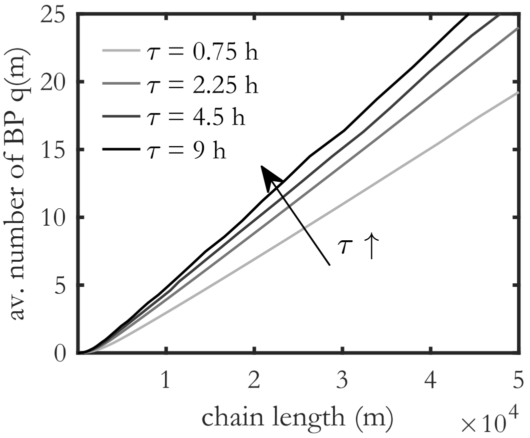

Figure 62: Comparison of the stationary average number of branching points depending on the chain length for different residence times. Small variations are due to the numerical accuracy.

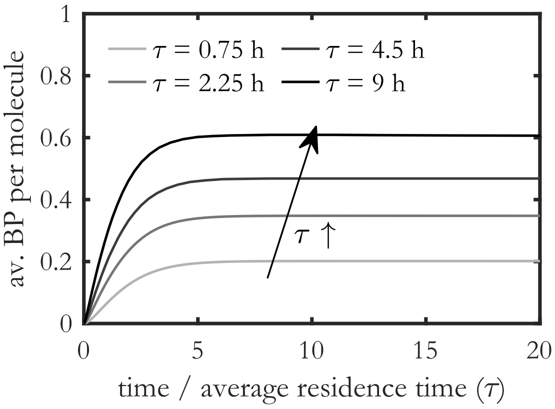

Figure 63: Comparison of the average number of branching points per molecule depending on time for different residence times.

Figure 64 presents the stationary number of branches per 1000 repeat units (RU) as a function of molecular weight in a double logarithmic plot. This type of diagram is useful for comparison with experimental data since most analytical methods determine branches per 100 or 1000 repeat units [66]. A low residence time leads to short chains which carry a relatively low number of branching points. High residence times, on the other hand, leads to formation of polymers with a high molecular weight and with a high content of branches.

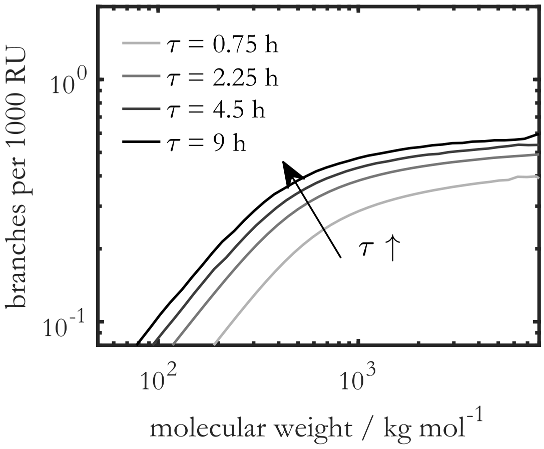

Figure 64: Comparison of the stationary average number of branching points per 1000 repeat units depending on molecular weight for different residence times.

In the following, the impact of the monomer concentration on the branching distribution is investigated. The reference case from Table 9 was modified with respect to feed rate and monomer concentration. The modified parameters are listed in Table 11.

Table 11: Parameter for the investigation of the influence of the monomer concentration.

Feed	
Monomer weight fraction w_{NVP}^{+}	0.05-0.2
Initiator weight fraction $w_{I_2}^{+}$	0.0002
Solvent weight fraction $w_{H_2O}^{+}$	1-w_{NVP}^{+}-$w_{I_2}^{+}$
Feed rate $\dot{m}_F$ [g min^{-1}]	4.6

Figure 65 shows the average number of branching points for different monomer concentrations along the chain length. While the average chain length decreases with monomer concentration, the number of branches per molecule increases. At high monomer conversion, side reactions like the TDB propagation become more favorable and more branching points are formed. The number of branching points for a monomer concentration of w_M=5 wt.-% is shown in Figure 65 only up to a certain chain length, because the concentration of longer chains is very low and numerical noise occurs.

Figure 66, shows that at higher monomer concentrations the average number of branching points per molecule increases. This is a consequence of increasing chain length.

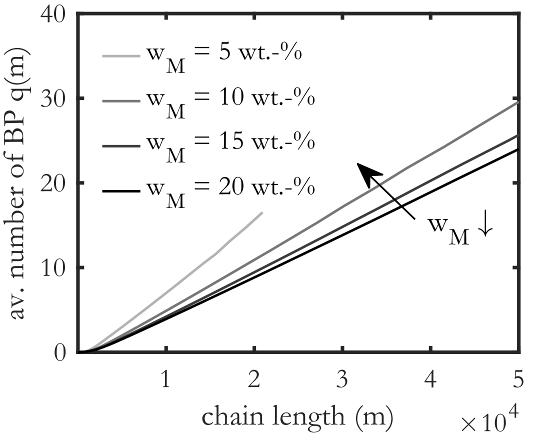

Figure 65: Comparison of the stationary average number of branching points depending on the chain length for different monomer concentrations with an average residence time τ=2.25 h.

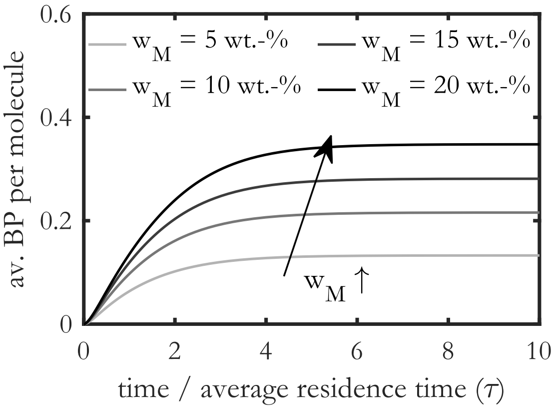

Figure 66: Comparison of the average number of branching points per molecule depending on time for different monomer concentrations with an average residence time τ=2.25 h.

Figure 67 presents the behavior of branching points per 1000 repeat units depending on the molecular weight for different monomer concentrations. A low monomer content leads to short chains and generally to a low molecular weight while carrying a relatively high number of branching points. Higher monomer content, on the other hand, leads to polymers with a lower content of branches compared to lower monomer content.

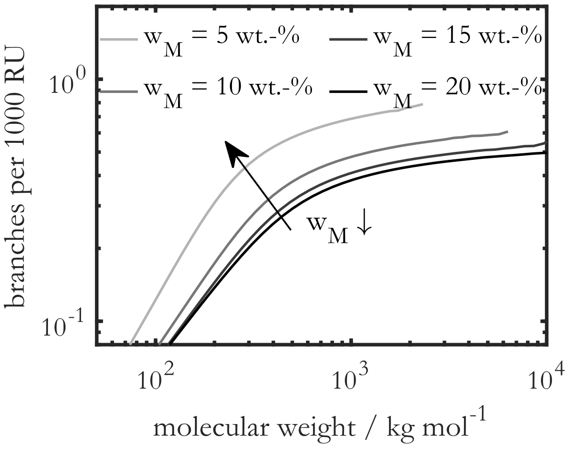

Figure 67: Comparison of the stationary average number of branching points per 1000 repeat units depending on molecular weight for different monomer concentrations with an average residence time τ=2.25 h.

4.4 Model validation with experimental results

In the following, the predictions of the developed kinetic model for the branching point distribution and the corresponding set of parameters will be compared to experimental data. Polymerizations in a stirred tank reactor were carried out varying residence times and monomer concentrations in [6] and will be evaluated in this work. During transition to steady-state samples were taken and analyzed by gel permeation chromatography (GPC), field flow fractionation (FFF) and high-performance liquid chromatography (HPLC). Molecular weight averages, monomer conversion, molecular weight distributions and branching points are compared to model predictions.

4.4.1 Molecular weight averages and monomer conversion

In Figure 68A to D, the simulations of the average molecular weight and the monomer conversion are compared to experimental results. Samples were taken at different times after startup and normalized by average residence time. The molecular weight M was determined using GPC resp. FFF, which were coupled with concentration and molar mass sensitive detectors. The theoretical background to the evaluation of experimental data has already been explained in Chapter 2.3.5. Figure 68A shows the plot of $\overline{M}_w$ for a CSTR reactor at different average residence times and a monomer weight fraction of 20 wt.-% in the feed. With increasing residence time, the average molecular weight increases. In general, the experimental data can be well reproduced by the simulations.

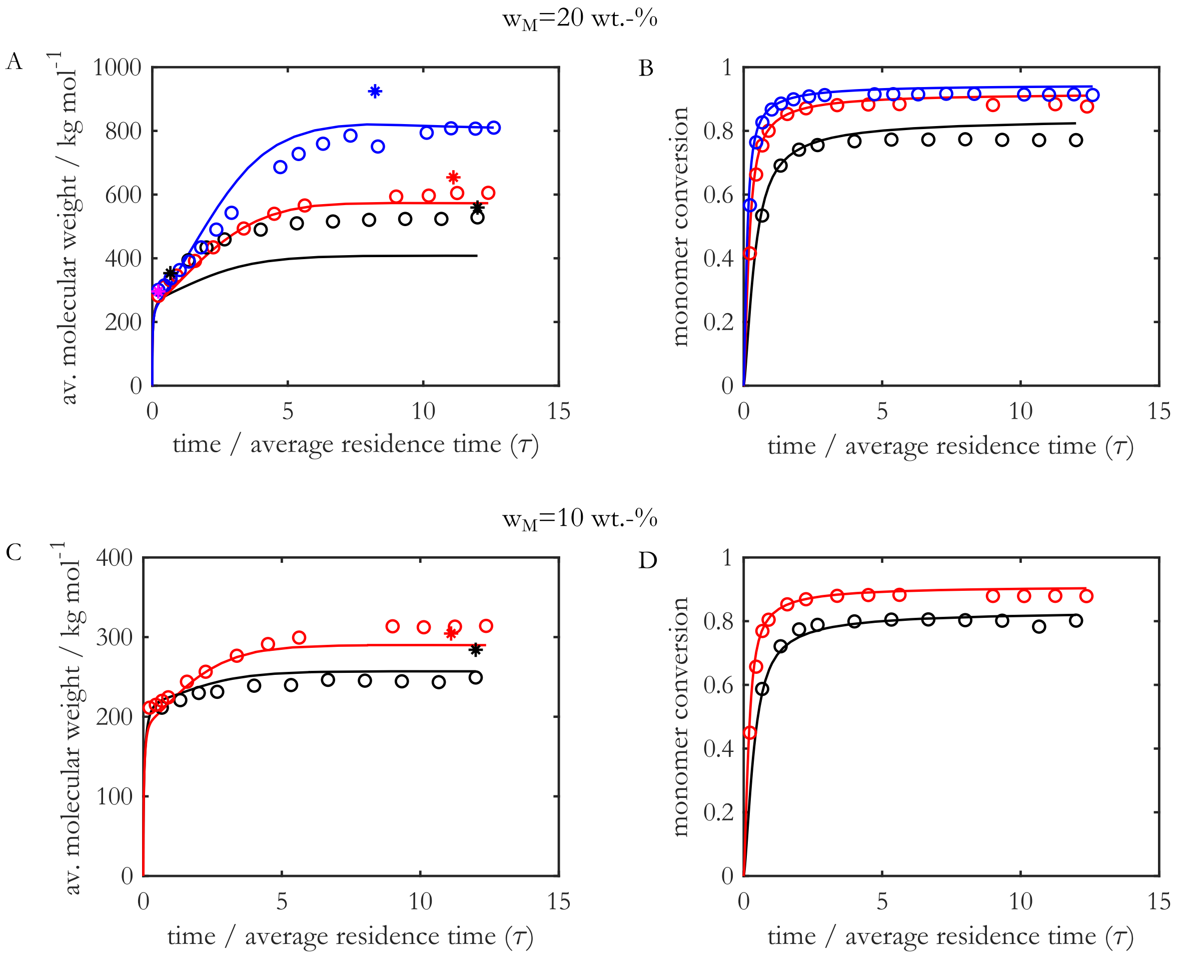

Figure 68: Comparison of the evolution of the average molecular weight and monomer conversion for simulations (lines) and experiments (GPC – circle; FFF – star) at different average residence times: black – 0.75 h; red – 2.25 h; blue – 4.5 h. A, B: w_M=20 wt.-%; C, D: w_M=10 wt.-%

Monomer conversions vs. reduced reaction times are plotted in Figure 68B. At higher average residence time, monomer conversion increases initially fast and quickly approaches the steady-state value. Predicted conversions are in good agreement with measurements, whereby the simulations slightly overestimate monomer conversion.

$\overline{M}_w$ for a CSTR at different average residence times and a monomer concentration of 10 wt.-% is plotted in Figure 68C. Again, the clear trend between $\overline{M}_w$ and residence time is obvious.

The corresponding monomer conversions plotted in Figure 68D also show good agreement between simulations and the experiments. Like for a feed concentration of 20 wt.-%, there is a slight overestimation by model predictions.

In general, the predictions of simulations and experimental data show good agreement with respect to the molecular weight averages and the monomer conversion except for w_M=20 wt.-% and $\bar{\tau}$=0.75 h. At low reaction times, the average molecular weight and the monomer conversion increase sharply. Then the curves slowly approach the steady state. It is evident that the average steady state molecular weight from GPC data for a monomer feed concentration of 20 wt.-% is slightly underestimated at low residence times. The experimental molecular weight for a monomer feed concentration of 10 wt.-% fit better to the simulations for both average residence times. The reason for this may be that $k_{p,TDB}$ is taken as constant although the propagation of TDB is a reaction between two macromolecules and might be diffusion-limited, which means that the reaction rate is affected by the size of the polymer chains. It can be expected that the coefficient would decrease with higher polymer content and a corresponding increase in viscosity. This is especially true for high average residence times and high monomer feed concentrations. Therefore, for smaller molecules (10 wt.-% monomer feed concentration) the diffusion limitation does not have such a strong impact. The results of the FFF for all residence times are underestimated by the simulations. The experimental results of GPC fit in total better to the simulations because the value for $k_{p,TDB}$ was adjusted to the molecular weights of GPC measurements in a previous work [6]. Since only a few samples were investigated with FFF, it is not possible to obtain a clear tendency.

4.4.2 Molecular weight distribution at steady state

To obtain molar mass distributions in addition to the mass average molecular weights, the calculation method from Chapter 2.3.5 is used.

The last sampling time (12x average residence times) was taken as the steady state for the average molecular weight for the experiments, which, according to Figure 68A and C, did not change after 10 average residence times.

Figure 69A shows the comparison of the normalized GPC distributions of the CSTR experiment with the simulation at an average residence time of $\bar{\tau}$=0.75 h and a monomer weight fraction of 20 wt.-% in the feed. For the FFF result, there is a broadening of the peak compared to the simulations and the results of the GPC. The simulation here slightly underestimates the molecular weight and for this reason the complete distribution is slightly shifted to smaller molecular weights. The comparison for the residence time of 2.25 h and a monomer weight fraction of 20 wt.-% in the feed is shown in Figure 69B. The GPC and FFF results are in better agreement with the simulation results than the results obtained with an average residence time of 0.75 h.

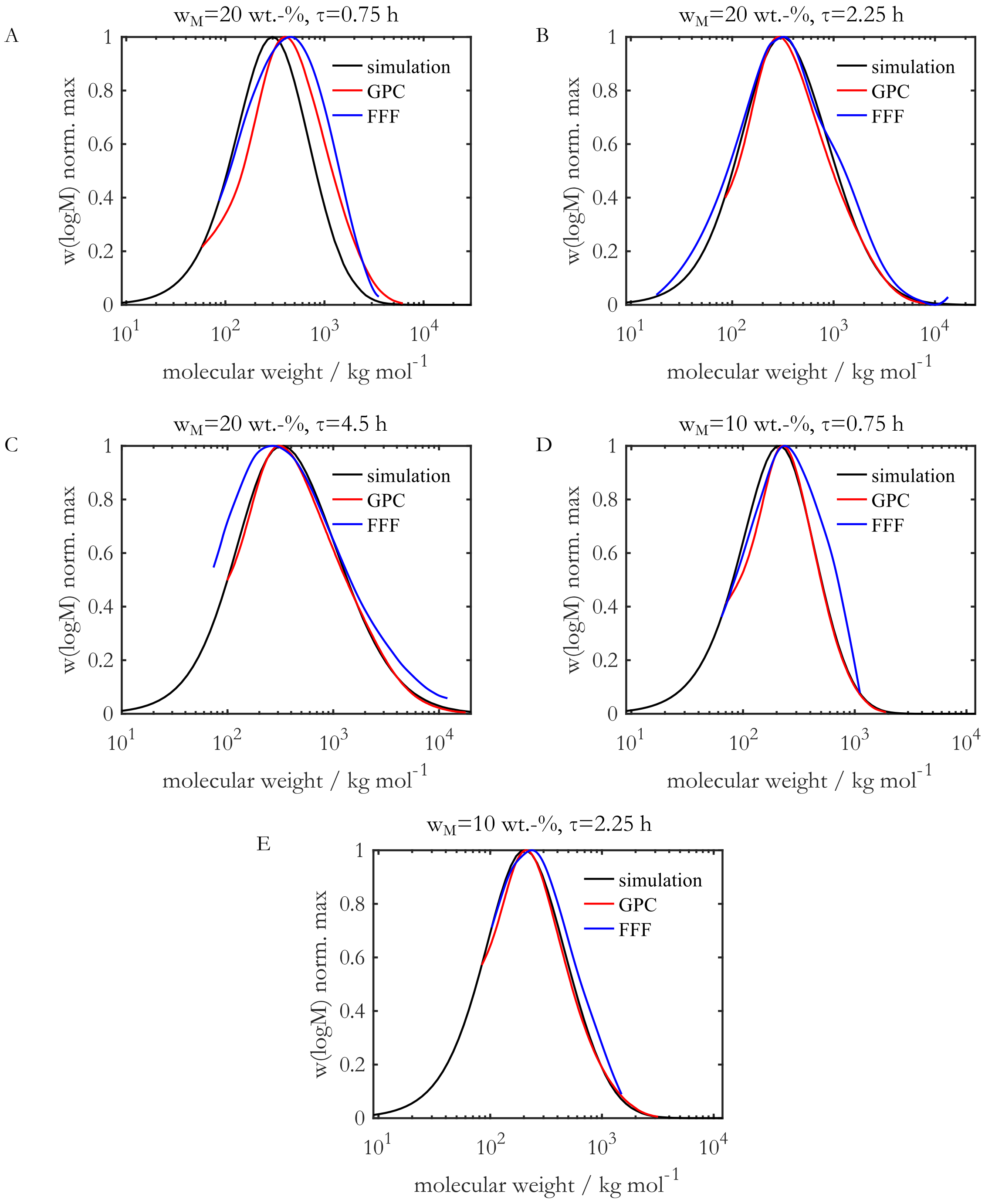

Figure 69: Comparison of the normalized GPC distribution from experiments and simulations at different average residence times and monomer feed concentrations. A: w_M=20 wt.-% and τ=0.75 h; B: w_M=20 wt.-% and τ=2.25 h; C: w_M=20 wt.-% and τ=4.5 h; D: w_M=10 wt.-% and τ=0.75 h; E: w_M=10 wt.-% and τ=2.25 h.

Figure 69C shows the distributions at a residence time of 4.5 h and a monomer feed concentration of 20 wt.-%. The GPC results are in very good agreement with the simulation. However, there is a widespread peak in the FFF results. In general, the molar mass distributions between simulation and experiment differ for 20 wt.-% monomer feed concentration at low residence time of 0.75 h and better agree for higher residence times. Again, this can be explained by the fact that a constant parameter for $k_{p,TDB}$ is inappropriate and thus the reaction rate does not depend on the pore size.

The normalized GPC distributions at an average residence time of 0.75 h and a monomer weight fraction of 10 wt.-% in the feed are shown in Figure 69D. Thereby, the results of the GPC show very good agreement and those of the FFF are broadened for high molecular weights.

The comparison at a residence time of 2.25 h and a monomer weight fraction of 10 wt.-% in the feed, which is shown in Figure 69E, also shows good agreement between the experimental results both for FFF and GPC and the simulations. In contrast to the experiments at higher monomer concentration, the experimental and simulated molar mass distributions agree better for a monomer concentration of 10 wt.-%, since diffusion limitation is not as important for smaller molecules.

As shown in Figure 69A to E, the steady state molecular weight distribution of CSTR experiments at different residence times and monomer weight fractions in the feed can be well represented by the simulations. Furthermore, the FFF results are shifted to higher molecular weights compared to the GPC results. The reason for this is that interactions between large molecules and the gel, which is used for the separation, can occur during separation with GPC. Moreover, shear degradation of polymer molecules with a molar weight over 10^6 g/mol is possible. The figures also show that for higher residence times a broadening of the distribution and a shift towards higher molecular weights take place. This can be explained by the fact that the increased residence time results in the formation of longer chains and increased branching.

4.4.3 Characterization of branching points

In the following, the experimental and simulated data are compared with respect to the branching points.

Figure 70A to F show the number of BP as well as the number of BP per 1000 repeat units (RU) for CSTR experiments along the molecular weight for different residence times and different monomer weight fractions in the feed. At a monomer weight fraction of 20 wt.-% in the feed, the simulations are in good agreement with the experimental data from GPC and FFF. The results for an average residence time of $\bar{\tau}$=0.75 h is shown in Figure 70A with the average number of branching points over the molecular weight and in Figure 70B the average number of branching points per 1000 repeat units. Here, the simulation results agree better with FFF than with GPC results.

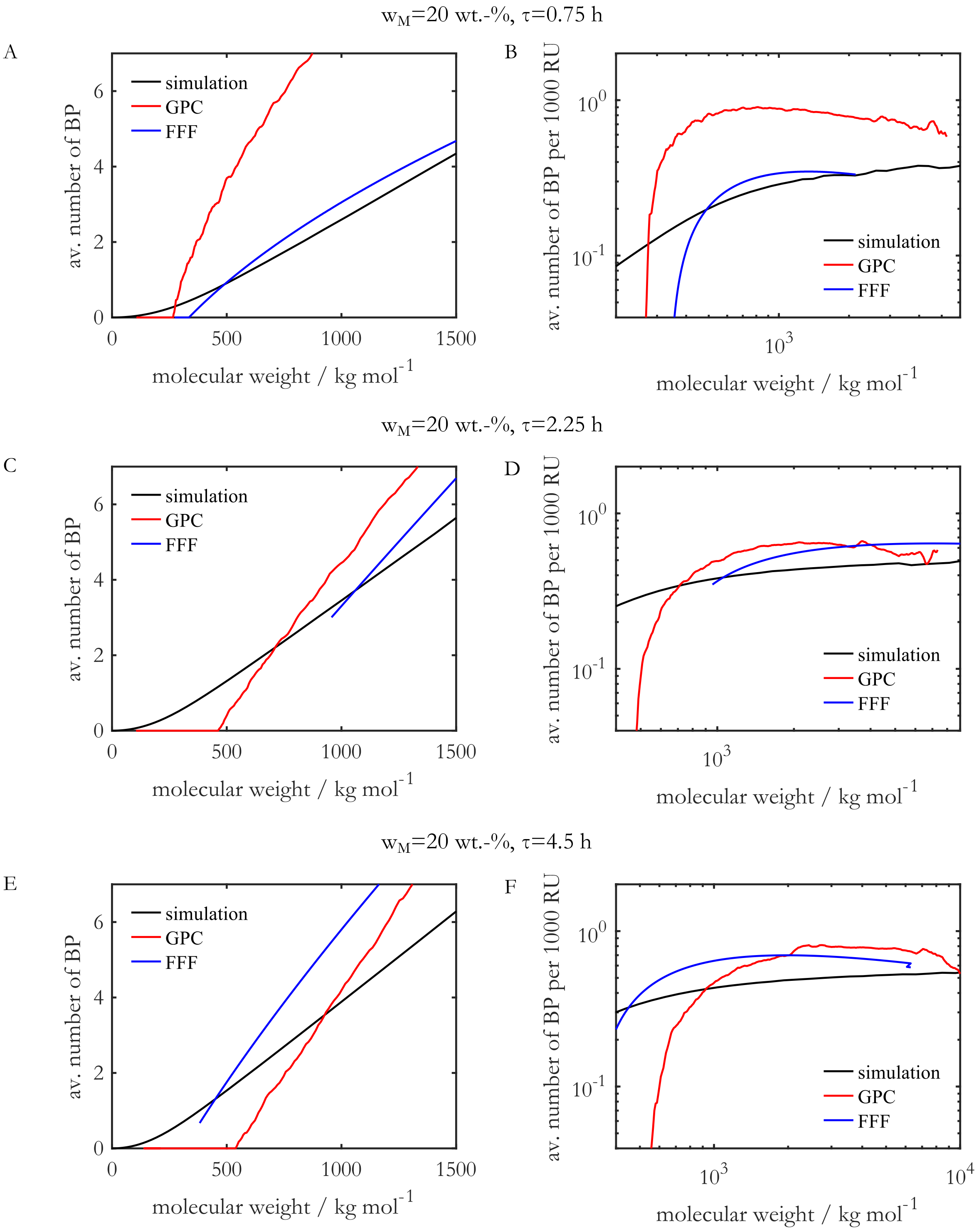

Figure 70: Comparison of the number of branching points and the number of branching points per 1000 RU from experiments and simulations at different average residence times and w_M=20 wt.-% A, B: τ=0.75 h; C, D τ=2.25 h; E, F τ=4.5 h

Furthermore, no branching points can be detected by the GPC and FFF at very small molecular weights. The reason for this is the instrument design, which cannot reliably measure particles sizes <10 nm with light scattering.

Figure 70C and D show the comparison at an average residence time of 2.25 h. The experimental results of the GPC and FFF are in good agreement for higher molecular weights. It can also be seen that there is a higher branching formation compared to the residence time of 0.75 h.

The comparison at a residence time of 4.5 h is shown in Figure 70E and F. The results conducted by the experiments can be represented by the simulations reasonably well. The simulation slightly underestimates the number of BP for higher molecular weights. Compared to lower residence times of 0.75 h and 2.25 h, there is a higher formation of branching points. Thus, for higher residence times, the increase in branches is higher than predicted by the model. The reason for this is that parameter $k_{p,TDB}$ is treated as a constant parameter, which is slightly underestimated in this case, because the increased monomer conversion with higher average residence times, leads to an increase of the probability of side reactions, such as the transfer to monomer and propagation of terminal double bonds.

At a monomer weight fraction of 10 wt.-% in the feed, the experimental data for a residence time of 0.75 h, in Figure 71A and B, can be well described by the simulations.

Figure 71C and D show the comparison at a residence time of 2.25 h and a monomer weight fraction of 10 wt.-% in the feed. In comparison with the residence time of 0.75 h, there is also an increased branching formation. This is again due to higher monomer conversion, which leads to an increase of the side reactions and thus to branching.

It has been shown that the experimental trends can be well covered by the simulations at NVP feed concentrations between 10 and 20 wt.-%. In most cases the number of branches is underestimated by the simulations. The presented results from CSTR experiments should only be interpreted qualitatively, since the description of the linear reference sample by a power law function relies on only two linear samples. An approximation with a higher number of linear samples could minimize the error. Moreover, due to the non-ideal separation of branched samples at low molecular weights, linear extrapolation was used for the GPC data which leads to additional errors.

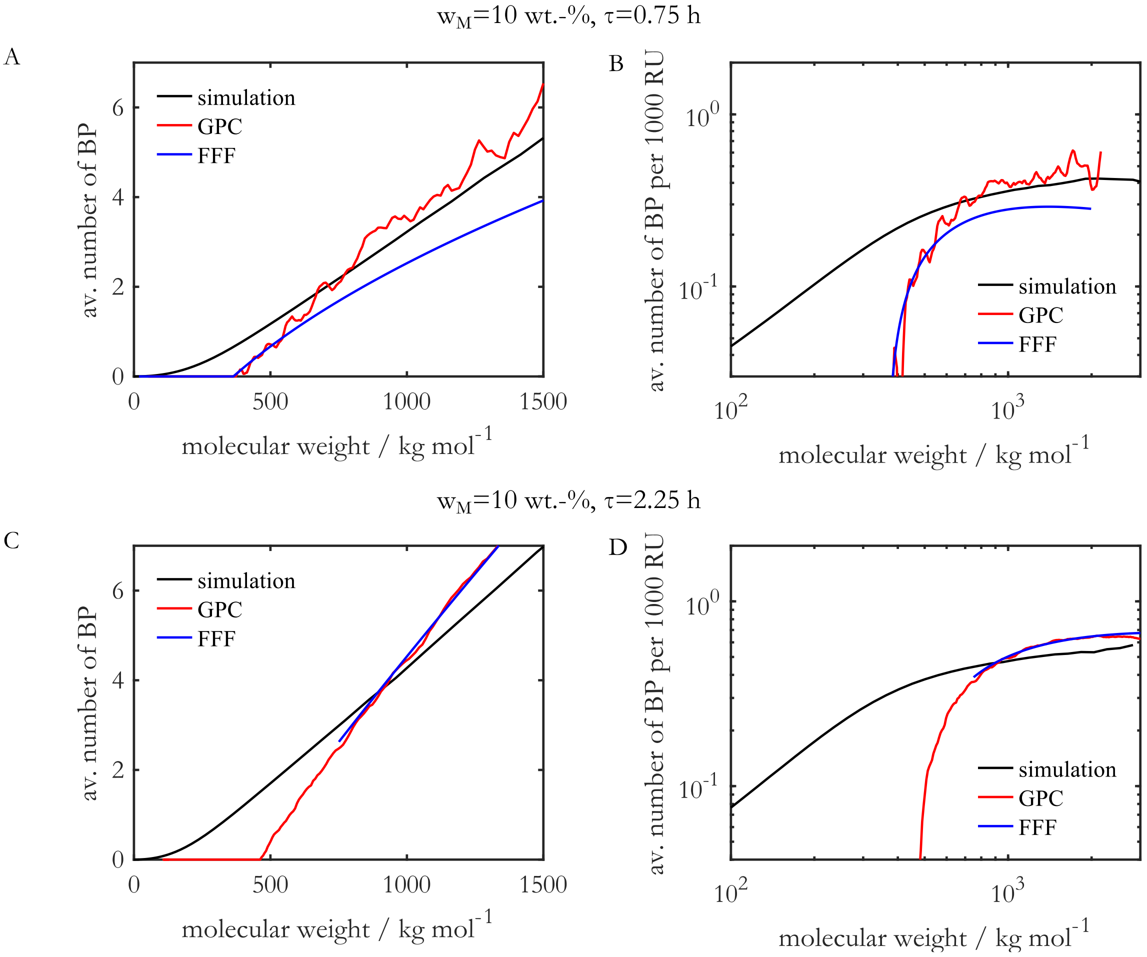

Figure 71: Comparison of the number of branching points and the number of branching points per 1000 RU from experiments and simulations at different average residence times and w_M=10 wt.-% A, B: τ=0.75 h; C, D: τ=2.25 h

4.5 Approximation of branching point distribution with zero-dimensional branching moments

Alternatively, the number of branching points can also be calculated via a correlation using 0D moments. Those offer the advantage that they are significantly computationally cheaper to calculate. This is useful for a CFD simulation, for example, if the branching distribution is desired to be dependent on the chain length. These moments can be calculated by

$$\mu_P^{M,J,L} = \sum_{j=0}^{\infty} j^J \sum_{m=1}^{\infty} m^M \sum_{l=0}^{\infty} l^L P_{m,j,l}. \tag{74}$$

The approach for a proportional relationship between the number of branching points and the chain length for 0D moments is as follows

$$c^{BP} = \sum_{m=1}^{\infty} \mu_P^{(m),0,1} = A_2 \sum_{m=1}^{\infty} m \cdot \mu_P^{(m),0,0} = A_2 \cdot \mu_P^{1,0,0} = \mu_P^{0,0,1}. \tag{75}$$

A proportional correlation offers the advantage that only 1 parameter has to be calculated. This can be calculated directly from the 1st chain length moment and a counter variable H^{BP}, which describes the concentration of branching points. Alternatively, a linear relationship between branching points and chain length for 0D moments can be described by

$$c^{BP} = \sum_{m=1}^{\infty} \mu_P^{(m),0,1} = A_2 \sum_{m=1}^{\infty} m \cdot \mu_P^{(m),0,0} + B_2 \sum_{m=1}^{\infty} \mu_P^{(m),0,0} = A_2 \cdot \mu_P^{1,0,0} + B_2 \cdot \mu_P^{0,0,0} = \mu_P^{0,0,1}. \tag{76}$$

After insertion into the reaction equations, the mathematical transformation is somewhat extensive and is therefore only presented in the Appendix A.3.10. The result for the two parameters A_2 and B_2 is

$$A_2 = \frac{\mu_P^{1,0,1}\mu_P^{0,0,0} - \mu_P^{1,0,0}\mu_P^{0,0,1}}{\mu_P^{2,0,0}\mu_P^{0,0,0} - \mu_P^{1,0,0}\mu_P^{1,0,0}}; B_2 = A_2 \cdot \left(-\frac{\mu_P^{1,0,0}}{\mu_P^{0,0,0}}\right) + \frac{c^{BP}}{\mu_P^{0,0,0}}. \tag{77}$$

For the reference case from Table 9, Figure 72 shows the correspondence of the BP model for the number of branching points over the chain length for the proportional and the linear correlation. The linear correlation shows a significantly better agreement. Figure 73 shows the agreement of the linear correlation for different residence times in a CSTR reactor. The trend for a higher number of branching points depending on residence times can also be shown by the correlation. Therefore, the deviation from the BP model becomes larger for smaller residence times.

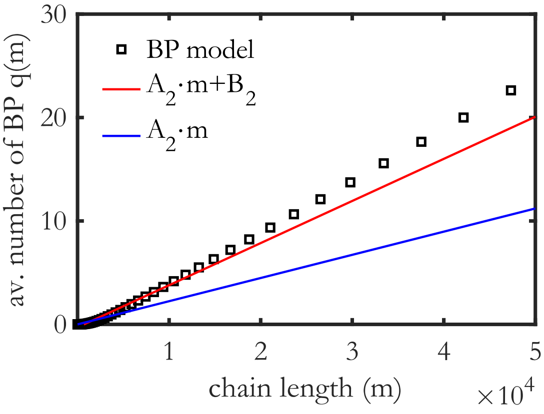

Figure 72: Number of branching points over the chain length for the reference case from Table 9. In red the linear and in blue the proportional correlation.

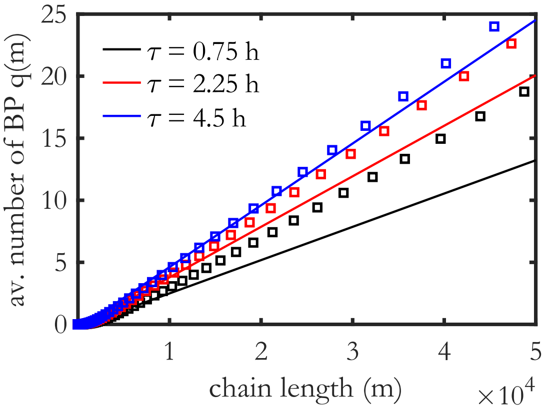

Figure 73: Number of branching points over the chain length for different residence time distributions with a monomer concentration of w_M=20 wt.-%. The dots show the BP model and the lines the linear correlation.

4.6 Conclusions

To describe the onset of fouling for the polymerization of N-Vinylpyrrolidone a detailed kinetic scheme has been developed. Rigorous simulation using the detailed kinetic would require a three-dimensional property space: chain length, terminal double bonds (TDB) and branching points (BP). In this chapter the approach of Zander [6] was extended in two directions. First, the parameters of the linear relation between chain length and number of TDB's are dynamically adapted by using a zero-dimensional moment model, which is calculated in parallel. Second, by calculation of the chain length distributed moments of the branching points, a one-dimensional model for the number of branching points along the chain length has been derived. Simulations of this one-dimensional model (termed BP moment model) together with the zero-dimensional model allow to calculate the polymer microstructure (chain length distribution, number of BP and TDB as function of chain length) during transient operation of a reactor. The new model was compared to a computationally expensive classes-model with full accordance.

To separate effects of hydrodynamics and kinetics, the new model was used to calculate polymer properties during transition of a CSTR to the steady state and showed the impact of residence time and monomer concentration.

To validate the kinetic model, simulated data were compared with experimental results obtained from CSTR experiments in [6] with NVP feed concentrations of 10 and 20 wt.-% and different average residence times. The polymer samples were analyzed using gel permeation chromatography, field flow fractionation und high performance liquid chromatography. In general, the simulations show good agreement with the experimental data. The evolution of the molecular weight average and monomer conversion as well as molecular weight distribution can be well represented by the model. Trends for different residence times and monomer concentrations can be represented correctly. The average number of branching points also shows qualitative agreement between the model-based simulations and the experimental data. Branching points increase steeply for higher residence times. This trend could be observed both in simulations and experimental data collected by GPC resp. FFF and support the validity of the reaction mechanism and the mathematical model. Additionally, the monomer content in the feed stream influences the formation of branched polymers. A lower monomer concentration leads to a higher number of branching points depending on the chain length.

However, the separation of polymer molecules by GPC may lead to a distortion of the results due to anchoring effects. Another source of uncertainty of the experimental data with respect to the branching points are the assumptions made for the calculation of branching points. Assuming a constant $k_{p,TDB}$ could be the reason, although the propagation of TDB may be diffusion-limited, which means the reaction rate is affected by the size of the polymer chains.

Further, a zero-dimensional approach was developed to calculate branching points for example in a CFD simulation.

5 Transport of statistic polymer moments[8]

The method of moments is a well-established technique for modelling polymerization reactions [36]. Instead of solving the balance equation of a distributed polymer only the statistical moments of the chain length distribution are calculated. For the simple case of a homogeneous polymerization the distributions of the living and dead chains can be expressed by three or more moments. Moments are calculated in units of concentration. Balance equation for each polymer species can thus be easily converted into moment equations. In many types of polymer reactions the moments close, otherwise a closing condition is required.

In cases where the assumptions of ideal mixing or a very simple flow field (plug flow) are inadequate, species transport by convective and diffusive transport must be accounted for. Velocity fields may be calculated by well-established CFD methods and can be directly applied to transport of polymeric species resp. to the transport of moments of the polymer size distributions. While the convective transport of polymer species can be converted to transport of moments directly, this is not the case for diffusive transport. Diffusive transport of moments is scarcely discussed in the literature. A rare example is provided by Arriola for convective and diffusive transport in a tubular reactor [67].

It will be shown that limiting cases of the general Maxwell-Stefan diffusion for ideal mixtures allow to derive a closed form for the transport equation of polymer moments. The first limiting case assumes for infinite dilution of the polymer chain, which means that friction between polymer chain is completely neglected and only friction between polymer chain and solvent (or monomers) is considered. Since the Maxwell-Stefan diffusion coefficient between solvent and polymer is relatively large, the diffusive fluxes of moments are usually overestimated. This might be irrelevant if diffusion is subordinate to convection. In special cases like spray polymerization [68]–[70], regions of low convective transport (i.e. behind mixing elements) or polymer fouling close to walls of micro reactors, the assumption of "No Polymer Friction" introduces large errors. This is especially true at high

---

[8] The majority of this chapter has been published in advance of this thesis under the terms of the Creative Commons Attribution License (CC BY 4.0) in [80]. Minor changes have been made and passages have been added for better comprehensibility and embedding in the context of this thesis.

polymer content. In this case the use a different limiting case of the Maxwell-Stefan model is superior, where we assume for infinite friction between the polymer chains, which means that a polymer chain cannot diffuse against other polymer chains. Thus, all polymer chains at a given location move as a whole against the solvent. As will be shown, this assumption also allows for closure of the transport model of polymer moments.

The outline of this chapter is as follows: First the general transport equation is derived for a homopolymer and Maxwell-Stefan equations for diffusive transport. Two limiting cases are then derived which allow to convert the transport equation of polymeric species to a closed set of moment equations. Finally, advantages and limitations of both limiting cases are discussed and results compared to simulations with the full Maxwell-Stefan model, for a simple system consisting of one solvent and two discrete polymer species of different chain length.

5.1 Multicomponent transport

In polymer reaction processes, where ideal mixing is assumed for, polymers are either treated in terms of their moments, or, if one is interested in details of size distribution, by adaptive numerical Galerkin methods [71]. The latter is also preferred in cases where moment equations do not close. To study complicated polymeric structures, like cross-linked networks, Monte Carlo methods are applied. When the impact of a distributed flow field on a polymerization process shall be studied, the method of moments is preferred, since other methods become computationally infeasible for practical purposes.

Usually, the mass-averaged velocity, e.g. in a CFD simulation, is known. Therefore, with the development of the equations in a mass-averaged reference frame is started.

The mass-induced velocity arises from the component velocities v_i, where w_i denotes the mass fraction on species i

$$v = \sum_i w_i v_i. \tag{78}$$

The mass balance for a species i then reads

$$\frac{\partial \rho_i}{\partial t} + \nabla \cdot v\, \rho_i + \nabla \cdot J_i = M_i r_i^{total} \tag{79}$$

with diffusive fluxes J_i relative to the mass averaged velocity. ρ_i is the mass density, M_i denotes the molecular mass, r_i^{total} the total reaction rate of species i.

Since reaction rates are expressed in terms of concentrations, a molar reference system is preferred for treating the moments of polymer systems. The mole balance for a species i reads

$$\frac{\partial c_i}{\partial t} + \nabla \cdot v^N c_i + \nabla \cdot J_i^N = r_i^{total} \tag{80}$$

with diffusive fluxes J_i^N relative to the molar average velocity

$$v^N = \sum_i x_i v_i \tag{81}$$

with the mole fraction x_i and the concentration c_i. To distinguish between a mass and a mole centered reference system, mole centered quantities are indicated by superscript N.

A component's velocity v_i can be calculated from molar fluxes by [72]

$$v_i = v^N + \frac{J_i^N}{c_i}. \tag{82}$$

The molar average velocity can be calculated with Equation (78), (82) and some math to

$$v^N = v - \sum_i \frac{J_i^N M_i}{\rho_i}. \tag{83}$$

With Equation (83) and the assumption of constant density, the balance Equation (80) becomes

$$\frac{\partial c_i}{\partial t} + \nabla \cdot \left(c_i \left(v - \frac{1}{\rho} \sum_i J_i^N M_i \right) \right) + \nabla \cdot J_i^N = r_i^{total}. \tag{84}$$

From polymer size distribution given in terms of repeating units s of (homo) polymer P denoted by $P(s)$ the kth-moment can be calculated by

$$\xi^k = \sum_{s=1}^{\infty} s^k c_{P(s)}. \tag{85}$$

The transport equation of moments is derived by multiplication of Equation (84) with s^k and summation over all polymer species $P(s)$ to

$$\frac{\partial \xi^k}{\partial t} + \nabla \cdot \left(\xi^k \left(v - \frac{1}{\rho} \sum_i J_i^N \, M_i \right) \right) + \sum_{s=1}^{\infty} \nabla \cdot s^k J_{P(s)}^N = \sum_{s=1}^{\infty} s^k \, r_{P(s)}^{total}. \tag{86}$$

The diffusive transport of moments of the polymer flux is denoted as

$$J_{\xi^k}^N = \sum_{s=1}^{\infty} s^k J_{P(s)}^N. \tag{87}$$

While convective transport can be readily written in terms of moments, the diffusive transport of moments $J_{\xi^k}^N$ requires further consideration.

The molecular weight of the polymers can be expressed by the chain length s and the molecular weight of one repeating unit MW_{seg}

$$M_{P(s)} = s \cdot M_{seg}. \tag{88}$$

After splitting the sum for low-molecular species (index "low") and polymer species, the balance equation develops to

$$\frac{\partial \xi^k}{\partial t} + \nabla \cdot \left(\xi^k \left(v - \frac{1}{\rho} \sum_i^{n_{low}} M_i J_i^N - \frac{1}{\rho} M_{seg} J_{\xi^1}^N \right) \right) + \nabla \cdot J_{\xi^k}^N = r_{\xi^k}^{total} \tag{89}$$

with the total reaction rate for the kth moment

$$r_{\xi^k}^{total} = \sum_{s=1}^{\infty} s^k \, r_{P(s)}^{total} \tag{90}$$

and the total polymer flux of all polymer distributions $J_{\xi^1}^N$.

However, to derive an expression for the diffusive fluxes of polymer moments, simplifications are needed. The treatment of the reaction rate in terms of moments is well established and can be found in [30].

5.2 Maxwell-Stefan diffusion for multicomponent mixtures

To derive an expression for diffusive transport of moments we start with the rigorous treatment of multicomponent mixture by the Maxwell-Stefan equation. The general Maxwell-Stefan equations for isothermal diffusion in n resp. J–component systems are [73]

$$d_i = \frac{x_i}{RT} \nabla \mu_i = -\sum_{j=1}^{J} \frac{x_i x_j \left(v_i - v_j\right)}{\mathfrak{D}_{ij}} \tag{91}$$

with the driving force d_i for species i, the ideal gas constant R, the temperature T, the chemical potential μ_i of species i, its molar fraction x_i, its overall transport velocity v_i and the Maxwell-Stefan diffusion coefficient $\mathfrak{D}_{ij}$ for interactions between species i and j.

Using Equation (82) the general Maxwell-Stefan equation can be expressed by molar fluxes

$$d_i = -\sum_{j=1}^{J} \frac{x_i x_j \left(v_i - v_j\right)}{\mathfrak{D}_{ij}} = -\sum_{j=1}^{J} \frac{x_j J_i^N - x_i J_j^N}{c \mathfrak{D}_{ij}}. \tag{92}$$

The overall concentration c can be calculated by

$$c = \sum_{i}^{J_{low}} c_i + \xi^0, \tag{93}$$

where J_{low} stands for all low molecular species with concentration c_i and ξ^0 is the 0th moment of all polymer distributions, the total polymer concentration. To line out the basic ideas it is sufficient to consider a ternary mixture consisting of a small molecule like solvent or monomer (S) and two polymeric components of the same type but with different molecular mass resp. chain length (P1=P(4000) and P2=P(2000)). The two discrete polymer species may represent two very narrow distributions of the same type of polymer. The ternary system will be used for comparison of the limiting cases with the full Maxwell-Stefan model.

For a ternary mixture the Maxwell-Stefan equations reads:

$$d_S = \frac{x_S}{RT}\nabla\mu_S = -\sum_{j=S}^{J}\frac{1}{c}\cdot\frac{x_j J_S^N - x_S J_j^N}{\mathfrak{D}_{Sj}} = -\frac{1}{c}\cdot\left(\frac{x_{P1}J_S^N - x_S J_{P1}^N}{\mathfrak{D}_{SP1}} + \frac{x_{P2}J_S^N - x_S J_{P2}^N}{\mathfrak{D}_{SP2}}\right), \tag{94}$$

$$\begin{aligned} d_{P1} = \frac{x_{P1}}{RT}\nabla\mu_{P1} &= -\sum_{j=P1}^{J}\frac{1}{c}\cdot\frac{x_j J_{P1}^N - x_{P1}J_j^N}{\mathfrak{D}_{P1j}} \\ &= -\frac{1}{c}\cdot\left(\frac{x_S J_{P1}^N - x_{P1}J_S^N}{\mathfrak{D}_{P1S}} + \frac{x_{P2}J_{P1}^N - x_{P1}J_{P2}^N}{\mathfrak{D}_{P1P2}}\right). \end{aligned} \tag{95}$$

With the closing condition that all fluxes need to add up to zero [73], the Jth (resp 3rd in our example) flow can be calculated from

$$J_J^N = -\sum\nolimits_i^{J-1} J_i^N. \tag{96}$$

For a ternary mixture with the elimination of J_3^N follows

$$\begin{aligned} d_S &= -\frac{1}{c}\cdot\left(\frac{x_{P1}J_S^N - x_S J_{P1}^N}{\mathfrak{D}_{SP1}} + \frac{x_{P2}J_S^N + x_S(J_S^N + J_{P1}^N)}{\mathfrak{D}_{SP2}}\right) \\ &= -\frac{1}{c}\cdot\left(\left(\frac{x_{P1}}{\mathfrak{D}_{SP1}} + \frac{x_{P2}+x_S}{\mathfrak{D}_{SP2}}\right)J_S^N + \left(\frac{x_S}{\mathfrak{D}_{SP2}} - \frac{x_S}{\mathfrak{D}_{SP1}}\right)J_{P1}^N\right), \end{aligned} \tag{97}$$

$$\begin{aligned} d_{P1} &= -\frac{1}{c}\cdot\left(\frac{x_S J_{P1}^N - x_{P1}J_S^N}{\mathfrak{D}_{SP1}} + \frac{x_{P2}J_{P1}^N + x_{P1}(J_S^N + J_{P1}^N)}{\mathfrak{D}_{P1P2}}\right) \\ &= -\frac{1}{c}\cdot\left(\left(-\frac{x_{P1}}{\mathfrak{D}_{SP1}} + \frac{x_{P1}}{\mathfrak{D}_{P1P2}}\right)J_S^N + \left(\frac{x_S}{\mathfrak{D}_{SP1}} + \frac{x_{P2}+x_{P1}}{\mathfrak{D}_{P1P2}}\right)J_{P1}^N\right). \end{aligned} \tag{98}$$

This example suggests the compact form

$$-cd_i = \sum_{j=1}^{J-1} B_{ij}J_j^N \tag{99}$$

with

$$B_{ii} = \left(\frac{x_i}{\mathfrak{D}_{iJ}} + \sum_{k=1;i\neq k}^{J}\frac{x_k}{\mathfrak{D}_{ik}}\right); \tag{100}$$

$$B_{ij} = -x_i \left(\frac{1}{\mathfrak{D}_{ij}} - \frac{1}{\mathfrak{D}_{iJ}} \right),$$

where the index J describes the last component (resp 3rd in our example) in the system.

Any formulation for the chemical potential in Equation (91) is applicable. The simplest case for the chemical potential (isothermal and ideal mixture) is used for the model development. Its gradient develops to

$$\begin{aligned} \nabla\mu_i &= \nabla\left(\mu_i^0 + RT \cdot ln(x_i\gamma_i)\right) = RT\nabla\big(ln(x_i) + ln(\gamma_i)\big) \\ &= RT\frac{1}{x_i}\nabla x_i \\ &+ RT\sum_{i=1}^{J}\frac{\partial ln(\gamma_i)}{\partial x_j}\nabla x_j = RT\frac{1}{x_i}\sum_{i=1}^{J}\left(\delta_{ij} + x_i\frac{\partial ln(\gamma_i)}{\partial x_j}\right)\nabla x_j \end{aligned} \tag{101}$$

with the chemical potential at a reference state μ_i^0, Kronecker delta δ_{ij} and the activity coefficient γ_i for species i. In case of an ideal mixture in which $\gamma_i = 1$, the chemical potential simplifies to

$$\nabla\mu_i = RT\frac{1}{x_i}\sum_{i=1}^{J}\delta_{ij}\,\nabla x_i = RT\frac{1}{x_i}\nabla x_i\,. \tag{102}$$

By inserting equation (102) in equation (99), the expression develops to

$$-\frac{c_i}{RT}RT\frac{1}{x_i}\nabla x_i = -c\nabla x_i = \sum_{j=1}^{J-1}B_{ij}J_j^N. \tag{103}$$

Therefore, a formulation follows, which is explicit in the fluxes J_j^N and suitable for numerical simulation code based on molar concentrations, by inverting the matrix B containing the elements B_{ij} as

$$J_j^N = \sum_{i=1}^{J-1} -c(B^{-1})_{ji}(\nabla x_i). \tag{104}$$

5.3 Limiting cases of the Maxwell-Stefan diffusion in polymer systems

The rigorous treatment of an infinite number of polymer species $P(s), s\ [1..\infty]$ and corresponding number of equations for the diffusive transport is infeasible. As already stated, representation in terms of moments is sufficient in most cases, but a closed set of expression for the diffusive transport of moments is required. The simplest way to obtain a closed expression would be to take the same diffusion coefficients between solvent and polymer and between polymer and polymer. In this case, however, the transport of the polymers would be greatly overestimated. With a choice of different diffusion coefficients, we do not obtain a closure condition for the diffusive transport of moments.

For this reason, a closer look at two limiting cases for the Maxwell-Stefan diffusion has been taken. A simplification can be achieved by assuming for an infinitely diluted solution. Then the sum on the right side of the Maxwell-Stefan Equation (91) for a component i can be interpreted as friction terms between species i and all other species j. If the solvent is abundant, only the friction between the solvent and all polymer chains is of interest, while the friction between polymer chains is neglected. This is the first limiting case called 'No Polymer Friction' for diffusive transport.

If the polymer content is high, friction between different polymer chains becomes the dominating mechanism, which restricts the movement of polymer chains. This is also a reliable assumption if the polymer is of high molecular weight, crosslinked or branched, such that entanglement considerably restricts the mobility of the polymer chains. In this case the Maxwell-Stefan equation can be simplified by assuming for the limiting case of infinite friction between polymer chains. The polymer then moves as a whole relative to the solvent; thus, gradients of polymeric species will not equilibrate. Consider a polymer membrane, consisting of two layers I and II, being infiltrated by a solvent (S). Both layers are of the same polymer, but of different chain length distribution. The solvent will equilibrate, but if the solvent fraction is not high it takes a very long time for the polymers to equilibrate. In many practical applications, equilibration is not achieved even in the long term.

An overview about the simplifications and the resulting models is shown in Figure 74.

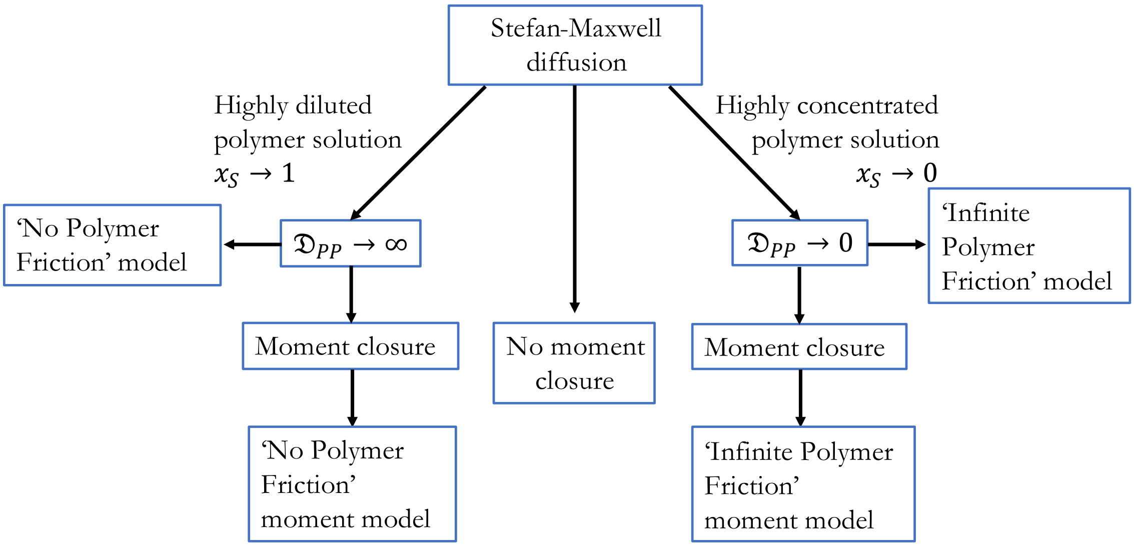

Figure 74: Overview of the developed models and simplifications.

5.3.1 Simulation model for the Maxwell-Stefan diffusion

Let's consider a polymer membrane with a total depth of L=200 µm, consisting of two layers I and II, being infiltrated by a solvent (S). Both layers are of the same polymer, but of different chain lengths. The degree of polymerization in the first layer is twice the one of layer two, which means that the chain length of polymer P1 is twice as the chain length of polymer P2. The solvent concentration in layer I (left side) is smaller than in layer II (right side). A visualization of the membrane is shown in Figure 75.

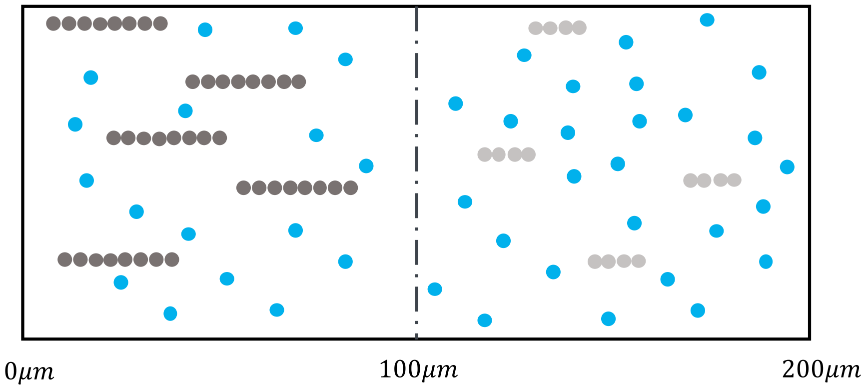

Figure 75: Illustrated polymer membrane consisting of two layers with the same polymer but with different chain lengths.

The assumed physical properties of this example are provided in Table 12. The binary diffusion coefficient of both the polymers interacting with the solvent is in the order of

$\mathfrak{D}_{SP1}=\mathfrak{D}_{SP2}=\mathfrak{D}_{SP}=10^{-9}$ m^{2}s^{-1}. No outer forced convection is imposed, and no chemical reactions are taking place.

Table 12: Physical data of solvent and two polymers of different molar weight.

	S	P1	P2
density $\rho \left[\frac{\mathrm{kg}}{\mathrm{m}^3}\right]$	1000	1000	1000
molar weight $M_W \left[10^{-3}\,\frac{\mathrm{kg}}{\mathrm{mol}}\right]$	18	400000	200000
degree of polymerization		4000	2000

The polymer concentration is the same in both membranes, whereas the first moment is higher in layer I. Hence, solvent concentration and mole fraction are lower there, and the polymer fraction is higher. Solvent is therefore driven from layer II into layer I. The results presented here are based on balance equations for the individual components as presented in Chapter 5.1 and the Maxwell-Stefan equations presented in Chapter 5.2. A diffusion coefficient of $\mathfrak{D}_{P1P2}=10^{-12}$ m^{2}s^{-1} was assumed between both polymer species. This is 3 orders smaller than that of the solvent against both polymers. Thus, the friction between the polymer chains is high and they are almost unable to move against each other but only against the solvent. The equilibration progress during the first 20 seconds is plotted in Figure 76. Clearly after 20 s only the solvent is fully equilibrated (∇x_S=0) and the two polymers are not due to the smaller diffusion coefficients. Of course, after sufficiently long time, the polymers will equilibrate as well. The final state (t→∞) of the system is shown in dashed red.

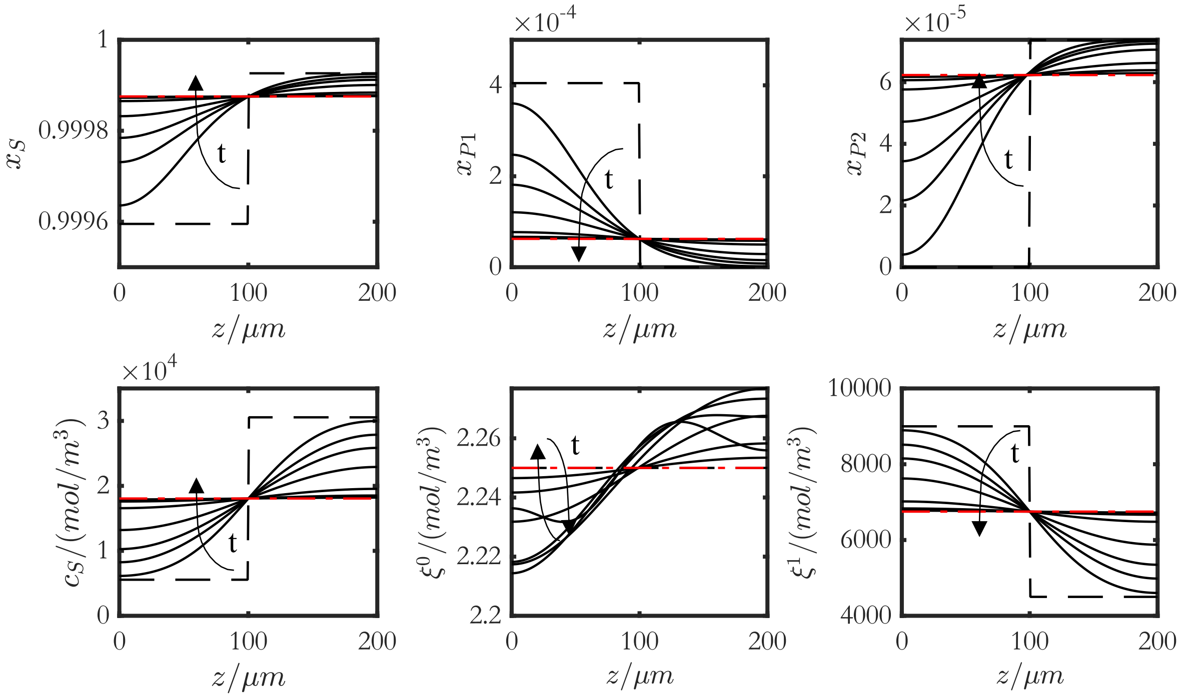

Figure 76: Results for t=[1,2,3,5,10,15,20] s for the Maxwell-Stefan approach with a diffusion coefficient between the polymers of $\mathfrak{D}_{P1P2} = 10^{-12}\frac{m^2}{s}$ and between solvent and polymer $\mathfrak{D}_{SP} = 10^{-9}\frac{m^2}{s}$. The initial conditions are dashed. The final state is dashed in red.

The total polymer concentration is shown as the 0th chain length moment in Figure 76 as well as the 1st chain length moment, which represents the concentration of repeat units within polymer chains. From Figure 77, where the detailed course of the 0th chain length moment is shown, it can be concluded that the total concentration of polymer shifts to layer II within the first three seconds. Later the diffusion of the polymers against each other compensates for this shift (5-20s).

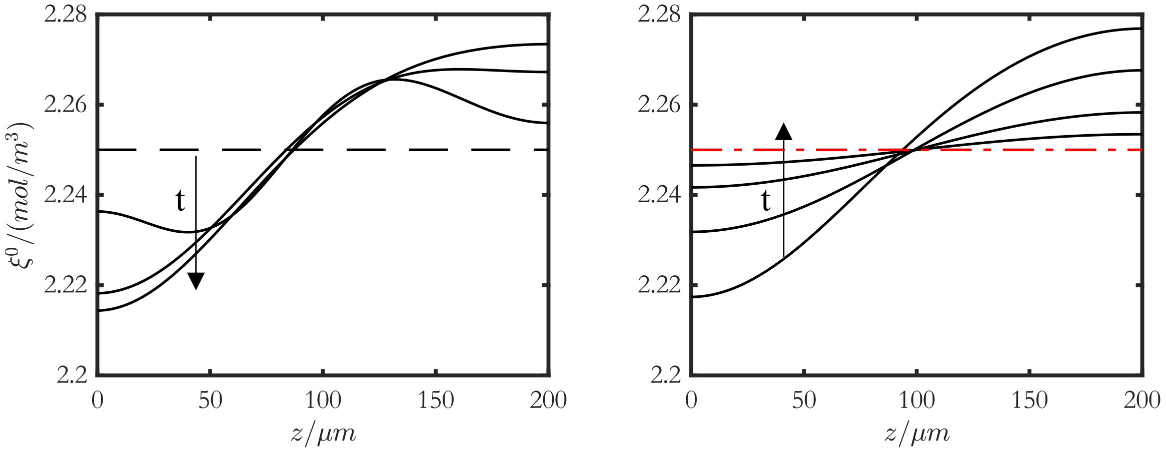

Figure 77: Detailed course of ξ^0 over the domain for different times according to Figure 76. Left side shows results for t=[1,2,3] s and right side results for t=[5,10,15,20] s. The initial condition is dashed. The final state is dashed in red.

The non-equilibrated state of ξ^0 after 20 s can be explained with the help of Figure 78, where the mole based averaged velocity v^N and the different fluxes are shown. The course of v^N shows the direction of the total mean transport of the components. As time progresses, the total transport becomes smaller. At the beginning, the solvent equilibrates from layer II into layer I due to the driving force of the chemical potential. The molar flux of the solvent is therefore negative. In contrast, polymer P1 must compensate for this flux and thus diffuses against the solvent into layer II (flux of P1 is positive). Polymer P2 diffuses with the solvent into layer I but tries to compensate the force of the solvent with the flux of the polymer P2. After 20 s the diffusive flux of polymer in layer I is still not zero, which means that it still diffuses against the polymer in layer II. Therefore, the overall molar flux J_P^N of polymer P1 and P2 is positive but stops after the equilibration of the solvent. After that, only small fluxes of each polymer components occur due to the small diffusion coefficient of $\mathfrak{D}_{P1P2}$=10^{-12} m^2s^{-1}.

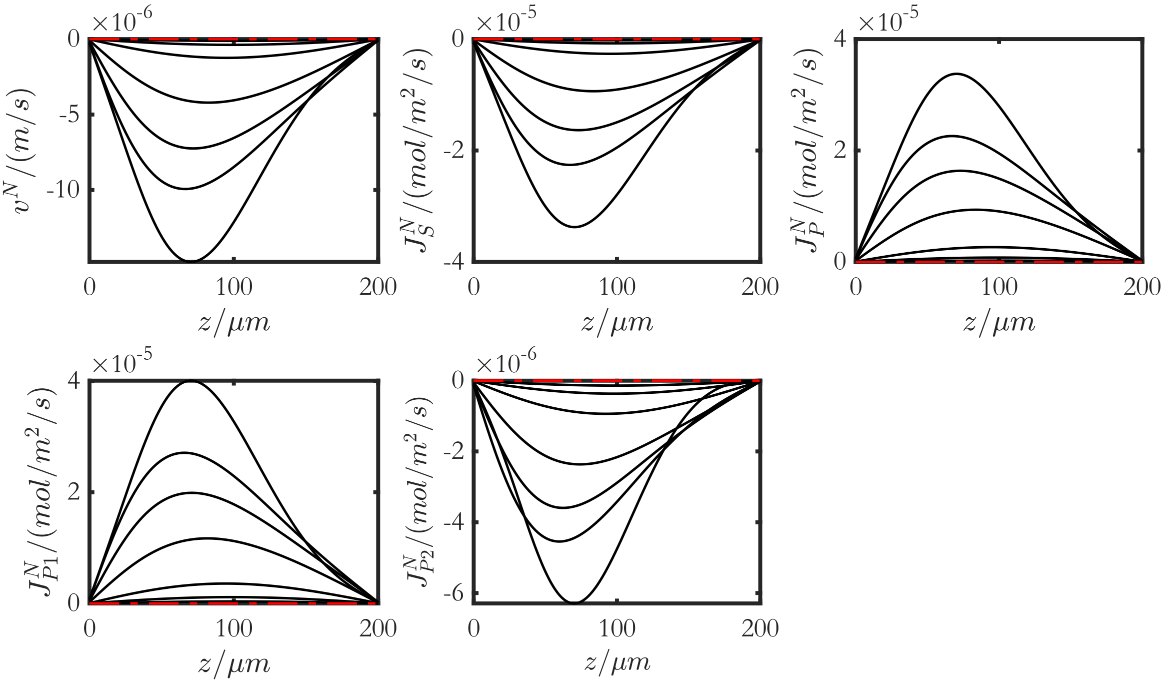

Figure 78: Velocities and fluxes for t=[1,2,3,5,10,15,20] s for the Maxwell-Stefan approach with a diffusion coefficient between the polymers of $\mathfrak{D}_{P1P2} = 10^{-12}\,\frac{m^2}{s}$ and between solvent and polymer $\mathfrak{D}_{SP} = 10^{-9}\,\frac{m^2}{s}$. The final state is dashed in red.

For distributed polymer systems, it is useful to describe the transport of moments. To derive the equations for such a transport, the polymer moments must close or a suitable closure condition must be applied. Next, two limiting cases are presented, in which this closure of the moments transport can be achieved by simplifications.

5.3.2 Maxwell-Stefan model for highly diluted polymer solutions ('No Polymer Friction' model)

The first limiting case describes diffusive polymer transport in a system with a high solvent content $x_S \rightarrow 1$. In this chapter, the derivation for this limiting case for the previously presented ternary mixture with solvent S, polymer P1 and P2 is presented. A detailed derivation for distributed polymer systems can be found in the Appendix A.4.1.

Starting from the Maxwell-Stefan equation for the polymer P1

$$d_{P1} = -\frac{1}{c}\left(B_{P1P1}J_{P1}^{N} + B_{P1S}J_{S}^{N}\right). \tag{105}$$

B_{P1P1} and B_{P1S} simplifies to

$$\begin{aligned} B_{P1P1} &= \left(\frac{x_{P1}}{\mathfrak{D}_{P1P2}} + \frac{x_S}{\mathfrak{D}_{P1S}} + \frac{x_{P2}}{\mathfrak{D}_{P1P2}}\right), \\ B_{P1S} &= -x_{P1}\left(\frac{1}{\mathfrak{D}_{P1S}} - \frac{1}{\mathfrak{D}_{P1P2}}\right). \end{aligned} \tag{106}$$

Due to high dilution, the friction between two polymer molecules approaches zero, which means that the diffusion coefficient leads to $\mathfrak{D}_{P1P2} \rightarrow \infty$ and $\frac{1}{\mathfrak{D}_{P1P2}} \rightarrow 0$. Thus, simplifications can be made for the previously derived Maxwell-Stefan diffusion in Equation (106). B_{P1j} simplifies to

$$\begin{aligned} B_{P1P1} &= \left(\frac{x_{P1} + x_{P2}}{\mathfrak{D}_{P1P2}} + \frac{x_S}{\mathfrak{D}_{P1S}}\right) = \frac{x_S}{\mathfrak{D}_{P1S}}, \\ B_{P1S} &= -x_{P1}\left(\frac{1}{\mathfrak{D}_{P_S S}} - \frac{1}{\mathfrak{D}_{P1P2}}\right) = -\frac{x_{P1}}{\mathfrak{D}_{P1S}} \end{aligned} \tag{107}$$

and Equation (105) to

$$d_{P1} = -\frac{1}{c}\left(\frac{x_S}{\mathfrak{D}_{P1S}}J_{P1}^{N} - \frac{x_{P1}}{\mathfrak{D}_{P1S}}J_{S}^{N}\right). \tag{108}$$

Multiplication by c^2 and by the diffusion coefficient, it follows

$$c^2\mathfrak{D}_{P1S}d_{P1} = \left(cx_{P1}J_S^N - cx_S\,J_{P1}^N\right) = \left(c_{P1}J_S^N - c_S\,J_{P1}^N\right). \tag{109}$$

After rearranging the equation, an expression for the polymer flux is obtained

$$J_{P1}^{N} = \frac{-c^2\mathfrak{D}_{P1\,S}d_{P1} + c_{P1}J_S^N}{c_S} = \frac{-c^2\mathfrak{D}_{P1\,S}\nabla x_{P1} + c_{P1}J_S^N}{c_S}. \tag{110}$$

This expression can be written in general terms for chains of length s with any number of low molecular weight species (solvents/monomers) as

$$J_{Ps}^{N}=\sum_{j=1}^{n_{low}}\frac{-c^{2}\mathfrak{D}_{P(s)j}\nabla x_{P(s)}+\zeta^{0}J_{j}^{N}}{c_{j}}. \tag{111}$$

After applying the moment approach $\xi^{k}=\sum_{s=1}^{\infty}s^{k}c_{P(s)}$, the diffusive flux for moments becomes

$$J_{\xi^{k}}^{N}=\sum_{s=1}^{\infty}s^{k}J_{P(s)}^{N}=\sum_{j=1}^{n_{low}}\frac{\xi^{k}J_{j}^{N}-\mathfrak{D}_{P(s)j}(c\nabla\,\xi^{k}-\xi^{k}\nabla c)}{c_{j}}. \tag{112}$$

From equation (112), the diffusive flux of moments depends only on the diffusion of the low molecular species, the moment itself and the total concentration.

5.3.3 Maxwell-Stefan model for concentrated polymer solutions ('Infinite Polymer Friction' model)

The second limiting case describes diffusive transport of polymers which are in a system with a low solvent content $x_S\rightarrow 0$. A simplification can be made by assuming that the Maxwell-Stefan diffusion coefficients between polymers of different chain length is identical, thus $\mathfrak{D}_{P(s)P(r)}=\mathfrak{D}_{PP}$. We start again with the Maxwell-Stefan equation for the polymer P1

$$d_{P1}=-\frac{1}{c}(B_{P1P1}J_{P1}^{N}+B_{P1S}J_{S}^{N}). \tag{113}$$

with B_{P1P1} and B_{P1S}

$$\begin{aligned}B_{P1P1}&=\left(\frac{x_{P1}}{\mathfrak{D}_{P1P2}}+\frac{x_{S}}{\mathfrak{D}_{P1S}}+\frac{x_{P2}}{\mathfrak{D}_{P1P2}}\right),\\ B_{P1S}&=-x_{P1}\left(\frac{1}{\mathfrak{D}_{P1S}}-\frac{1}{\mathfrak{D}_{P1P2}}\right).\end{aligned} \tag{114}$$

Assuming high polymer content, we take the limit $\mathfrak{D}_{P1P2}\rightarrow 0$, which implies that all polymers are transported with the same diffusive velocity and the friction between the polymer chains is infinite.

Multiplication of Equation (113) with this diffusion coefficient leads to

$$\mathfrak{D}_{P1P2}d_{P1}=-\mathfrak{D}_{P1P2}\,\frac{1}{c}(B_{P1P1}J_{P1}^{N}+B_{P1S}J_{S}^{N}) \tag{115}$$

with B_{P1P1} and B_{P1S}

$$D_{P1P2}B_{P1P1} = \left(\frac{\mathfrak{D}_{P1P2}(\,x_{P1} + x_{P2})}{\mathfrak{D}_{P1P2}} + \frac{\mathfrak{D}_{P1P2}x_S}{\mathfrak{D}_{P1S}}\right) = x_{P1} + x_{P2},$$
$$D_{P1P2}B_{P1S} = -x_{P1}\left(\frac{\mathfrak{D}_{P1P2}}{\mathfrak{D}_{P1S}} - \frac{\mathfrak{D}_{P1P2}}{\mathfrak{D}_{P1P2}}\right) = x_{P1}. \tag{116}$$

Inserting Equation (116) into Equation (115) and multiplication with c^2, it follows a relation for the flux of the polymer P1

$$J_{P1}^{N} = -\frac{c_{P1}}{c_{P2} + c_{P1}}J_S^N = \frac{c_{P1}}{c_{P2}}J_{P2}^N \tag{117}$$

and analogous for P2

$$J_{P2}^{N} = -\frac{c_{P2}}{c_{P2} + c_{P1}}J_S^N = \frac{c_{P2}}{c_{P1}}J_{P1}^N. \tag{118}$$

The total polymer flux J_P^N arises from the summation of both terms to

$$J_P^N = J_{P1}^N + J_{P2}^N = J_{P1}^N + \frac{c_{P2}}{c_{P1}}J_{P1}^N = \frac{c_{P1} + c_{P2}}{c_{P1}}J_{P1}^N. \tag{119}$$

J_{P1}^N follows with the total polymer concentration c_P resp. the 0th moment ζ^0 and the total polymer flux

$$J_{\xi^0}^N = J_P^N \tag{120}$$

to

$$J_{P1}^N = \frac{c_{P1}}{c_P}J_P^N = \frac{c_{P1}}{\xi^0}J_{\xi^0}^N. \tag{121}$$

After applying the definition of moments, $\xi^k = \sum_{s=1}^{\infty} s^k c_{P1}$, the diffusive flux for moments becomes

$$J_{\xi^k}^N = \sum_{s=1}^{\infty} s^k J_{P1}^N = \frac{\sum_{s=1}^{\infty} s^k c_{P1}}{\xi^0}J_P^N = \frac{\xi^k}{\xi^0}J_P^N. \tag{122}$$

Generalization to homo polymer distributions with segment number s the following expression applies

$$cx_{P(s)} \sum_{P(r)=1}^{\infty} J_{P(r)}^{N} = \left(\sum_{P(r)=1}^{\infty} c_{P(r)} \right) J_{P(s)}^{N} = \xi^{0} J_{P(s)}^{N}, \tag{123}$$

respectively

$$J_{P(s)}^{N} = \frac{c_{P(s)}}{\xi^{0}} \sum_{P_r=1}^{\infty} J_{P(r)}^{N} = \frac{c_{P(s)}}{\xi^{0}} J_{P}^{N}. \tag{124}$$

A more detailed deviation can be found in the Appendix A.4.2. After applying the moment definition again, $\xi^{k} = \sum_{s=1}^{\infty} s^{k} c_{P(s)}$, the diffusive flux for moments develops to

$$J_{\xi^k}^{N} = \sum_{s=1}^{\infty} s^{k} J_{P(s)}^{N} = \frac{\sum_{s=1}^{\infty} s^{k} c_{P(s)}}{\xi^{0}} J_{P}^{N} = \frac{\xi^{k}}{\xi^{0}} J_{\xi^{0}}^{N}. \tag{125}$$

Finally, the flux of higher polymer moments only depends on the flux of the 0th polymer moment

$$J_{\xi^k}^{N} = \frac{\xi^{k}}{\xi^{0}} J_{\xi^{0}}^{N} . \tag{126}$$

In other words, the diffusive transport of higher moments is related to the diffusive flux of the 0th moment. If the total concentration of polymers is constant, no equilibration of higher moments will take place. This preserves spatial inhomogeneities of the polymer and is a realistic physical behavior for polymer solutions with low solvent content. It is also physically consistent as all polymer moments have the same species velocity, regardless of the degree of the polymer moment.

5.3.4 Model summary

To summarize the previous described findings, Table 13 shows an overview about the different simplifications to describe the transport of moments in a respective system.

Table 13: Overview of equations to be implemented in a polymer system with constant density.

Balance equation for low-molecular species

$$\frac{\partial c_i}{\partial t} + \nabla \cdot \left(c_i \left(v - \frac{1}{\rho} \sum_i^{n_{low}} MW_i J_i^N - \frac{1}{\rho} MW_{seg} J_{\xi^1}^N \right) \right) + \nabla \cdot J_i^N = r_i^{total}$$

Balance equation for polymer moments of a representative polymer distribution P

$$\frac{\partial \xi_P^k}{\partial t} + \nabla \cdot \left(\xi_P^k \left(v - \frac{1}{\rho} \sum_i^{n_{low}} MW_i J_i^N - \frac{1}{\rho} MW_{seg} J_{\xi^1}^N \right) \right) + \nabla \cdot J_{\xi_P^k}^N = r_{\xi_P^k}^{total}$$

With the flux $J_{\xi^1}^N$, which is the summation of the 1st moment over <u>all</u> polymer distributions.

$$J_{\xi^1}^N = \sum_P^J J_{\xi_P^1}$$

Molar average velocity

$$v^N = v - \frac{1}{\rho} \sum_i J_i^N MW_i$$

Highly diluted polymer solution $\boldsymbol{x_S} \rightarrow \mathbf{1}$ ('No Polymer Friction' model)

Transport of low molecular species

$$J_j^N = \sum_{i=1}^{J-1} -c(B^{-1})_{ji}(\nabla x_i)$$

Transport of the 0th moment

$$J_{\xi_P^0}^N = \sum_{i=1}^{J-1} -c(B^{-1})_{jP}(\nabla x_P)$$

Transport of higher polymer moments of
a representative polymer distribution P

$$J_{\xi_P^k}^N = \sum_{j=1}^{n_{low}} \frac{\xi_P^k J_j^N - \mathfrak{D}_{P_s j}\left(c \nabla \xi_P^k - \xi_P^k \nabla c\right)}{c_j}$$

Highly concentrated polymer solution $\boldsymbol{x_S} \rightarrow \mathbf{0}$ ('Infinite Polymer Friction' model)

Transport of low molecular species

$$J_j^N = \sum_{i=1}^{J-1} -c(B^{-1})_{ji}(\nabla x_i)$$

Transport of the 0th moment

$$J_{\xi_P^0}^N = \sum_{i=1}^{J-1} -c(B^{-1})_{jP}(\nabla x_P)$$

Transport of higher polymer moments of
a representative polymer distribution P

$$J_{\xi_P^k}^N = \frac{\xi_P^k}{\xi_P^0} J_{\xi_P^0}^N$$

An extension to multiple polymer distributions can be made by calculating the diffusive fluxes for all distributions separately. From this the overall diffusive fluxes for all polymer distributions $J_{\xi k}^{N}$ can be calculated. Finally, the balance equations can be calculated for each species and polymer distribution.

5.4 Results using ideal mixture approach for limiting cases

The results presented here are based on the calculation of the balance equations for the individual components as mentioned acc. to Equation (110) resp. (117). Note that the moments are an exact solution and not an approximation. The same results can thereby be obtained with the 'No Polymer Friction' moment model and the 'Infinite Polymer Friction' moment model. For comparison to the full model in terms of the molar mass fractions of the individual species, the component balance equations were chosen here. Validity of moment balances was checked.

5.4.1 Model comparison for polymers in diluted systems

This setup represents diffusion of polymer chains in a system with high solvent content $x_S \rightarrow 1$. The results for the different mole fractions for the first 20 seconds can be seen in Figure 79 for the full Maxwell-Stefan model and the 'No Polymer Friction' model. The figure shows that the assumption $\mathfrak{D}_{P1P2} \rightarrow \infty$ shows good agreement to the full model for solutions with a very high solvent content. In systems with a high solvent content, two polymer molecules almost never touch. For this reason, it is a good assumption to assume a diffusion coefficient of $\mathfrak{D}_{P1P2} \rightarrow \infty$, which means that there is no friction between the two polymer chains. Figure 79 shows that after 20 seconds simulation time the solvent and polymer fractions have balanced out.

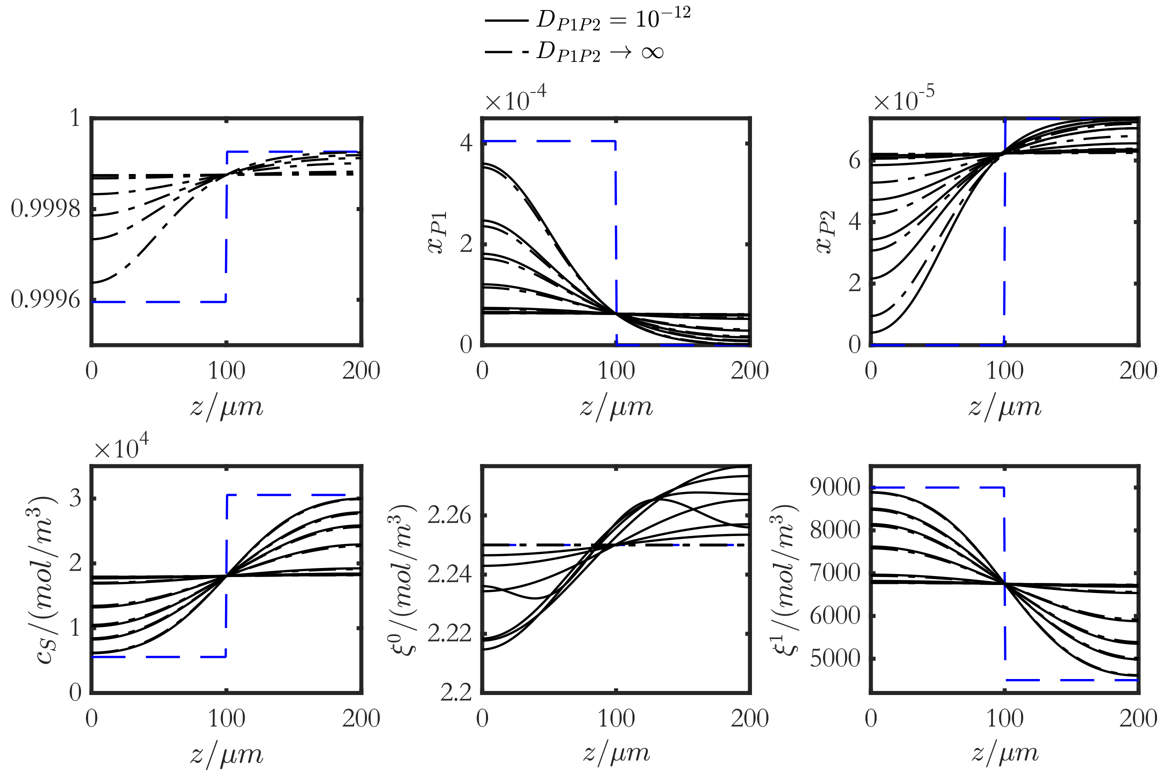

Figure 79: Results for t=[1,2,3,5,10,15,20] s for the full Maxwell-Stefan model (solid lines) with a diffusion coefficient between the Polymers of $\mathfrak{D}_{P1P2} = 10^{-12}\frac{m^2}{s}$ compared to the 'No Polymer Friction' model (dashed lines) for highly diluted systems. The diffusion coefficient between solvent and polymer was chosen to $\mathfrak{D}_{SP} = 10^{-9}\frac{m^2}{s}$ in both the models. The initial conditions are dashed in blue.

Figure 80 shows the 'Infinite Polymer Friction' model in comparison to the full model for highly diluted systems, whereas the assumption $D_{P1P2} \to 0$ is inappropriate for this case. The course can be explained as follows. The mole fraction for the solvent is equilibrated after that time, but the mole fractions for the polymers aren't. Since the driving force for the solvent tends to zero $\nabla x_S = 0$, the transport of the whole system stops. This can be explained by calculating the fluxes in this state

$$\boldsymbol{d_S} = 0 = -\frac{1}{c}\cdot\left(\left(\frac{x_{P1}}{\mathfrak{D}_{SP1}}+\frac{x_{P2}+x_S}{\mathfrak{D}_{SP2}}\right)J_S^N+\left(\frac{x_S}{\mathfrak{D}_{SP2}}-\frac{x_S}{\mathfrak{D}_{SP1}}\right)J_{P1}^N\right) \tag{127}$$

which means that J_{P1}^N directly follows from J_S^N or vice versa. From the driving force for polymer P2 which is always zero

$$\mathfrak{D}_{P1P2}\boldsymbol{d_{P1}} = 0 = x_{P2}J_{P1}^N - x_{P1}J_{P2}^N \tag{128}$$

follows that J_{P2}^{N} directly depends on J_{P1}^{N} and vice versa. From Equation (96) follows a trivial linear equation system for the fluxes with all fluxes

$$J_i = 0. \tag{129}$$

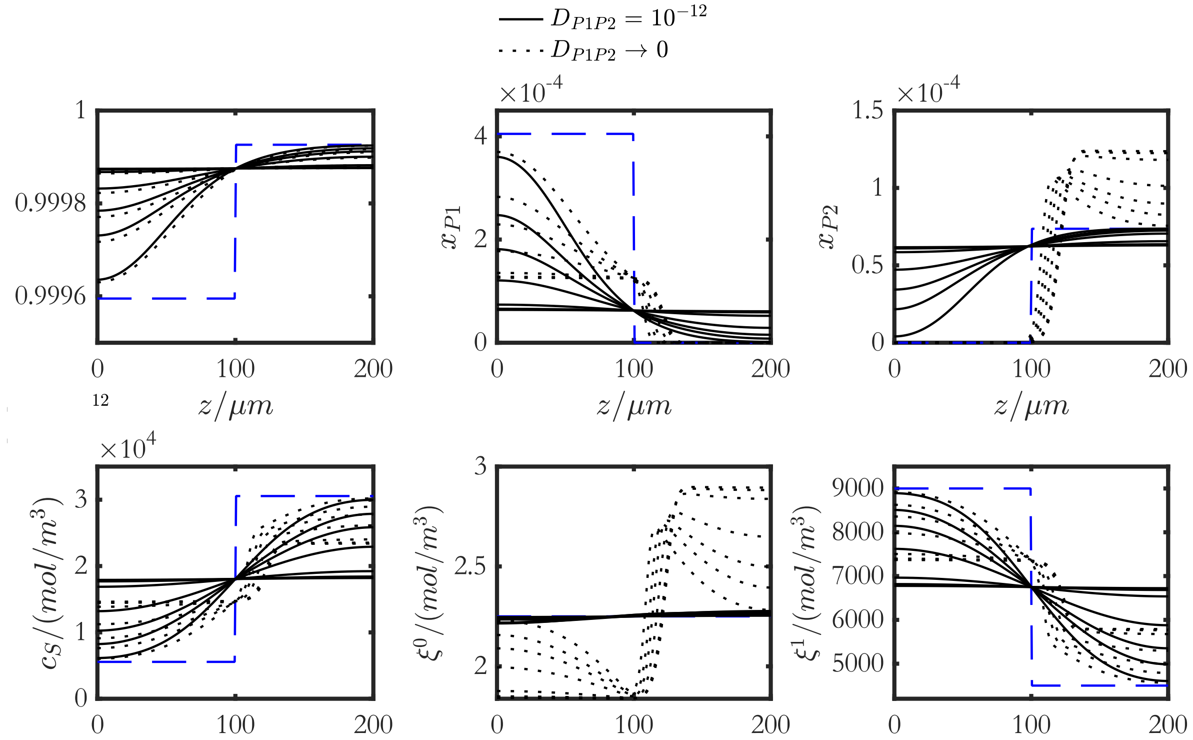

Figure 80: Results for t=[1,2,3,5,10,15,20] s for the full Maxwell-Stefan model (solid lines) with a diffusion coefficient between the Polymers of $\mathfrak{D}_{P1P2} = 10^{-12}\frac{m^2}{s}$ compared to the 'Infinite Polymer Friction' model (dotted lines) for highly diluted systems. The diffusion coefficient between solvent and polymer was chosen to $\mathfrak{D}_{SP} = 10^{-9}\frac{m^2}{s}$ in both the models. The initial conditions are dashed in blue.

5.4.2 Model comparison for polymers in concentrated systems

This setup represents diffusion of polymer chains in a system with low solvent content $x_S \to 0$. The results for the different mole fractions for the first 20 seconds are depicted in Figure 81 for the full model and the 'No Polymer Friction' model. The figure shows that the assumption $\mathfrak{D}_{P1P2} \to \infty$ is inappropriate for this case. In systems with a low solvent content, the polymer molecules touch each other, which means that there is high friction between the molecules. Therefore, the assumption with a diffusion coefficient of $\mathfrak{D}_{P1P2} \to \infty$, which implies no friction between polymer molecules, is not suitable. In the 'No Polymer Friction' model, the mole fractions of both the solvent and the polymers equalize, whereas in the full model, the fractions of the polymers do not equalize, at least not in the first 20 s. However, after an infinitely long simulation time, the mole fractions of the polymers are also balanced. In this context, we neglect the very slow interaction between polymer molecules because the friction between these molecules is much higher due to the lower diffusion coefficient.

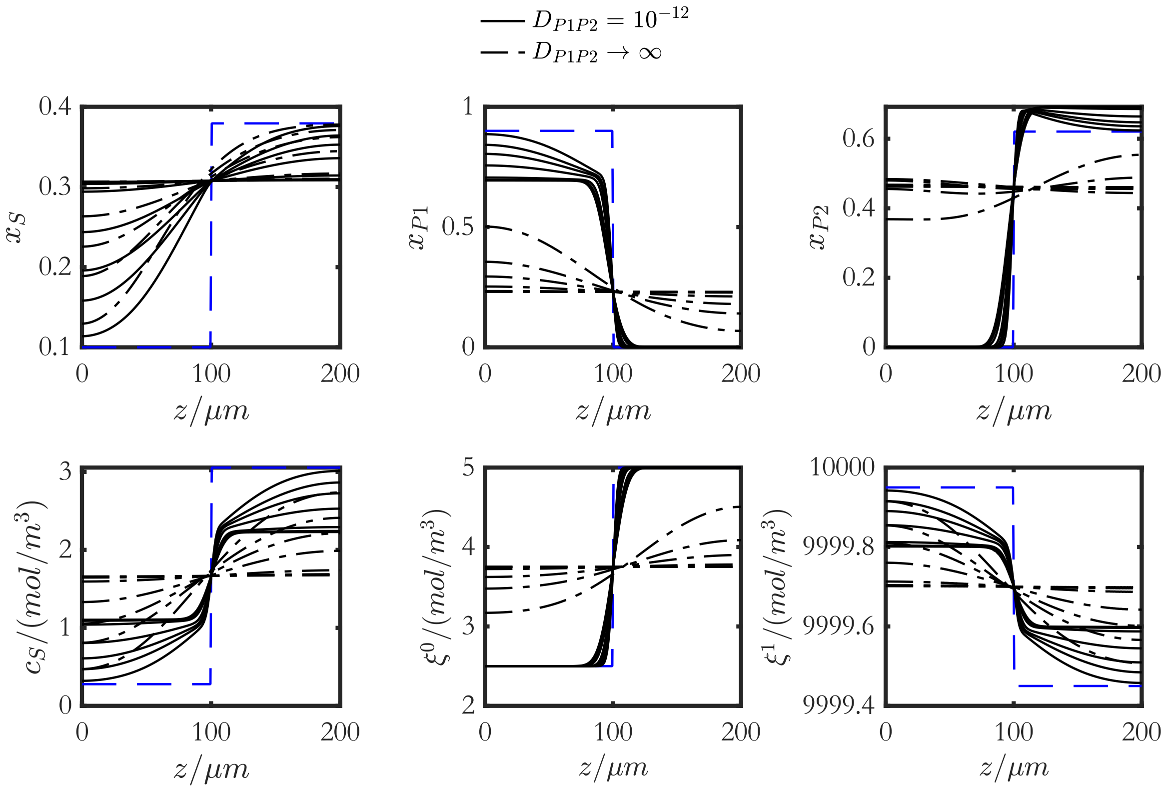

Figure 81: Results for t=[1,2,3,5,10,15,20] s for the full Maxwell-Stefan model (solid lines) with a diffusion coefficient between the Polymers of $\mathfrak{D}_{P1P2} = 10^{-12}\,\frac{m^2}{s}$ compared to the 'No Polymer Friction' model (dashed lines) for concentrated systems. The diffusion coefficient between solvent and polymer was chosen to $\mathfrak{D}_{SP} = 10^{-9}\,\frac{m^2}{s}$ in both the models. The initial conditions are dashed in blue.

Figure 82 shows the comparison between the full Maxwell-Stefan model and the 'Infinite Polymer Friction' model. The assumption $\mathfrak{D}_{P1P2} \to 0$ for solutions with a high polymer content is in good agreement with the full model. Again, the mole fraction for the solvent is equilibrated after that time, but the mole fractions for the polymers aren't. Since the driving force for the solvent equals to zero $\nabla x_S = 0$, the transport of the whole system stops. For a system with a high polymer content, this behaviour is certainly a good assumption.

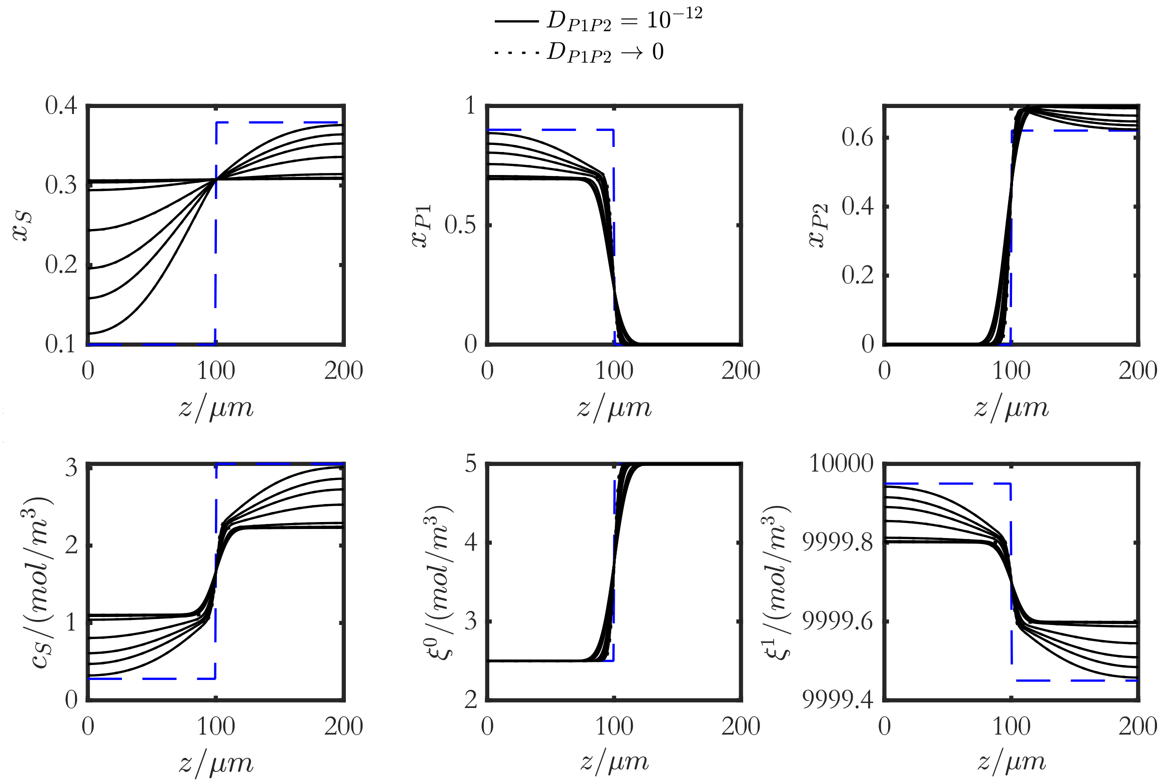

Figure 82: Results for t=[1,2,3,5,10,15,20] s for the full Maxwell-Stefan model (solid lines) with a diffusion coefficient between the Polymers of $\mathfrak{D}_{P1P2} = 10^{-12}\frac{m^2}{s}$ compared to the 'Infinite Polymer Friction' model (dotted lines) for concentrated systems. The diffusion coefficient between solvent and polymer was chosen to $\mathfrak{D}_{SP} = 10^{-9}\frac{m^2}{s}$ in both the models. The initial conditions are dashed in blue.

5.5 Results using PC-SAFT equation of state

The assumption of the ideal mixture to calculate the chemical potential is not or only partially suitable for a polymer system. A better description of the thermodynamics of polymer systems is provided by the PC-SAFT equation of state [74]. The basics of the equation of state and the PC-SAFT parameters used for the binary system water and PVP have already been described in Chapter 2.3.6. Since a system with a high polymer content is of great importance for the PVP system under investigation, the initial conditions are selected according to Chapter 5.4.2. Numerical problems arise due to very strong gradients (e.g. Figure 82), which can result in very small or negative mole fractions. This makes the calculation using the PC-SAFT equation of state problematic, so the initial conditions were weakened somewhat. For a better comparison, the results for the assumption of an ideal mixture are presented first. Figure 83 therefore shows the results for the first 20 seconds with the assumption of an ideal mixture. The results are similar to those in Figure 82 and the concentrations are only scaled by the use of a tanh function. Therefore, the curves are not described in more detail.

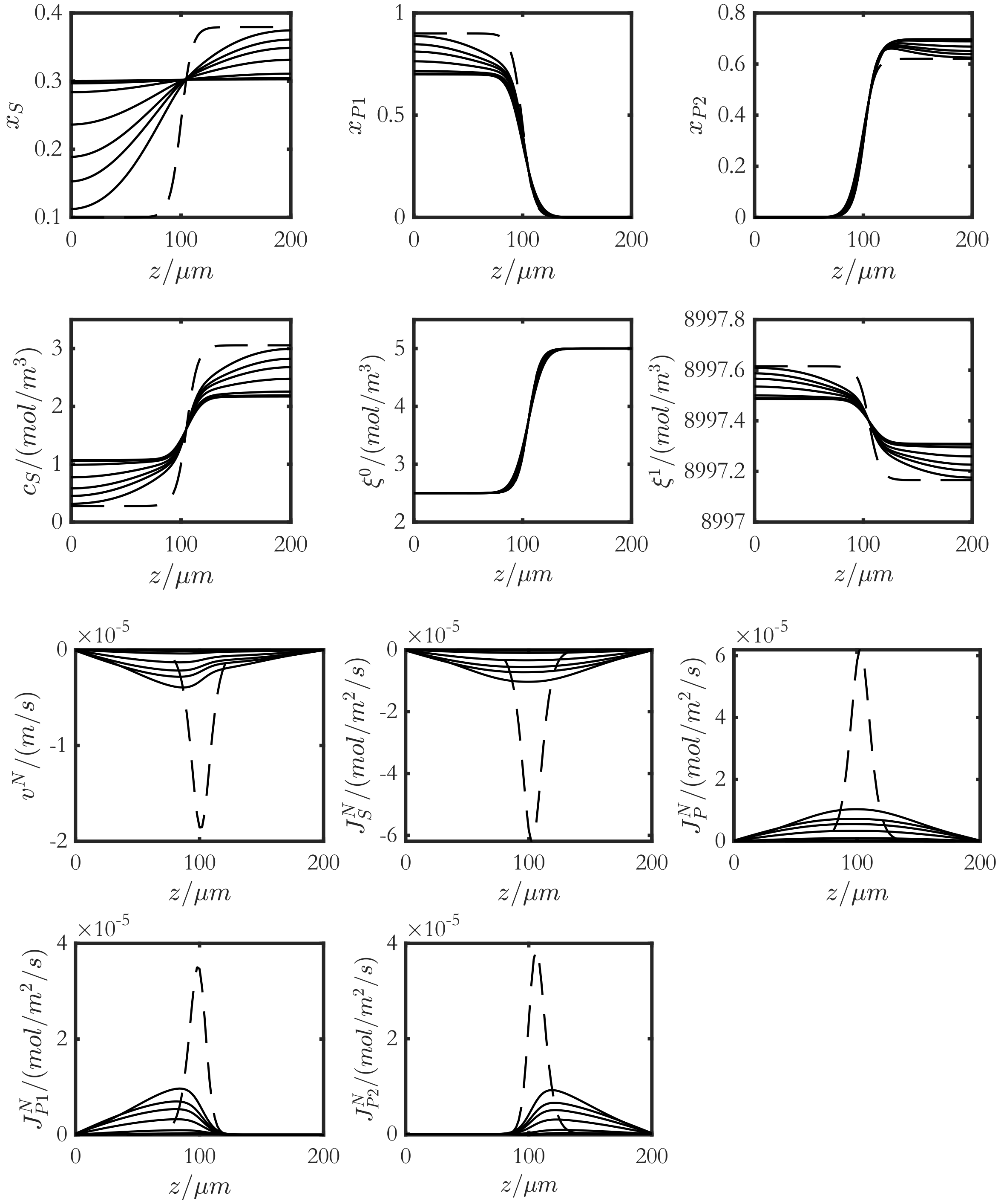

Figure 83: Results for t=[1,2,3,5,10,15,20] s with **ideal mixture** assumption for the Maxwell-Stefan approach with a diffusion coefficient between the polymers of $\mathfrak{D}_{P1P2} = 10^{-12}\frac{m^2}{s}$ and between solvent and polymer $\mathfrak{D}_{SP} = 10^{-9}\frac{m^2}{s}$. The initial conditions are dashed.

Associated with the concentration profiles, the mole-related total velocity and the fluxes of the individual species are shown in Figure 83. The mole average velocity v^N is negative, which means that molecules are transported to the left. This is mainly caused by the movement of the solvent. Polymer P1 and P2, on the other hand, diffuse to the right, with P1 doing so on the left-hand side of the membrane and P2 on the right-hand side.

If the simulation is continued after 20 seconds, it can be seen from Figure 84, that despite the driving force for the solvent ($\nabla x_S=0$) is zero, the solvent concentration is still balanced. This happens because the polymer is not yet balanced and can still diffuse against each other (much more slowly). The system is therefore completely balanced for an infinite period of time.

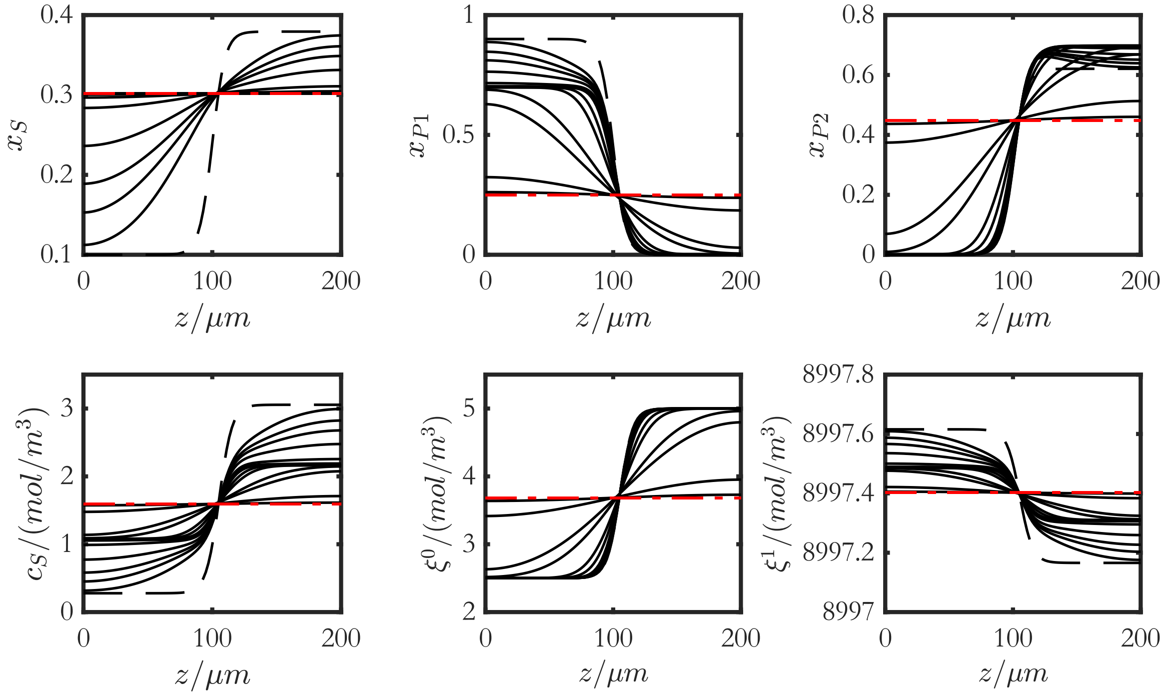

Figure 84: Results for t=[1,2,3,5,10,15,20,50,100,500,1000,5000,10000,50000] s with **ideal mixture** assumption for the Maxwell-Stefan approach with a diffusion coefficient between the polymers of $\mathfrak{D}_{P1P2} = 10^{-12}\frac{m^2}{s}$ and between solvent and polymer $\mathfrak{D}_{SP} = 10^{-9}\frac{m^2}{s}$. The initial conditions are dashed. The final state is dashed in red.

In comparison to the results just presented, the results obtained with the PC-SAFT equation of state are shown in Figure 85 and is therefore directly comparable with Figure 83. However, there are major differences between the two results. Especially when the mole fraction and the concentration of the solvent are considered. First, the curves of the first 20 seconds can be explained together with the velocities, fluxes, and chemical potential. In the first 20 s of simulation time, the transport of the solvent is dominant. The molar flux of the solvent as well as the mole-average velocity v^N is approx. two or three times as high compared to Figure 83. For this reason, the solvent is mainly transported from the right to the left side during this time. This difference is caused by the different calculation of the driving force, which in the case of the ideal mixture is determined by the gradient of the molar fractions and in the case of the PC-SAFT calculation by the gradient of the chemical potential, which is according to Equation (101) the sum of the molar fraction with activation coefficient. Due to the increased transport of the solvent, the molar proportions of the substances also shift as a result compared to Figure 83. With increasing simulation time, the driving force for the transport of the solvent becomes smaller and smaller until the chemical potential is balanced over the domain. At this point, the solvent concentration is equalized and does not move any further. For the ideal mixture, as soon as the molar proportion of the solvent is equalized, the equalization of the solvent concentration is caused by the diffusion of the polymers and therefore takes place very slowly. It is also interesting to note that the 1st polymer moment is balanced after this time, whereas this is not the case in Figure 83. However, the polymer concentration is not yet balanced after this time. If we were to consider the limiting case ($\mathfrak{D}_{P1P2} \rightarrow 0$), the system would solidify at this point.

In our case, the system then continues to equilibrate (Figure 86). The concentration and chemical potential of the solvent are unaffected. The driving force of the fluxes is now the chemical potential of the polymer. However, as the diffusion coefficient is 3 orders of magnitude smaller than between the solvent and the polymer, the equilibration therefore takes significantly longer. As the simulation time progresses, the chemical potential of the polymer P1 is equalized, which means that the polymer concentration is also equalized. If the polymer and solvent concentrations are equilibrated, the molar proportions are also balanced.

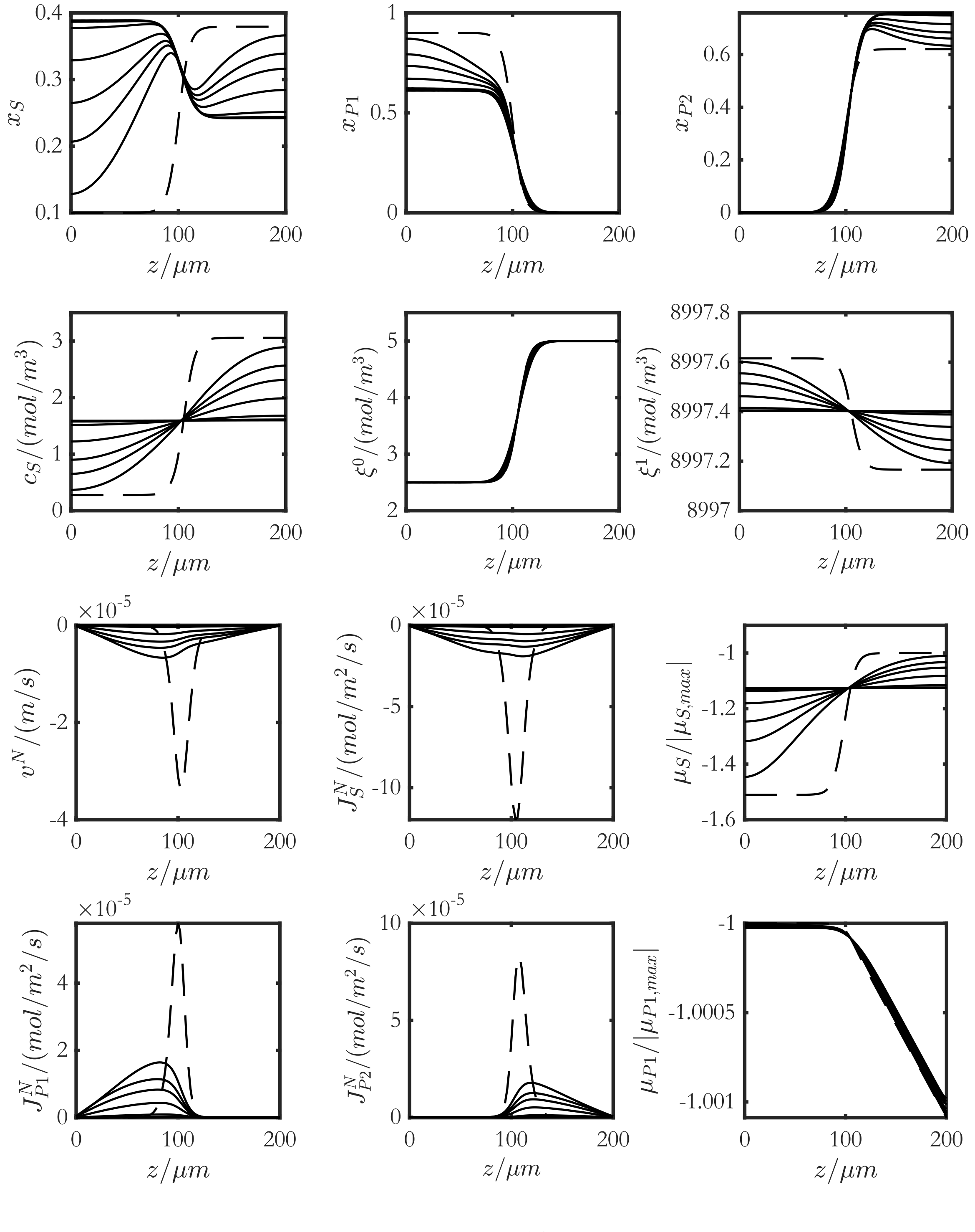

Figure 85: Results for t=[1,2,3,5,10,15,20] s with **PC-SAFT** equation of state for the Maxwell-Stefan approach with a diffusion coefficient between the polymers of $\mathfrak{D}_{P1P2} = 10^{-12}\frac{m^2}{s}$ and between solvent and polymer $\mathfrak{D}_{SP} = 10^{-9}\frac{m^2}{s}$. The initial conditions are dashed.

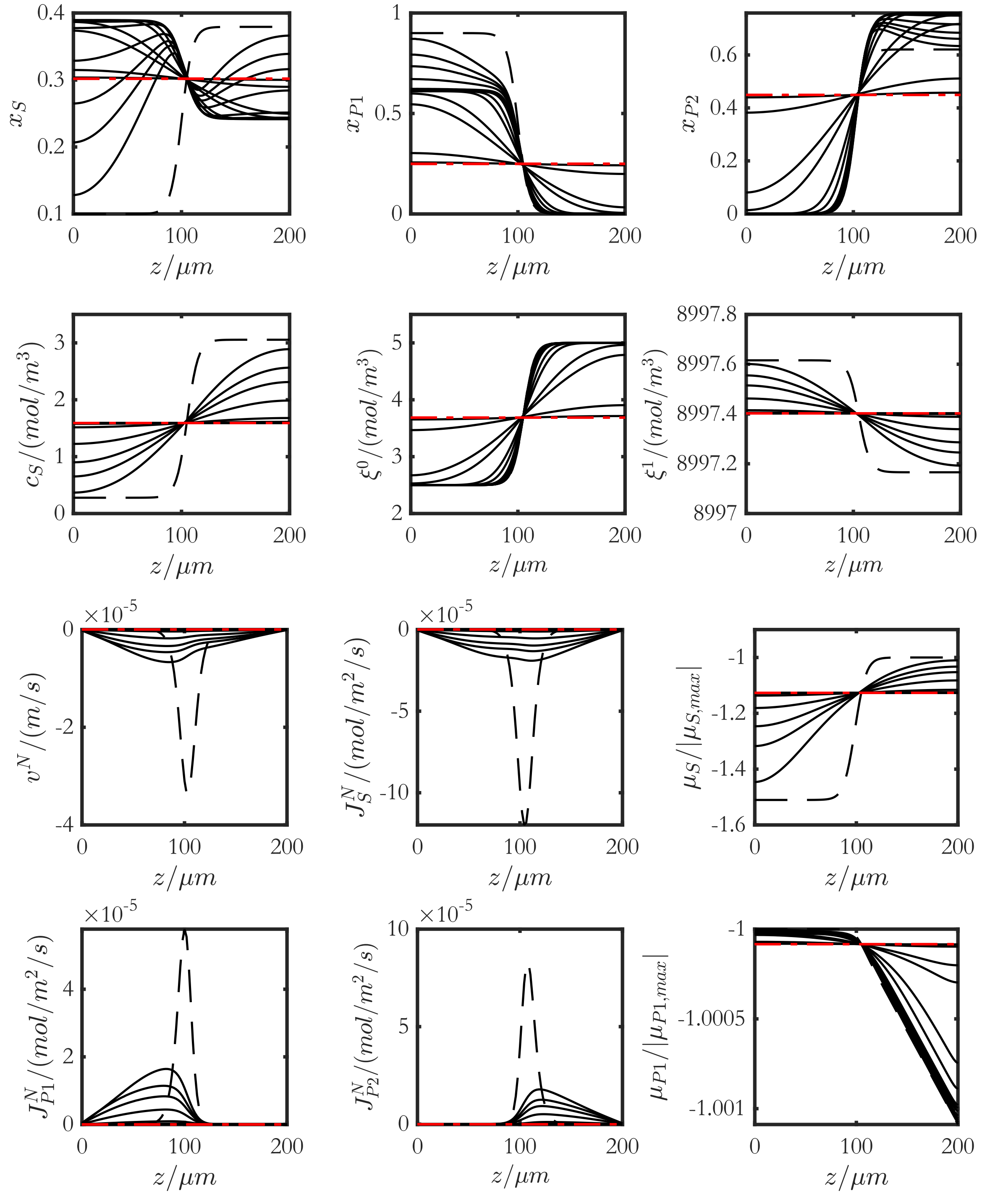

Figure 86: Results for t=[1,2,3,5,10,15,20,50,100,500,1000,5000,10000,50000] s with **PC-SAFT** equation of state for the Maxwell-Stefan approach with a diffusion coefficient between the polymers of $\mathfrak{D}_{P1P2} = 10^{-12}\frac{m^2}{s}$ and between solvent and polymer $\mathfrak{D}_{SP} = 10^{-9}\frac{m^2}{s}$. The initial conditions are dashed. The final state is dashed in red.

5.6 Modeling binary Maxwell-Stefan diffusion coefficients

Diffusion coefficients between polymer and solvent or monomer have so far only been estimated roughly. Dynamic light scattering measurements have been conducted for various Kollidon (K12, K30, K90)-water solutions. The theory of DLS was briefly introduced in Chapter 2.3.6 and the measurement setup is described in Appendix A.1.4. Measurements were conducted at different polymer concentrations and different temperatures (25 °C, 40 °C and 55 °C).

Figure 87 shows the hydrodynamic radius for different K30 concentrations at a temperature of T=25 °C as an example. It can be observed that the hydrodynamic radius increases for very small angles of 30-50 ° and then remains constant. This can be observed for all K30 concentrations at all measured temperatures. For polymer chains with lower (K12) or higher molecular weight like K90, these observations could not be made like displayed in Figure 88 and the hydr. diameter remains constant.

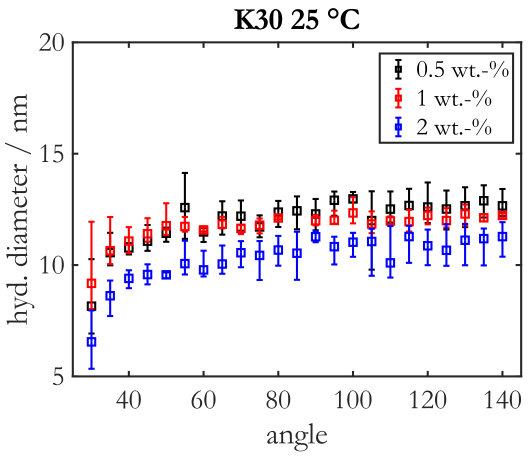

Figure 87: Hydrodynamic radius plotted as function of scattering angle for different Kollidon 30 concentrations at T=25 °C. Error bars indicate the variability of the data.

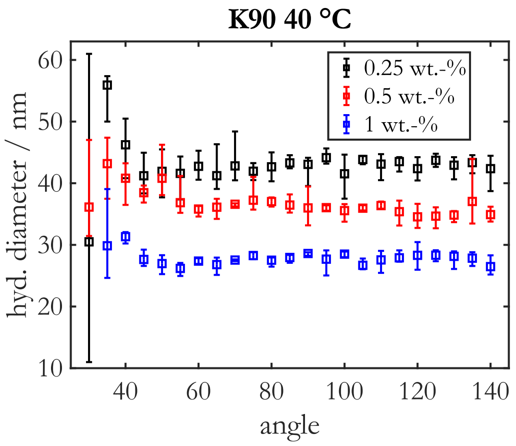

Figure 88: Hydrodynamic radius plotted as function of scattering angle for different Kollidon 90 concentrations at T=40 °C. Error bars indicate the variability of the data.

The averaged diffusion coefficient can then be plotted for each polymer (K12, K30 and K90) over the concentration as shown in Figure 89 for a specific temperature. A total of 3 different concentrations were measured for each polymer at all three temperatures, so that the quality of a linear approximation is improved. The intercept can then be read off to determine the binary diffusion coefficient of the polymer in infinite dilution or the diffusion of one polymer molecule in solvent. Figure 90 then shows the diffusion coefficient in infinite dilution of K30 for different temperatures as an example. The diffusion coefficient at the desired system temperature of T=85 °C for K30 can then be calculated using a linear approximation to

$$\mathfrak{D}_{SP}(x_P \rightarrow 0, T = 85\,°C) = 4.24 \cdot 10^{-11}\, m^2 s^{-1}. \tag{130}$$

This procedure can be carried out for each polymer. Direct extrapolation of the diffusion coefficient from Figure 89 for different polymer concentrations should be avoided, as DLS always captures the movement of several molecules. Instead, extrapolating to $x_P \rightarrow 0$ depicts the movement of one polymer molecule, which corresponds to a Maxwell-Stefan diffusion coefficient.

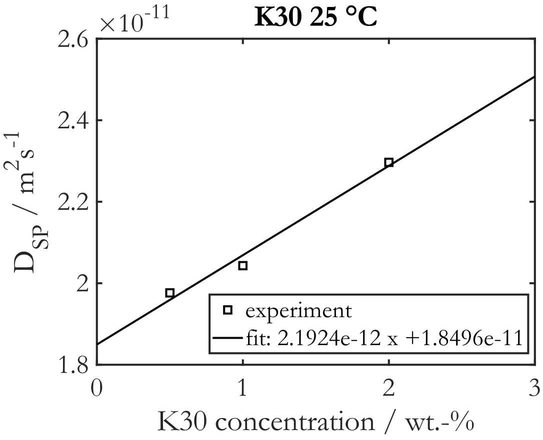

Figure 89: Diffusion coefficient of different K30 concentrations at T=25 °C, shown as squares. A linear adjustment calculation has been added, shown as a line.

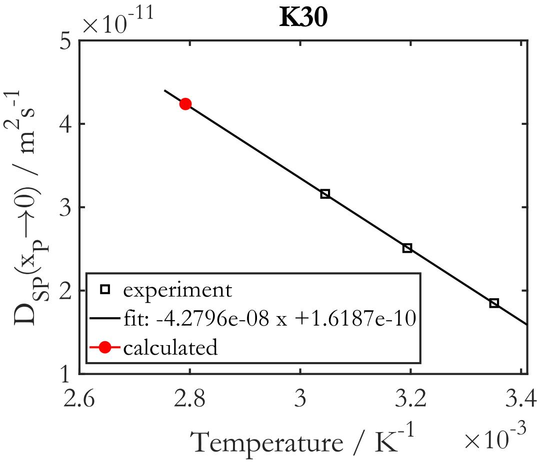

Figure 90: Binary diffusion coefficient in infinite dilution at different temperatures, shown as squares. A linear adjustment calculation has been added, shown as a line. Red dot marks the calculated value at T=85 °C.

For all polymers, diffusion coefficients can be plotted against the molecular weight in Figure 91. This results in different binary diffusion coefficients for the different Kollidones at infinite dilution.

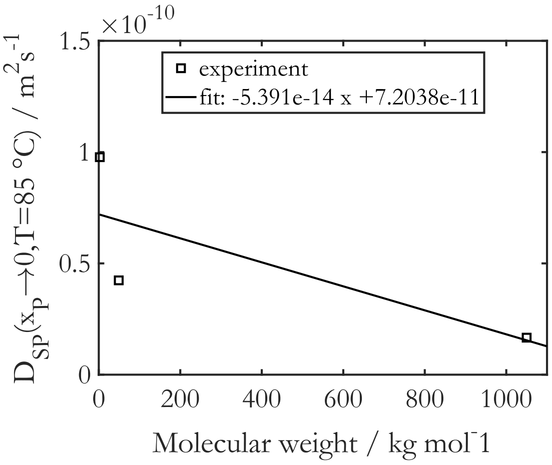

Figure 91: Binary diffusion coefficients in infinitely diluted solution of different molecular weights (K12, K30, K90) at T=85 °C, shown as squares. A linear adjustment calculation has been added, shown as a line.

According to Stierle et al. [75], the binary Maxwell-Stefan diffusion coefficient can be calculated from the self-diffusion coefficients. The relationship is depicted in Figure 92. Since the polymer P is present in infinite dilution in the solvent water S, the self-diffusion coefficient of the polymer is $D_P^{self,\infty} = \mathfrak{D}_{SP}(x_P \rightarrow 0)$. $D_P^{self,0}$ on the other hand, corresponds to the self-diffusion coefficient of polymer in the polymer-rich solution.

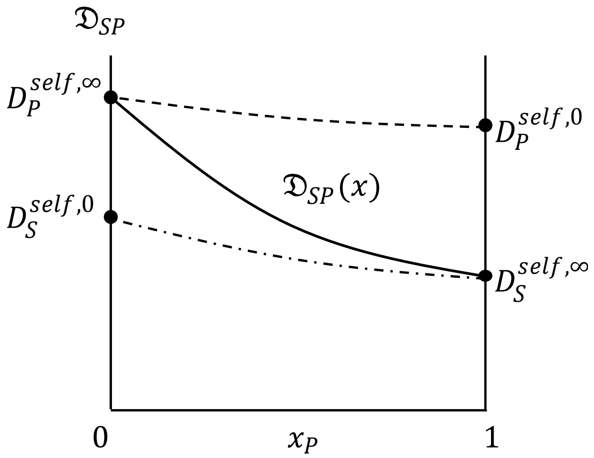

Figure 92: Illustration of the connection between the binary Maxwell-Stefan diffusion coefficient $\mathfrak{D}_{SP}$ and the self-diffusion coefficients D_P^{self} and D_S^{self}. Adapted from [75].

Darken's equation [76], [77]

$$\mathfrak{D}_{ij}(x) = \left(x_i \mathfrak{D}_j^{self}(x) + x_j \mathfrak{D}_i^{self}(x)\right) \Gamma_{ij}^{\alpha} \tag{131}$$

with the thermodynamic factor $\Gamma_{ij} = \frac{x_i}{k_B T}\left(\frac{\partial \mu}{\partial x_j}\right)_{T,p,\sum_i x_i = 1}$ and the empirical parameter α, can then be used to calculate the binary diffusion coefficient between solvent and polymer for a given molecular weight and mole fraction. The effect of nonideality is neglected and therefore the thermodynamic factor is set to $\Gamma_{ij} = 1.$ Self-diffusion coefficients of water are typically measured in water [78], which corresponds to $D_S^{self,0}$. It is practically impossible to measure the self-diffusion coefficient of water in an infinite polymer solution $D_S^{self,\infty}$. Due to the very high solvent concentration (molar) in polymer systems, the self-diffusion coefficient of the solvent $D_S^{self,\infty} = 0$ is set to zero. Darken's equation therefore develops to

$$\mathfrak{D}_{SP}(x_P, T = 85\ °C, MW) = x_S D_P^{self}(T = 85\ °C, MW) \tag{132}$$

This calculation approach is compared with another method of [7] in Chapter 6.4.4.

5.7 Conclusions

To adequately describe a polymer system for example in a CFD simulation, a mathematical formulation for the transport of moments of polymer distributions is necessary. To derive such a formulation, the polymer moments must close, or a suitable closing condition must be applied. In this chapter, first the full Maxwell-Stefan model was presented, which does not close for polymer moments in case of different binary diffusion coefficients. Two different limiting cases for the Maxwell-Stefan model that provide closure were suggested, providing good agreement with the full model for the respective application. The 'No Polymer Friction' model applies for highly diluted polymer solutions where friction between polymer molecules can be neglected. Here excellent agreement can be observed. Conversely, at high polymer concentrations the 'Infinite Polymer Friction' model is suitable, where friction between the polymers is extremely high, so that they effectively do not diffuse against each other but only with the solvent. For this reason, the system 'solidifies' as soon as the solvent is equilibrated.

Using these limiting cases of the rigorous Maxwell-Stefan theory has the advantage that the transport equation for moments of polymer species close. Which of the two formulations is more suitable depends on the polymer content of the solution, the average chain length of the polymer, the degree of branching of the polymer, and the molecular weight.

Additionally, the PC-SAFT equation of state offers a way to describe a polymer system in a thermodynamically more suitable way, yielding in significantly different results compared to the ideal mixture approach, particularly with much higher diffusive fluxes.

In order to determine binary diffusion coefficients of the polymer-water solution, binary diffusion coefficients of different Kollidon-water mixtures at low polymer concentrations were measured by dynamic light scattering. Thus, diffusion coefficients at infinite dilution can be determined by extrapolation to subsequently calculate binary Maxwell-Stefan diffusion coefficients at arbitrary concentrations and molecular weights using Darken's equation.

6 Wall layer formation in capillary tubular reactors[9]

The experimental investigations in Chapter 3 have shown that a highly viscous wall layer forms in capillary reactors, which is more or less pronounced depending on the process conditions. Similar observations have already been made in the work of [7], [14], [15], [79].

To optimize process conditions and predict fouling during reactor scale-up, it is necessary to understand the causes of deposit formation and derive a model that allows to describe the growth of a deposit layer. Further, it is important to understand the interplay between hydrodynamics, reaction kinetics and the transport of polymers.

The reaction mechanism of the NVP polymerization has been studied extensively and was described in Chapter 4. The kinetic model was successfully validated against experimental data in a CSTR reactor. Additionally, the transport of polymers was considered by two limiting cases of the Maxwell-Stefan diffusion approach developed in Chapter 5 and validated for the respective application. For both of these limiting cases a mathematical closure for the transport equation of polymer moments could be found.

The kinetics model and the transport model for polymers are implemented together with a viscosity model in an in-house developed CFD solver in OpenFOAM®. The CFD model can be used to describe the wall layer formation and is later validated by experimental findings in the capillary reactor for a wide range of concentrations. Furthermore, influencing factors for the wall layer formation such as the transport model for the polymers, the viscosity model, side reactions and the estimation of the diffusion coefficients can be examined. With DLS measurements from Chapter 5 a reliable description for the binary Maxwell-Stefan diffusion coefficient was found. A thermodynamic correct representation can finally be made with the PC-SAFT equation of state coupled with neural networks to describe the diffusive flux of the components.

---

[9] The majority of this chapter has been published in advance of this thesis under the terms of the Creative Commons Attribution License (CC BY 4.0) in [82]. Minor changes have been made and passages have been added for better comprehensibility and embedding in the context of this thesis.

6.1 CFD Model

The dynamics of isothermal, single-phase systems are determined by the momentum balance

$$\frac{\partial \rho \boldsymbol{v}}{\partial t} + \nabla \cdot \rho \boldsymbol{v} \boldsymbol{v} + \nabla \cdot \boldsymbol{\tau} = -\nabla p \tag{133}$$

and the total mass balance

$$\frac{\partial \rho}{\partial t} + \nabla \cdot \rho \boldsymbol{v} = 0 \tag{134}$$

where ρ is the mass density, $\boldsymbol{v}$ is the barycentric velocity or center-of-mass velocity, τ is the viscous stress tensor and p is the pressure. The correlation for the viscous stress tensor is

$$\boldsymbol{\tau} = \eta \left[(\nabla \boldsymbol{v} + \nabla^T \boldsymbol{v}\,) - \frac{2}{3} \nabla \cdot \boldsymbol{v} \right] \tag{135}$$

with the shear viscosity η. Newtonian behavior was assumed, and the dilatation effects' contribution was disregarded [7]. The concentration dependence of viscosity is accounted for using a correlation depending on polymer weight fraction and average molecular weight, which will be introduced in Chapter 6.1.2.

In multicomponent systems, the balance equations for individual species must also be considered to account for changes in composition. The latter is expressed in terms of the molar densities c_j. Since polymer systems can be efficiently modeled using statistical moments of the concentration distribution defined in molar concentrations, the component balances were chosen in molar form as displayed in Chapter 5.1, Equation (80).

When diffusive transport or chemical processes take place in multicomponent systems, the overall density ρ is not always constant and instead relies on the mixture's molecular composition [7]. An equation of state may often be used to characterize this dependency. Another option is to establish a constraint, which may be used in CFD solvers for incompressible fluids, in terms of volume fractions [7]

$$\textstyle\sum_j \frac{V_j}{V} = 1, \tag{136}$$

with the volume V_j that species j occupies in the total volume V, resp. for ideal mixtures by neglecting excess volume [7] to

$$\sum_j \frac{\rho_j}{\rho_j^0} = 1 \tag{137}$$

with the pure density ρ_j^0 of species j assumed constant for isothermal, incompressible fluids. Using the time derivative of Equation (137), the divergence of the barycentric velocity [7]

$$\nabla \cdot \boldsymbol{v} = \nabla \cdot \sum_j M_j \boldsymbol{J}_j^N \frac{\rho_j^0 - \rho}{\rho \rho_j^0} + \sum_j \frac{M_j}{\rho_j^0} r_j^{total} \tag{138}$$

can be calculated. The total mass density can be expressed as

$$\rho = \sum_j c_j M_j = \sum_j \rho_j. \tag{139}$$

In CFD simulations of incompressible systems, the total mass balance is usually not solved explicitly, but the momentum balance is solved in a predictor-corrector scheme with the divergence Equation (138) as a constraint. As can be seen from Equation (138), the divergence can be zero only if $\rho_j^0 = \rho = const.$ which means that the velocity field is source-free [7]. Changes in composition brought on by diffusion or chemical reactions cause incompressible fluids with concentration-dependent densities to expand or contract, which results in a nonzero divergence of the barycentric velocity field [7].

Figure 93 shows an overview of the developed CFD model, which was implemented in an OpenFOAM® environment. Besides solving the momentum and component balances, the reaction kinetics was implemented with a zero-dimensional moment model of the polymer distribution. The viscosity is parameterized using a correlation depending on polymer weight fraction and average molecular weight. In addition, the newly developed mass transport model for polymer moments derived from limiting cases of Maxwell- Stefan diffusion is implemented in the solver. The individual blocks are therefore discussed in more detail below.

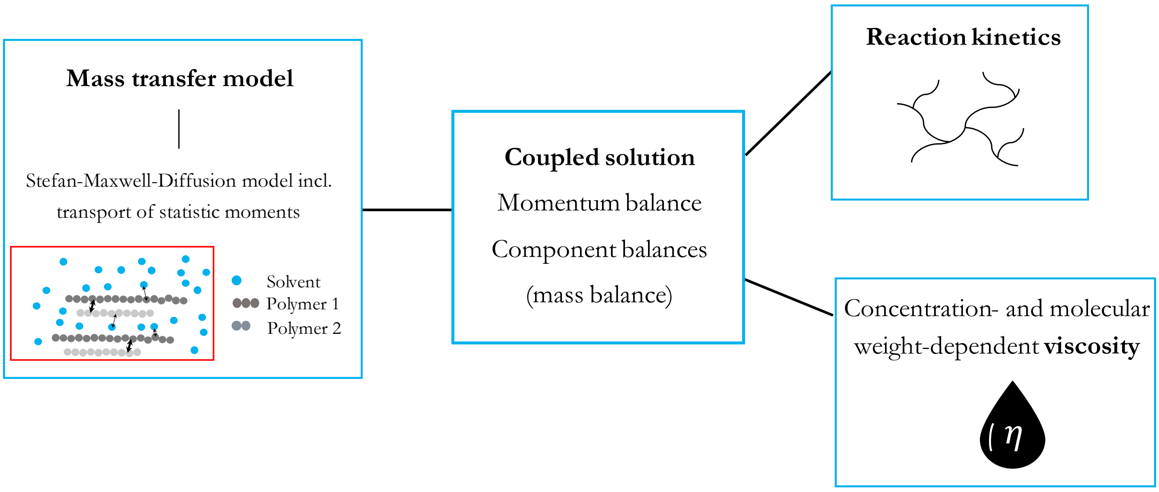

Figure 93: Overview about the developed CFD model with implemented reaction kinetics, concentration- and molecular weight-dependent viscosity and a mass transfer model.

6.1.1 Mass transfer model

The development of the mass transfer model was described in detail in Chapter 5 and therefore only the necessary equations are discussed here.

The diffusive material flows J_j^N can be calculated with the help of the Maxwell-Stefan model

$$-c\nabla x_i = -\nabla c_i + \frac{c_i}{c}\nabla c = \sum_{j=1}^{J-1} \boldsymbol{B}_{ij} \cdot \boldsymbol{J}_j^N. \tag{140}$$

Again, an ideal mixture was assumed. A form of the Maxwell-Stefan model which is explicit in the flows J_j^N and suitable for implementation in CFD codes is

$$\boldsymbol{J}_j^N = \sum_{i=1}^{J-1} -(\boldsymbol{B}^{-1})_{ji} \cdot \left(\nabla c_i - c_i \frac{1}{\mathrm{c}} \nabla c\right) = \sum_{i=1}^{J-1} -\boldsymbol{D}_{ji}^F \cdot \left(\nabla c_i - c_i \frac{1}{\mathrm{c}} \nabla c\right) \tag{141}$$

and can be obtained by inverting the matrix B [7]. The matrix $D^F = B^{-1}$ is the diffusion matrix which elements are Fickian type diffusion coefficients [7]. Since the fluxes J_j^N have been defined relative to the molar averaged velocity v^N, the following holds true

$$\boldsymbol{J}_J^N = -\sum_{j=1}^{J-1} \boldsymbol{J}_j^N. \tag{142}$$

Typically, in a mixture of J components, J-1 balance equations are solved and the concentration of the Jth component is calculated from a constraint, e.g., using the volume fractions as

$$c_J = \frac{\rho_J^0}{M_J} - \sum_{j=1}^{J-1} \frac{M_j}{M_J} \frac{\rho_J^0}{\rho_j^0} c_j. \tag{143}$$

In systems containing polymers, the property distributions of the polymer species are usually described by their moments to keep the computational effort at a manageable level. Consequently, component balances for statistical moments of the polymer distribution and, consequently, reaction rates and diffusive fluxes for these moments must be ascertained by constitutive relations, appear alongside balance equations for low molecular weight species.

For a model for diffusive fluxes of the moments of polymer distributions derived under the assumption that polymers do not diffuse with respect to each other [80], the Maxwell-Stefan diffusion coefficients for polymers of all chain lengths s and r are defined as $D_{P_s P_r} \to 0$. The result is a definition of the fluxes of chain length moments of the polymer population P via the flux of zero chain length moments (Equation (126)) and was described as the "Infinite Polymer Friction" model in Chapter 5.3.3. This model is assumed to be the standard for the investigations in the following chapters.

In summary, the model equations used are the momentum balance in Equation (133), which is used in a pressure correction scheme together with the divergence Equation (138) as a constraint and the molar component balances

$$\frac{\partial c_j}{\partial t} = -\nabla \cdot \left(\boldsymbol{v} - \frac{1}{\rho} \sum_i M_i \boldsymbol{J}_i^N \right) c_j - \nabla \cdot \boldsymbol{J}_j^N + r_j^{total}. \tag{144}$$

The latter is solved for those polymer moments relevant to the kinetic model and all low molecular weight species except the solvent, whose concentration is calculated from constraint Equation (143).

For radical species with low concentrations and a very short lifespan, diffusive fluxes are not taken into account [7]. Therefore, when the solvent S is considered as the Jth species, the Maxwell-Stefan equations simplify to a system of three equations for the undissociated initiator I_2, the monomer M, and the polymer population P. The nonzero entries of the Fick's diffusion matrix for use in Equation (141), D^F are [7]

$$D^F_{I_2,I_2} = D^F_{M,M} = \frac{c\mathfrak{D}_0\mathfrak{D}_P}{\left(c_{I_2} + c_M + c_{LM}\right)\mathfrak{D}_P + c_P\mathfrak{D}_0}, \tag{145}$$

$$D^F_{P,P} = \frac{c\mathfrak{D}_P}{c_P + c_{LM} + c_{I_2} + c_M}, \tag{146}$$

$$D^F_{M,P} = \frac{c_M(\mathfrak{D}_0 - \mathfrak{D}_P)}{c\mathfrak{D}_0\mathfrak{D}_P} \cdot D^F_{M,M} \cdot D^F_{P,P}, \tag{147}$$

$$D^F_{I_2,P} = \frac{c_{I_2}(\mathfrak{D}_0 - \mathfrak{D}_P)}{c\mathfrak{D}_0\mathfrak{D}_P} \cdot D^F_{I_2,I_2} \cdot D^F_{P,P} \tag{148}$$

With the assumption that $\mathfrak{D}_{i,j} = \mathfrak{D}_0$ for diffusive interactions between all low molecular weight species and $\mathfrak{D}_{i,P} = \mathfrak{D}_P$ for diffusive interactions between all low-molecular-weight species and polymers, and the diffusive fluxes are [7]

$$\boldsymbol{J}^N_{I_2} = -D^F_{I_2,I_2} \cdot \left(\nabla c_{I_2} - c_{I_2}\frac{1}{c}\nabla c\right) - D^F_{I_2,P} \cdot \left(\nabla \xi^P_0 - \xi^P_0\frac{1}{c}\nabla c\right), \tag{149}$$

$$\boldsymbol{J}^N_{M} = -D^F_{M,M} \cdot \left(\nabla c_{M} - c_{M}\frac{1}{c}\nabla c\right) - D^F_{M,P} \cdot \left(\nabla \xi^P_0 - \xi^P_0\frac{1}{c}\nabla c\right), \tag{150}$$

$$\boldsymbol{J}^N_{\xi^P_0} = -D^F_{P,P} \cdot \left(\nabla \xi^P_0 - \xi^P_0\frac{1}{c}\nabla c\right), \tag{151}$$

$$\boldsymbol{J}^N_{\xi^P_{k,l}} = \frac{\xi^P_{k,l}}{\xi^P_{0,0}}\boldsymbol{J}^N_{\xi^P_{0,0}}, \tag{152}$$

$$\boldsymbol{J}^N_S = -\boldsymbol{J}^N_{I_2} - \boldsymbol{J}^N_M - \boldsymbol{J}^N_{\xi^P_{0,0}}. \tag{153}$$

The parameter k and l indicate different property coordinates, e.g. number of chains, number of TDB,… Equation (152) describes the "Infinite Polymer Friction" model at this point, which has already been described in Chapter 5.3.3. The influence of the transport model is examined later in Chapter 6.4.1, where this equation is replaced by Equation (112).

The Stokes-Einstein relation served as the inspiration for scaling the Maxwell-Stefan diffusion coefficients by η_{rel} [7]

$$\mathfrak{D}_{0/P} = \frac{\mathfrak{D}_{0/P}^{0}}{\eta_{rel}} \tag{154}$$

with the reference Maxwell-Stefan diffusion coefficient $\mathfrak{D}_{0/P}^{0}$ for $w_P \rightarrow 0$ to include the effect of decreasing diffusion coefficients with increasing solution viscosity [7]. Diffusion coefficients are influenced by concentrations as well as the length of the polymer chain. An estimate for the ratio

$$\frac{\mathfrak{D}_P}{\mathfrak{D}_0} = \left(\frac{\xi^1}{\xi^0}\right)^{-0.6} \tag{155}$$

was inspired by the Zimm theory [7]. However, this approximation can only be rough because the latter was developed for monodisperse, linear polymers in diluted solution.

The influence of the choice of model for estimating the diffusion coefficient of the polymers is examined in Chapter 6.4.4. This estimation is then replaced by a different description from Chapter 5.6.

6.1.2 Viscosity correlation

The viscosity has a very large influence on the formation of the wall layer in continuous tubular reactors. To correctly represent the formation of the layer, the dependence of viscosity on polymer weight fraction w_P and weight average molecular weight M_w must be accounted for. This can be achieved by using Huggin's equation [32]

$$\eta = \eta_{ref}(1 + [\eta]w_P + k_H[\eta]^2 w_P^2) \tag{156}$$

with the reference viscosity η_{ref}=1.02 mPas and the constant k_H. In combination with the Mark-Houwink equation

$$[\eta] \propto M^{\alpha}\ with\, \alpha = 0.5 - 0.8 \tag{157}$$

a relation of viscosity on polymer weight fraction and molecular weight can be formulated

$$\eta = \eta_{ref}(1 + k_1 w_P M_w^{\alpha} + k_2(w_P\ M_w^{\alpha})^2). \tag{158}$$

After a series expansion to the complete virial equation [32], it follows

$$\eta = \eta_{ref}\left(1 + \sum k_j (w_P\, M_w^{\alpha})^j\right). \tag{159}$$

Since the free radical polymerization of N-vinylpyrrolidone is investigated at T=85 °C, viscosity measurements of different PVP blends (K12, K30, K90) were performed only at this temperature and parameters are fitted. The analytical setup is described in Appendix A.1.5. Through these measurements it is possible to perform a parameter fit. The scatter of k_1 can be reduced by using a three-term equation [32]. The correlation is given in Equation (160).

$$\begin{aligned}\eta(@85\,°C) = \eta_{ref}& \\ \cdot 0.004411 &\left(1 + 364.97\left(\frac{w_P}{0.2}\left(\frac{M_w}{5e5\,\frac{g}{mol}}\right)^{0.45}\right)\right. \\ &- 697.75\left(\frac{w_P}{0.2}\left(\frac{M_w}{5e5\,\frac{g}{mol}}\right)^{0.45}\right)^{3} \\ &\left.+ 7148.7\left(\frac{w_P}{0.2}\left(\frac{M_w}{5e5\,\frac{g}{mol}}\right)^{0.45}\right)^{5}\right)\end{aligned} \tag{160}$$

The parity plot in Figure 94 shows the validity of the correlation and shows very good agreement between predicted and experimentally determined values.

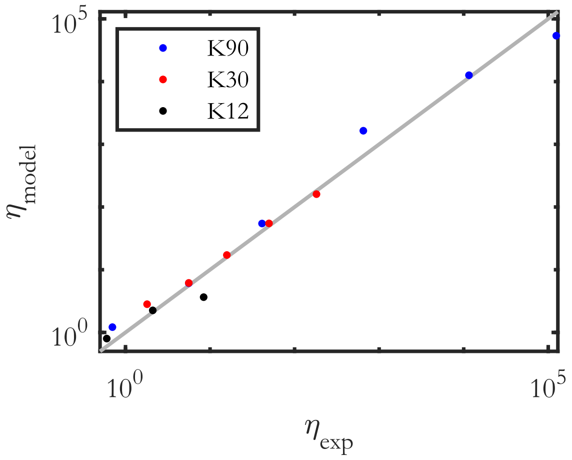

Figure 94: Parity plot of the measured and predicted viscosities for different Kollidones.

The choice of viscosity model is essential for describing fouling and the wall layer structure. The influence of viscosity is therefore investigated in Chapter 6.4.2. Here, this correlation is compared to a simpler version without the dependence on the molecular weight.

6.1.3 Reaction kinetics

The kinetic model used in the simulations is the "TDB double moment model" published by Zander et al. [6].

6.2 Simulation domain

The standard reactor has a total length of 3 m and an inner diameter of 1.76 mm. For comparison 3D simulations have been conducted by using a wedge geometry. For the comparison to experimental results, the reactor is initially filled with water as in the experiments. The inlet velocity was chosen the same as in the experiments to 12 mm/s and the feed concentrations as well from 5-20 wt.-% monomer and 0.002-0.02 wt.-% initiator. This corresponds to average residence times of 250 s. The remaining parameters for the reference case are defined in Table 14.

Table 14: Reference set of parameters for the simulations.

Parameter	Reference value
Reference viscosity η_{ref}	$1.02 \cdot 10^{-3}$ Pas
Diffusion coefficient between low molecular species $\mathfrak{D}_0^0$	$7.5 \cdot 10^{-9}$ $\mathrm{m^2\,s^{-1}}$
Quotient of the diffusion coefficient between polymer and low molecular species and the coefficient between low molecular species $\mathfrak{D}_P/\mathfrak{D}_0$	0.014
Monomer density ρ_M^0 [62]	989.72 $\mathrm{kg\,m^{-3}}$
Solvent density ρ_S^0 [62]	958.57 $\mathrm{kg\,m^{-3}}$
ρ_j^0 (all other)	1200 $\mathrm{kg\,m^{-3}}$
Molecular weight of Monomer M_M	0.1114 $\mathrm{kg\,mol^{-1}}$
Molecular weight of Initiator M_{I_2}	0.2712 $\mathrm{kg\,mol^{-1}}$
Molecular weight Solvent M_S	0.0180 $\mathrm{kg\,mol^{-1}}$

The computational grid is shown schematically in Figure 95. Here, the grid was scaled in y-direction, with the grid cells also coarsened for visualization purposes. A grid of 80000 cells was chosen to be appropriate. A mesh study is presented in the Appendix A.5.1.

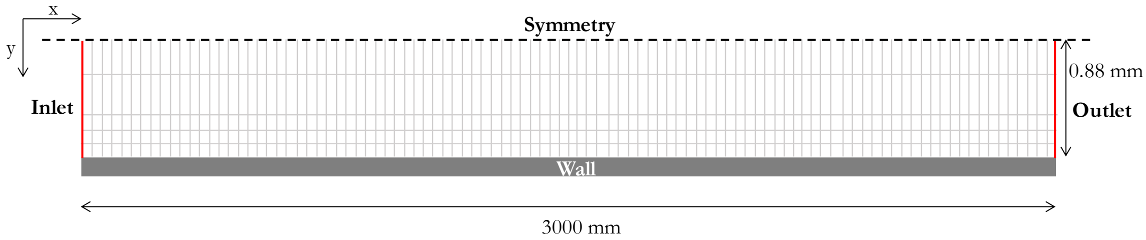

Figure 95: Geometry for the three-dimensional simulation of the tube reactor. The y-axis was scaled for visualization purposes and the grid was coarsened. Adapted from [7].

A line of symmetry was formed from the plane of symmetry, resulting in a wedge-shaped geometry with an angle of 5° as shown in Figure 96.

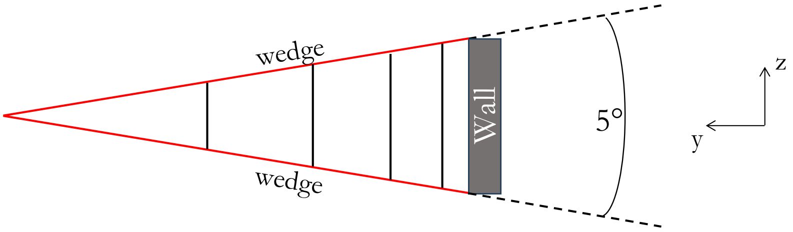

Figure 96: Simulation geometry of the capillary reactor. x- and y-axis were scaled for visualization. Adapted from [7].

The boundary conditions are those typical for a channel flow [7]. In addition to the wall and symmetry boundary conditions shown in Figure 96, Dirichlet boundary conditions were specified for all concentrations, barycentric velocity at the inlet and zero gradient Neumann boundary conditions at the outlet. For pressure p, a zero-gradient Neumann boundary condition was specified at the inlet and a zero-value Dirichlet boundary condition at the outlet. As initial conditions the initial velocity and pressure field were set to zero within the simulation domain.

6.3 Validation of the CFD model

To further predict wall layer formation depending on process and geometry conditions, the model must be validated by experiments conducted in the capillary reactor, which have already been presented in Chapter 3.1.

6.3.1 Calculating residence time distribution with a passive tracer

In order to stay as close as possible to the experiments, the solvent was introduced into the reactor at the start of the simulation. After the start of polymerization, a salt concentration was added at certain times, as in the experiment. The tracer is implemented as a passive species, without interaction with the other species. Thus, the transport equation reads as

$$\frac{\partial c_T}{\partial t} = -\nabla \cdot \left(\boldsymbol{v} - \frac{1}{\rho} \sum_{i \neq T} M_i \boldsymbol{J}_i^N \right) c_T - \nabla \cdot \boldsymbol{J}_T^N \tag{161}$$

with

$$\boldsymbol{J}_T^N = -\mathfrak{D}_T \cdot \left(\nabla c_T - c_T \frac{1}{c} \nabla c \right) \tag{162}$$

and the Fickian type diffusion coefficient D_T. The input signal was generated via a "look-up table". To allow comparison between experiment and simulation, the input signal was normalized and then scaled to the time-dependent input concentration. The output signal was calculated over the area average by summing over all areas which are part of the output.

6.3.2 Results for the simulated residence time distributions compared to experiments

Figure 97 shows the comparison of the residence time distribution (RTD) for the experiments and simulations for different monomer and initiator concentrations. In Figure 97A the RTD with a 20 wt.-% monomer feed concentration is shown. The residence time distribution of water is plotted as reference. Furthermore, tracer injections were made after 2, 15, 30 and 60 minutes after the start of polymerization. The time for breakthrough shortens over time on stream while the tailing increases. The reason is the formation of a highly viscous wall layer. Due to cross section narrowing, the breakthrough of the tracer shifts to shorter times and tailing increases due to reduced transport in the viscous wall layer. Simulated residence time distributions show the same trends. Figure 97B shows the residence time distributions for a lower monomer concentration of 5 wt.-%. The tends are less pronounced compared to higher monomer concentrations but still clearly visible. The simulated RTDs are again in good agreement with experimental data. Figure 97C shows a 10 times lower initiator concentration compared to case A (0.002 wt.-% instead of 0.02 wt.-%). The breakthrough of the tracer occurs slightly faster, and the tailing is less pronounced for higher times. As with lower monomer concentration, a lower initiator concentration also results in smaller wall deposits. In all cases, simulations are in qualitatively good agreement with the experimental findings and general trends are good predicted. The tailing of the distributions in the experiments is more pronounced as in the simulations. This can be attributed to estimated transport properties of the tracer.

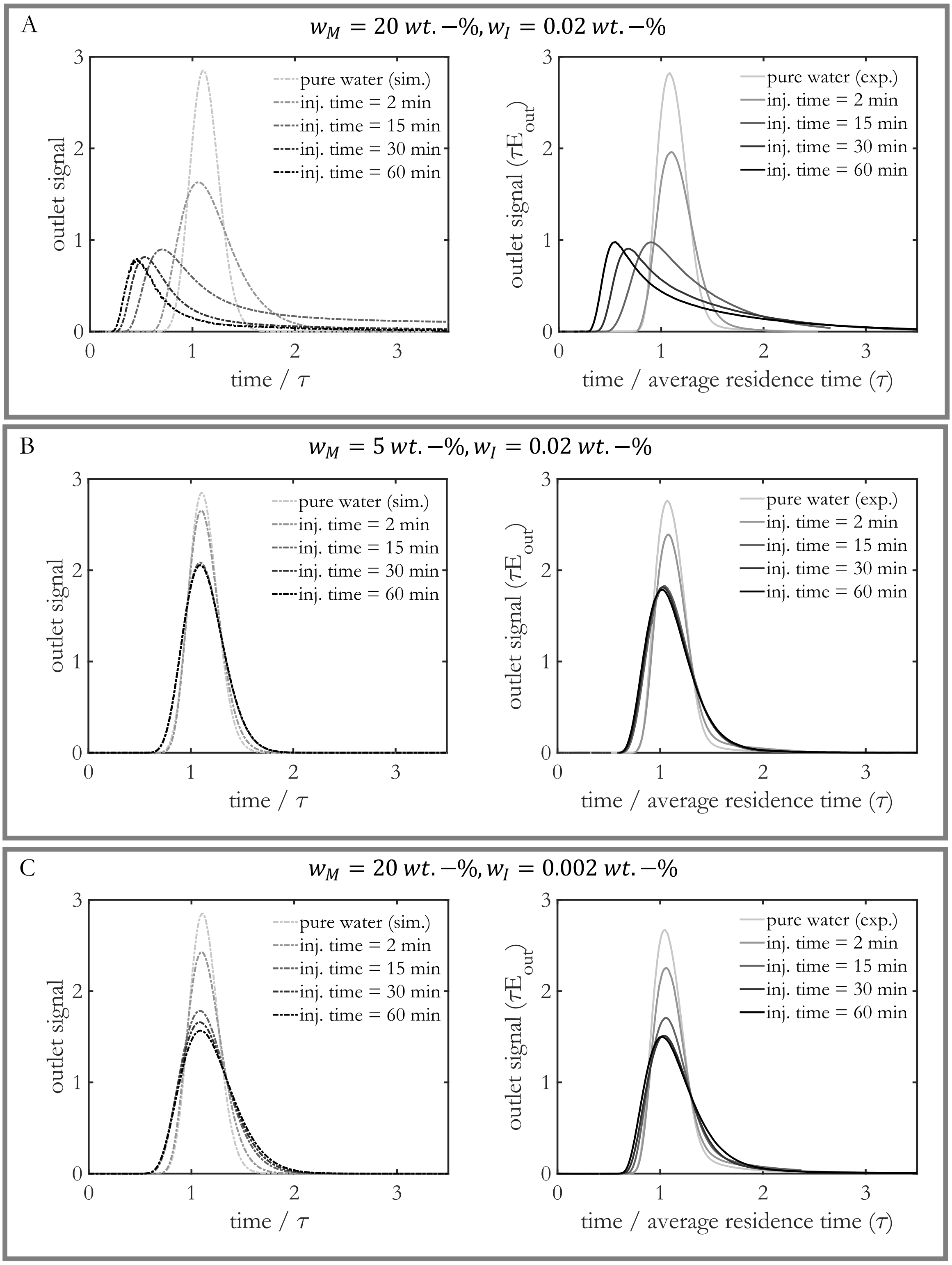

Figure 97: Residence time distributions for simulations (left) and experiments (right) at different monomer and initiator concentrations.

In addition to the different process conditions, different geometric variants of the capillary reactor will also be compared with the experiment. Figure 98 shows the residence time distributions of a capillary reactor with twice the length of the standard case with the same residence time (twice the input speed) in A and with a larger diameter with the same residence time in B. The initial build-up of the wall layer (2 min) due to the increasing viscosity can be reproduced well in both cases. However, the simulation overestimates the wall layer formation for both a longer reactor and a larger reactor cross-section. This can be explained by the fact that in the experiment a wall layer or entangled polymers are torn off at higher shear due to the flow. Unfortunately, this cannot currently be reproduced in the simulation.

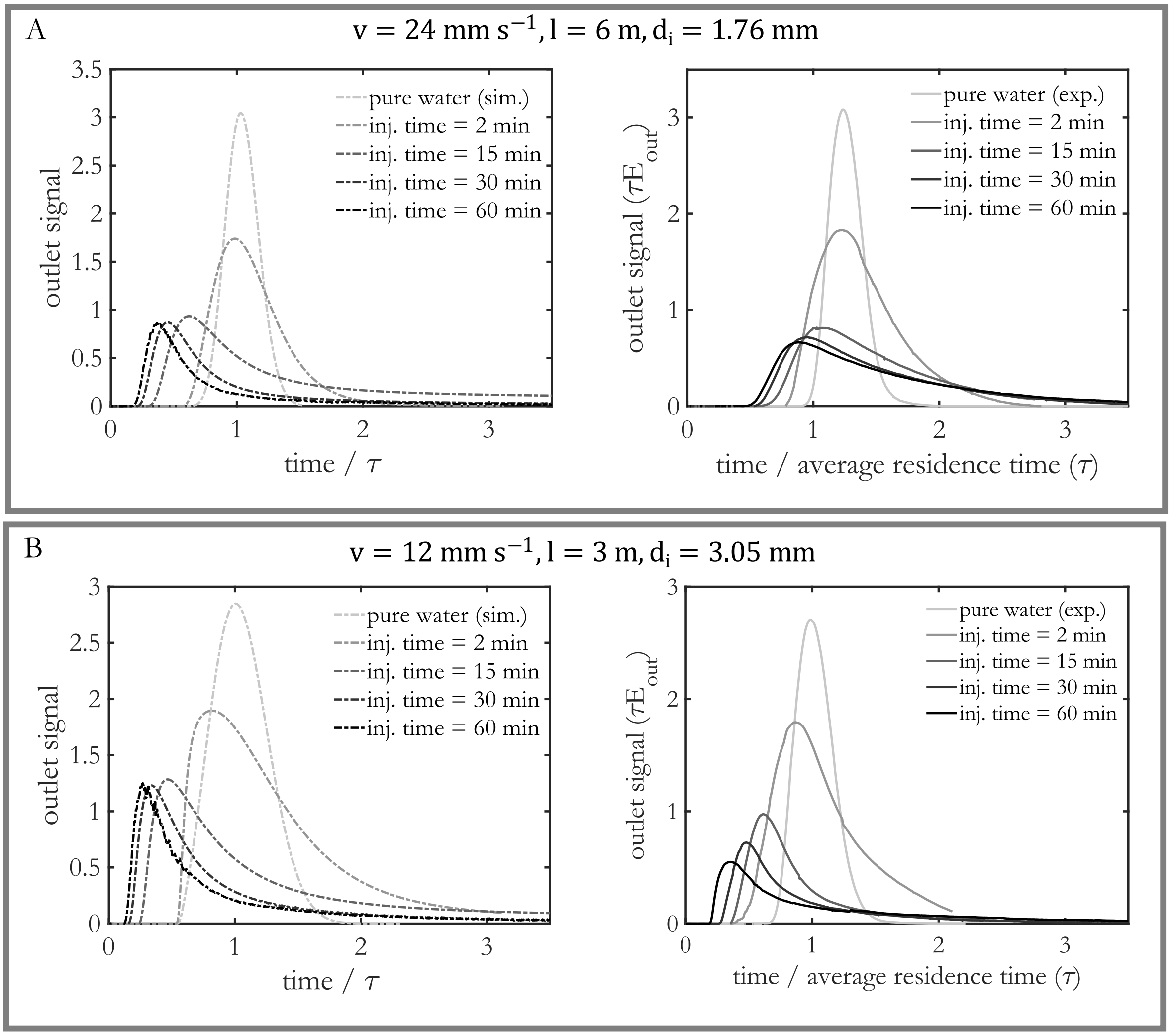

Figure 98: Residence time distributions for simulations (left) and experiments (right) for different geometric reactor conditions.

6.4 Influencing factors of wall layer formation in a capillary tubular reactor

From the experimental results of the tests in the capillary reactor, it became clear that a highly viscous wall layer forms in the reactor, which begins to gel after a certain time. To correctly depict the formation of this wall layer, it is important to select a suitable transport model for the polymers, which was introduced in Chapter 5 and the CFD results are presented below. Furthermore, the difference between simple viscosity models and the in-house developed correlation is shown as well as the influence of side reactions and the use of different diffusion coefficients between low molecular species and polymers. To analyze these influencing factors, a reference case for the process conditions is defined in Table 15 and is used if not stated otherwise. For the investigation of the influencing factors, the initial conditions are previously calculated plug flow solutions for numerical reasons.

Table 15: Parameter set for the process conditions for the reference case.

Parameter	Reference value
Monomer feed concentration	w_M=20 wt.-%
Initiator feed concentration	w_I=0.02 wt.-%
Solvent feed concentration	$w_S=1-w_I-w_M$
Flow velocity	v=12 mm/s
Reynolds-number	$Re_{in} = \frac{\rho v_{in} d}{\eta} \approx 21$

6.4.1 Influence of the transport model of the polymers

First, the CFD results relating to the "No Polymer Friction" model from Chapter 5.3.2 are presented in Figure 99. The figure shows the relative viscosity and the polymer weight fraction for 2 different operating times (A: 22 min and B: 100 min). Both the viscosity and the polymer weight fraction do not change with the reaction time. At the same time, both values increase with the reactor length, but no wall layer is formed. This behavior of the polymer solution can be explained by the fact that there is no friction between the polymers, and they can therefore diffuse freely against all other molecules. Due to this enormously high transport of the polymers, there is no accumulation near the wall.

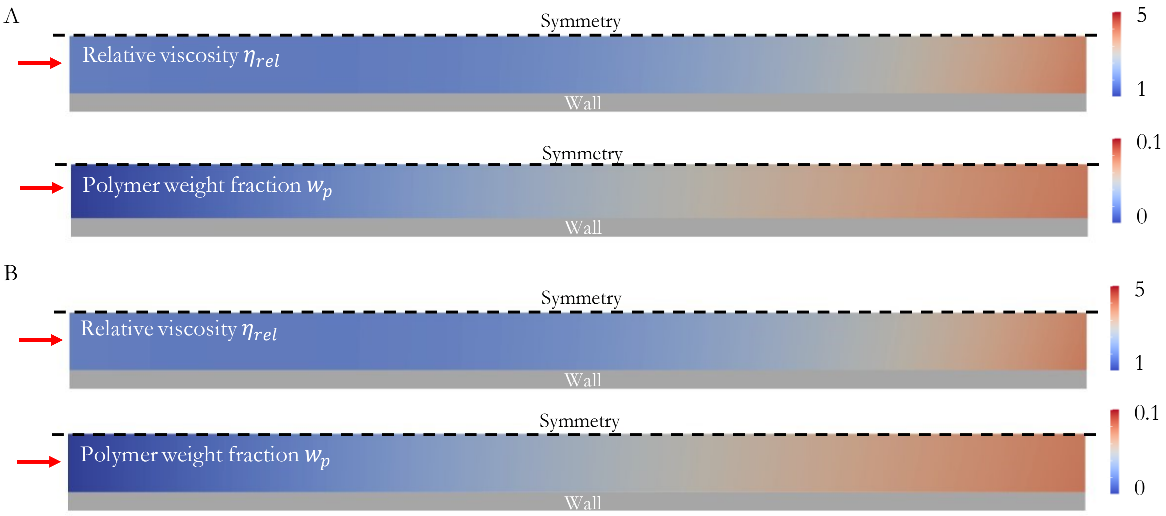

Figure 99: Simulation results for the relative viscosity η_{rel} and the polymer weight fraction w_P for two different times (A: 22 min and B: 100 min reaction time) for a monomer concentration of w_M=20 wt.-% and an initiator concentration of w_I=0.02 wt.-%. Simulations conducted with the 'No Polymer Friction model'.

As this transport model is therefore unable to depict wall layer formation, this model is no longer used.

In addition to the "No Polymer Friction" model, the "Infinite Polymer Friction model" has also been implemented. To gain a better understanding of the formation of the wall layer, the relative viscosity η_{rel} and polymer weight fraction w_P is shown in Figure 100 for 22 min and 100 min time on stream. After 22 min a viscous wall layer is formed at a certain distance to the reactor entrance, which exhibits a high polymer weight fraction. This wall layer grows uniformly up to the reactor outlet. Over time the polymer content of the layer increases up to w_P=0.5 (100 min), much higher than possible with average conversion (approx. 30 %). That means that with a feed concentration of 20 wt.-% and a monomer conversion of 30 %, a polymer weight fraction in the stream would be around 6 wt.-%.

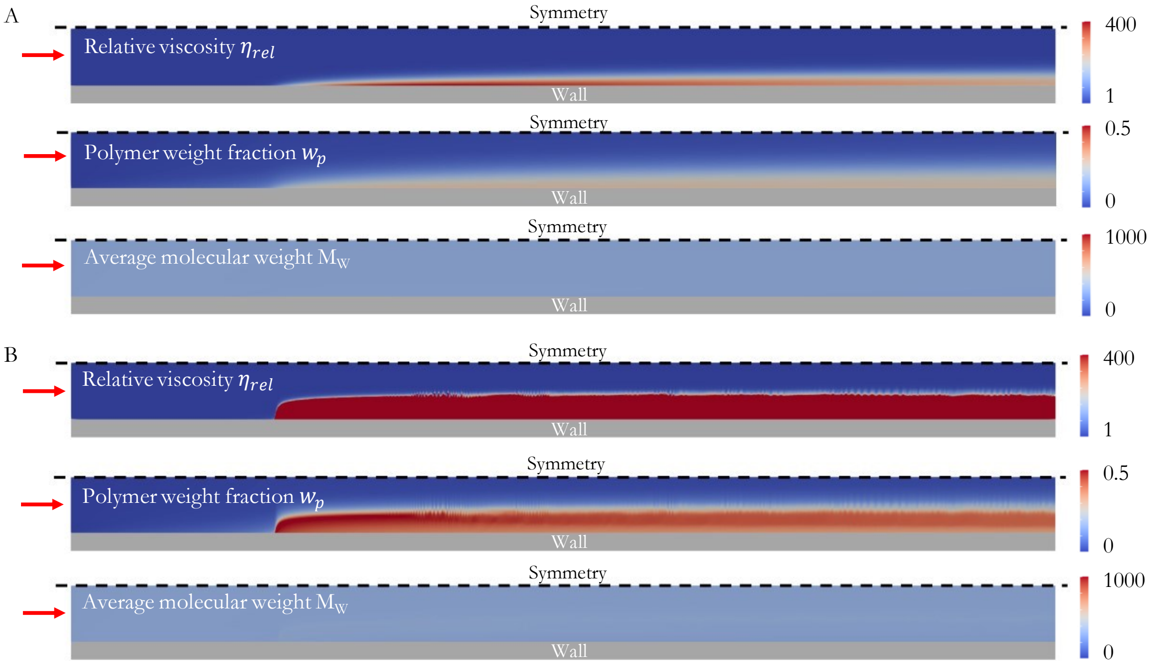

Figure 100: Simulation for the relative viscosity η_{rel}, the polymer weight fraction w_P, and the average molecular weight M_W for two different reaction times (A: 22 min and B: 100 min reaction time) for a monomer concentration of w_M=20 wt.-% and an initiator concentration of w_I=0.02 wt.-%. Simulations conducted with the 'Infinite Polymer Friction model'.

For these results, the formation of side reactions is eliminated, since, as presented later, they are not essential for the formation of a wall layer. The "Infinite Polymer Friction" model can therefore depict the formation of a wall layer, and this model will therefore be used for further investigations.

6.4.2 Influence of the viscosity model

In this chapter, the influence of the viscosity model on the calculation of the wall layer will be explained. A somewhat simpler way of describing the viscosity was introduced in [61] and used in [7] without considering the molecular weight. The viscosity is therefore calculated according to

$$\eta = \eta_{ref}\, exp\left(C_\eta w_P\right) \tag{163}$$

with the constant $C_\eta = 14.75$.

The results will first be presented using the reference case. The maximum value of the polymer weight fraction w_P and the relative viscosity η_{rel} over the full simulation domain were calculated to compare the viscosity models. Figure 101 shows the relative viscosity of the two models. The newly developed correlation (Equation (160)) shows an earlier increase in the relative viscosity, as this also depends on the molecular weight. In Figure 102 the polymer weight fraction is shown for both the models. Here, a higher maximum value is achieved over time by the "simplified" viscosity model and this behavior is therefore overestimated.

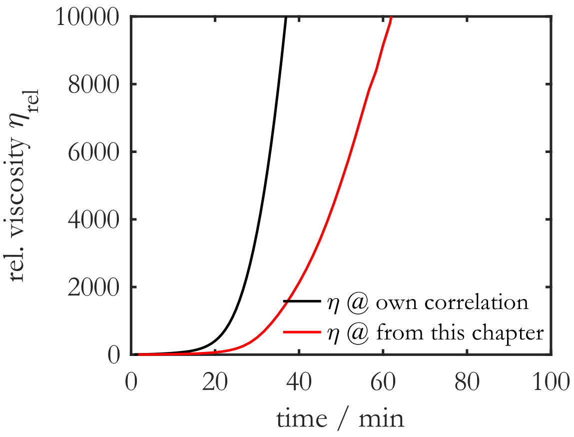

Figure 101: Max. rel. viscosity η_{rel} over the reaction time for different viscosity models at a monomer concentration of w_M=20 wt.-% and an initiator concentration of w_I=0.02 wt.-%.

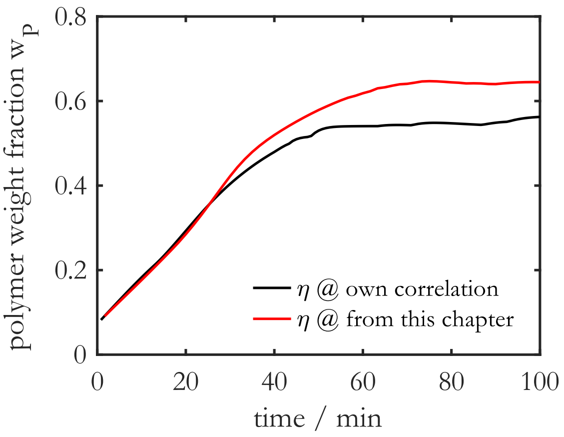

Figure 102: Max. polymer weight fraction w_P over the reaction time for different viscosity models at a monomer concentration of w_M=20 wt.-% and an initiator concentration of w_I=0.02 wt.-%.

To be able to further assess that this model is significantly less suitable for describing wall layer formation, residence time simulations were also carried out. These are shown in Figure 103 and 104 and can be compared directly with those of the own developed model in Figure 97A and C. Compared to the own developed viscosity model, the wall layer is somewhat less pronounced in the "simplified" model for the reference case. However, only minor differences are recognizable here, as this "simple" correlation was adapted for such process conditions. The differences become clearer in Figure 104, where the residence time distributions for a reduced initiator feed concentration (w_I=0.002 wt.-%) are shown. Here it becomes clear that there is no dependence of the viscosity on the chain length and that the formation of the wall layer is only very slightly recognizable. However, the lower initiator concentration results in longer chains and thus higher molecular weights, which can be only correctly depicted by the own developed model. To be able to correctly reproduce a wide range of different process conditions, a dependence of the viscosity on the molecular weight is necessary.

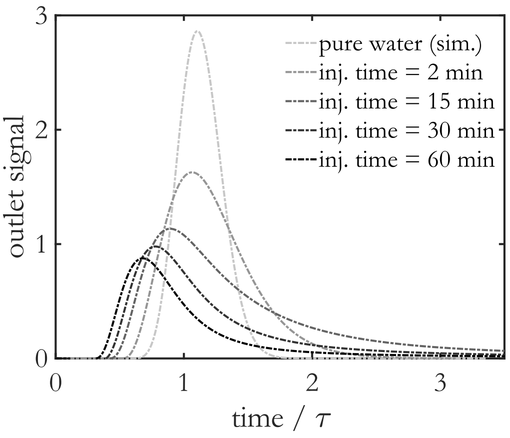

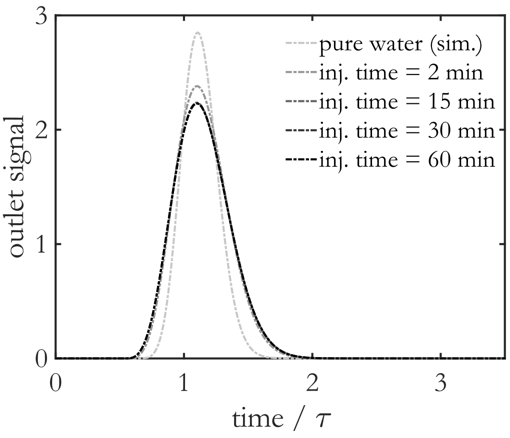

Figure 103: Residence time distributions with the viscosity model from this chapter (simulation) for a monomer concentration of w_M=20 wt.-% and an initiator concentration of w_I=0.02 wt.-%.

Figure 104: Residence time distributions with the viscosity model from this chapter (simulation) for a monomer concentration of w_M=20 wt.-% and an initiator concentration of w_I=0.002 wt.-%.

6.4.3 Influence of side reactions

In this section, CFD simulations with side reactions are presented. The simulations are intended to provide a prediction of fouling formation processes as a function of the monomer and initiator content as a function of time. The process parameters therefore cover a wide range of applications.

As already mentioned, a wall layer is formed even without taking side reactions into account. At the same time, the flow field is only slightly influenced. However, these reactions influence the structure of the polymers. This can be seen in Figure 105 where the average molecular weight and the polymer weight fraction is depicted and can be compared to Figure 100. After 22 min reaction time, almost no differences can be seen between the simulations with and without side reactions (Figure 105A). Since the simulation with side reactions stops after 64 min due to gelation under these process conditions, only this state can be shown (Figure 105B). It is already clear at this stage that the weight average molecular weight is orders of magnitude greater than without side reactions.

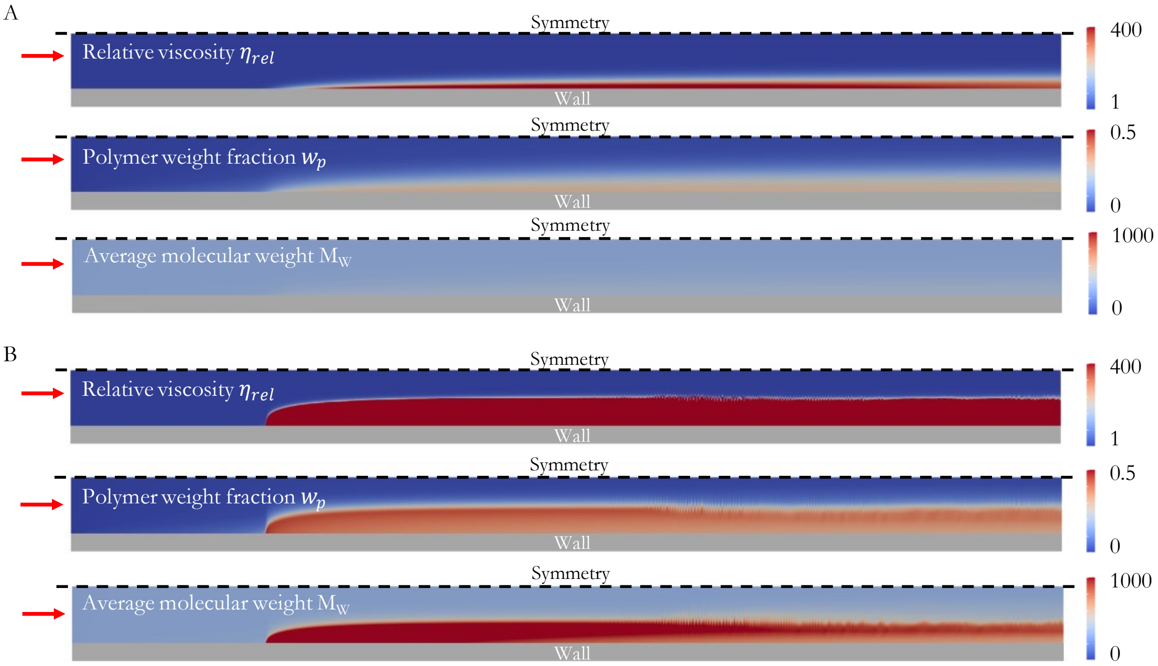

Figure 105: Simulation results for the relative viscosity η_{rel}, the polymer weight fraction w_P, and the average molecular weight M_W for two different reaction times (A: 22 min and B: 64 min reaction time) for a monomer concentration of w_M=20 wt.-% and an initiator concentration of w_I=0.02 wt.-%. Simulations conducted with side reactions.

To investigate this further and to compare different process conditions, the maximum value of the entire simulation domain of the mass average molecular weight (M_W), the polymer weight fraction w_P and the relative viscosity η_{rel} was determined in each case. Figure 106 and 107 show the mass-average molecular weights of the different monomer and initiator concentrations. Figure 106 indicate that the molecular weight increases extremely sharply after a certain reaction time due to side reactions taking place. The higher the monomer concentration, the earlier and the steeper this increase takes place. At a monomer concentration of only w_M=5 wt.-%, no increase in molecular weight until an operating time of 200 min is recognizable. Such a strong increase in molecular weight, as is the case with w_M=10-20 wt.-%, is an indication of fouling. The calculation then diverges. In contrast, for w_M=5 wt.-% a stationary behavior occurs, the calculation converges, and no fouling occurs.

Figure 107 shows the same phenomenon at different initiator concentrations. The higher the initiator concentration, the earlier and steeper the increase in molecular weight. At an initiator concentration of w_I=0.002 wt.-%, there is still an increase in molecular weight, but much later and less steep. In comparison to the curves with side reactions, the simulations without side reactions show that the molecular weight remains at a constant level.

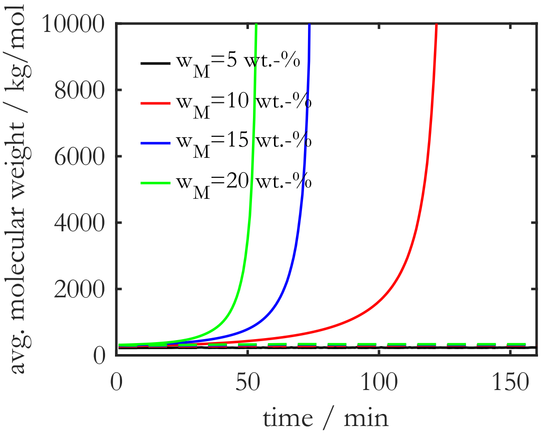

Figure 106: Max. average molecular weight over the reaction time for different monomer concentrations at an initiator concentration of w_I=0.02 wt.-%. Solid lines show results with side reactions, dashed lines without.

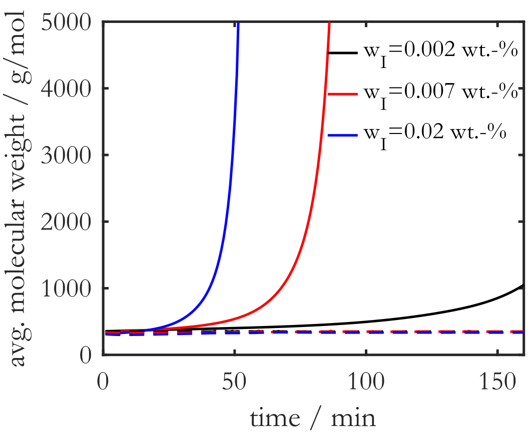

Figure 107: Max. average molecular weight over the reaction time for different initiator concentrations at a monomer concentration of w_M=20 wt.-%. Solid lines show results with side reactions, dashed lines without.

Figure 108 and 109 show the maximum polymer weight fraction w_P over time for different monomer and initiator concentrations. Figure 108 shows that an earlier and steeper increase can be observed with increasing monomer content. However, the polymer weight fraction tends towards a constant value until the end of the operating time. Interestingly, this constant value for all w_M=10-20 wt.-% is approx. w_P= 0.55. At a monomer weight fraction of w_M=5 wt.-%, there is a significantly more moderate increase in the polymer weight fraction, as the side reactions are significantly reduced at such a low concentration. Figure 109 shows the same trend for different initiator concentrations. As the concentration increases, there is an earlier and steeper increase in the polymer weight fraction. At an initiator concentration of only w_I=0.002 wt.-%, an increase in the polymer content still can be seen. In contrast, the results without side reactions show that the polymer share increases slightly more here. As no side reactions take place, the main reactions occur more frequently.

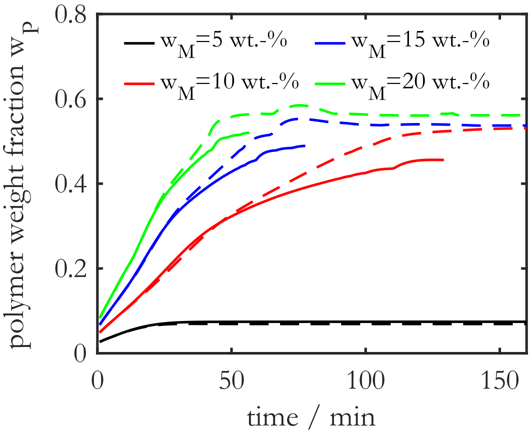

Figure 108: Max. Polymer weight fraction w_P over the reaction time for different monomer concentrations at an initiator concentration of w_I=0.02 wt.-%. Solid lines show results with side reactions, dashed lines without.

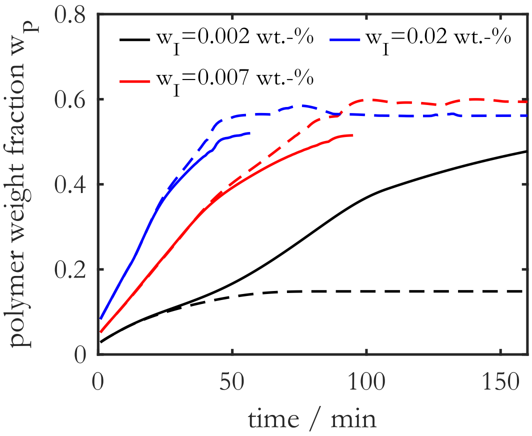

Figure 109: Max. Polymer weight fraction w_P over the reaction time for different initiator concentrations at a monomer concentration of w_M=20 wt.-%. Solid lines show results with side reactions, dashed lines without.

Figure 110 and 111 show the maximum relative viscosity over the operating time. Figure 110 shows the behavior at different monomer concentrations, whereby it is clear that the curves are similar to those of molecular weight due to the direct dependence of the viscosity correlation on the molecular weight. An extremely steep increase in viscosity again indicates the formation of a wall layer. It can be concluded that in the case of w_M=5 wt.-% no formation occurs in the period under consideration. Figure 110 shows the relative viscosity for different initiator concentrations. Analogous to the monomer concentration, a similar trend can be observed. In contrast to the results with side reactions, the simulations without these reactions show that the relative viscosity increases somewhat more smoothly.

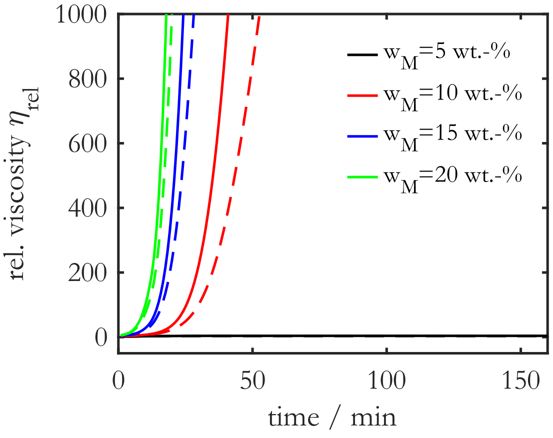

Figure 110: Max. relative viscosity η_{rel} over the reaction time for different monomer concentrations at an initiator concentration of w_I=0.02 wt.-%. Solid lines show results with side reactions, dashed lines without.

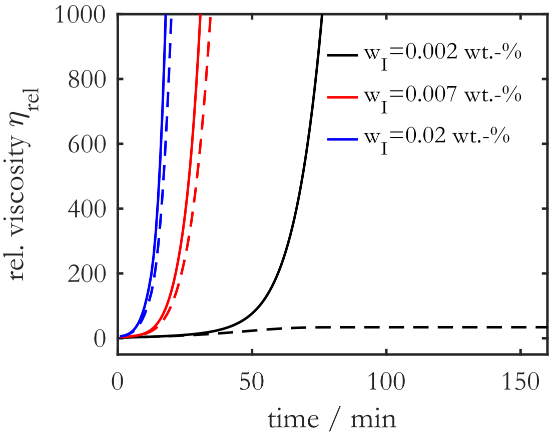

Figure 111: Max. relative viscosity η_{rel} over the reaction time for different initiator concentrations at a monomer concentration of w_M=20 wt.-%. Solid lines show results with side reactions, dashed lines without.

The monomer conversion curve for the different process conditions is shown in Figure 112 resp. 113. For both, monomer and initiator concentrations, the conversion decreases with increasing operating time due to the formation of the wall layer. With increasing concentration, this happens correspondingly faster. Furthermore, the conversion decrease is stronger if side reactions are considered. As side reactions take place, less monomer is polymerized within the wall layer, as side reactions to high molecular weight polymers take place.

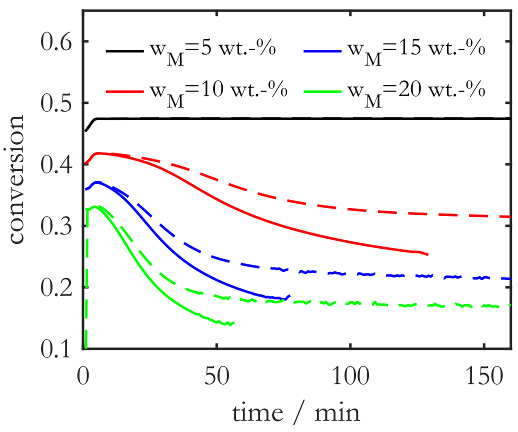

Figure 112: Monomer conversion at reactor outlet over the reaction time for different monomer concentrations at an initiator concentration of w_I=0.02 wt.-%. Solid lines show results with side reactions, dashed lines without.

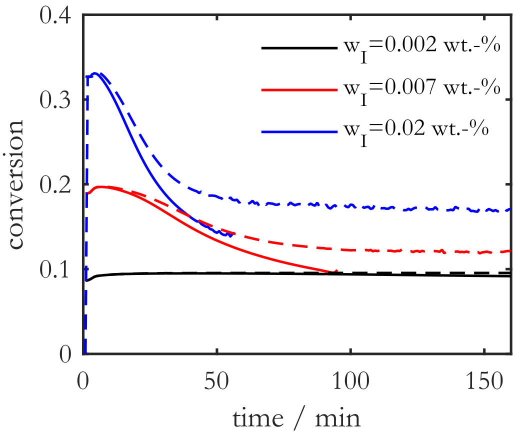

Figure 113: Monomer conversion at reactor outlet over the reaction time for different initiator concentrations at a monomer concentration of w_M=20 wt.-%. Solid lines show results with side reactions, dashed lines without.

Further, with considering side reactions the viscosity increase is steeper leading to less monomer consumption. For a monomer concentration of w_M=5 wt.-% as well as an initiator concentration of w_I=0.002 wt.-% no drop in conversion is recognizable.

In summary, it can be said that the side reactions have no influence on the timescale of the buildup and the height of the wall layer but have a strong influence on the structure of the polymers polymerized in this layer. In contrast to the experimental results from Chapter 3.1.2, the simulations predict fouling, which means a gelation of the polymers in the wall layer for an initiator content of w_I=0.002 wt.-%, whereas in the experiment there is no fouling but only wall layer formation.

6.4.4 Influence of different estimates of the diffusion coefficients

In Chapter 6.4.1 the major influence that the modeling of the diffusion model has on wall layer formation was presented. If the diffusion of the solvent/monomer against the polymer is high, no wall layer is formed. In this chapter, the influence of the modeling of the binary diffusion coefficient between polymer and solvent/monomer is presented. Equation (155) describes the status how the diffusion coefficients are scaled in the simulations and can be calculated for the reference case to $\mathfrak{D}_P = 0.014\mathfrak{D}_0$. Again, $\mathfrak{D}_0$ represents diffusive interactions between all low molecular weight species and $\mathfrak{D}_P$ diffusive interactions between all low-molecular-weight species and polymers. In Chapter 5.6 dynamic light scattering measurements to determine binary diffusion coefficients were carried out and a correlation for the binary diffusion coefficient between the polymer and the solvent depending on the molecular weight and the molar fraction was developed. Figure 114 shows the max. polymer weight fraction for both the approaches and for limiting cases of Equation (155). The polymer weight fraction as well as the max. relative viscosity (Figure 115) therefore depends very much on the choice of the diffusion coefficient. The limiting case with a very low diffusion coefficient between polymer and solvent/monomer $(\mathfrak{D}_P = 10^{-6}\mathfrak{D}_0)$ shows that extremely high polymer weight fractions and very steep gradients in viscosity are achieved. In contrast, a very high diffusion coefficient $(\mathfrak{D}_P = \mathfrak{D}_0)$ shows that no wall layer is formed. These results agree with those from Chapter 6.4.1, where high polymer diffusion ('No Polymer Friction model') resulted in no wall layer formation. The other two results lie between these limiting cases. However, it is interesting to note that the new correlation for the diffusion coefficient parameterized with the DLS measurements, are in good agreement to $\mathfrak{D}_P = 0.014\mathfrak{D}_0$. The new correlation predicts slightly lower diffusion coefficients and therefore marginally higher polymer weight fractions and viscosity.

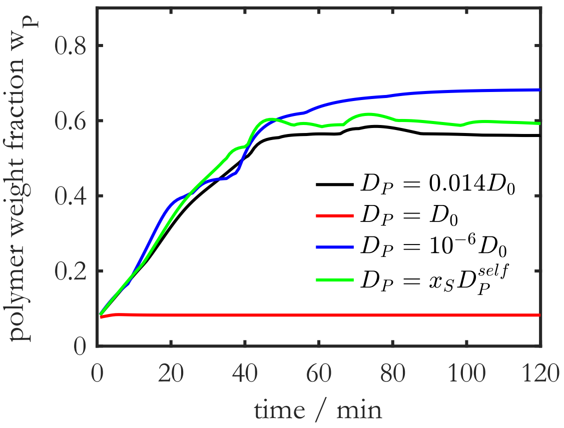

Figure 114: Max. polymer weight fraction w_P over the reaction time for a monomer concentration of w_M=20 wt.-% and an initiator concentration of w_I=0.02 wt.-% conducted with different diffusion coefficients between polymer and low molecular spezies $\mathfrak{D}_P$. $\mathfrak{D}_0$ represents diffusive interactions between all low molecular weight specie

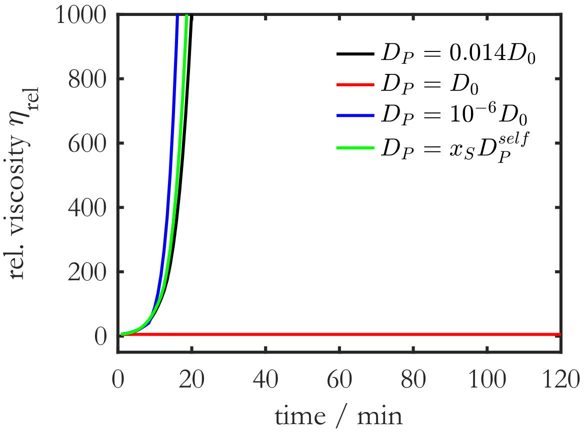

Figure 115: Max. relative viscosity η_{rel} over the reaction time for a monomer concentration of w_M=20 wt.-% and an initiator concentration of w_I=0.02 wt.-% conducted with different diffusion coefficients between polymer and low molecular spezies $\mathfrak{D}_P$. $\mathfrak{D}_0$ represents diffusive interactions between all low molecular weight specie

Figure 116 shows the residence time distributions for different injection times conducted with the new correlation for the diffusion coefficient from Chapter 5.6. A comparison with Figure 97A (left) shows that the wall layer is quite similar pronounced for all injection times.

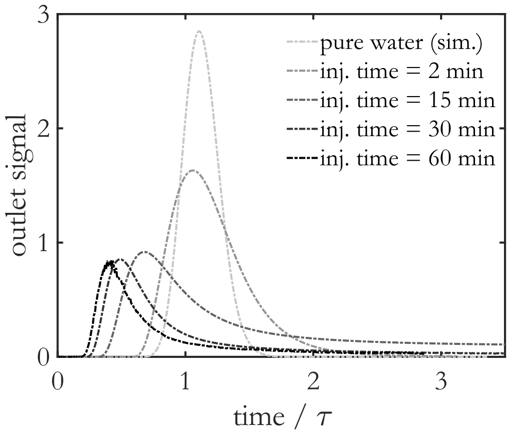

Figure 116: Residence time distributions with the Stokes-Einstein diffusion coefficient from Chapter 5.6 for a monomer concentration of w_M=20 wt.-% and an initiator concentration of w_I=0.02 wt.-%.

By measuring diffusion coefficients and the correlation from Chapter 5.6 to calculate binary diffusion coefficients, it is now possible to describe diffusion coefficients with an experimentally parameterized correlation.

6.5 CFD Simulations with PC-SAFT calculated chemical potentials

As already mentioned in Chapter 5.5, a thermodynamic description by an ideal mixture is usually insufficient for a polymer system. At the same time, it could be shown that the use of the PC-SAFT equation of state shows clear differences compared to the assumption of ideal mixture. The resulting fluxes are much higher with the PC-SAFT approach than with the ideal mixture. In this chapter, the PC-SAFT equation of state is used in a CFD simulation to calculate the driving force, i.e. the chemical potential. Equation (101) gives the following form for the driving force for Maxwell-Stefan diffusion

$$\nabla\mu_i = \nabla\left(\mu_i^0 + RT \cdot ln(x_i\gamma_i)\right) = RT\nabla\big(ln(x_i) + ln(\gamma_i)\big) = RT\big(\nabla ln(x_i) + \nabla ln(\gamma_i)\big). \quad (164)$$

Since there is currently no interface between FeOs and OpenFOAM® and a simultaneous calculation of the equation of state for each time step would be too computationally expensive, a characteristic map is generated for all possible states of the activity coefficient $\gamma_i = f(\bar{M}_w, x_P, x_M)$ using PC-SAFT. This map is then approximated using machine learning resp. a neural network (NN). Therefore, a NN with two hidden layers and 15 neurons per layer for each species was chosen to be appropriate. The trained NNs, which are matrices and vectors of weights and biases, can then be integrated into the OpenFOAM® environment, and the activity coefficients can be calculated. For a more detailed description see the Appendix A.5.3. The quality of the NNs play a very important role here, as otherwise numerical instabilities occur.

Figure 117 shows the relative viscosity η_{rel} and the polymer weight fraction $w_{P,}$ for two different reaction times. Over time, a wall layer is formed with a much lower polymer content than in Figure 100 which also influences the viscosity in this wall layer. This is because the diffusion of the polymers against the solvent is significantly higher compared to the standard case.

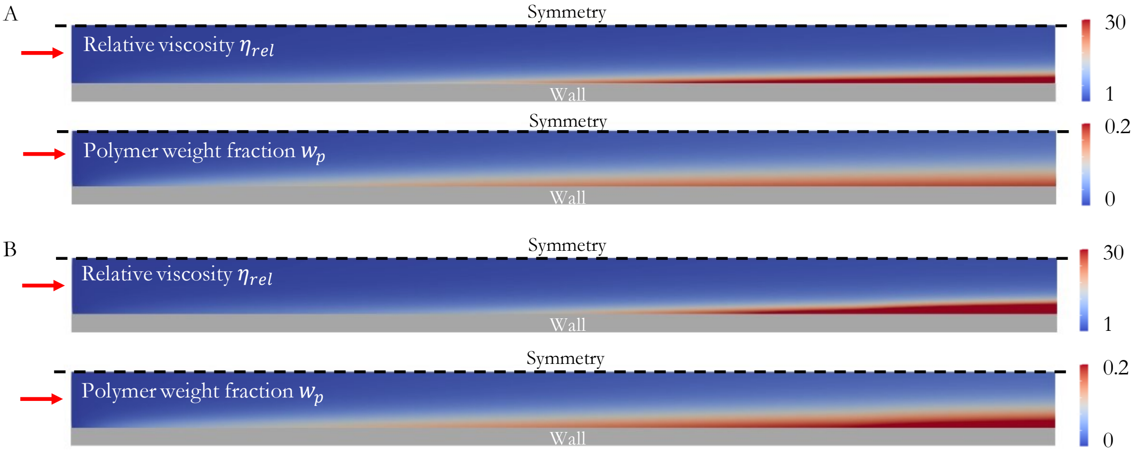

Figure 117: Simulation results for the relative viscosity η_{rel}, the polymer weight fraction w_P, and the average molecular weight M_W for two different reaction times (A: 22 min and B: 100 min reaction time) for a monomer concentration of w_M=20 wt.-% and an initiator concentration of w_I=0.02 wt.-%. Simulations conducted with PC-SAFT equation of state.

Figure 118 and 119 show the max. polymer weight fraction and the max. relative viscosity. No extreme increase in viscosity is observed due to the increased diffusion.

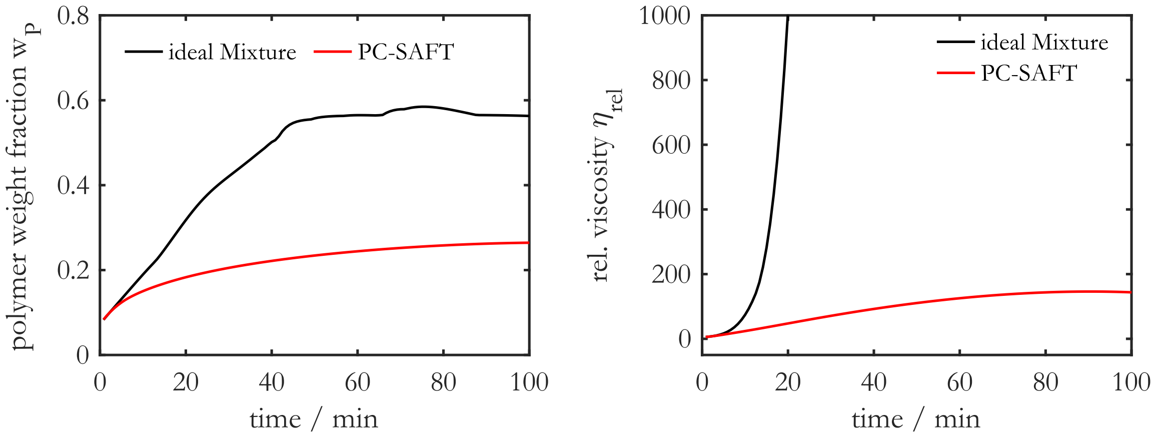

Figure 118: Max. polymer weight fraction w_P over the reaction time for a monomer concentration of w_M=20 wt.-% and an initiator concentration of w_I=0.02 wt.-% conducted with ideal Mixture and PC-SAFT.

Figure 119: Max. relative viscosity η_{rel} over the reaction time for a monomer concentration of w_M=20 wt.-% and an initiator concentration of w_I=0.02 wt.-% conducted with ideal Mixture and PC-SAFT.

Figure 120 shows the residence time distributions for different injection times conducted with PC-SAFT equation of state. Again, the wall layer is less pronounced as compared to the case of ideal mixture (Figure 97A). This is particularly evident for late injection times (30 min and 60 min). The cross-section of the reactor is less constricted, so the wall layer is smaller here.

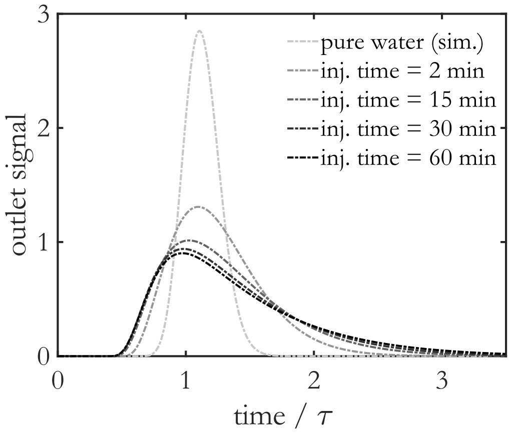

Figure 120: Residence time distributions for PC-SAFT Simulations for a monomer concentration of w_M=20 wt.-% and an initiator concentration of w_I=0.02 wt.-%.

The PC-SAFT equation of state can be used to describe a polymer system thermodynamically in a more suitable way. In this case, the diffusion is significantly greater due to the driving force of the Maxwell-Stefan diffusion which does not only depend on the molar fractions but also on the activity coefficients. To enable experimental validation of the results, the viscosity correlation and/or transport properties must be adjusted, because the system is very sensitive for small changes. No adjustments have been made here for reasons of comparability. The results presented using the PC-SAFT equation of state should therefore only be considered conceptually and not quantitatively.

6.6 Conclusions

In this chapter it could be shown how a CFD model was developed including two different transport models for polymers, a new and reliable viscosity correlation depending on polymer weight fraction and molecular weight, and the reaction kinetics. Additionally, a profound correlation for binary Maxwell-Stefan diffusion coefficients parameterized with DLS measurements could be implemented. The model was validated for different process conditions in a capillary reactor using residence time measurements, showing very good agreement for the different conditions, which vary over a large parameter space. Furthermore, different geometries of the capillary reactor were validated with good agreement.

Different influencing factors for the wall layer formation in a capillary reactor were investigated. The transport models of the polymers presented previously in Chapter 5 significantly impact the formation of the wall layer. This highly viscous layer only occurs for the "No Polymer Friction" model, indicating that no wall layer is formed for sufficiently high polymer diffusion. Different viscosity models also greatly influence the modeling of fouling processes. By making viscosity dependent on molecular weight and polymer weight fraction, wall layer formation can be reliably predicted under different process conditions. Side reactions that lead to highly branched polymers have only minor influence on the formation of the wall layer. However, if side reactions are considered, very long-chain polymers with a high molecular weight are formed. As soon as gelation begins (infinite increase in molecular weight), the simulation terminates. The calculation of the diffusion coefficient between polymer and solvent/monomer has so far mostly been estimated. By measuring the binary diffusion coefficients using DLS and subsequently parameterizing a correlation function, diffusion coefficients can be reliably calculated within the CFD depending on the molecular weight and composition. The CFD results agree very well with the previously used estimation.

By means of the novel and complete thermodynamic description of the chemical potential using PC-SAFT and subsequent approximation by a neural network, it is possible to describe a polymer system thermodynamically more reliable. This has a strong influence on the diffusive transport of the species, resulting in a less pronounced wall layer, due to the high diffusive flux. These results should be viewed more conceptually.

In summary, the special development of a CFD model including a mass transport model with the transport of polymer species plus a parameterized correlation for diffusion coefficients, 0-dimensional reaction kinetics and a viscosity model depending on polymer weight fraction and molecular weight could be presented. Using this model, a qualitatively correct and meaningful description of the fouling behavior can be made depending on process conditions and reactor geometry.

7 Conclusion and Outlook

This work provided a comprehensive investigation into fouling in continuous reactors exemplified by the radical polymerization of N-vinylpyrrolidone. Various measurement techniques, process conditions, and reactor geometries were explored experimentally. Both residence time measurements and UV/VIS spectroscopy can be used to identify the formation of deposits at an early stage, which is not possible with the pressure signal. The sound understanding of the deposition phenomena gained from the experimental results has again demonstrated the positive effect of changing the process conditions and reactor geometry on the deposition formation in tubular reactors. The use of hydrophobic coatings was identified as effective in reducing fouling, though complete prevention remained elusive. If fouling occurs, a chemical cleaning with sodium hypochlorite is favorable.

The subsequent focus on modeling fouling in a continuous reactor led to three essential contributions: the reaction kinetics, the transport of polymers and the hydrodynamics. The development of a novel detailed kinetic branching point model enabled correct dynamic simulation of branching point distributions depending on structural coordinates. Validation of the kinetic model using experimental data showed good agreement, particularly for the molecular weight distribution, monomer conversion and number of branching points.

Furthermore, the necessity of a mathematical formulation for the transport of moments of polymer distributions in CFD simulations was investigated in this work. Two limiting cases of the Maxwell-Stefan diffusion provided suitable solutions for respective use cases which depend on polymer content, average chain length, degree of branching, and molecular weight. The use of the PC-SAFT equation of state to describe the driving force was emphasized as thermodynamically more suitable. The solution for this therefore differs significantly from the ideal mixture due to an increased diffusive transport. A reliable description of the binary diffusion coefficient between polymer and solvent/monomer could be developed using dynamic light scattering measurements.

The interplay between hydrodynamics, kinetics and transport of the polymers could be investigated using a self-developed CFD model. For this purpose, both transport models for polymer diffusion, the developed reaction kinetics, a specially parameterized viscosity relationship depending on the polymer weight fraction and the molecular weight and a profound correlation for binary Maxwell-

Stefan diffusion coefficients parameterized with DLS measurements were integrated into the CFD model. The model was successfully validated for different process conditions and geometries by means of experimental residence time measurements in the capillary reactor. When investigating the factors that influence the formation of wall layers, the study showed the significant influence of viscosity models and provided insights into the influence of side reactions on the polymer properties. Furthermore, the description of the diffusion coefficients between polymer and solvent/monomer has a very large influence. The PC-SAFT equation of state can be used to calculate a map of thermodynamic states, which is then approximated with a neural network and implemented in OpenFOAM®. A thermodynamic description via the PC-SAFT equation of state increases the diffusive transport.

In summary, the comprehensive investigation carried out in this thesis provides valuable insights into experimental fouling behavior, polymerization kinetics and transport models. The combination of these enables the development of a complete model for predicting fouling in continuous reactors. This has paved the way for a more accurate and predictive understanding of continuous reactor systems. At the same time, the combination of experimental findings and advanced modelling approaches sets the stage for future advances in optimizing reactor performance and mitigating fouling problems in industrial processes.

Different processes (diffusion, adsorption, or surface arrangements) take place on different time scales at the interface of the reactor wall, and these are dominated by different driving forces. The observation and description of the interface between the reactor wall and the reaction medium should therefore be of particular importance for future research, as attached polymers form the basis for subsequent gel formation. However, the kinetic energy introduced from outside is of great importance to increase the "shearing" of the polymers.

Literature

[1] D. Kohlmann *et al.*, "Modular, Flexible, and Continuous Plant for Radical Polymerization in Aqueous Solution," *Macromol. React. Eng.*, vol. 10, no. 4, pp. 339–353, 2016, doi: 10.1002/mren.201500079.

[2] J. Urrutia and J. M. Asua, "Reactor Fouling in Emulsion Polymerization," *Ind. Eng. Chem. Res.*, vol. 60, no. 29, pp. 10502–10510, 2021, doi: 10.1021/acs.iecr.1c00097.

[3] S. Fries, "Modelling of Fouling Mechanisms in the LDPE Synthesis," Technical University of Darmstadt, 2019.

[4] J. Urrutia, A. Peña, and J. M. Asua, "Reactor Fouling by Preformed Latexes," *Macromol. React. Eng.*, vol. 11, no. 1, p. 1600043, Feb. 2017, doi: 10.1002/mren.201600043.

[5] P. Deglmann, M. Hellmund, K. Hungenberg, U. Nieken, C. Schwede, and C. Zander, "Side Reactions in Aqueous Phase Polymerization of N -Vinyl-Pyrrolidone as Possible Source for Fouling," *Macromol. React. Eng.*, p. 1900021, Aug. 2019, doi: 10.1002/mren.201900021.

[6] C. Zander, K. D. Hungenberg, T. Schall, C. Schwede, and U. Nieken, "Modeling Strategies for the Propagation of Terminal Double Bonds During the Polymerization of N-Vinylpyrrolidone and Experimental Validation," *Macromol. React. Eng.*, vol. 14, no. 3, 2020, doi: 10.1002/mren.202000009.

[7] C. Zander, "Fouling during solution polymerization in continuously operated reactors," Universität Stuttgart, 2021.

[8] A. Pistone, C. Scolaro, and A. Visco, "Mechanical properties of protective coatings against marine fouling: A review," *Polymers (Basel).*, vol. 13, no. 2, pp. 1–19, 2021, doi: 10.3390/polym13020173.

[9] S. N. Kazi, G. G. Duffy, and X. D. Chen, "Fouling and Fouling Mitigation on Different Heat Exchanging," *Proc. Int. Conf. Heat Exch. Fouling Clean. VIII - 2009*, vol. 2009, pp. 367–377, 2009.

[10] R. Jradi, C. Marvillet, and M. Razak Jeday, “Fouling in Industrial Heat Exchangers: Formation, Detection and Mitigation,” in *Heat Transfer - Fundamentals, Enhancement and Applications*, IntechOpen, 2023. doi: 10.5772/intechopen.102487.

[11] Z. Qu *et al.*, “Methodology for removing fouling within liquid-filled pipelines based on ultrasonic guided waves cavitation effect,” *Appl. Acoust.*, vol. 157, p. 107018, 2020, doi: 10.1016/j.apacoust.2019.107018.

[12] S. Gupta, H. Gomaa, and M. B. Ray, “Fouling control in a submerged membrane reactor: Aeration vs membrane oscillations,” *Chem. Eng. J.*, vol. 432, no. October 2021, p. 134399, 2022, doi: 10.1016/j.cej.2021.134399.

[13] C. Bernstein, *Methoden zur Untersuchung der Belagsbildung in chemischen Reaktoren*. Hamburg: Universität Hamburg, 2017.

[14] S. Fries, D. M. Castañeda-Zúñiga, J. Duchateau, P. Neuteboom, C. T. Porras, and M. Busch, “Fouling in the High Pressure LDPE Process: Experimental and Computational Investigation Approach,” *Macromol. Symp.*, vol. 360, no. 1, pp. 78–86, 2016, doi: 10.1002/masy.201500112.

[15] M. Hellmund, “Kinetik und Modellierung der kontinuierlichen Polymerisation von N-Vinylpyrrolidon,” University of Stuttgart, 2020.

[16] C. Kiparissides, “On the Elucidation of Polymer Fouling Mechanisms and Ethylene Decomposition in High-Pressure LDPE Tubular Reactors,” *Macromol. React. Eng.*, vol. 16, no. 6, pp. 1–26, 2022, doi: 10.1002/mren.202200023.

[17] A. Hohlen, W. Augustin, and S. Scholl, “Quantification of Polymer Fouling on Heat Transfer Surfaces During Synthesis,” *Macromol. React. Eng.*, vol. 14, no. 1, 2020, doi: 10.1002/mren.201900035.

[18] A. Böttcher *et al.*, “Fouling Pathways in Emulsion Polymerization Differentiated with a Quartz Crystal Microbalance (QCM) Integrated into the Reactor Wall,” *Macromol. React. Eng.*, vol. 16, no. 2, p. 2100045, Apr. 2022, doi: 10.1002/mren.202100045.

[19] M. Osenberg *et al.*, “Ultrasound Sensor for Process and Fouling Monitoring in Emulsion Polymerization Processes,” in *2022 IEEE Sensors*, Oct. 2022, vol. 2022-Octob, pp. 1–4. doi: 10.1109/SENSORS52175.2022.9967228.

[20] N. Zhang, M. A. Halali, and C. F. de Lannoy, "Detection of fouling on electrically conductive membranes by electrical impedance spectroscopy," *Sep. Purif. Technol.*, vol. 242, no. November 2019, p. 116823, 2020, doi: 10.1016/j.seppur.2020.116823.

[21] F. Gao, L. Wang, H. Zhang, and J. Wang, "Realtime and in-situ monitoring of membrane fouling with fiber-optic reflectance UV-vis spectrophotometry (FORUS)," *Chem. Eng. J. Adv.*, vol. 4, no. October, p. 100058, 2020, doi: 10.1016/j.ceja.2020.100058.

[22] N. Movsesian, S. Hirth, J. Speros, and M. Gupta, "Robust Vapor-Deposited Antifouling Fluoropolymer Coatings for Stainless Steel Polymerization Reactor Components," *Ind. Eng. Chem. Res.*, vol. 59, no. 34, pp. 15264–15270, 2020, doi: 10.1021/acs.iecr.0c02646.

[23] F. Wang, H. Zhang, B. Yu, S. Wang, Y. Shen, and H. Cong, "Review of the research on anti-protein fouling coatings materials," *Prog. Org. Coatings*, vol. 147, no. July, p. 105860, 2020, doi: 10.1016/j.porgcoat.2020.105860.

[24] Y. Higaki, M. Kobayashi, D. Murakami, and A. Takahara, "Anti-fouling behavior of polymer brush immobilized surfaces," *Polym. J.*, vol. 48, no. 4, pp. 325–331, 2016, doi: 10.1038/pj.2015.137.

[25] J. H. Jhaveri and Z. V. P. Murthy, "A comprehensive review on anti-fouling nanocomposite membranes for pressure driven membrane separation processes," *Desalination*, vol. 379, pp. 137–154, 2016, doi: 10.1016/j.desal.2015.11.009.

[26] N. Gottschalk, J. C. Kuschnerow, H. Föste, W. Augustin, and S. Scholl, "Experimental investigation on fouling of a polymer dispersion on modified surfaces," *Chemie-Ingenieur-Technik*, vol. 87, no. 5, pp. 600–608, 2015, doi: 10.1002/cite.201400126.

[27] W. Benzinger, U. Schygulla, M. Jäger, and K. Schubert, "Anti Fouling Investigations With Ultrasound in a Microstructured Heat Exchanger," *Proc. 6th Int. Conf. Heat Exch. Fouling Clean. - Challenges Oppor.*, 2005.

[28] F. S. Rohman *et al.*, "Nonlinear Control of Fouling in Polyethylene Reactors," *ACS Omega*, vol. 7, no. 44, pp. 39648–39661, 2022, doi: 10.1021/acsomega.2c03078.

[29] A. Gul, J. Hruza, and F. Yalcinkaya, "Fouling and chemical cleaning of microfiltration membranes: A mini-review," *Polymers (Basel).*, vol. 13, no. 6, 2021, doi: 10.3390/polym13060846.

[30] K.-D. Hungenberg and M. Wulkow, *Modeling and Simulation in Polymer Reaction Engineering*. Weinheim, Germany: Wiley-VCH Verlag GmbH & Co. KGaA, 2018. doi: 10.1002/9783527685738.

[31] S. Schwarz, T. Frey, M. Hoffmann, M. Grünewald, and M. Schlüter, "CFD-Based Compartment Modeling of Continuous Polymer Reactors in Milli-Structured Apparatuses by Use of the Mean Age Theory," *Ind. Eng. Chem. Res.*, vol. 62, no. 31, pp. 12109–12119, 2023, doi: 10.1021/acs.iecr.3c00947.

[32] D. W. Van Krevelen and K. Te Nijenhuis, *Properties of Polymers*. Elsevier, 2009. doi: 10.1016/B978-0-08-054819-7.00027-3.

[33] M. Rubinstein and R. H. Colby, *Polymer physics*. Oxford: Oxford University Press, 2003.

[34] S. Podzimek, *Light Scattering, Size Exclusion Chromatography and Asymmetric Flow Field Flow Fractionation: Powerful Tools for the Characterization of Polymers, Proteins and Nanoparticles*. Hoboken, NJ, USA: John Wiley & Sons, Inc., 2011. doi: 10.1002/9780470877975.

[35] P. D. Iedema and H. C. J. Hoefsloot, "Predicting molecular weight and degree of branching distribution of polyethylene for mixed systems with a constrained geometry metallocene catalyst in semibatch and continuous reactors," *Macromolecules*, vol. 36, no. 17, pp. 6632–6644, Aug. 2003, doi: 10.1021/ma034405q.

[36] T. Meyer and J. T. F. F. Keurentjes, *Handbook of Polymer Reaction Engineering*. Weinheim, Germany: Wiley, 2005. doi: 10.1002/9783527619870.

[37] U. Ritgen, *Analytische Chemie I*. Berlin, Heidelberg: Springer Berlin Heidelberg, 2019. doi: 10.1007/978-3-662-60495-3.

[38] B. Hosemann, "Kinetik von Verzweigungsreaktionen in der VDF / HFP Copolymerisation," Technische Universität Clausthal, 2017.

[39] B. H. Zimm and W. H. Stockmayer, "The dimensions of chain molecules containing branches and rings," *J. Chem. Phys.*, vol. 17, no. 12, pp. 1301–1314, 1949, doi: 10.1063/1.1747157.

[40] J. Stetefeld, S. A. McKenna, and T. R. Patel, "Dynamic light scattering: a practical guide and applications in biomedical sciences," *Biophys. Rev.*, vol. 8, no. 4, pp. 409–427, 2016, doi: 10.1007/s12551-016-0218-6.

[41] B. J. Berne and R. Pecora, *Dynamic Light Scattering: With Applications to Chemistry, Biology, and Physics*. New York: Dover Publications, 2000.

[42] J. Gross and G. Sadowski, "Perturbed-Chain SAFT: An Equation of State Based on a Perturbation Theory for Chain Molecules," pp. 1244–1260, 2001.

[43] J. Gross and G. Sadowski, "Application of the Perturbed-Chain SAFT Equation of State to Associating Systems," *Ind. Eng. Chem. Res.*, vol. 41, no. 22, pp. 5510–5515, Oct. 2002, doi: 10.1021/ie010954d.

[44] P. Rehner, G. Bauer, and J. Gross, "FeOs: An Open-Source Framework for Equations of State and Classical Density Functional Theory," *Ind. Eng. Chem. Res.*, vol. 62, no. 12, pp. 5347–5357, 2023, doi: 10.1021/acs.iecr.2c04561.

[45] A. Tihic, G. M. Kontogeorgis, N. Von Solms, and M. L. Michelsen, "A predictive group-contribution simplified PC-SAFT equation of state: Application to polymer systems," *Ind. Eng. Chem. Res.*, vol. 47, no. 15, pp. 5092–5101, 2008, doi: 10.1021/ie0710768.

[46] W. Reppe, "Vinylierung," *Justus Liebigs Ann. Chem.*, vol. 601, no. 1, pp. 81–138, Dec. 1956, doi: 10.1002/jlac.19566010106.

[47] C. E. Schildknecht, "Vinyl and Related Polymers," *Monograph*, pp. 1–723, 1952.

[48] G. R. Sunkara, M. M. Tadavarthi, V. K. Tadekoru, S. K. Tadikonda, and S. R. Bezawada, "Density, refractive index, and speed of sound of the binary mixture of 1-butyl-3-methylimidazolium tetrafluoroborate + N -vinyl-2-pyrrolidinone from T = (298.15 to 323.15) K at atmospheric pressure," *J. Chem. Eng. Data*, vol. 60, no. 3, pp. 886–894, 2015, doi: 10.1021/je500936y.

[49] A. Prudic, Y. Ji, C. Luebbert, and G. Sadowski, "Influence of humidity on the phase behavior of API/polymer formulations," *Eur. J. Pharm. Biopharm.*, vol. 94, pp. 352–362, 2015, doi: 10.1016/j.ejpb.2015.06.009.

[50] P. Rehner and J. Gross, "Multiobjective Optimization of PCP-SAFT Parameters for Water and Alcohols Using Surface Tension Data," *J. Chem. Eng. Data*, vol. 65, no. 12, pp. 5698–5707, 2020, doi: 10.1021/acs.jced.0c00684.

[51] R. Privat, J. N. Jaubert, and Y. Privat, "A simple and unified algorithm to solve fluid phase

equilibria using either the gamma-phi or the phi-phi approach for binary and ternary mixtures," *Comput. Chem. Eng.*, vol. 50, pp. 139–151, 2013, doi: 10.1016/j.compchemeng.2012.11.006.

[52] S.-C. Wang, "Artificial Neural Network," in *Interdisciplinary Computing in Java Programming*, Boston, MA: Springer US, 2003, pp. 81–100. doi: 10.1007/978-1-4615-0377-4_5.

[53] E. Spoor, S. Welzel, U. Nieken, and M. Rädle, "UV/VIS-Spectroscopic Inline Measurement for the Detection of Fouling Processes during the Polymerization of N-Vinylpyrrolidone," *Reactions*, vol. 4, no. 1, pp. 176–188, Mar. 2023, doi: 10.3390/reactions4010011.

[54] V. Neßlinger, S. Welzel, F. Rieker, D. Meinderink, U. Nieken, and G. Grundmeier, "Thin Organic-Inorganic Anti-Fouling Hybrid-Films for Microreactor Components," *Macromol. React. Eng.*, vol. 17, no. 1, p. 2200043, Feb. 2023, doi: 10.1002/mren.202200043.

[55] R. F. Cournoyer and S. Siggia, "Interaction of Polyvinylpyrrolidone and Iodine.," *J Polym Sci Part A-1 Polym Chem*, vol. 12, no. 3, pp. 603–612, 1974, doi: 10.1002/pol.1974.170120311.

[56] S. Siggia, "The Chemistry of Polyvinylpyrrolidone-Iodine**General Aniline and Film Corporation, Easton, Pa.," *J. Am. Pharm. Assoc. (Scientific ed.)*, vol. 46, no. 3, pp. 201–204, Mar. 1957, doi: 10.1002/jps.3030460317.

[57] I. Sebe *et al.*, "Polymer structure and antimicrobial activity of polyvinylpyrrolidone-based iodine nanofibers prepared with high-speed rotary spinning technique," *Int. J. Pharm.*, vol. 458, no. 1, pp. 99–103, 2013, doi: 10.1016/j.ijpharm.2013.10.011.

[58] I. M. Wienk, E. E. B. Meuleman, Z. Borneman, T. van den Boomgaard, and C. A. Smolders, "Chemical treatment of membranes of a polymer blend: Mechanism of the reaction of hypochlorite with poly(vinyl pyrrolidone)," *J. Polym. Sci. Part A Polym. Chem.*, vol. 33, no. 1, pp. 49–54, 1995, doi: 10.1002/pola.1995.080330105.

[59] M. Stach *et al.*, "Propagation Rate Coefficient for Radical Polymerization of N -Vinyl Pyrrolidone in Aqueous Solution Obtained by PLP−SEC," *Macromolecules*, vol. 41, no. 14, pp. 5174–5185, Jul. 2008, doi: 10.1021/ma800354h.

[60] L. Uhelská, D. Chorvát, R. A. Hutchinson, S. Santanakrishnan, M. Buback, and I. Lacík, "Radical Propagation Kinetics of N -Vinylpyrrolidone in Organic Solvents Studied by Pulsed-Laser Polymerization-Size-Exclusion Chromatography (PLP-SEC)," *Macromol. Chem. Phys.*,

vol. 215, no. 23, pp. 2327–2336, Dec. 2014, doi: 10.1002/macp.201400329.

[61] J. Schrooten, M. Buback, P. Hesse, R. A. Hutchinson, and I. Lacík, *Termination kinetics of 1−vinylpyrrolidin−2−one radical polymerization in aqueous solution*, vol. 212, no. 13. p. 1400−1409. doi: 10.1002/macp.201100021.

[62] S. Santanakrishnan *et al.*, *Kinetics and modeling of batch and semibatch aqueous−phase NVP free−radical polymerization*, vol. 4, no. 8. p. 499−509. doi: 10.1002/mren.201000007.

[63] F. Haaf, A. Sanner, and F. Straub, "Polymers of N-Vinylpyrrolidone: Synthesis, Characterization and Uses," *Polym. J.*, vol. 17, no. 1, pp. 143–152, Jan. 1985, doi: 10.1295/polymj.17.143.

[64] J. Schrooten, M. Buback, P. Hesse, R. A. Hutchinson, and I. Lacík, "Termination kinetics of 1-vinylpyrrolidin-2-one radical polymerization in aqueous solution," *Macromol. Chem. Phys.*, vol. 212, no. 13, pp. 1400–1409, Jul. 2011, doi: 10.1002/macp.201100021.

[65] P. D. Iedema, M. Wulkow, and H. C. J. Hoefsloot, "Modeling molecular weight and degree of branching distribution of low-density polyethylene," *Macromolecules*, vol. 33, no. 19, pp. 7173–7184, 2000, doi: 10.1021/ma991711o.

[66] J. Randall, "A Review of High Resolution Liquid Nuclear Magnetic Resonance Characterizations of Ethylene-Based Polymers," *J. Macromol. Sci. Part C*, vol. 29, no. 2–3, pp. 201–317, 1989, doi: 10.1080/07366578908055172.

[67] D. J. Arriola, "Modeling of Addition Polymerization Systems," University of Wisconsin, 1989.

[68] W. Säckel and U. Nieken, "Modellierung reaktiver Sprühtrocknungsprozesse am Beispiel der Sprühpolymerisation," *Chemie-Ingenieur-Technik*, vol. 86, no. 4, pp. 438–448, 2014, doi: 10.1002/cite.201300148.

[69] W. Säckel and U. Nieken, "Structure Formation within Spray-Dried Droplets; Mathematical Modelling of Spray Polymerisation," in *Process-Spray*, Cham: Springer International Publishing, 2016, pp. 89–125. doi: 10.1007/978-3-319-32370-1_3.

[70] K. Franke, H.-U. Moritz, and W. Pauer, "Beeinflussung der Eigenschaften von Sprühpolymerisationsprodukten," *Chemie Ing. Tech.*, vol. 89, no. 4, pp. 490–495, Apr. 2017,

doi: 10.1002/cite.201600141.

[71] M. Wulkow, "The simulation of molecular weight distributions in polyreaction kinetics by discrete Galerkin methods," *Macromol. Theory Simulations*, vol. 5, no. 3, pp. 393–416, May 1996, doi: 10.1002/mats.1996.040050303.

[72] R. B. Bird, W. E. Stewart, and E. . Lightfoot, "Transport phenomena," *Appl. Mech. Rev.*, vol. 55, no. 1, pp. R1–R4, Jan. 2002, doi: 10.1115/1.1424298.

[73] R. Taylor and R. Krishna, "MULTICOMPONENT MASS TRANSFER," in *Multicomponent Diffusion*, Elsevier, 1976, pp. 141–154. [Online]. Available: https://linkinghub.elsevier.com/retrieve/pii/B9780444413260500149

[74] G. Sadowski, *Polymer Thermodynamics*, vol. 238. Berlin, Heidelberg: Springer Berlin Heidelberg, 2011. doi: 10.1007/978-3-642-17682-1.

[75] R. Stierle and J. Gross, "Hydrodynamic density functional theory for mixtures from a variational principle and its application to droplet coalescence," *J. Chem. Phys.*, vol. 155, no. 13, 2021, doi: 10.1063/5.0060088.

[76] L. S. Darken, "Diffusion, mobility and their interrelation through free energy in binary metallic systems," *Trans. Met. Soc. Aime*, vol. 175, p. 184, 1948, [Online]. Available: https://xlink.rsc.org/?DOI=tf9484400184

[77] S. Sridhar, "A commentary on 'diffusion, mobility and their interrelation through free energy in binary metallic systems,' L.S. Darken: Trans. AIME, 1948, vol. 175, p. 184ff," *Metall. Mater. Trans. A Phys. Metall. Mater. Sci.*, vol. 41, no. 3, pp. 543–562, 2010, doi: 10.1007/s11661-010-0177-7.

[78] M. Holz, S. R. Heil, and A. Sacco, "Temperature-dependent self-diffusion coefficients of water and six selected molecular liquids for calibration in accurate 1H NMR PFG measurements," *Phys. Chem. Chem. Phys.*, vol. 2, no. 20, pp. 4740–4742, 2000, doi: 10.1039/b005319h.

[79] M. F. Cunningham, H. K. Mahabadi, and K. F. O'Driscol, "Bulk polymerization in tubular reactors iii. Modelling fouling behaviour," *Polym. React. Eng.*, vol. 1, no. 2, pp. 245–287, 1993, doi: 10.1080/10543414.1992.10744431.

[80] S. Welzel, W. Säckel, and U. Nieken, "Modeling of Diffusive Transport of Polymers Moments Using Limiting Cases of the Maxwell–Stefan Model," *Macromol. React. Eng.*, vol. 17, no. 1, p. 2200045, Feb. 2023, doi: 10.1002/mren.202200045.

[81] S. Welzel, J. Burmeister, O. Höppchen, and U. Nieken, "Validation of an Extended Kinetic Model of Free-Radical N -Vinylpyrrolidone Polymerization," *Macromol. React. Eng.*, vol. 2200075, p. 2200075, Feb. 2023, doi: 10.1002/mren.202200075.

[82] S. Welzel, C. Zander, and U. Nieken, "Wall Layer Formation in Continuously Operated Tubular Reactors for Free-Radical Polymerizations," *Chemie Ing. Tech.*, vol. 95, no. 5, pp. 642–650, May 2023, doi: 10.1002/cite.202200195.

[83] W. W. Parson, *Modern Optical Spectroscopy*. 2015. doi: 10.1007/978-3-662-46777-0.

[84] J. N. Israelachvili, *Intermolecular and Surface Forces*. Elsevier, 2011. doi: 10.1016/C2011-0-05119-0.

[85] S. Welzel and U. Nieken, "Fouling During Polymerization in Different Continuous Reactor Setups," *Chemie-Ingenieur-Technik*, no. 0, pp. 1–10, 2024, doi: 10.1002/cite.202400086.

[86] S. Welzel, C. Zander, K. Hungenberg, and U. Nieken, "Modeling of the Branching Point Distribution During the Polymerization of N -Vinylpyrrolidone," *Macromol. React. Eng.*, vol. 16, no. 4, p. 2200005, Aug. 2022, doi: 10.1002/mren.202200005.

Appendix

A.1 Experimental and analytical setup

This chapter in the appendix of this thesis gives additional information about the used experimental and analytical setup to determine the shown results in the main text.

A.1.1 Materials

BASF SE provided N-vinylpyrrolidone that had been stabilized with 0.5% NaOH and was then purified by distillation under vacuum to eliminate the stabilizer and high-molecular components. Unstabilized NVP was frozen directly after distillation and defrosted just before the experiments. The initiator (V-50, Wako Chemicals) was used as given after being kept in the refrigerator. As a solvent, deionized water has been employed.

Sodium hypochlorite solution (12% Cl, stabilized, technical) was used as supplied by Carl Roth GmbH + Co. KG.

A.1.2 Further equipment for polymerization reactions

A.1.2.1 Experimental setup for polymerization reactions in a CSTR reactor

The CSTR experiments to validate the kinetic model were carried out in [6] isothermally at T=85 °C in a 650 ml Juchheim stirred tank reactor made of stainless steel. Figure 121 shows a simplified flow sheet of the setup for the tank reactor experiments. A mixture of monomer and solvent was prepared for one storage container, and the initiator, which had been dissolved in the solvent, was prepared for the other. Both containers were degassed under vacuum. Throughout the entire experiment, the storage container was flushed by argon to prevent oxygen from entering. Two Knauer HPLC piston pumps were used to pump the feed streams, and Bronkhorst Coriolis mass flow meters and PI controllers were used to control the flow rates. Before entering the reactor, the feed streams from both tanks were mixed in a 1:1 ratio using a static T-piece with 0.5 mm thru-holes and a 10 μm frit in the center port.

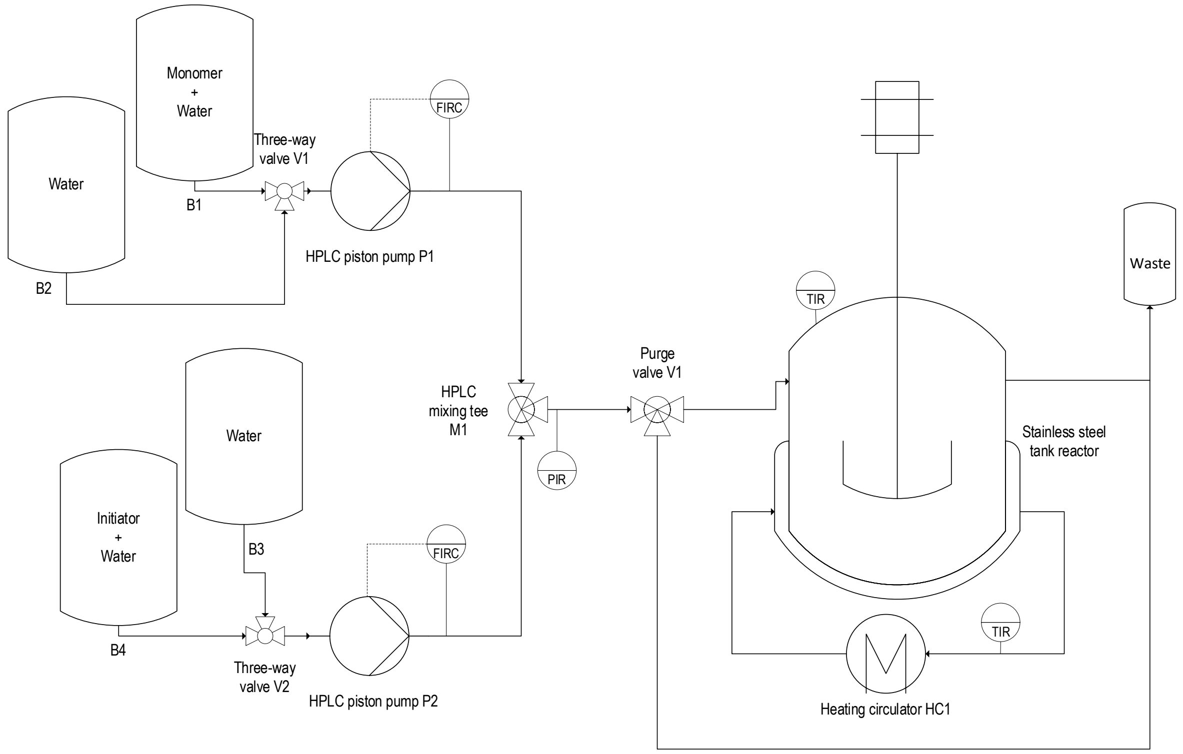

Figure 121: Simplified flow sheet of the setup for CSTR experiments [6].

A.1.3 Analytical setup for polymer characterization [81]

Monomer conversion was determined by HPLC measurements using an Agilent 1260 series setup, a mixture of water and acetonitrile (90:10) as an eluent at 0.5 ml min^{-1} flow rate. 3 µl was the injection volume. A Poroshell 120EC-C18 column was used for separation, UV adsorption was measured at 235 nm. The results of three injections were averaged. Molecular weight averages and distributions as well as the radius of gyration are determined from GPC on a setup delivered by PSS (Polymer Standard Service, Mainz, Germany) using DMAc with 5 g l^{-1} LiBr as eluent at 0.8 ml min^{-1}. For separation a column set containing a 100 Å column and two columns with 100000 Å pore size (GRAM ultrahigh columns set) have been used. As a concentration sensitive detector, the refractive index was measured by an Agilent 1260 Infinity II detector. The PSS SLD7100 multi-angle light scattering detector was used as a molar sensitive detector. Combining both signals allow to obtain absolute molecular weight averages and distributions. The data has been recorded using the WinGPC software. Since it was not possible to carry out structural analysis with WinGPC due to non-adjustable filters, the raw data of the detector was processed by a self-written Matlab® code [7]. The weight average molecular weight was directly calculated from the detector data. To obtain the molecular weight distributions, a linear approximation of the measured calibration curve was used where only molecular weights above 100 kg mol^{-1} were considered. Since the molecular weight averages and distributions as well as the conformation plot are strongly influenced by the anchoring effect [34], which means that parts of large branched polymers can behave as independent, enter pores and anchor the entire molecules. Those are delayed and elute at higher elution volumes than their corresponding hydrodynamic volume. For comparison the CSTR samples were additionally measured at BASF SE using FFF. For this, the Asymmetrical Flow Field-Flow Fractionation (AF4) system (Eclipse separation system AF4, Wyatt Technology, USA) with a trapezoidal channel with a nominal thickness of 350 μm (Spacer W350 μm, Wyatt Technology, USA) was used. The channel was equipped with a membrane of regenerated cellulose with 10 kDa cutoff (PLGC, Reg. Cellulose 10 kD, Millipore, USA). The AF4 was coupled with a UV detector (DAD 1290 Infinity II, Agilent Technologies), a multi-angle light scattering detector (MALS, Dawn Heleos-II, Wyatt Technology, USA), and a differential refractive index (dRI) detector (Optilab T-rEX, Wyatt Technology, USA). The AF4 data were analyzed using Astra software, version 7.3 (Wyatt Technology, USA). A refractive index of PVP in water of dn/dc = 0.173 ml/g was used to calculate the molar mass.

A.1.4 Analytical setup for DLS measurements

Using a 3D LS Spectrometer (LS Instruments, Switzerland), dynamic light scattering (DLS) studies were captured. A diode-pumped laser with a wavelength of λ = 561 nm (Cobolt, Sweden) is installed in the spectrometer. Decalin serves as the index matching fluid, and a thermostat (Julabo, Germany) controls the decaling bath's temperature to maintain a measurement temperature of T = (25.0 ± 0.1, 40.0± 0.1 and 55.0± 0.1) °C. Test tubes made of borosilicate (Fisher Scientific, USA) were filled with the polymer samples. The different intensities of the incident laser ($I_{0,max} \approx$ 81 mW) were utilized to get clear detector count rates. The measurement methodology involved five 15-second repeats for each of the desired scattering angles, which ranged from 30 ° to 140 °.

A.1.5 Analytical setup for viscosity measurement of Kollidon-water mixtures

The measurements were carried out on a rheometer (MCR 302, Anton Paar GmbH, Graz, Austria) in the shear rate range from 0.1 s^{-1} to 100 s^{-1}. A cylinder geometry with a diameter of 27 mm was used. 6 points per decade were recorded with a measurement point duration of 20 s. For the highly viscous samples, a cylinder geometry with a diameter of 11 mm was used. To prevent evaporation of the sample, the samples were coated with a thin layer of low-viscosity kerosene oil before starting the measurement.

A.2 Further Experimental findings

A.2.1 Residence time distributions for further different process conditions

In addition to the residence time measurements presented in Chapter 3.1, further process conditions were tested, which are presented below.

In Figure 122 the area normalized response signal for w_M=10 wt.-% and w_I=0.02 wt.-% can be seen. The breakthrough of the tracer does not occur as strongly at earlier times as in the w_M=20 wt.-% and w_I=0.02 wt.-% example, but the tailing is pronounced at later operating times. An operating time of 72 h was possible under these process conditions and from an operating time of 24 h the residence time distribution becomes unstable, as gel formation takes place from this time onwards. At the same time, it can be observed that the signal no longer changes after this operating time. After the experiment, the reactor was rinsed with water and a signal was recorded again, with the result that the original water signal cannot be achieved again, but the reactor has significantly less polymer on the walls compared to the example with w_M=20 wt.-%.

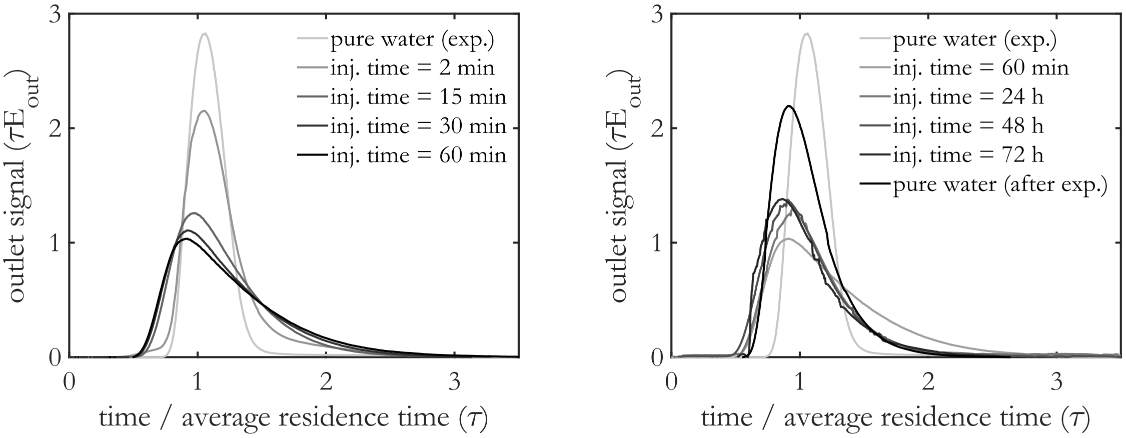

Figure 122: Evolution of the area-normalized response signal E_{out} at different times for w_M=10 wt.-% and w_I=0.02 wt.-%.

In Figure 123, on the other hand, the area normalized response signal of a different feed initiator concentration with w_I=0.007 wt.-% and w_M=20 wt.-% is shown. Up to an operating time of 60 min, the breakthrough of the tracer occurs at an earlier point in time and the tailing becomes larger. Compared to w_M=10 wt.-% and w_I=0.02 wt.-%, this behavior is more pronounced. In the further course of the experiment, the residence time distribution still changes strongly after 60 min - 48 h. This suggests that an already formed wall layer is detaching or growing up again.

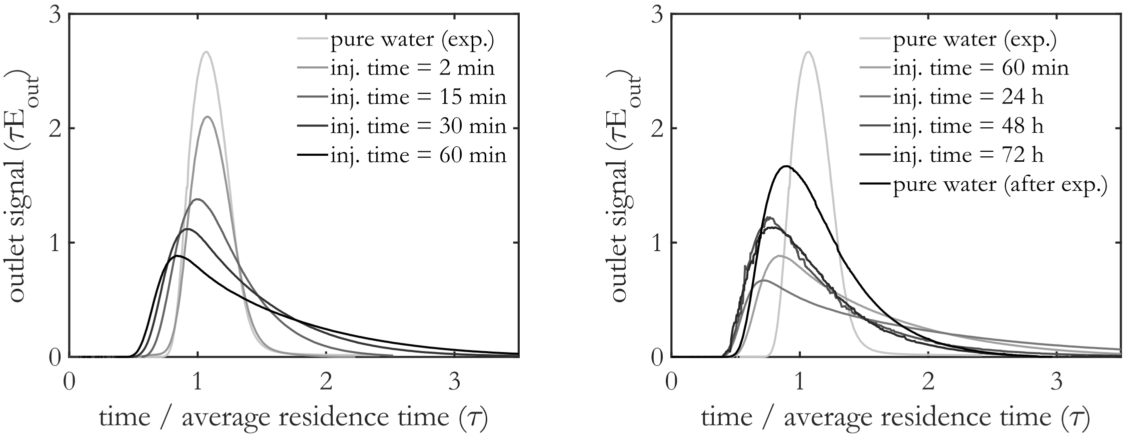

Figure 123: Evolution of the area-normalized response signal E_{out} at different times for w_M=20 wt.-% and w_I=0.007 wt.-%.

A.2.2 Residence time distributions in an ultrasonic thermal bath

In addition to different process conditions and geometries of the capillary reactor, the application of ultrasonic waves on the fouling behavior was investigated. For this purpose, a standard capillary reactor with a length of l=3000 mm and an inner diameter of d_i=1.76 mm was placed in an Emmi Emag 420-HC ultrasonic bath during polymerization. The bath has an ultrasonic power of 1500 W with a 12 PZT Wide beam oscillating system and a frequency of 28 kHz. Process conditions of monomer feed concentration w_M=20 wt.-% and initiator feed concentration w_I=0.02 wt.-% were used. Unfortunately, a reactor temperature of T=80 °C could only be used because the ultrasonic bath is limited to that temperature. In Figure 124 the evolution of the area-normalized response signal at different injection times is shown. A wall layer forms in the capillary reactor despite the use of ultrasonic waves. Due to the slightly lower temperature compared to Figure 11, the peak of the tracer is not so strongly shifted to earlier times. Compared to operation without ultrasound, the residence time distributions for operating times (>60 min) are significantly calmer. This indicates that although a highly viscous wall layer is formed, no gelation of this wall layer takes place.

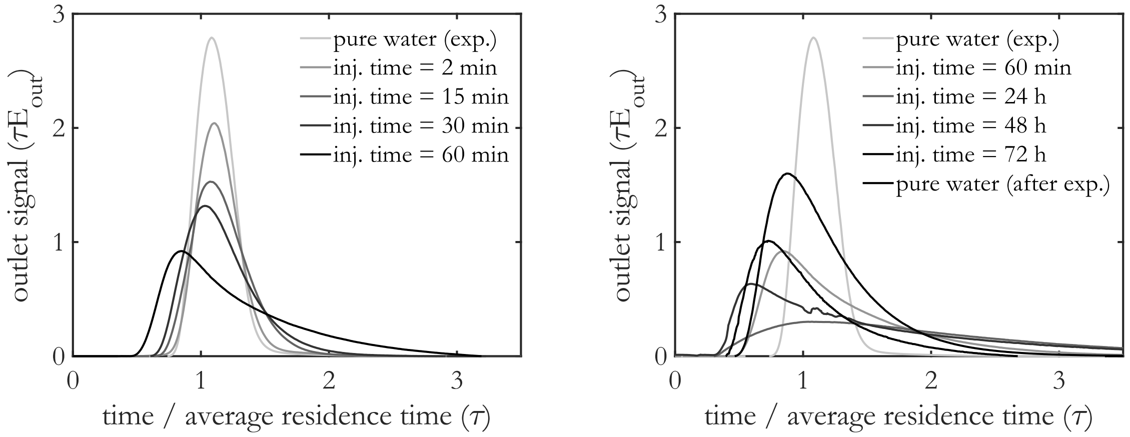

Figure 124: Evolution of the area-normalized response signal E_{out} at different times for w_M=20 wt.-% and w_I=0.02 wt.-% in an ultrasonic bath.

Figure 125, shows the conversion curve for this experiment compared to an experiment at T=85 °C, with monomer feed concentration w_M=20 wt.-% and initiator feed concentration w_I=0.007 wt.-%. Both experiments are in a similar conversion range and can therefore be compared.

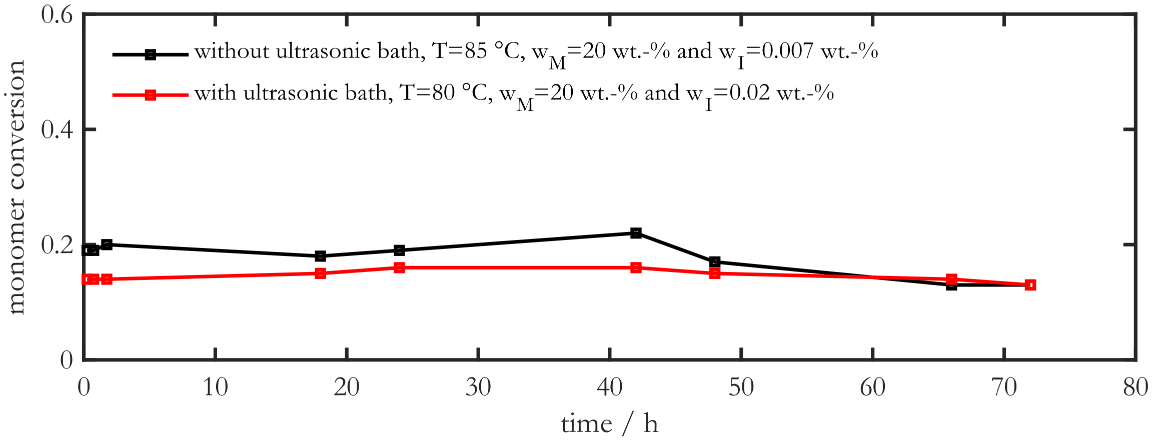

Figure 125: Conversion curve over the entire operating with or without the use of an ultrasonic bath at different operating conditions.

If the residence time curves from Figure 124 are compared to Figure 123, it is clear that these curves are similar to those in the ultrasonic bath, but the curves in Figure 123 fluctuate significantly more, which indicates a stronger gelation process.

Figure 126 shows the pressure loss over the reaction time compared to the experiment without ultrasonic bath at T=85 °C. It can be seen that there is almost no increase in pressure when ultrasonic waves are used. This minimal increase may be due to the reactor outlet, where the reactor medium is still at high temperature but is no longer in the bath. For the experiment without the ultrasonic bath, there is a significantly earlier and stronger increase in pressure.

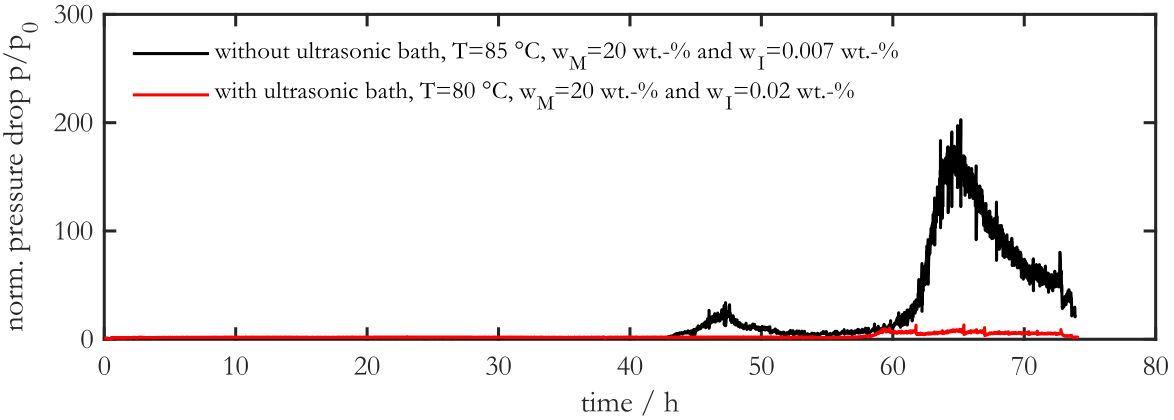

Figure 126: Pressure curve over the entire operating time with or without the use of an ultrasonic bath at a monomer content of w_M=20 wt.-% and an initiator concentration of w_I=0.02 wt.-%.

In summary, it can be said that the use of an ultrasonic bath results in almost no gelation of the wall layer in a capillary reactor, which increases the operating time significantly.

A.2.3 Optical measurement with UV/VIS in a half shell reactor[10]

A summary of the UV/VIS measurements was presented in Chapter 3.2. Here, the experimental setup, the preliminary investigations and then the experimental findings are presented. These results have already been successfully published in [53].

A.2.3.1 Optical measurement setup

Light is irradiated onto a sample as the fundamental measuring principle, and the backscattered light is detected. Mostly scattering and absorption processes take place during the interaction of the light with the sample, resulting in a lower measuring signal than the light that was originally irradiated. These light losses are condensed into the extinction E, which expresses how the measurement signal has changed since the process began. Two signals altogether are captured. Since the measurement

---

[10] The majority of this chapter has been published in advance of this thesis under the terms of the Creative Commons Attribution License (CC BY 4.0) in [53]. Minor changes have been made and passages have been added for better comprehensibility and embedding in the context of this thesis.

signal changes most drastically at 320 nm during the reaction process, this wavelength corresponds to the first signal. Since there is no change in the qualitative spectral profile during the reaction, the second signal acts as a reference and is located in the 450 nm wavelength region. By figuring out altered scattering qualities and reducing the measurement signal to the portion brought on by structural changes, the reference enables an offset correction to be made.

A Heraeus Noblelight XD 6265-08TJ deuterium lamp serves as the source of illumination. It offers a continuous spectrum, with the UV region between 160 and 400 nm having the highest intensity. The light from the lamp is focused into a bundle of three separate fibers passing through a lens with a 12 mm focal length. These fibers direct the light to a rod probe that is mounted inside the reactor's half-shell. The rod probe features an inside bundle of seven glass fibers and an outside diameter of 1.6 mm. The configuration of the fibers is shown in Figure 127. The light source is attached to the middle three fibers, which direct the light into the reactor and onto the sample. The detection modules are attached to the two left and right fibers. This fiber configuration was designed to minimize location-dependent variations in backscatter by placing the detector fibers at an equal distance from the light that is being irradiated.

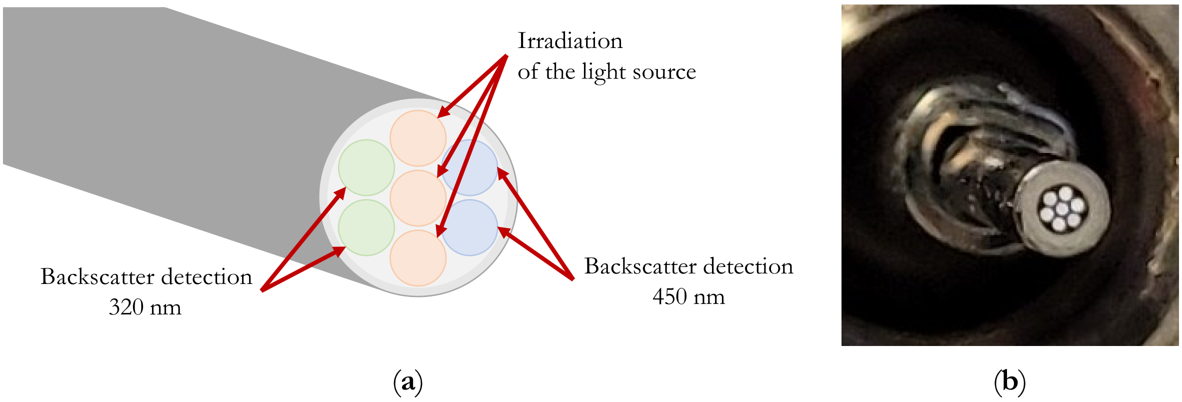

Figure 127: (a) Schematic of the probe tip and location of the optical fibers; (b) Photo of the polished probe tip [53].

Customized Photo Multipliers (CPMs) modules from Proxivision (Bensheim, Germany) are used to detect backscattered light. The advantage of CPMs is their great sensitivity and minimal background noise. Between the lens and the CPMs, further optical filters are put in place to filter the incoming light down to the necessary wavelength range. A bandpass filter (320/40 BrightLine HC) from Semrock with a bandwidth of 40 nm limits the first detection range at 320 nm. The model CM92B (CPM) has an increased sensitivity in the 165–650 nm range. A bandpass filter (450/50 AT bandpass) from Chroma with a bandwidth of 50 nm allows for the second detection range to be at 450 nm.

The CPM that is mounted behind it is a type CM93LB with greater sensitivity in the 185–650 nm range. Figure 128 provides a schematic representation of the measurement system's configuration.

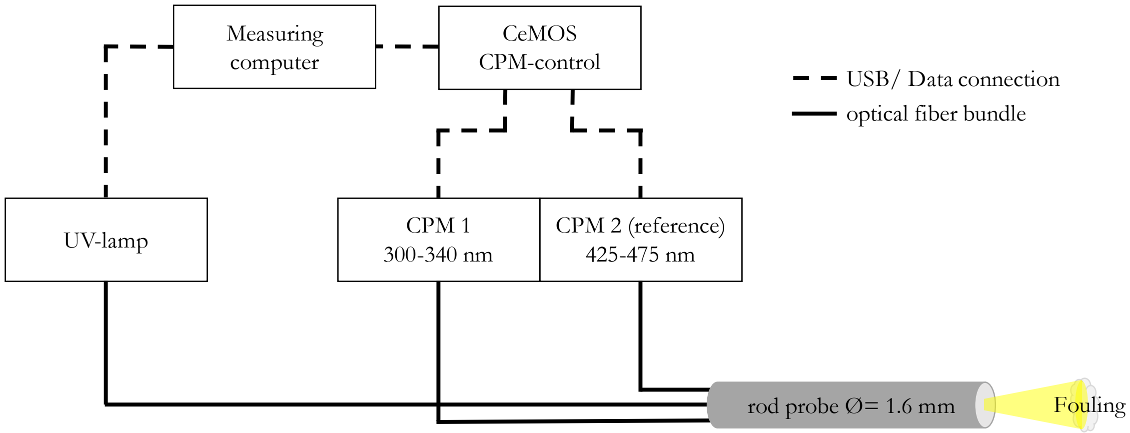

Figure 128: Scheme of the measurement setup [53].

A.2.3.2 Reactor setup

The experimental setup for testing the optical measurement technique under reaction conditions is shown in a simplified flow sheet in Figure 129 with a ContiPlant half-shell reactor of Fluitec mixing + reaction solutions AG.

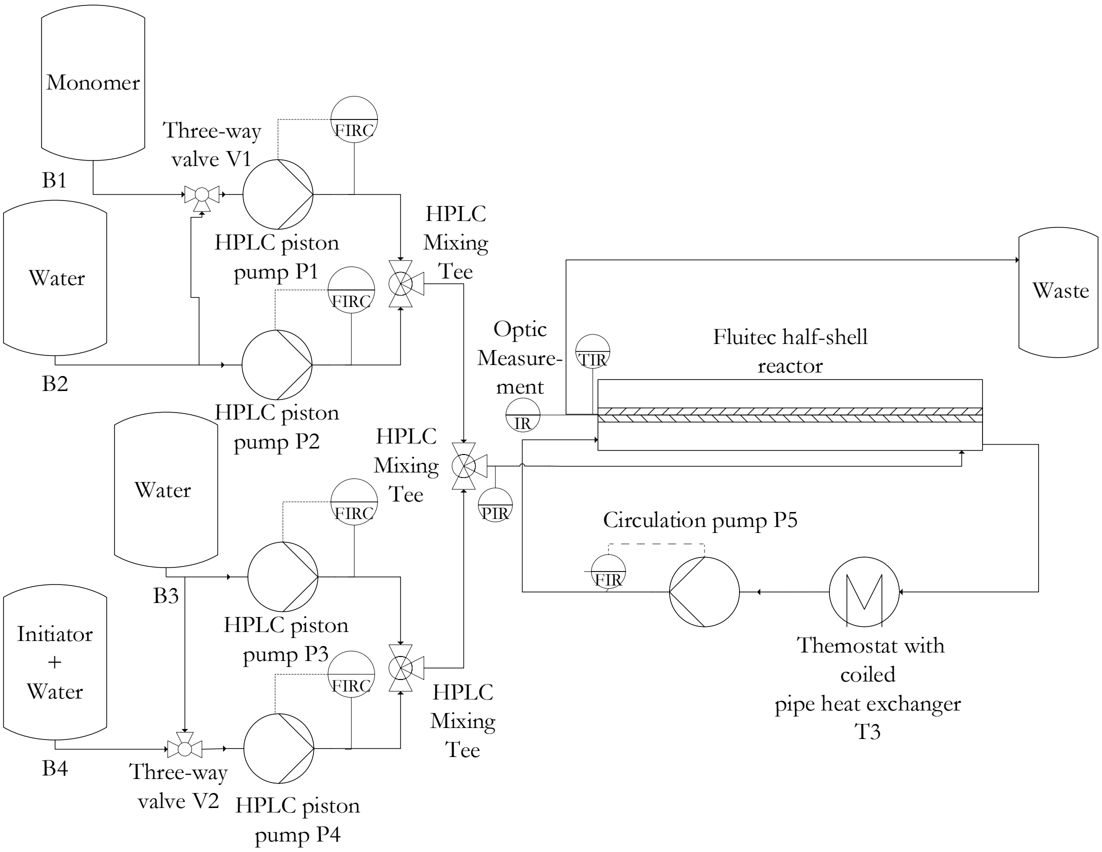

Figure 129: Simplified flow sheet of the experimental setup with the Fluitec ContiPlant half-shell reactor [53].

The degassed monomer, the solvent, and an initiator solution were prepared in four storage containers which are labelled B1 to B4 (Figure 129). The mass flow rates were chosen to yield a velocity of 6 mm/s. To achieve a good micro-mixing quality, the feed streams of P1 and P2 as well as those of P3 and P4 have been premixed using 1/16" HPLC T-connectors and are then mixed again with a 1:1 mass flux ratio in a second 1/16" HPLC T-connector.

The reactor was heated using coiled pipe heat exchanger, which has been placed in an oil bath thermostat (T3) and a water circuit including the circulation pump P5. A circulation flux between 7 and 8 l/min and an oil bath temperature of 100 °C was chosen to adjust a temperature of the heating medium of 86 °C at the reactor inlet. The temperature drops in the water circuit around 1 °C due to heat losses. At the start of the experiment the reactor was flooded with the monomer-water solution, then the initiator-water solution was added.

The reactor system consists of one Fluitec ContiPlant half-shell reactor, shown in Figure 130, with an internal diameter of 12.3 mm and a length of 495 mm. 6 mixing elements, consisting of 5 CSE-X4 and 1 CSE-X8 from Fluitec, were placed in the reactor for each experiment. The operating run of each time was 8 hours. The mixing elements are provided with a hole with a diameter of d=1.6 mm. This hole allows to pass the rod probe through the mixers and to place the tip between 2 mixing elements. A 12.3 mm wide sleeve guarantees the distance between these mixing elements. In the experiments, the space between the last and penultimate mixing element was chosen because here most deposit formation occurs. The planar surface of a mixer without a hole serves as a reflection surface. The probe tip was placed inside the mixing element from the direction of the reactor outlet (against the direction of flow) to allow as little fouling as possible on the probe tip.

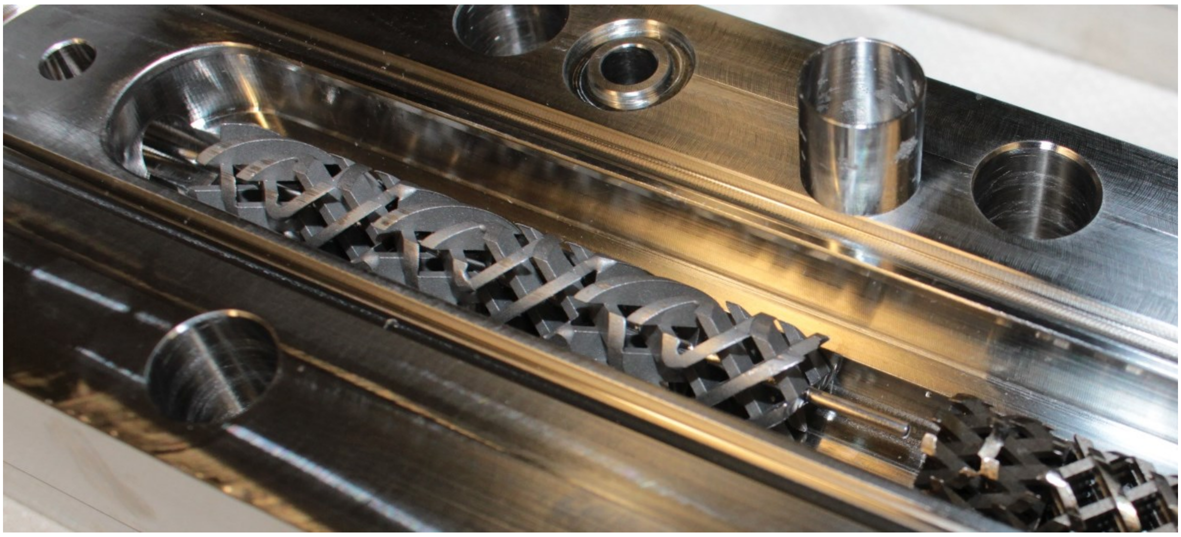

Figure 130: Half-shell reactor with build in rod probe [53].

A.2.3.3 Pre-characterization of the rod probe

The spectra are initially measured at different reactant and product concentrations because the measurement method with the CPMs only offers a time course of the measurement signal, and the influences of the separate components cannot be distinguished. To test the influence of the entire bandwidth, the CPMs are swapped out with a standard Zeiss MCS 601 UV-NIR spectrometer (Oberkochen, Germany) as the detecting device.

Below, three measurement series are analyzed. Every measurement series is a mixture of NVP, PVP, and water. To guarantee a constant chain length of the PVP, the sales product of BASF SE, Kollidon K30, was used. The NVP concentration was raised from 5 to 20 wt.-% for the first set of measurements, which were conducted at a constant PVP concentration of 2.5 wt.-% (Figure 131). The PVP concentration has increased from 2.5 to 5 wt.-% in the second set of measurements, whereas the NVP concentration remains constant at 10 wt.-% (Figure 132). By raising the concentration of NVP from 12 to 20 weight percent and lowering the concentration of PVP from 8 to 2.5 weight percent during the third series of measurements, a shift in conversion is imitated (Figure 133). The measurement ranges of the CPMs are shown and calculated as extinction in addition to the spectra.

The Lambert Beer's law (Equation (165)) can be used to calculate the extinction [83]

$$E_\lambda = -log_{10}\left(\frac{I}{I_0}\right) = \varepsilon_\lambda \cdot c \cdot d. \qquad (165)$$

I_0 corresponds to the H_2O spectrum of the measurement series and I to the measured concentration. The extinction is computed in relation to the bandwidth of the optical filters to make the results from the spectra similar to the measurements of the CPMs. The integral of the spectrum was calculated for the individual bandwidths of the filters and Equation (165) was used to get the associated extinction value. As a result, there is one extinction value E for each filter range, which can be used to fix the offset by subtracting from one another. Equation (166) is the overall equation for the extinction

$$E = -\log_{10}\left(\frac{I(320\,nm)}{I_0(320\,nm)}\right) + \log_{10}\left(\frac{I(450\,nm)}{I_0(450\,nm)}\right) \qquad (166)$$

with $E = E_{320nm} - E_{450nm}$.

Figure 131 shows that in the 320 nm region a decline in signal of around 1000 counts occurs when the NVP concentration is increased from 5 to 20 weight percent at constant PVP concentration. Figure 131's calculation of absorbance indicates an increase from 0.094 to 0.113.

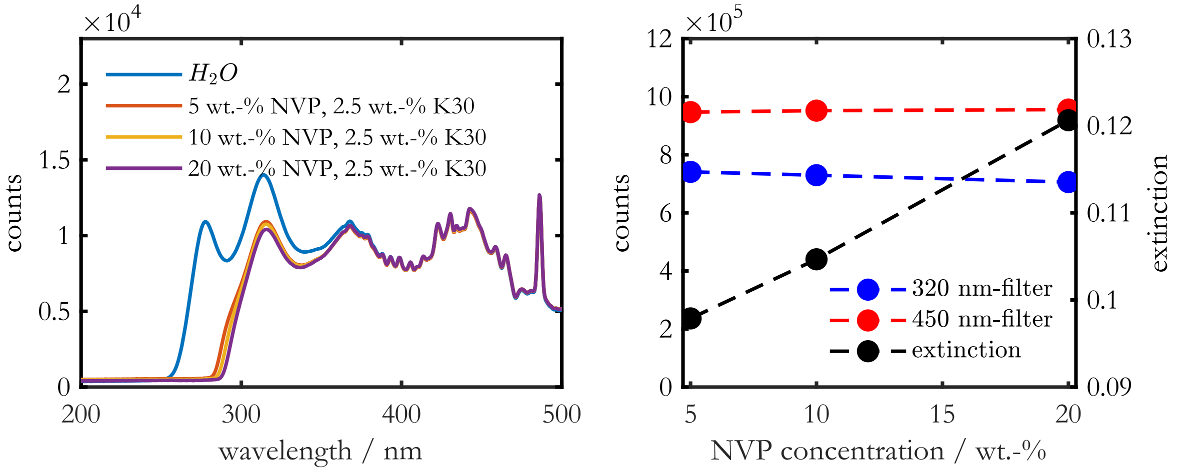

Figure 131: Measured raw data spectra (left) and processed data (right) of NVP and PVP dissolved in water of measurement series with increasing NVP concentration. Adapted from [53].

There is also a signal decline of roughly 1600 counts in the second set of measurements at constant NVP concentration and rise in PVP concentration from 2.5 to 5 wt.-% (Figure 132). As a result, the extinction rises to 0.172 from 0.098. When the NVP concentration is altered, the signal lowers by 66.7 counts/(wt.-%), and when the PVP concentration is changed, the signal drops by 640 counts/(wt.-%), according to a comparison of the changes in the spectra of the two series of tests. Because of the PVP, this leads to a greater influence by factor 9.6. When expressed as extinction, this influence gains much greater weight. This yields a change of 0.029 extinctions/(wt.-%) for PVP and 0.001 extinctions/(wt.-%) for NVP. As a result, PVP has a 22-fold larger impact on extinction. This indicates that NVP has little effect on the extinction measurement and that the signal mostly tells us how much PVP is present in the reactor.

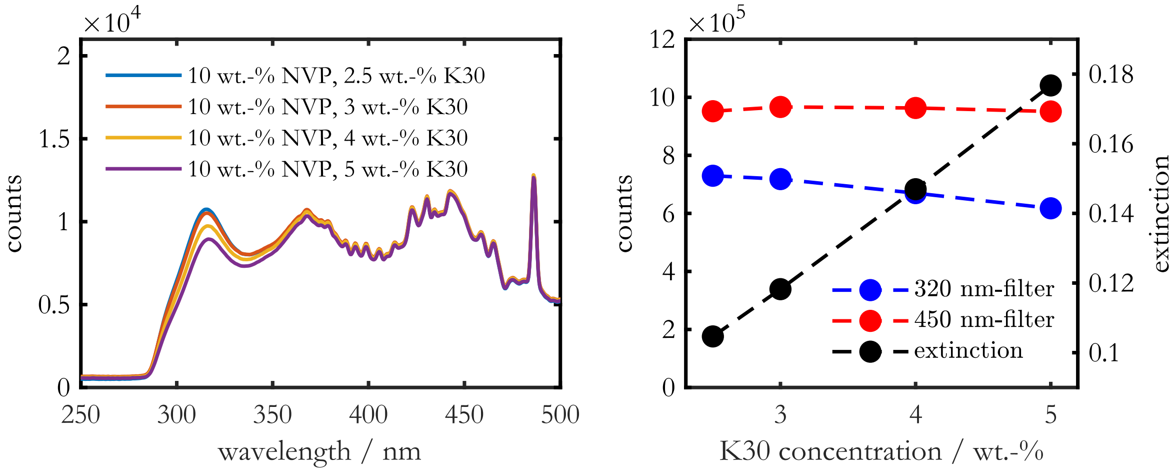

Figure 132: Measured raw data spectra (left) and processed data (right) of NVP and PVP dissolved in water of measurement series with increasing PVP concentration. Adapted from [53].

Measurement series three was used to replicate the signal behavior for varying conversion (Figure 133). While the PVP concentration falls from 8 to 2.5 wt.-%, the NVP concentration rises from 12 to 20 wt.-%. The spectroscopic measurement signal increases by roughly 3000 counts in the 300–340 nm range as the reactant concentration rises and the product concentration falls, indicating a decline in conversion. This leads to an increase of 0.147 for the extinction in Figure 133 for a conversion increase from 11 to 40%, showing that PVP dominates and overlaps the NVP signal in the extinction signal.

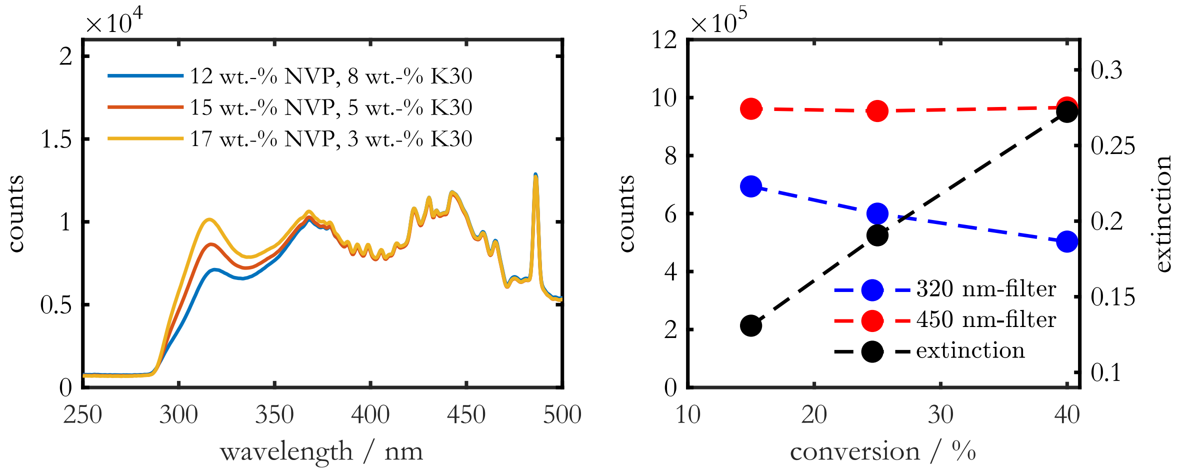

Figure 133: Measured raw data spectra (left) and processed data (right) of NVP and PVP dissolved in water of measurement series with increasing conversion. Adapted from [53].

Furthermore, the spectra of the three series of measurements (Figure 131-133) demonstrate that the reference in the 450 nm bandwidth is appropriate for offset correction because concentration variations do not significantly alter it.

A.2.3.4 Fouling detection in the half shell reactor with different feed conditions

The half-shell reactor is used for a series of measurements at different process conditions with an operating time of about 8 hours at 85 °C. Every five seconds, each CPM records a measured value. Figure 134 displays the measured data for a monomer concentration of 20 weight percent and an initiator concentration of 0.02 weight percent. The raw data output from the CPMs is shown in the graphs for the 320 nm and 450 nm filters. As previously mentioned, Lambert Beer's law (Equation (165)) is used to calculate these two measurement curves. The raw data and the extinction were plotted together in Figure 134. Reduced noise, decreased interference effects (such as compensating for the signal jump at 3:53), and improved stability and reproducibility of the measurement data are the benefits of the processing.

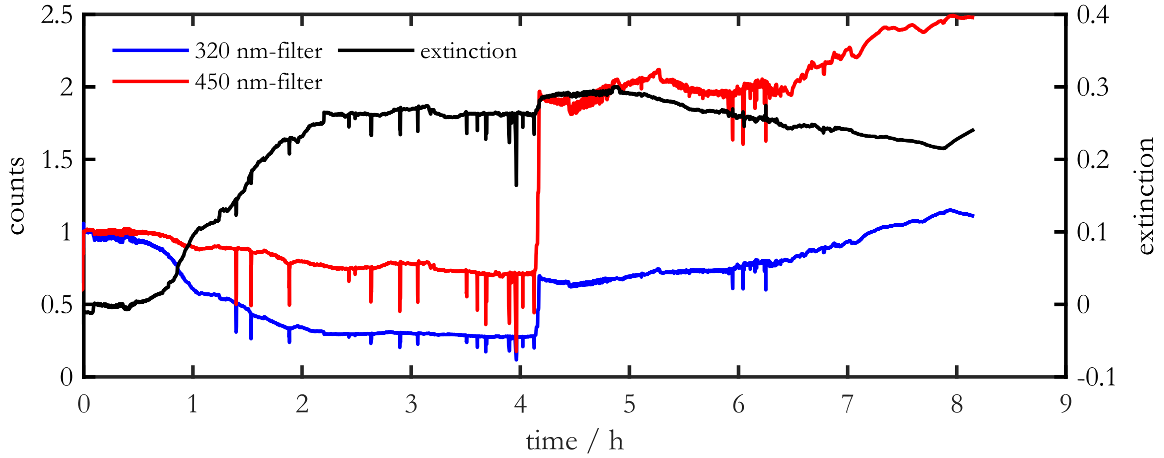

Figure 134: Continuous measurement in a half-shell reactor at 85 °C with a monomer feed concentration of 20 wt.-% and an initiator feed concentration of 0.02 wt.-%. Adapted from [53].

The extinction curves for different monomer concentrations at 85 °C and 0.02 weight percent initiator concentration are displayed in Figure 135. The measured values increase earlier and exhibit a higher extinction when the monomer concentration is higher. At the same time, the extinction signal decreases more strongly towards the end of the experiments at higher monomer concentrations. In light of Figure 133, the results are interpreted as follows: a decrease in extinction is correlated with a decrease in product concentration, or a lower conversion, and an increase in extinction is correlated with an increase in product concentration or a higher conversion.

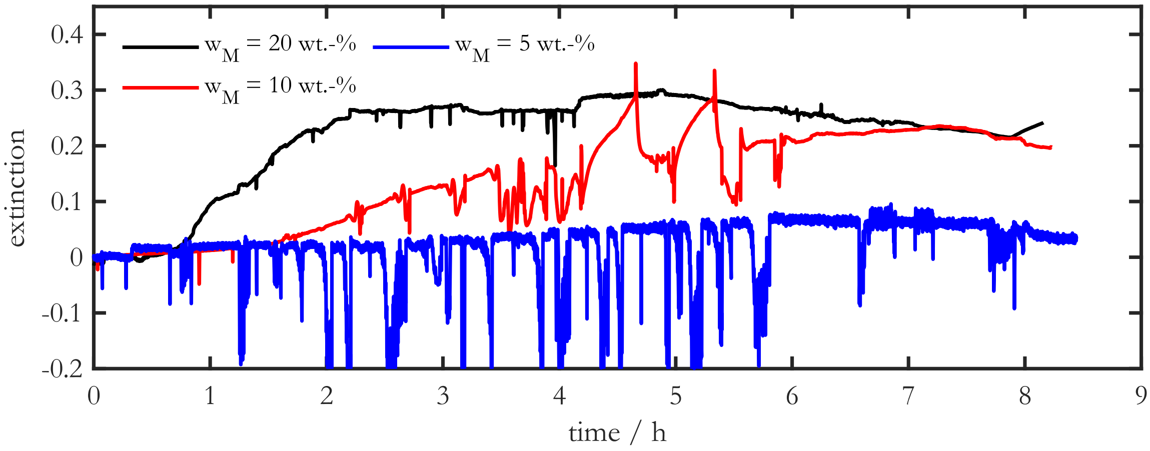

Figure 135: Extinction measurement of different monomer feed concentrations in the half-shell reactor at 85 °C and an initiator feed concentration of 0.02 wt.-%. Adapted from [53].

The HPLC measurement according to Chapter 2.3.1 resp. 2.3.5, which is displayed in Figure 136, can demonstrate that the monomer conversion stays constant for the first three hours. This implies that a higher product concentration in front of the probe is the cause of the increase in extinction. In turn, a higher concentration of the product may indicate reactor fouling.

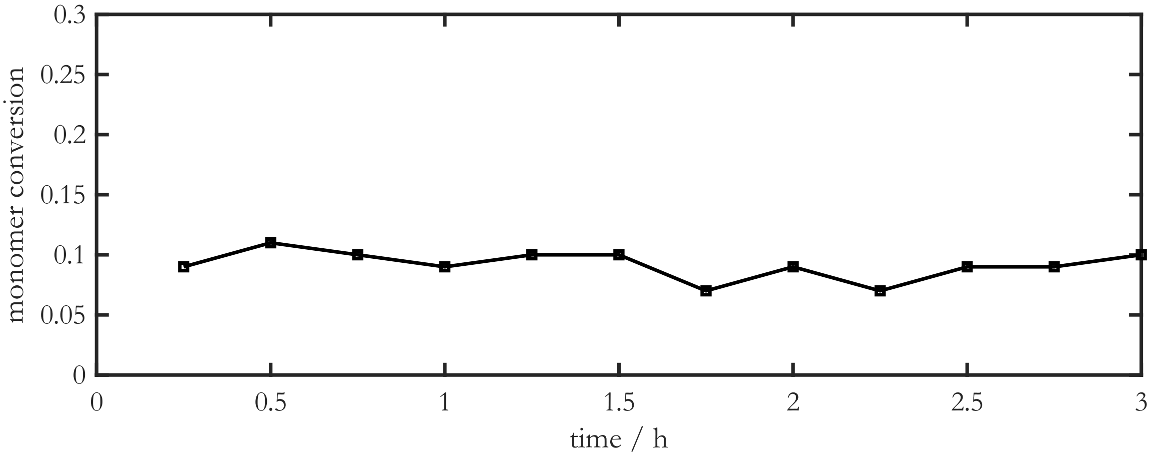

Figure 136: Measurement of the conversion with HPLC over the time of 3 h for a starting concentration of 20 wt.-% NVP and an initiator concentration of 0.02 wt.-%. Adapted from [53].

This can be demonstrated after opening the reactor after three hours operating time and looking at the probe tip in Figure 137. There is no fouling on the mixing elements, but a layer of fouling has developed on the probe tip. A decrease in extinction is visible later in Figure 135 at a monomer concentration of 20 weight percent, beginning at 4:33 h. This can be interpreted as a decrease in conversion due to the reduction in reactor volume caused by fouling. Figure 137 shows the fouling and volume reduction after an 8 h reaction time. The effects of layer growth and conversion decrease cancel each other out in the signal constant range of 2:11 h-4:33 h. In general, it is also evident that the steepness of the increase and the monomer concentration are correlated with the extinction maximum. Nitrogen (N2) bubbles that form in the decay of the initiator and flow past the probe can be the cause of outlier values and abrupt drops in the signal.

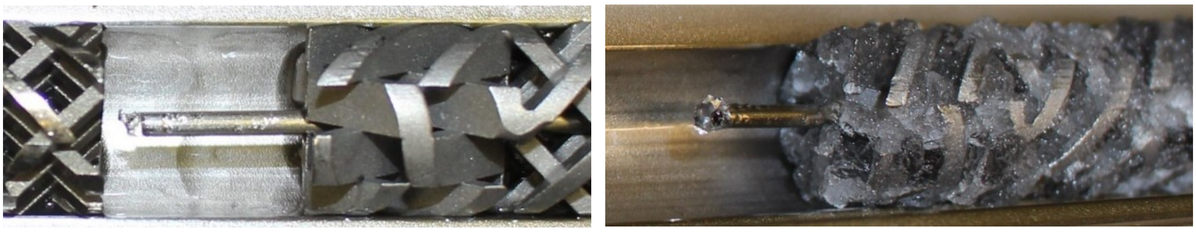

Figure 137: Tip of the rod probe and mixing elements after approx. 3:00 h reaction time (left) and after 8:00 h reaction time (right). Adapted from [53].

An additional set of measurements examines the change of the initiator feed concentration at a reactor temperature of 85 °C and a constant monomer feed concentration of 20 weight percent. Figure 138 presents the findings. It is possible to interpret the extinction increase and decrease analogously to Figure 135. The signal is weaker and rises later at lower initiator concentrations, which is an example of how the concentration of the initiator influences the signal. Nearly no fouling happens at an initiator concentration of 0.002 weight percent, and the graph's trajectory is roughly constant.

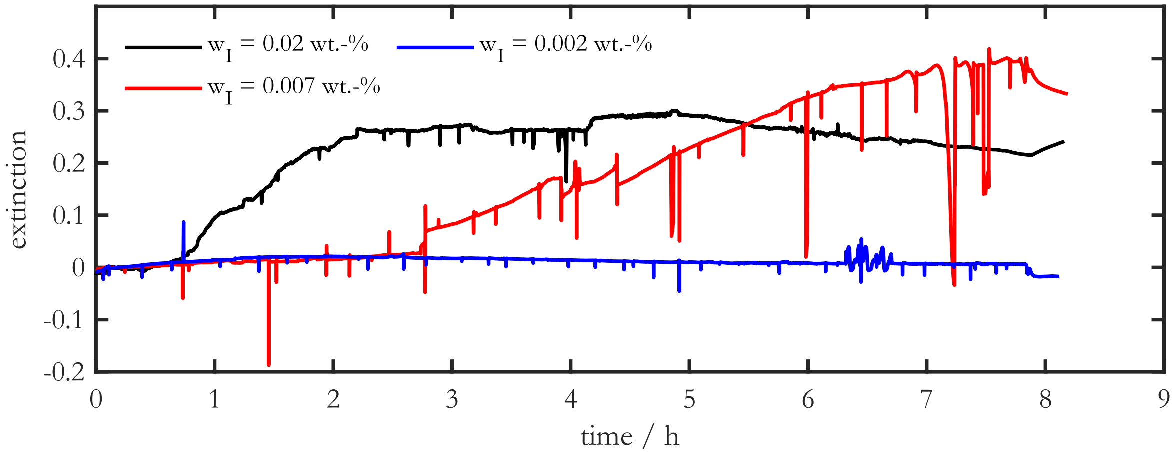

Figure 138: Extinction measurement of different initiator feed contents in the half-shell reactor at 85 °C and a monomer content of 20 wt.-%. Adapted from [53].

Evolution of the pressure drop

Further pressure measurements were carried out to compare the spectroscopic measurements. The reaction conditions of Figure 139 (top) are the same as those of Figure 135, and the conditions of Figure 139 (bottom) are the same as those of Figure 138.

Figure 139 (top) displays typically pressure curves which corresponds to reactor fouling. A stable pressure curve can be observed for all process conditions in the first five hours. After eight hours, the 10 weight percent curve increases to a norm pressure of roughly 6. For the 20 weight percent curve, the increase is flatter and ends at a norm pressure of roughly 3. The pressure doesn't rise for 5 weight percent until six hours of operation time and has the lowest final norm. pressure drop of approximately 2.5. The pressure increase that starts at approximately 5 hours is similar to the extinction signal decrease that happens at roughly the same time in Figure 135. However, the drawback of pressure measurement is that no statement can be made regarding the reaction progress during the first five hours, making early detection impossible. Furthermore, there is no correlation between the monomer concentration and the signal maximum in the pressure curves.

The only curve in Figure 139 (bottom) that shows an increase in pressure is the "0.02 wt.-% initiator" curve. No pressure increase was observed in the measurements with 0.007 weight percent and 0.002 weight percent initiator concentration, hence no conclusions about the reaction could be drawn from them. This shows the higher sensitivity of the spectroscopic measurement system when compared to the extinction in Figure 138, where a signal influence can be measured at least for the 0.007 wt.-% measurement series.

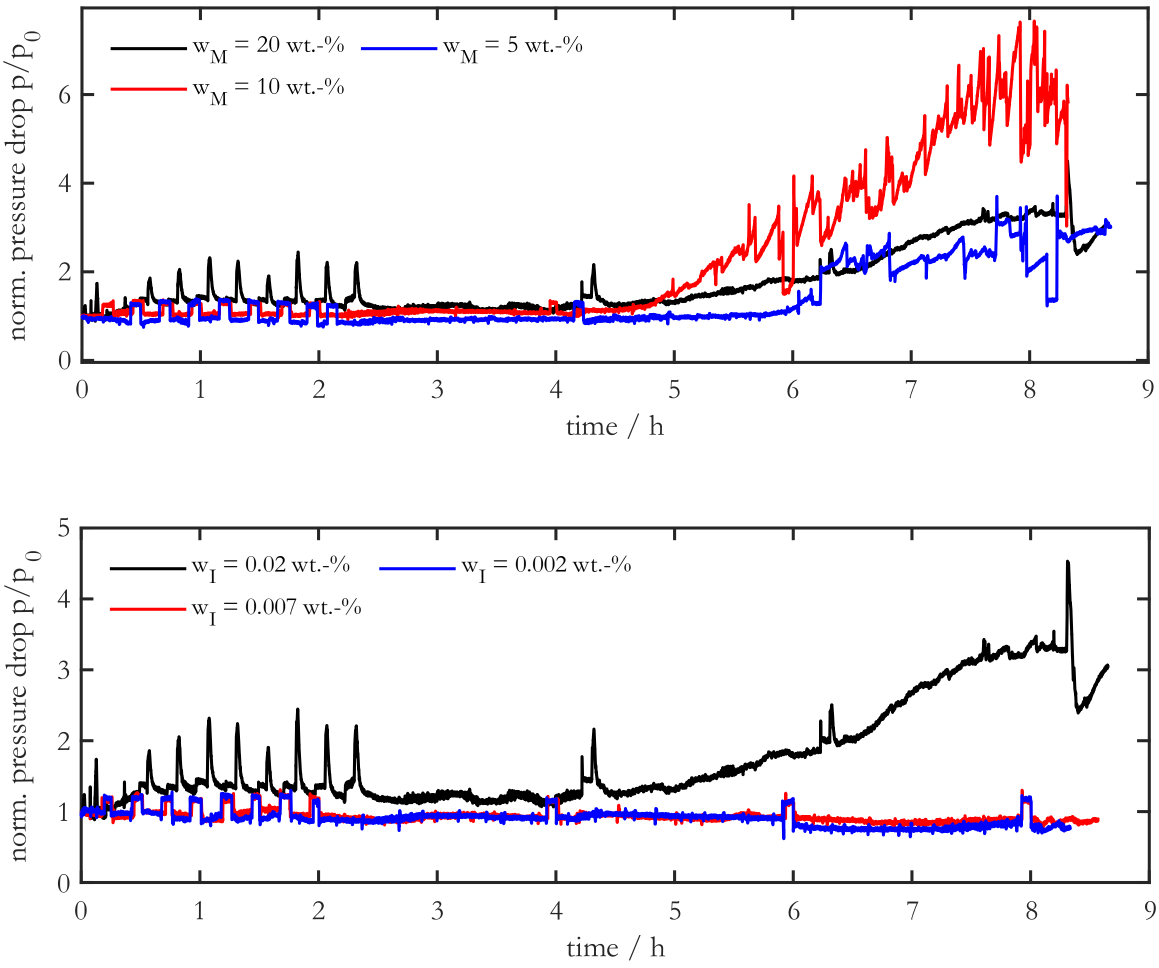

Figure 139: Pressure profile over reaction time with varying NVP concentration and an initiator content of 0.02 wt.-%. (top) and varying initiator concentration and a monomer content of 20 wt.-%. (bottom). Adapted from [53].

Figure 140, which shows a static mixing element after 8 hours of operation for 0.002 weight percent initiator concentration, can help to explain this. Fouling is not observed with a very low initiator concentration at that operating time. It is important to note that the conversion falls within a very small range (less than 5%).

Figure 140: Steel mixer after 8 h of operation with an initiator concentration of w_I=0.002 wt.-% [53].

Polymer analytics

Using HPLC, the monomer conversion could be analyzed according to Chapter 2.3.5. Figure 141 shows the curve for different monomer concentrations resp. for different initiator concentrations. A lower monomer concentration and a higher initiator concentration leads to an increased conversion. In general, the conversion curve is relatively constant at all concentrations, except at a concentration of w_M=20 wt.-% and w_I=0.02 wt.-%. Here it can be seen towards the end of the experiment that the conversion decreases very sharply. This is consistent with the findings from Figure 135 that the conversion decreases from a reaction time of 4 h due to fouling.

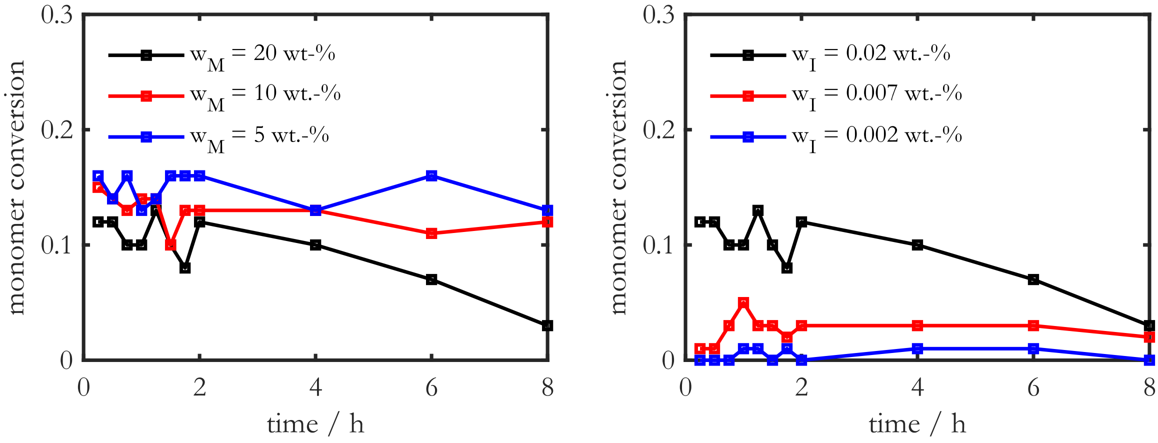

Figure 141: Comparison of the evolution of the monomer conversion from experiments at different monomer feed concentrations with w_I=0.02 wt.-% (left) and different initiator feed concentrations with w_M=20 wt.-% (right).

Using GPC, the molecular weight distribution and thus also the weight-average molecular weight could be determined for different monomer and initiator concentrations (Figure 142-143). Samples with an initiator content of w_I=0.002 wt.-% could not be analyzed due to the extremely low polymer content (see Figure 141 (right)). Figure 142 shows, that the average molecular weight increases with increasing monomer concentration, whereas the molecular weight decreases with increasing initiator content. It is interesting to note from Figure 142 (left) that the molecular weight increases slightly with increasing reaction time from 250 kg mol^{-1} to 270 kg mol^{-1} for a monomer feed content of w_M=20 wt.-%. and an initiator content of w_I=0.002 wt.-%. It can be assumed that high-molecular polymers, which have a very long residence time due to fouling, are flushed into the outlet.

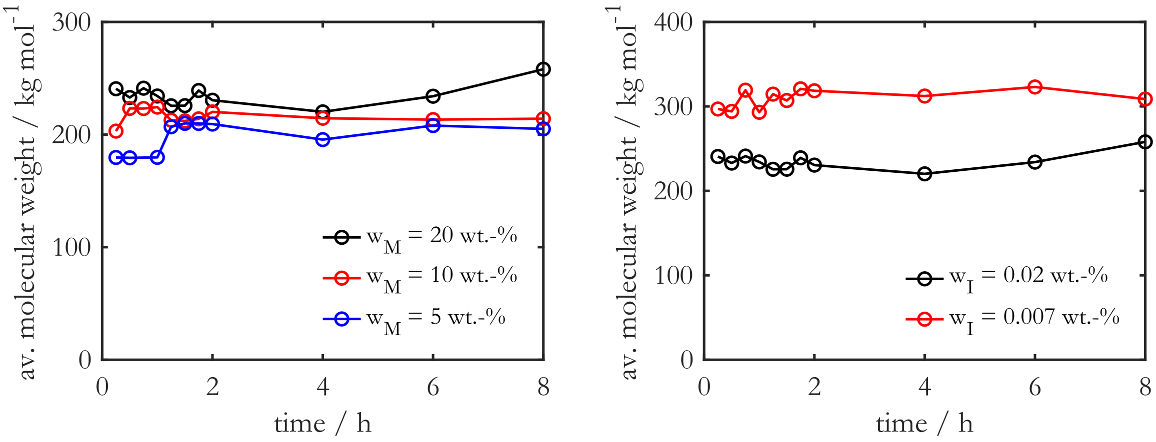

Figure 142: Comparison of the evolution of the weight average molecular weight from experiments at different monomer feed concentrations with w_I=0.02 wt.-% (left) and different initiator feed concentrations with w_M=20 wt.-% (right).

Figure 143 shows the normalized GPC distribution for different monomer and initiator feed concentrations. With increased monomer concentration, the distribution is shifted further towards higher molecular weights and becomes broader. In addition, the figure shows that with decreasing initiator concentration the distribution is shifted to higher molecular weights as well.

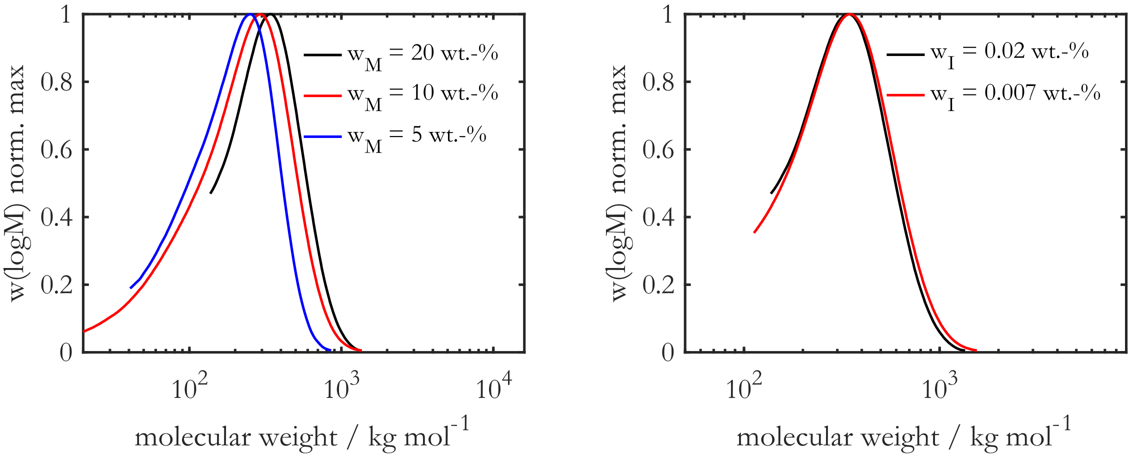

Figure 143: Comparison of the normalized GPC distribution from experiments for different monomer feed concentrations with w_I=0.02 wt.-% (left) and different initiator feed concentrations with w_M=20 wt.-% (right) at t=0.25 h.

The average number of branching points over the chain length for different monomer and initiator concentrations can then be compared in Figure 144 at an operating time of 8 h. As already discussed, with increasing monomer concentration the polymer molecules are becoming longer. Therefore, with increasing monomer concentration the number of branching points is getting high for long polymer molecules while the slope for all concentrations is approximately the same. As in the capillary reactor, a lower initiator concentration results in fewer branching points depending on the chain length because side reactions are occurring less likely.

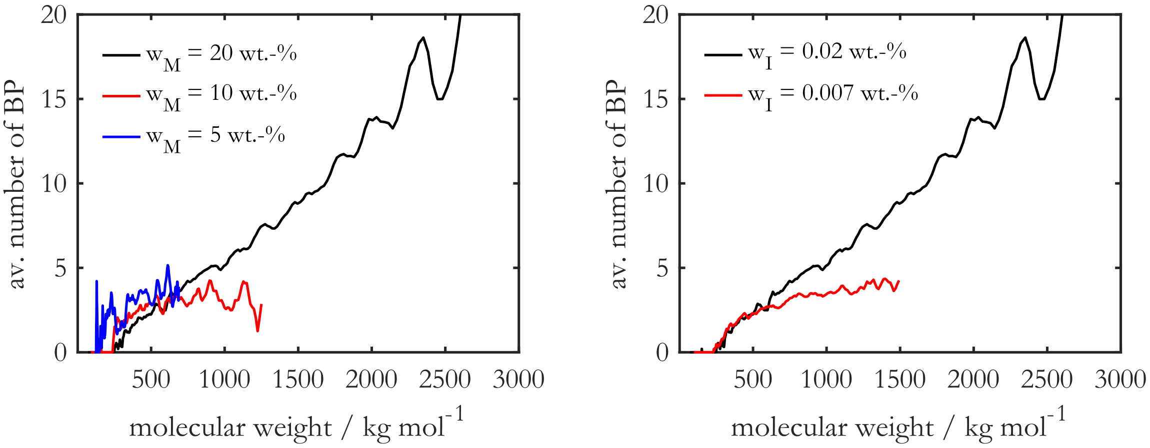

Figure 144: Comparison of the av. number of branches from experiments for different monomer feed concentrations with w_I=0.02 wt.-% (left) and different initiator feed concentrations with w_M=20 wt.-% (right) at t=8 h.

The behavior during the operating time can then be investigated in more detail for a monomer concentration of w_M=20 wt.-% and an initiator concentration of w_I=0.02 wt.-%. Figure 145 shows the GPC distribution and the number of branching points for different operating times. It is very interesting that with increasing operating time the molecular weight distribution becomes broader and is shifted to higher molecular weights. Furthermore, the number of branches increases as the chain length increases. However, the slope of the curve is also increased for higher operating times.

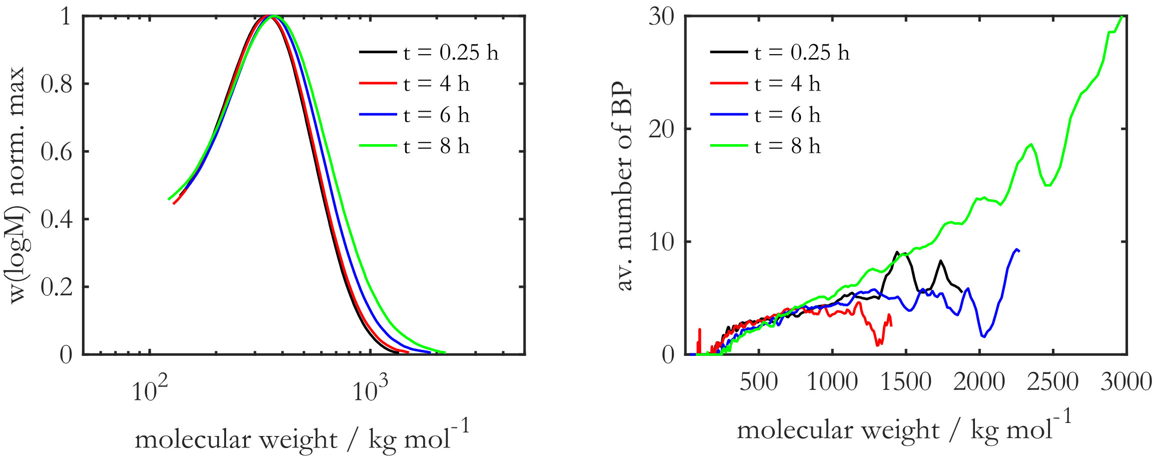

Figure 145: Comparison of the normalized GPC distribution (left) and av. number of branches (right) from experiments for different operating times at w_M=20 wt.-% and w_I=0.02 wt.-%.

A.2.4 Fouling detection in the half shell reactor with different pre-mixing

In this section, the measurements for premixing and pre-tempering with different premixing units are presented. The spectroscopy measurement technique in the half-shell reactor as shown in Figure 9 could be evaluated in parallel. The measuring point is located quite close (1 mixer rod) to the reactor outlet. The rod probe measures in the direction of flow against the planar surface of the last mixer and can detect the growth of a layer on this surface. Furthermore, the growth of a possible fouling layer can also occur directly at the tip of the probe. The pressure signal, the gravimetric determination of the gel quantity and the optical assessment were used to evaluate the fouling for the different pre-mixers. The process conditions are shown in Table 16. The used mixer elements were cleaned with NaClO according to Chapter 3.4 before each experiment.

Table 16: Reactor and process conditions in the half-shell reactor for pre-mixing and pre-tempering experiments.

Process conditions
Monomer feed concentration: w_M=20 wt.-%
Initiator feed concentration: w_I=0.02 wt.-%
Mean flow velocity: v=3 mm/s
Reactor temperature: T=85 °C
Operating time: 18 h

Table 17 shows the tested constellations of Ehrfeld pre-mixers and a standard HPLC-t mixer as a reference.

Table 17: Tested pre-mixer and associated conditions.

LH2-Mixer (Ambient temperature: 25/25 µm mixing plate, 60 °C pre-temperature: 50/50 µm mixing plate)
Cascade mixer
Standard HPLC-t-mixer

Figure 146 shows the LH2 (left) and the cascade mixer (right). The LH2 mixer was tested with a 25/25 µm and a 50/50 µm mixing plate.

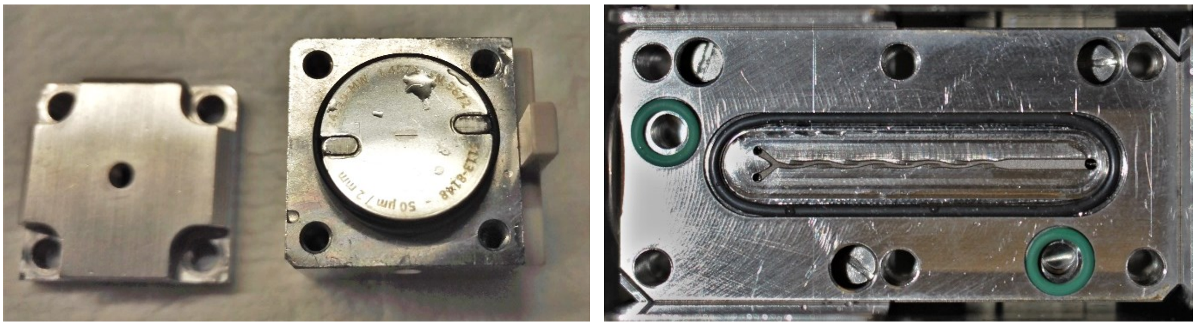

Figure 146: LH2 (left) und cascade mixer (right) from Ehrfeld Mikrotechnik BTS.

Figure 147 shows the differential pressure curve between the inlet and outlet, normalized to the initial pressure, of the different pre-mixers and the pre-tempering. The signal of the LH2 mixer with a mixing plate of 25/25 µm is the least affected by fluctuations. The pressure loss at the end of the test is also the smallest. The pressure signal with pre-tempering to 60 °C, on the other hand, increases only a bit after 15 h of operation. The final pressure is therefore not greatly increased either. The pressure signal of the cascade mixer and the standard HPLC-t mixer show strong fluctuations after some time, which can be attributed to a stronger deposit formation.

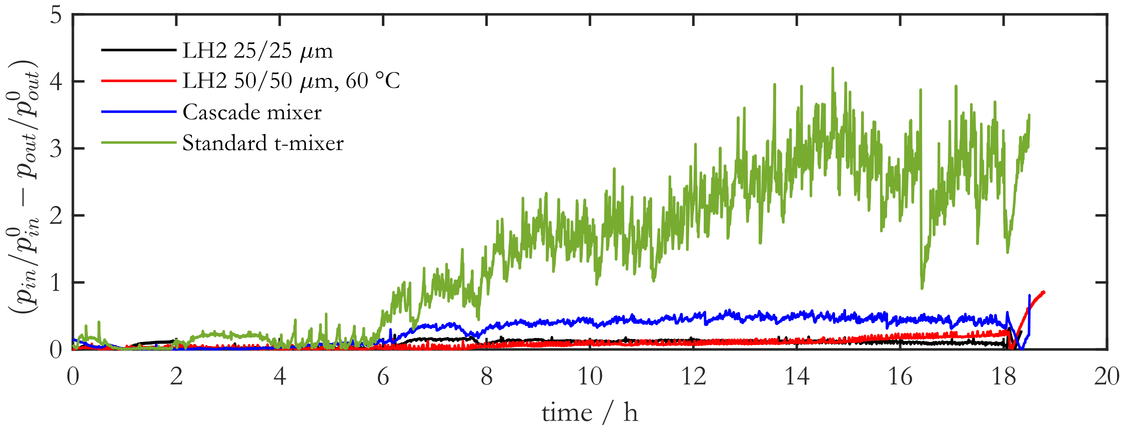

Figure 147: Pressure curve of the different pre-mixers and pre-tempering.

After each test, the mixers were removed from the half-shell reactor and a gravimetric analysis of the gel was carried out (Table 18). The amount of gel with premixing in the LH2 mixer at room temperature with a 25/25 µm is similar to 50/50 µm mixing plate with pre-tempering. Here, the amount of fouling is gravimetrically the lowest. The cascade mixer and the standard t-mixer perform worst. At this point it must be mentioned that a gravimetric determination of the gel quantity by weighing the mixer elements is extremely inaccurate, as it is not possible to determine the complete quantity of gel on the walls of the reactor.

Table 18: Gravimetric determination of the gel amount after each run.

Gel amount (LH2 ambient temperature 25/25 µm mixing plate)	Gel amount (LH2 60 °C pre-tempering 50/50 µm mixing plate)	Gel amount (cascade mixer)	Gel amount (standard t-mixer)
28.7g	28.29g	33.98g	33.91

This is followed by a visual impression of the mixers used. With all tested pre-mixers, the static mixing elements looked like the one displayed in Figure 148 as an example, so there are hardly any visual differences between the mixers. This means that the mixers are affected by fouling despite "good" pre-mixing. The time frame in which the fouling occurs is therefore decisive.

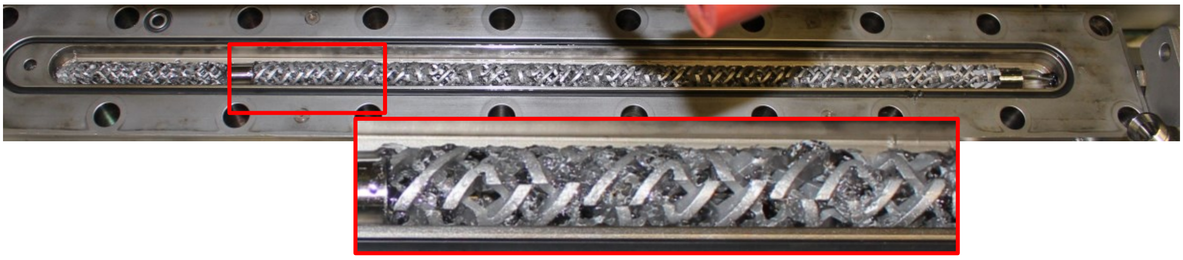

Figure 148: Fouling formation with pre-mixing by the LH2 mixer at ambient temperature with 25/25 µm mixing plate.

The results of the spectroscopy regarding pre-mixing and pre-tempering are presented below. Figure 149 shows the extinction signal according to Equation (165) from Chapter 3.2. From the spectroscopy signal, it can be concluded that the signal of the standard t-mixer increases the fastest and therefore indicates the fastest deposit formation. In contrast, the signal of the cascade mixer also increases very quickly, which indicates a similar unsatisfactory premixing regarding the formation of a deposit layer. The LH2 mixer with a mixing plate of 25/25 µm performs best in terms of premixing. Pre-tempering has a minor influence on the formation of fouling, which is made clear by the almost uniform increase in the signal in contrast to pre-tempering at room temperature. In general, a relatively high level of noise can be seen in the measurement signal for all signals. This noise is probably the result of nitrogen formation due to initiator decomposition during the reaction.

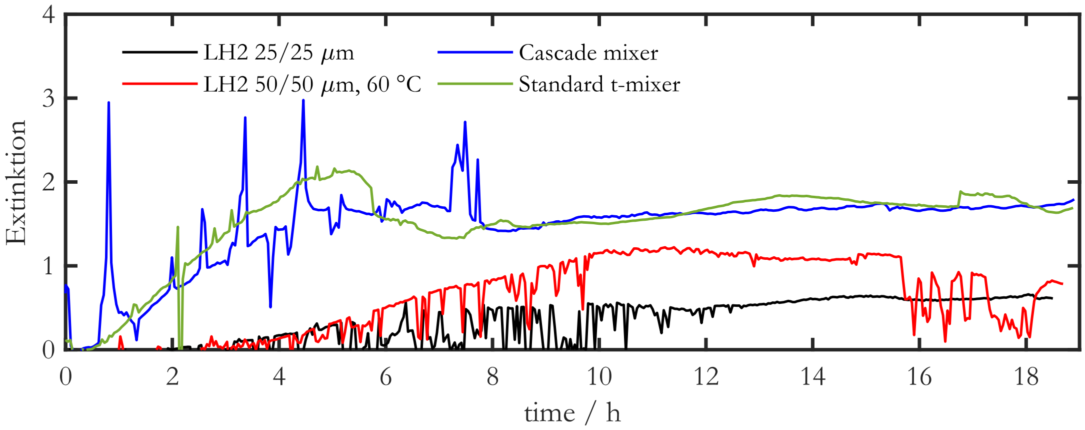

Figure 149: Extinction over the reaction time for the different pre-mixers and pre-tempering.

In summary, pre-mixing has an influence on the speed of gel formation. The LH2 mixer with a mixing plate of 25/25 µm performed best. Pre-tempering has a minor influence on the formation of fouling, whereby the reactor can be operated in a higher conversion range, which can mean a clear advantage.

A.3 Kinetic Models

A.3.1 Extension of the reaction scheme to include transfer to polymers containing TDB

In this chapter, the effect of two more possible reactions is investigated, the transfer to TDB by hydrogen abstraction and the propagation of the resulting internal double bonds (IDB). In an earlier work [5], three different ways for the transfer to monomer reaction were identified with different kinetic coefficients. The fastest and thus most likely pathway has already been implemented in the model as a transfer to the monomer reaction [6]. Instead of the transfer to monomer, the second most likely reaction rate can be used to describe a transfer reaction to polymer containing TDB. The resulting reaction is displayed in Figure 150. In contrast to the transfer to monomer reaction, the H abstraction is in alpha position to the amido N-atom and not to the carbonyl group. The reaction consumes one TDB and one IDB (circled red) is formed.

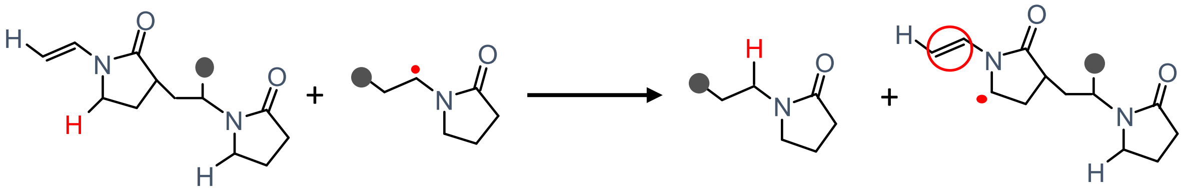

Figure 150: Transfer to Polymer containing terminal double bonds.

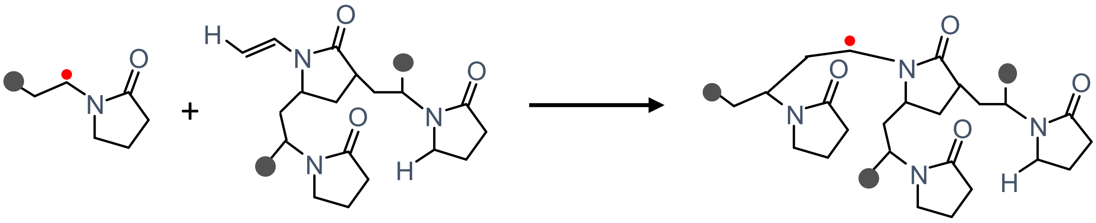

Figure 151: Propagation of internal double bonds.

The propagation reaction of IDB is shown in Figure 151 with an additional branching point while consuming one IDB. The reaction rate was chosen the same as for the propagation of the TDB reaction ($k_{p,IDB}$=$k_{p,TDB}$). By repeating this reaction, highly branched polymers are formed. Therefore, the reactions need to be considered for model development. The resulting extended reaction scheme for the reaction system of N-Vinylpyrrolidone is shown in Table 19 with the full set of the kinetic coefficients in Table 8. The coefficient for the transfer to polymer containing TDB was chosen to $\frac{k_{tr,TDB}}{k_p} = 6.01 \cdot 10^{-5}$, because the H abstraction is in alpha position to the amido N-atom, which was determined in [5].

Table 19: Extended set of reactions for the polymerization of N-Vinylpyrrolidone in aqueous solution with the chain length n/m, the number of terminal double bonds i/j, the number of branching points k/l and number of internal double bonds r/s.

Initiator dissociation/ Initiation	$I_2 \overset{k_d}{\rightarrow} 2f_d I \;/\; I + M \overset{k_p}{\rightarrow} R_{1,0,0,0}$
Propagation	$R_{n,i,k,r} + M \overset{k_p}{\rightarrow} R_{n+1,i,k,r}$
Termination by recombination	$R_{n,i,k,r} + R_{m,j,l,s} \xrightarrow{k_{t,c}} P_{n+m,i+j,k+l,r+s}$
Transfer to monomer	$R_{n,i,k,r} + M \xrightarrow{k_{tr,M}} P_{n,i,k,r} + R_{1,1,0,0}$
Transfer to Polymer containing TDB	$R_{n,i,k,r} + P_{m,j,l,s} \xrightarrow{j \cdot k_{tr,TDB}} P_{n,i,k,r} + R_{m,j-1,l,s+1}$
Propagation of terminal double bonds	$R_{n,i,k,r} + P_{m,j,l,s} \xrightarrow{j \cdot k_{p,TDB}} R_{n+m,i+j-1,k+l+1,r+s}$
Propagation of internal double bonds	$R_{n,i,k,r} + P_{m,j,l,s} \xrightarrow{s \cdot k_{p,IDB}} R_{n+m,i+j,k+l+1,r+s-1}$

A.3.2 Reducing the number of IDB in BP models

The propagation rate of the IDB depends directly on the number of IDB like the propagation of TDB on the number of TDB. Like the number of TDB, the number of IDB is not considered as a distributed property coordinate for modelling in the BP models. The number of TDB can be modelled by a proportional or linear relationship as introduced in [6]. For convenience to calculate only one parameter here, the number of IDB is approximated by a proportional relationship

$$s(m) = A_3 \cdot m. \tag{167}$$

The relationship depends on the chain length m and on the parameter A_3. The parameter A_3 can be determined from the average IDB concentration c^{IDB} per chain

$$c^{IDB} = \sum_{m=1}^{\infty} X_m^1 = A_3 \sum_{m=1}^{\infty} m \cdot X_m^0 = A_3\,\mu_P^1 \tag{168}$$

with the 0th and 1st moment on the number of the internal double bonds X_m^0 resp. X_m^1

$$X_m^S = \sum_{j=0}^{\infty}\sum_{l=0}^{\infty}\sum_{s=0}^{\infty} s^S P_{m,j,l,s} \tag{169}$$

and the 1st chain length moment for dead polymers $\mu_P^{1,0,0,0}$ (consistent to notation from Chapter 4.2.2)

$$\mu_P^{M,0,0,0} = \sum_{m=1}^{\infty} m^M\,\mathrm{X}_{\mathrm{m}}^S \tag{170}$$

which results in

$$s(m) = \frac{c^{IDB}}{\mu_P^1} \cdot m. \tag{171}$$

To account for the average concentration of internal double bonds a massless reaction product, a counter variable H^{IDB} , is again introduced as auxiliary quantity

$$c^{IDB} = \sum_{m=1}^{\infty}\sum_{j=0}^{\infty}\sum_{l=0}^{\infty}\sum_{s=0}^{\infty} sP_{m,j,l,s} = H^{IDB}. \tag{172}$$

The transfer to TDB reaction step and subsequent propagation was implemented to complete the reaction scheme since analogous to transfer to monomer, a transfer to TDB can also occur. In this chapter, the relevance of this reaction step will now be verified and thus a sensitivity study on the number of internal double bonds will be performed.

A.3.3 Sensitivity study on the number of internal double bonds

First, an estimate is shown of how likely the transfer to TDB reaction is compared to the transfer to monomer reaction. For comparison the reference case from Table 9 is used. The term "$\mathrm{H}^{\mathrm{TDB}}$" is used for the formation of terminal double bonds by transfer to monomer and "$\mathrm{H}^{\mathrm{IDB}}$" by transfer to polymer containing TDB. Figure 152 shows the concentration of the counter variables over the conversion for the reference case. It can be seen that the transfer to monomer reaction is three orders more probable.

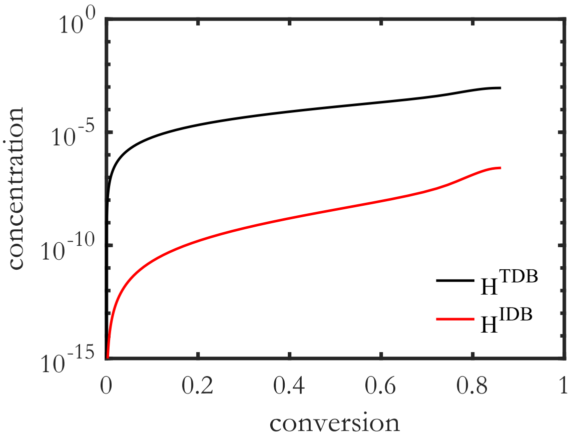

Figure 152: Concentration of the counter variables H^{TDB} and H^{IDB} versus the conversion for the reference case.

Subsequently, the influence of the transfer to polymer containing TDB reaction and the subsequent propagation reaction, will be clarified by comparing the model with these two reactions to a model without. Figure 153 (left) shows the average number of branching points for the reference case for both the models. The model without transfer to TDB slightly underestimates the number of branching points. In Figure 153 (right) the average branching points per molecule, the normalized GPC distribution (Figure 154 left) and the monomer conversion (Figure 154 right) are in very good agreement of both the models. Only minor changes occur because of the newly implemented reactions.

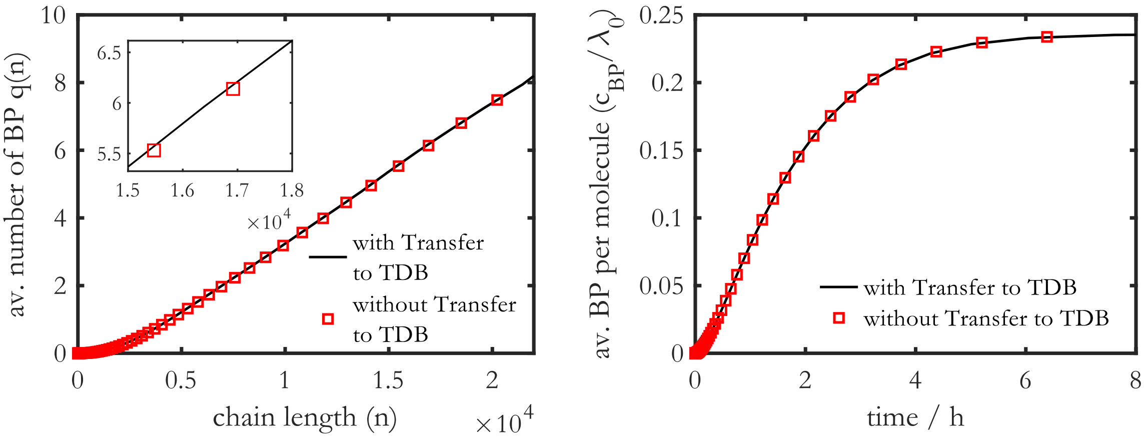

Figure 153: Comparison of the average number of branching points q(n) as a function of the chain length (left) and average branching points per molecule (right) for the BP moment with and without Transfer to TDB for the reference case.

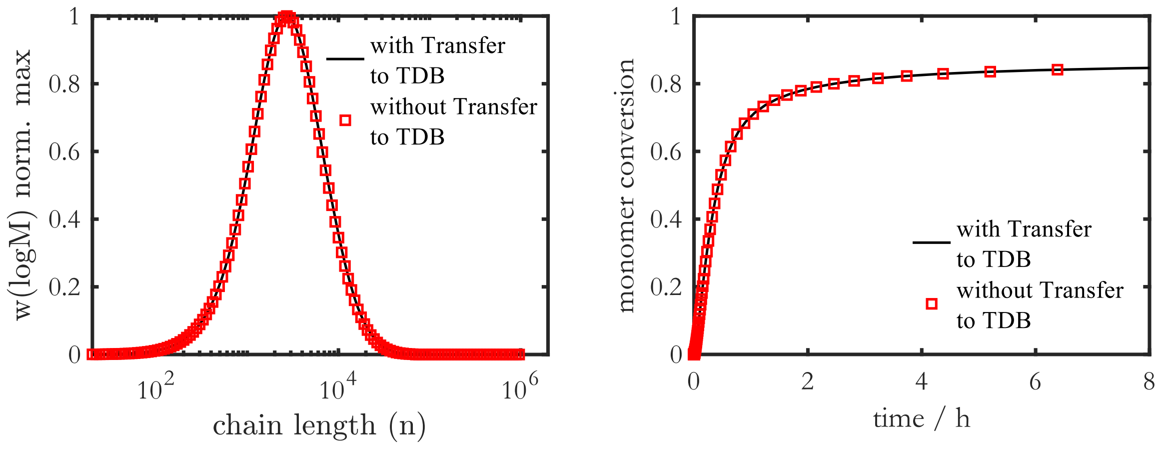

Figure 154: Comparison of the normalized GPC distribution (left) and monomer conversion (right) for the BP moment with and without Transfer to TDB for the reference case.

Thus, it can be summarized that these two new reactions have almost no effect on the number of branches as well as the reaction progress and GPC distribution. These reaction steps will therefore be neglected in further investigations.

A.3.4 Sensitivity study on the branching point distribution with changing initiator feed conditions

In the following, the impact of initiator concentration on the branching distribution is investigated. The reference case from Table 9 was modified with respect to feed rate and initiator concentration. The modified parameters are listed in Table 20.

Table 20: Parameter for the investigation of the influence of the initiator concentration.

Feed	
Monomer weight fraction w_{NVP}^{+}	0.2
Initiator weight fraction $w_{I_2}^{+}$	0.00002-0.0002
Solvent weight fraction $w_{H_2O}^{+}$	$1\text{-}w_{NVP}^{+}\text{-}w_{I_2}^{+}$
Feed rate $\dot{m}_F$ [g min^{-1}]	4.6

In Figure 155, the average number of branching points increases with increasing initiator concentration in the feed stream. This is due to the fact that a higher initiator concentration results in a higher monomer conversion, resulting in lower monomer concentrations in the system. Due to the dependence of the side reactions on the monomer concentration, the number of BPs increases with increasing initiator concentration in the feed. Figure 156 shows the average number of BPs per molecule. The number of BPs per molecule increases with increasing initiator concentration. At very low initiator concentrations, longer chains are formed, but these cannot form as many branches. The reason for this is the lower monomer conversion for lower initiator concentrations and the associated reduction in the probability of side reactions.

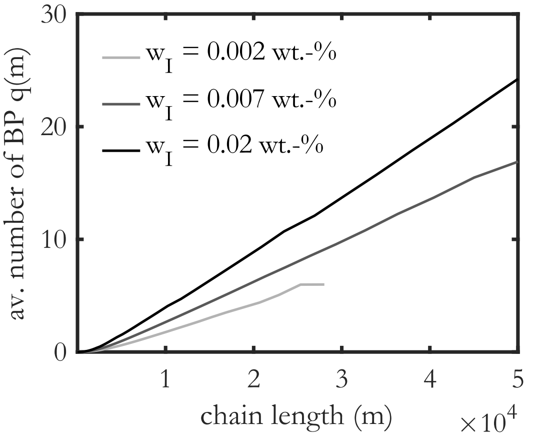

Figure 155: Comparison of the average number of branching points depending on the chain length for different initiator feed concentrations with an average residence time τ=2.25 h.

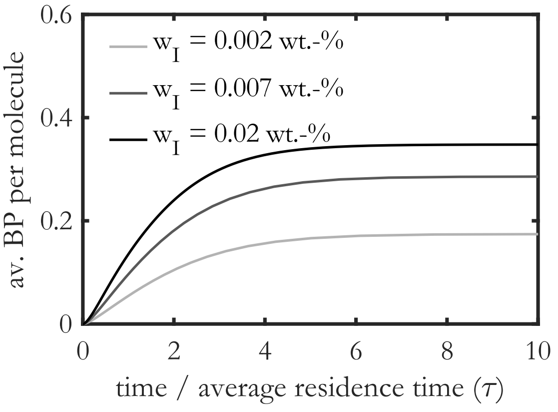

Figure 156: Comparison of the average number of branching points per molecule depending on time for different initiator feed concentrations with an average residence time τ=2.25 h.

The plot of the average number of BPs at 1000 RU, which is shown in Figure 157, also reflects this result. The number thus increases with increasing initiator concentration.

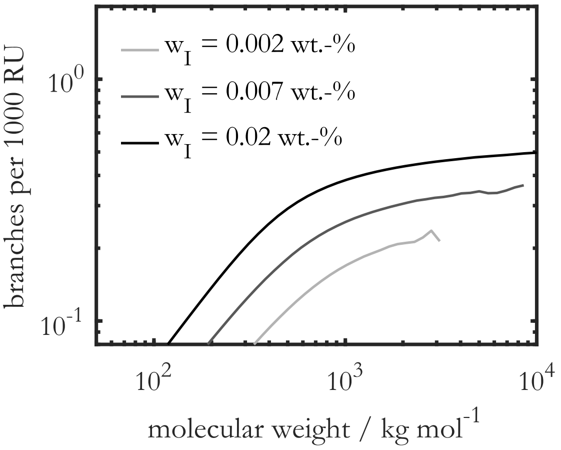

Figure 157: Comparison of the average number of branching points per 1000 repeat units depending on molecular weight for different initiator feed concentrations with an average residence time τ=2.25 h.

A.3.5 Full set of equations for the TDB double moment model

The full set of equations developed in [6] is shown below.

$$\frac{dI_2}{dt} = -k_d f_d I_2 \tag{173}$$

$$\frac{dI}{dt} = -k_p M I + 2 k_d f_d I_2 \tag{174}$$

$$\frac{dM}{dt} = -k_p M I - k_p M \mu_R^{0,0,0} - k_{tr,M} M \mu_R^{0,0,0} \tag{175}$$

Zeroth chain length moments

$$\frac{d\mu_R^{0,0,0}}{dt} = k_p M I - k_{t,c}\mu_R^{0,0,0}\mu_R^{0,0,0} \tag{176}$$

$$\begin{aligned}\frac{d\mu_R^{0,1,0}}{dt} = {} & -k_{t,c}\mu_R^{0,1,0}\mu_R^{0,0,0} - k_{tr,M}M\left(\mu_R^{0,1,0} - \mu_R^{0,0,0}\right) \\ & + k_{p,TDB}\left(\mu_R^{0,0,0}\mu_P^{0,2,0} - \mu_R^{0,0,0}\mu_P^{0,1,0}\right)\end{aligned} \tag{177}$$

$$\begin{aligned}\frac{d\mu_R^{0,2,0}}{dt} = {} & -k_{t,c}\mu_R^{0,2,0}\mu_R^{0,0,0} - k_{tr,M}M\left(\mu_R^{0,2,0} - \mu_R^{0,0,0}\right) + k_{p,TDB}(2\mu_R^{0,1,0}\mu_P^{0,2,0} \\ & - 2\mu_R^{0,1,0}\mu_P^{0,1,0} + \mu_R^{0,0,0}\mu_P^{0,3,0} - 2\mu_R^{0,0,0}\mu_P^{0,2,0} + \mu_R^{0,0,0}\mu_P^{0,1,0})\end{aligned} \tag{178}$$

$$\frac{d\mu_P^{0,0,0}}{dt} = \frac{1}{2}k_{t,c}\mu_R^{0,0,0}\mu_R^{0,0,0} + k_{tr,M}M\mu_R^{0,0,0} - k_{p,TDB}\mu_R^{0,0,0}\mu_P^{0,1,0} \tag{179}$$

$$\frac{d\mu_P^{0,1,0}}{dt} = k_{t,c}\mu_R^{0,1,0}\mu_R^{0,0,0} + k_{tr,M}M\mu_R^{0,1,0} - k_{p,TDB}\mu_R^{0,0,0}\mu_P^{0,2,0} \tag{180}$$

$$\frac{d\mu_P^{0,2,0}}{dt} = k_{t,c}\left(\mu_R^{0,2,0}\mu_R^{0,0,0} + \mu_R^{0,1,0}\mu_R^{0,1,0}\right) + k_{tr,M}M\mu_R^{0,2,0} - k_{p,TDB}\mu_R^{0,0,0}\mu_P^{0,3,0} \tag{181}$$

First chain length moments

$$\begin{aligned}\frac{d\mu_R^{1,0,0}}{dt} &= k_p MI + k_p M\mu_R^{0,0,0} - k_{t,c}\mu_R^{1,0,0}\mu_R^{0,0,0} - k_{tr,m}M\left(\mu_R^{1,0,0} - \mu_R^{0,0,0}\right) \\ &\quad + k_{p,TDB}\mu_R^{0,0,0}\mu_P^{1,1,0}\end{aligned} \tag{182}$$

$$\begin{aligned}\frac{d\mu_R^{1,1,0}}{dt} &= k_p M\mu_R^{0,1,0} - k_{t,c}\mu_R^{1,1,0}\mu_R^{0,0,0} - k_{tr,m}M\left(\mu_R^{1,1,0} - \mu_R^{0,0,0}\right) \\ &\quad + k_{p,TDB}(\mu_R^{1,0,0}\mu_P^{0,2,0} - \mu_R^{1,0,0}\mu_P^{0,1,0} + \mu_R^{0,1,0}\mu_P^{1,1,0} + \mu_R^{0,0,0}\mu_P^{1,2,0} \\ &\quad - \mu_R^{0,0,0}\mu_P^{1,1,0}\end{aligned} \tag{183}$$

$$\begin{aligned}\frac{d\mu_R^{1,2,0}}{dt} &= k_p M\mu_R^{0,2,0} - k_{t,c}\mu_R^{1,2,0}\mu_R^{0,0,0} - k_{tr,m}M\left(\mu_R^{1,2,0} - \mu_R^{0,0,0}\right) \\ &\quad + k_{p,TDB}\big(2\mu_R^{1,1,0}\mu_P^{0,2,0} - 2\mu_R^{1,1,0}\mu_P^{0,1,0} + \mu_R^{1,0,0}\mu_P^{0,3,0} - 2\mu_R^{1,0,0}\mu_P^{0,2,0} \\ &\quad + \mu_R^{1,0,0}\mu_P^{0,1,0} + \mu_R^{0,2,0}\mu_P^{1,1,0} + 2\mu_R^{0,1,0}\mu_P^{1,2,0} - 2\mu_R^{0,1,0}\mu_P^{1,1,0} \\ &\quad + \mu_R^{0,0,0}\mu_P^{1,3,0} - 2\mu_R^{0,0,0}\mu_P^{1,2,0} + \mu_R^{0,0,0}\mu_P^{1,1,0}\big)\end{aligned} \tag{184}$$

$$\frac{d\mu_P^{1,0,0}}{dt} = k_{t,c}\mu_R^{1,0,0}\mu_R^{0,0,0} + k_{tr,m}M\mu_R^{1,0,0} - k_{p,TDB}\mu_R^{0,0,0}\mu_P^{1,1,0} \tag{185}$$

$$\frac{d\mu_P^{1,1,0}}{dt} = k_{t,c}\left(\mu_R^{1,0,0}\mu_R^{0,1,0} + \mu_R^{1,1,0}\mu_R^{0,0,0}\right) + k_{tr,m}M\mu_R^{1,1,0} - k_{p,TDB}\mu_R^{0,0,0}\mu_P^{1,2,0} \tag{186}$$

$$\begin{aligned}\frac{d\mu_P^{1,2,0}}{dt} &= k_{t,c}\left(\mu_R^{1,0,0}\mu_r^{0,2,0} + 2\mu_R^{1,1,0}\mu_R^{0,1,0} + \mu_R^{1,2,0}\mu_R^{0,0,0}\right) + k_{tr,m}M\mu_R^{1,2,0} \\ &\quad - k_{p,TDB}\mu_R^{0,0,0}\mu_P^{1,3,0}\end{aligned} \tag{187}$$

Second chain length moments

$$\begin{aligned}\frac{d\mu_R^{2,0,0}}{dt} &= k_pMI + k_pM\left(2\mu_R^{1,0,0} + \mu_R^{0,0,0}\right) - k_{t,c}\mu_R^{2,0,0}\mu_R^{0,0,0} - k_{tr,m}M\left(\mu_R^{2,0,0} - \mu_R^{0,0,0}\right) \\ &\quad + k_{p,TDB}\left(2\mu_R^{1,0,0}\mu_P^{1,1,0} + \mu_R^{0,0,0}\mu_P^{2,1,0}\right)\end{aligned} \tag{188}$$

$$\begin{aligned}\frac{d\mu_R^{2,1,0}}{dt} &= k_pM\left(2\mu_R^{1,1,0} + \mu_R^{0,1,0}\right) - k_{t,c}\mu_R^{2,1,0}\mu_R^{0,0,0} - k_{tr,m}M\left(\mu_R^{2,1,0} - \mu_R^{0,0,0}\right) \\ &\quad + k_{p,TDB}\left(\mu_R^{2,0,0}\mu_P^{0,2,0} - \mu_R^{2,0,0}\mu_P^{0,1,0}\right. \\ &\quad + 2\left(\mu_R^{1,1,0}\mu_P^{1,1,0} + \mu_R^{1,0,0}\mu_P^{1,2,0} - \mu_R^{1,0,0}\mu_P^{1,1,0}\right) + \mu_R^{0,1,0}\mu_P^{2,1,0} \\ &\quad \left. + \mu_R^{0,0,0}\mu_P^{2,2,0} - \mu_R^{0,0,0}\mu_P^{2,1,0}\right)\end{aligned} \tag{189}$$

$$\begin{aligned}\frac{\mu_R^{2,2,0}}{dt} &= k_pM\left(2\mu_R^{1,2,0} + \mu_R^{0,2,0}\right) - k_{t,c}\mu_R^{2,2,0}\mu_R^{0,0,0} - k_{tr,m}M\left(\mu_R^{2,2,0} + \mu_R^{0,0,0}\right) \\ &\quad + k_{p,TDB}(2\mu_R^{2,1,0}\mu_P^{0,2,0} - 2\mu_R^{2,1,0}\mu_P^{0,1,0} + \mu_R^{2,0,0}\mu_P^{0,3,0} - 2\mu_R^{2,0,0}\mu_P^{0,2,0} \\ &\quad + \mu_R^{2,0,0}\mu_P^{0,1,0} \\ &\quad + 2\left(\mu_R^{1,2,0}\mu_P^{1,1,0} + 2\mu_R^{1,1,0}\mu_P^{1,2,0} - 2\mu_R^{1,1,0}\mu_P^{1,1,0} + \mu_R^{1,0,0}\mu_P^{1,3,0}\right. \\ &\quad \left. - 2\mu_R^{1,0,0}\mu_P^{1,2,0} + \mu_R^{1,0,0}\mu_P^{1,1,0}\right) + \mu_R^{0,2,0}\mu_P^{2,1,0} + 2\mu_R^{0,1,0}\mu_P^{2,2,0} \\ &\quad - 2\mu_R^{0,1,0}\mu_P^{2,1,0} + \mu_R^{0,0,0}\mu_P^{2,3,0} - 2\mu_R^{0,0,0}\mu_P^{2,2,0} + \mu_R^{0,0,0}\mu_P^{2,1,0})\end{aligned} \tag{190}$$

$$\frac{d\mu_P^{2,0,0}}{dt} = k_{t,c}\left(\mu_R^{2,0,0}\mu_R^{0,0,0} + \mu_R^{1,0,0}\mu_R^{1,0,0}\right) + k_{tr,m}M\mu_R^{2,0,0} - k_{p,TDB}\mu_R^{0,0,0}\mu_P^{2,1,0} \tag{191}$$

$$\begin{aligned}\frac{d\mu_P^{2,1,0}}{dt} &= k_{t,c}\left(\mu_R^{2,0,0}\mu_R^{0,1,0} + 2\mu_R^{1,0,0}\mu_R^{1,1,0} + \mu_R^{2,1,0}\mu_R^{0,0,0}\right) + k_{tr,m}M\mu_R^{2,1,0} \\ &\quad - k_{p,TDB}\mu_R^{0,0,0}\mu_P^{2,2,0}\end{aligned} \tag{192}$$

$$\begin{aligned}\frac{\mu_P^{2,2,0}}{dt} &= k_{t,c}\left(\mu_R^{2,0,0}\mu_R^{0,2,0} + 2\mu_R^{2,1,0}\mu_R^{0,1,0} + \mu_R^{2,2,0}\mu_R^{0,0,0} + \mu_R^{1,0,0}\mu_R^{1,2,0} + 2\mu_R^{1,1,0}\mu_R^{1,1,0}\right. \\ &\quad \left. + \mu_R^{1,2,0}\mu_R^{1,0,0}\right) + k_{tr,m}M\,\mu_R^{2,2,0} - k_{p,TDB}\,\mu_R^{0,0,0}\mu_P^{2,3,0}\end{aligned} \tag{193}$$

A.3.6 Full set of balance equations for the BP model

In this section of the supporting information, the complete set of balance equations for reaction scheme from Table 10 is shown. From now on, the index for TDB is dropped for notation purposes. The $+=$ duet indicates the contribution of the respective reaction. The overall moments are defined with Equation (194) and Equation (195):

$$\mu_R^{0,K=0} = \sum_{k=0}^{\infty}\sum_{n=1}^{\infty} R_{n,k} \qquad \mu_P^{0,L=0} = \sum_{l=0}^{\infty}\sum_{m=1}^{\infty} P_{m,l} \tag{194}$$

$$\mu_R^{1,K=0} = \sum_{k=0}^{\infty}\sum_{n=1}^{\infty} nR_{n,k} \qquad \mu_P^{1,L=0} = \sum_{l=0}^{\infty}\sum_{m=1}^{\infty} mP_{m,l} \tag{195}$$

Initiator dissociation/

Initiation

$$\begin{aligned} \frac{dI_2}{dt} &+= -k_d f_d I_2 \\ \frac{dI}{dt} &+= 2k_d f_d I_2 - k_p IM \\ \frac{dR_{1,0}}{dt} &+= k_p MI \\ \frac{dM}{dt} &+= -k_p MI \end{aligned} \tag{196}$$

Propagation

$$\begin{aligned} \frac{dM}{dt} &+= -k_p M \sum_{n=1}^{\infty}\sum_{k=0}^{\infty} R_{n,k} = -\,k_p M \mu_R^{0,K=0} \\ \frac{dR_{n,k}}{dt} &+= k_p M\left(-R_{n-1,k} + R_{n,k}\right) \end{aligned} \tag{197}$$

Termination by recombination

$$\frac{dR_{n,k}}{dt} += -k_{t,c}R_{n,k}\sum_{n=1}^{\infty}\sum_{k=0}^{\infty}R_{n,k} = -k_{t,c}\mu_R^{0,K=0}R_{n,k}$$

$$\frac{dP_{m,l}}{dt} += \frac{1}{2}k_{t,c}\sum_{n=1}^{m-1}\sum_{k=0}^{l}R_{n,k}R_{m-n,l-k} \tag{198}$$

Transfer to monomer

$$\frac{dR_{1,0}}{dt} += k_{tr,M}M\sum_{n=1}^{\infty}\sum_{k=0}^{\infty}R_{n,k} = k_{tr,M}M\mu_R^{0,K=0}$$

$$\frac{dM}{dt} += -k_{tr,M}M\sum_{n=1}^{\infty}\sum_{k=0}^{\infty}R_{n,k} = -k_{tr,M}M\mu_R^{0,K=0} \tag{199}$$

$$\frac{dR_{n,k}}{dt} += -k_{tr,M}MR_{n,k}$$

$$\frac{dP_{m,l}}{dt} += k_{tr,M}MR_{m,l}$$

Propagation of terminal double bonds

$$\frac{dR_{n,k}}{dt} += k_{p,TDB}\left(-R_{n,k}\sum_{m=1}^{\infty}\sum_{l=0}^{\infty}p(m)\,P_{m,l} + \sum_{m=1}^{n-1}\sum_{l=0}^{k-1}p(m)\,P_{m,l}\,R_{n-m,k-l-1}\right) \tag{200}$$

$$\frac{dP_{m,l}}{dt} += -k_{p,TDB}\,p(m)\,P_{m,l}\sum_{n=1}^{\infty}\sum_{k=0}^{\infty}R_{n,k} = -k_{p,TDB}\,p(m)\,P_{m,l}\mu_R^{0,K=0}$$

A.3.7 Moment balances with the branching moment for the living species and dead species

The branching moments were already introduced in section 4.2.2. In this section of the Appendix the whole derivation of the branching moments is shown.

$$\phi_n^K = \sum_{k=0}^{\infty} k^K R_{n,k} \tag{201}$$

$$\Psi_m^L = \sum_{l=0}^{\infty} l^L P_{m,l} \tag{202}$$

Propagation

$$\frac{d\phi_n^K}{dt} = \frac{d\left(\sum_{k=0}^{\infty} k^K R_{n,k}\right)}{dt} += k_p M\left(-\phi_{n-1}^K + \phi_n^K\right) \tag{203}$$

Termination by recombination

$$\frac{d\phi_n^K}{dt} += -k_{t,c}\mu_R^{0,K=0}\phi_n^K$$

$$\begin{aligned} \frac{d\Psi_m^L}{dt} &+= \frac{1}{2}k_{t,c}\sum_{l=0}^{\infty} l^L \sum_{n=1}^{m-1}\sum_{k=0}^{l} R_{n,k}\, R_{m-n,l-k} \\ &= \frac{1}{2}k_{t,c}\sum_{n=1}^{m-1}\sum_{k=0}^{\infty} R_{n,k}\left(\sum_{l=k}^{\infty} l^L\, R_{m-n,l-k}\right) \\ &= \frac{1}{2}k_{t,c}\sum_{n=1}^{m-1}\sum_{k=0}^{\infty} R_{n,k}\left(\sum_{l=0}^{\infty} (l+k)^L\, R_{m-n,l}\right) \end{aligned} \tag{204}$$

Transfer to monomer

$$\begin{aligned} \frac{d\phi_n^K}{dt} &+= -k_{tr,M} M \phi_n^K \\ \frac{d\Psi_m^L}{dt} &+= k_{tr,M} M \phi_m^L \end{aligned} \tag{205}$$

Propagation of terminal double bonds

$$
\begin{aligned}
\frac{d\phi_n^K}{dt} += {} & k_{p,TDB} \sum_{k=0}^{\infty} k^K \left(-R_{n,k} \sum_{m=1}^{\infty} \sum_{l=0}^{\infty} p(m)\, P_{m,l} \right. \\
& \left. + \sum_{m=1}^{n-1} \sum_{l=0}^{k-1} p(m)\, P_{m,l}\, R_{n-m,k-l-1} \right) \\
& = k_{p,TDB} \left(-\phi_n^K \sum_{m=1}^{\infty} p(m)\, \Psi_m^0 \right. \\
& \left. + \sum_{m=1}^{n-1} \sum_{l=0}^{\infty} p(m)\, P_{m,l} \left(\sum_{k=l+1}^{\infty} k^M\, R_{n-m,k-l-1} \right) \right) \\
& = k_{p,TDB} \left(-\phi_n^K \sum_{m=1}^{\infty} p(m)\, \Psi_m^0 \right. \\
& \left. + \sum_{m=1}^{n-1} \sum_{l=0}^{\infty} p(m)\, P_{m,l} \left(\sum_{i=1}^{\infty} (i+l)^K\, R_{n-m,i-1} \right) \right) \\
& = k_{p,TDB} \left(-\phi_n^K \sum_{m=1}^{\infty} p(m)\, \Psi_m^0 \right. \\
& + \sum_{m=1}^{n-1} \sum_{l=0}^{\infty} p(m)\, P_{m,l} \left(\sum_{k=0}^{\infty} (k+l \right. \\
& \left. \left. + 1)^K\, R_{n-m,k} \right) \right)
\end{aligned}
\qquad (206)
$$

$$
\begin{aligned}
\frac{d\Psi_m^L}{dt} += {} & -k_{p,TDB}\, p(m) \sum_{l=0}^{\infty} l^L\, P_{m,l} \mu_R^{0,K=0} \\
& = -k_{p,TDB}\, p(m)\, \Psi_m^L \mu_R^{0,K=0}
\end{aligned}
$$

0th branching moments

Propagation

$$\frac{d\phi_n^0}{dt} += k_p M(-\phi_{n-1}^0 + \phi_n^0) \tag{207}$$

Termination by recombination

$$\frac{d\phi_n^0}{dt} += -k_{t,c}\mu_R^{0,K=0}\phi_n^0$$

$$\frac{d\Psi_m^0}{dt} += \frac{1}{2}k_{t,c}\sum_{n=1}^{m-1}\sum_{k=0}^{\infty}R_{n,k}(\sum_{l=0}^{\infty}(l+k)^0\,R_{m-n,l}) \tag{208}$$

$$= \frac{1}{2}k_{t,c}\sum_{n=1}^{m-1}\phi_n^0\phi_{m-n}^0$$

Transfer to monomer

$$\frac{d\phi_n^0}{dt} += -k_{tr,M}M\phi_n^0$$

$$\frac{d\Psi_m^0}{dt} += k_{tr,M}M\phi_m^0 \tag{209}$$

Propagation of terminal double bonds

$$\frac{d\phi_n^0}{dt} += k_{p,TDB}\left(-\phi_n^0\sum_{m=1}^{\infty}p(m)\,\Psi_m^0 + \sum_{m=1}^{n-1}\sum_{l=0}^{\infty}p(m)\,P_{m,l}\left(\sum_{k=0}^{\infty}(k+l+1)^0R_{n-m,k}\right)\right)$$

$$= \;k_{p,TDB}\left(-\phi_n^0\sum_{m=1}^{\infty}p(m)\,\Psi_m^0 + \sum_{m=1}^{n-1}p(m)\Psi_m^0\phi_{n-m}^0\right) \tag{210}$$

$$\frac{d\Psi_m^0}{dt} += \;-k_{p,TDB}\,p(m)\,\Psi_m^0\mu_R^{0,K=0}$$

1st branching moments

Propagation

$$\frac{d\phi_n^1}{dt} += k_p M(-\phi_{n-1}^1 + \phi_n^1) \tag{211}$$

Termination by recombination

$$\frac{d\phi_n^1}{dt} \mathrel{+}= -k_{t,c}\mu_R^{0,K=0}\phi_n^1$$

$$\frac{d\Psi_m^1}{dt} \mathrel{+}= \frac{1}{2}k_{t,c}\sum_{n=1}^{m-1}\sum_{k=0}^{\infty} R_{n,k}\sum_{l=0}^{\infty}(l+k)^1\, R_{m-n,l} \qquad (212)$$

$$= k_{t,c}\sum_{n=1}^{m-1}\phi_n^1\phi_{m-n}^0$$

Transfer to monomer

$$\frac{d\phi_n^1}{dt} \mathrel{+}= -k_{tr,M}M\phi_n^1$$

$$\frac{d\Psi_m^1}{dt} \mathrel{+}= k_{tr,M}M\phi_m^1 \qquad (213)$$

Propagation of terminal double bonds

$$\frac{d\phi_n^1}{dt} \mathrel{+}= k_{p,TDB}\left(-\phi_n^1\sum_{m=1}^{\infty}p(m)\,\Psi_m^0 \right. \qquad (214)$$

$$\left. + \sum_{m=1}^{n-1}\sum_{l=0}^{\infty}p(m)\,P_{m,l}\sum_{k=0}^{\infty}(k+l+1)^1 R_{n-m,k}\right)$$

$$= k_{p,TDB}\left(-\phi_n^1\sum_{m=1}^{\infty}p(m)\,\Psi_m^0\right.$$

$$+\sum_{m=1}^{n-1}p(m)\left(\sum_{l=0}^{\infty}l\,P_{m,l}\phi_{n-m}^0 + \sum_{k=0}^{\infty}k\,\Psi_m^0\,R_{n-m,k}\right.$$

$$\left.\left. + \Psi_m^0\phi_{n-m}^0\right)\right)$$

$$= k_{p,TDB}\left(-\phi_n^1\sum_{m=1}^{\infty}p(m)\,\Psi_m^0\right.$$

$$\left. + \sum_{m=1}^{n-1}p(m)\,(\Psi_m^1\phi_{n-m}^0 + \Psi_m^0\phi_{n-m}^1 + \Psi_m^0\phi_{n-m}^0)\right)$$

$$\frac{d\Psi_m^1}{dt} \mathrel{+}= -k_{p,TDB}\,p(m)\,\Psi_m^1\mu_R^{0,K=0}$$

Full set of equations for a CSTR

$$\frac{dI_2}{dt} = -k_d f_d I_2 + \frac{\dot{V}^+}{V_R}(I_2^+ - I_2) \tag{215}$$

$$\frac{dI}{dt} = 2k_d f_d I_2 - k_p IM - \frac{\dot{V}^+}{V_R} I \tag{216}$$

$$\frac{dR_{1,0}}{dt} = k_p MI + k_{tr,M} M \mu_R^{0,K=0} - \frac{\dot{V}^+}{V_R} R_{1,0} \tag{217}$$

$$\frac{dM}{dt} = -k_p MI - k_p M \mu_R^{0,K=0} - k_{tr,M} M \mu_R^{0,K=0} + \frac{\dot{V}^+}{V_R}(M^+ - M) \tag{218}$$

$$\begin{aligned} \frac{d\phi_n^0}{dt} &= k_p M(-\phi_{n-1}^0 + \phi_n^0) - k_{t,c}\mu_R^{0,K=0}\phi_n^0 - k_{tr,M} M \phi_n^0 \\ &\quad + k_{p,TDB}\left(-\phi_n^0 \sum_{m=1}^{\infty} p(m)\, \Psi_m^0 + \sum_{m=1}^{n-1} p(m) \Psi_m^0 \phi_{n-m}^0\right) - \frac{\dot{V}^+}{V_R}\phi_n^0 \end{aligned} \tag{219}$$

$$\frac{d\Psi_m^0}{dt} = \frac{1}{2} k_{t,c} \sum_{n=1}^{m-1} \phi_n^0 \phi_{m-n}^0 + k_{tr,M} M \phi_m^0 - k_{p,TDB}\, p(m)\, \Psi_m^0 \mu_R^{0,K=0} - \frac{\dot{V}^+}{V_R}\Psi_m^0 \tag{220}$$

$$\begin{aligned} \frac{d\phi_n^1}{dt} &= k_p M(-\phi_{n-1}^1 + \phi_n^1) - k_{t,c}\mu_R^{0,K=0}\phi_n^1 - k_{tr,M} M \phi_n^1 \\ &\quad + k_{p,TDB}\left(-\phi_n^1 \sum_{m=1}^{\infty} (m)\, \Psi_m^0 \right. \\ &\quad \left. + \sum_{m=1}^{n-1} p(m)\, (\Psi_m^1 \phi_{n-m}^0 + \Psi_m^0 \phi_{n-m}^1 + \Psi_m^0 \phi_{n-m}^0)\right) - \frac{\dot{V}^+}{V_R}\phi_n^1 \end{aligned} \tag{221}$$

$$\frac{d\Psi_m^1}{dt} = k_{t,c} \sum_{n=1}^{m-1} \phi_n^1 \phi_{m-n}^0 + k_{tr,M} M \phi_m^1 - k_{p,TDB}\, p(m)\, \Psi_m^1 \mu_R^{0,K=0} - \frac{\dot{V}^+}{V_R}\Psi_m^1 \tag{222}$$

A.3.8 Formulation of the BP moment model in terms of reaction modules

Initiation

$$I_2 \xrightarrow{f_d\, k_d} 2I$$

$$I + M \xrightarrow{k_p} \phi_1^0$$

Propagation

$$\phi_n^0 + M \xrightarrow{k_p} \phi_{n+1}^0$$

$$\phi_n^1 + [M] \xrightarrow{k_p} \phi_{n+1}^1$$

Termination by combination

$$\phi_n^0 + \phi_m^0 \xrightarrow{k_{t,c}} \Psi_{n+m}^1$$

$$\phi_n^1 + [\phi_m^0] \xrightarrow{k_{t,c}} \Psi_{n+m}^1$$

Transfer to monomer

$$\phi_n^0 + M \xrightarrow{k_{tr,M}} \phi_1^0 + \Psi_n^0$$

$$\phi_n^1 + [M] \xrightarrow{k_{tr,M}} \Psi_n^1$$

Propagation of TDBs

$$\phi_n^0 + \Psi_m^0 \xrightarrow{p(m)\cdot k_{p,TDB}} \phi_{n+m}^0 + H^B$$

$$[\phi_n^0] + \Psi_m^1 \xrightarrow{p(m)\cdot k_{p,TDB}} \phi_{n+m}^1$$

$$\phi_n^1 + [\Psi_m^0] \xrightarrow{p(m)\cdot k_{p,TDB}} \phi_{n+m}^1$$

$$[\phi_n^0] + [\Psi_m^0] \xrightarrow{p(m)\cdot k_{p,TDB}} \phi_{n+m}^1$$

A.3.9 Contributions to balance equations for the model extension with transfer to polymers containing TDB

$$\begin{aligned}\frac{dR_{n,k}}{dt} \mathrel{+}= {} & k_{tr,TDB}\left(-R_{n,k}\sum_{m=1}^{\infty} p(m)\cdot\ P_m + p(n)\,P_{n,\mathrm{k}}\lambda_0\right) \\ & + k_{p,\mathrm{I}DB}\,(-R_{n,k}\sum_{m=1}^{\infty}\sum_{l=0}^{\infty} s(m)\,P_{m,l} + \sum_{m=1}^{n-1}\sum_{l=0}^{k-1} s(m)\,P_{m,l}\,R_{n-m,k-l-1})\end{aligned} \tag{223}$$

$$\begin{aligned}\frac{d\phi_n^M}{dt} \mathrel{+}= {} & k_{tr,TDB}\left(-\phi_n^M\sum_{m=1}^{\infty} p(m)\cdot P_m + p(n)\Psi_n^M\lambda_0\right) + k_{p,\mathrm{I}DB}\,(-\phi_n^M\sum_{m=1}^{\infty} s(m)\,\Psi_m^0 \\ & + \sum_{m=1}^{n-1}\sum_{l=0}^{\infty} s(m)\,P_{m,l}\,(\sum_{i=1}^{\infty}(i+l)^M R_{n-m,i-1})\end{aligned} \tag{224}$$

$$\begin{aligned}\frac{d\phi_n^0}{dt} \mathrel{+}= {} & k_{tr,TDB}\left(-\phi_n^0\sum_{m=1}^{\infty} p(m)\cdot P_m + p(n)\Psi_n^0\lambda_0\right) \\ & + k_{p,\mathrm{I}DB}\left(-\phi_n^0\sum_{m=1}^{\infty} s(m)\,\Psi_m^0 + \sum_{m=1}^{n-1} s(m)\Psi_m^0\phi_{n-m}^0\right)\end{aligned} \tag{225}$$

$$\begin{aligned}\frac{d\phi_n^1}{dt} \mathrel{+}= {} & k_{tr,TDB}\left(-\phi_n^1\sum_{m=1}^{\infty} p(m)\cdot P_m + p(n)\Psi_n^1\lambda_0\right) \\ & + k_{p,\mathrm{I}DB}\left(-\phi_n^0\sum_{m=1}^{\infty} s(m)\,\Psi_m^0 + \sum_{m=1}^{n-1} s(m)\Psi_m^0\phi_{n-m}^0\right)\end{aligned} \tag{226}$$

$$\begin{aligned}\frac{dP_{n,k}}{dt} \mathrel{+}= {} & k_{tr,TDB}\,(-p(n)\cdot P_{n,k}\lambda_0 + R_{n,k}\sum_{m=1}^{\infty} p(m)\cdot P_m) \\ & - k_{p,\mathrm{I}DB}\,s(n)P_{n,k}\sum_{m=1}^{\infty}\sum_{l=0}^{\infty} R_{m,l}\end{aligned} \tag{227}$$

$$\frac{d\Psi_n^M}{dt} \mathrel{+}= k_{tr,TDB}\left(-p(n)\Psi_n^M\lambda_0 + \phi_n^M\sum_{m=1}^{\infty} p(m)\cdot P_m)\right) - k_{p,\mathrm{I}DB}\,s(n)\,\Psi_n^M\lambda_0 \tag{228}$$

$$\frac{d\Psi_n^0}{dt} += k_{tr,TDB}\left(-p(n)\Psi_n^0\lambda_0 + \phi_n^0\sum_{m=1}^{\infty} p(m)\cdot P_m\right) - k_{p,\mathrm{ID}B}\, s(n)\,\Psi_n^0\lambda_0 \tag{229}$$

$$\frac{d\Psi_n^1}{dt} += k_{tr,TDB}\left(-p(n)\Psi_n^1\lambda_0 + \phi_n^1\sum_{m=1}^{\infty} p(m)\cdot P_m\right) - k_{p,\mathrm{ID}B}\, s(n)\,\Psi_n^1\lambda_0 \tag{230}$$

$$\frac{dH^{IDB}}{dt} += k_{tr,M}\lambda^0\sum_{m=1}^{\infty} p(m)\cdot P_m - k_{p,\mathrm{ID}B}\sum_{n=1}^{\infty}\sum_{k=0}^{\infty} R_{n,k}\sum_{m=1}^{\infty}\sum_{l=0}^{\infty} s(m)P_{m,l} \tag{231}$$

A.3.10 Derivation of the zero-dimensional approximations for the branching points

A linear approach was chosen in the main text to approximate the branching point distribution via zero-dimensional branching moments. The derivation of the parameter B_2 has already been presented in Chapter 4.5. Since the derivation of parameter A_2 is somewhat more intensive, it is only described here. The linear correlation for the av. number of branching points (Equation (76)) can be expressed in a short form

$$q(m) = A_2\cdot m + B_2 \tag{232}$$

We start with the share in the balance equation of the "propagation of TDB" reaction to for the zero-dimensional first branching moment:

$$\begin{aligned}\frac{d\Psi_m^1}{dt} &+= k_{p,TDB}\,p(m)\mu_R^{0,0,0}\Psi_m^1 = k_{p,TDB}\,p(m)\mu_R^{0,0,0}q(m)\Psi_m^0\\ &= k_{p,TDB}\,p(m)\mu_R^{0,0,0}\left(A_2\left(m-\frac{\mu_P^{1,0,0}}{\mu_P^{0,0,0}}\right)+\frac{\mu_P^{0,0,1}}{\mu_P^{0,0,0}}\right)\Psi_m^0\\ &= k_{p,TDB}\,p(m)\mu_R^{0,0,0}\left(A_2 m\Psi_m^0 - A_2\frac{\mu_P^{1,0,0}}{\mu_P^{0,0,0}}\Psi_m^0+\frac{\mu_P^{0,0,1}}{\mu_P^{0,0,0}}\Psi_m^0\right)\end{aligned} \tag{233}$$

$p(m)$ describes the correlation for the average number of terminal double bonds here. The zeroth chain length moment of this would be

$$\frac{d\mu^{0,0,1}}{dt} = \sum_m m^0\frac{d\Psi_\mathrm{m}^1}{dt} += \sum_m m^0\, k_{p,TDB}\mu_R^{0,0,0}p(m)q(m)\Psi_m^0 \tag{234}$$

Now we only focus on the part that is affected by the sum

$$\begin{aligned}
\sum_m p(m)q(m)\Psi_m^0 &= \left(A\left(m-\frac{\mu_P^{1,0,0}}{\mu_P^{0,0,0}}\right)+\frac{\mu_P^{0,1,0}}{\mu_P^{0,0,0}}\right)\cdot\left(A_2\left(m-\frac{\mu_P^{1,0,0}}{\mu_P^{0,0,0}}\right)+\frac{\mu_P^{0,0,1}}{\mu_P^{0,0,0}}\right)\cdot\Psi_m^0\\
&=\sum_m\left[AA_2\left(m-\frac{\mu_P^{1,0,0}}{\mu_P^{0,0,0}}\right)^2+\frac{\mu_P^{0,1,0}}{\mu_P^{0,0,0}}A_2\left(m-\frac{\mu_P^{1,0,0}}{\mu_P^{0,0,0}}\right)\right.\\
&\left.+\frac{\mu_P^{0,0,1}}{\mu_P^{0,0,0}}A\left(m-\frac{\mu_P^{1,0,0}}{\mu_P^{0,0,0}}\right)+\frac{\mu_P^{0,1,0}}{\mu_P^{0,0,0}}\frac{\mu_P^{0,0,1}}{\mu_P^{0,0,0}}\right]\ \Psi_m^0\\
&=AA_2\mu_P^{2,0,0}-2AA_2\frac{\mu_P^{1,0,0}}{\mu_P^{0,0,0}}\mu_P^{1,0,0}+AA_2\left(\frac{\mu_P^{1,0,0}}{\mu_P^{0,0,0}}\right)^2\ \mu_P^{0,0,0}\\
&+A_2\frac{\mu_P^{0,1,0}}{\mu_P^{0,0,0}}\left(\mu^{1,0,0}-\mu^{1,0,0}\right)+A\frac{\mu_P^{0,0,1}}{\mu_P^{0,0,0}}\left(\mu^{1,0,0}-\mu^{1,0,0}\right)+\frac{\mu_P^{0,1,0}\mu_P^{0,0,1}}{\mu_P^{0,0,0}}\\
&=AA_2\mu_P^{2,0,0}-AA_2\frac{\left(\mu_P^{1,0,0}\right)^2}{\mu_P^{0,0,0}}+\frac{\mu_P^{0,1,0}\mu_P^{0,0,1}}{\mu_P^{0,0,0}}
\end{aligned}\tag{235}$$

The comparison to

$$\begin{aligned}
\frac{d\mu^{0,0,1}}{dt}=\sum_m m^0\frac{d\Psi_\mathrm{m}^1}{dt}+&=\sum_m m^0\,k_{p,TDB}\mu_R^{0,0,0}p(m)\Psi_m^1\\
&=\sum_m m^0\,k_{p,TDB}\mu_R^{0,0,0}\left(A\left(m-\frac{\mu_P^{1,0,0}}{\mu_P^{0,0,0}}\right)+\frac{\mu_P^{0,1,0}}{\mu_P^{0,0,0}}\right)\Psi_m^1\\
&=\sum_m k_{p,TDB}\mu_R^{0,0,0}\left(A\mu_P^{1,0,1}+A\frac{\mu_P^{1,0,0}}{\mu_P^{0,0,0}}\mu_P^{0,0,1}+\frac{\mu_P^{0,1,0}}{\mu_P^{0,0,0}}\mu_P^{0,0,1}\right)
\end{aligned}\tag{236}$$

gives us

$$A\mu_P^{1,0,1}+A\frac{\mu_P^{1,0,0}}{\mu_P^{0,0,0}}\mu_P^{0,0,1}+\frac{\mu_P^{0,1,0}}{\mu_P^{0,0,0}}\mu_P^{0,0,1}=\ AA_2\mu_P^{2,0,0}-AA_2\frac{\left(\mu_P^{1,0,0}\right)^2}{\mu_P^{0,0,0}}+\frac{\mu_P^{0,1,0}\mu_P^{0,0,1}}{\mu_P^{0,0,0}}.\tag{237}$$

A_2 therefore develops to

$$A_2=\frac{\mu_P^{0,0,0}\mu_P^{1,0,1}-\mu_P^{1,0,0}\mu_P^{0,0,1}}{\mu_P^{2,0,0}\mu_P^{0,0,0}-\mu_P^{1,0,0}\mu_P^{1,0,0}}.\tag{238}$$

A.4 Transport of polymer moments – full mathematical description[11]

In Chapter 5.3, the mathematical description of Maxwell-Stefan diffusion for the two limiting cases was clearly described using a 3-component system. At this point, the derivation is presented in general terms for a J-component system.

A.4.1 Maxwell-Stefan limiting case for highly diluted polymer solutions

Starting from the Maxwell-Stefan equation for chains of length s

$$\boldsymbol{d}_{P(s)} = \sum_{j=1}^{J-1} -\frac{1}{c} B_{P(s)j} \boldsymbol{J}_j^N \tag{239}$$

in which $\boldsymbol{J}$ includes all low molecular species and polymers $P(s)$. Splitting the sum into one part with only low molecular species $\boldsymbol{n_{low}}$ and another part with all polymer chain lengths, which generally $r \to \infty$.

$$\boldsymbol{d}_{P(s)} = \sum_{j=1}^{n_{low}} -\frac{1}{c} B_{P(s)j} \boldsymbol{J}_j^N + \sum_{P(r)=1}^{\infty} -\frac{1}{c} B_{P(s)P(r)} \boldsymbol{J}_{P(r)}^N \tag{240}$$

B_{ij} develops to

$$\begin{aligned} B_{P(s)P(s)} &= \left(\frac{x_{P(s)}}{\mathfrak{D}_{P(s)J}} + \sum_{k=1;P(s)\neq k}^{J} \frac{x_k}{\mathfrak{D}_{P(s)k}} \right), \\ B_{P(s)P(r)} &= -x_{P(s)} \left(\frac{1}{\mathfrak{D}_{P(s)P(r)}} - \frac{1}{\mathfrak{D}_{P(s)J}} \right), \\ B_{P(s)j} &= -x_{P(s)} \left(\frac{1}{D_{P(s)j}} - \frac{1}{D_{P(s)J}} \right). \end{aligned} \tag{241}$$

---

[11] The majority of this chapter has been published in advance of this thesis under the terms of the Creative Commons Attribution License (CC BY 4.0) in [80]. Minor changes have been made and passages have been added for better comprehensibility and embedding in the context of this thesis.

The friction between two polymer molecules approaches zero, which means that the diffusion coefficient leads to $\mathfrak{D}_{P(s)P(r)} \rightarrow \infty$. Therefore, the sum over all polymer chains can be simplified to

$$\sum_{P(r)=1}^{\infty} \boldsymbol{J}_{P(r)}^{N} = \boldsymbol{J}_{P(s)}^{N}. \tag{242}$$

B_{ij} for all polymers develops to

$$\begin{aligned} B_{P(s)P(s)} &= \left(\frac{x_{P(s)}}{\mathfrak{D}_{P(s)J}} + \sum_{k=1;P(s)\neq k}^{J} \frac{x_k}{\mathfrak{D}_{P(s)k}} \right) = \sum_{k=1;P(s)\neq k}^{n_{low}} \frac{x_k}{\mathfrak{D}_{P(s)k}}, \\ B_{P(s)P(r)} &= -x_{P(s)} \left(\frac{1}{\mathfrak{D}_{P(s)P(r)}} - \frac{1}{\mathfrak{D}_{P(s)J}} \right) = 0, \\ B_{P(s)j} &= -x_{P(s)} \left(\frac{1}{D_{P(s)j}} - \frac{1}{D_{P(s)J}} \right) = -\frac{x_{P(s)}}{D_{P(s)j}}. \end{aligned} \tag{243}$$

Equation (240) simplifies to

$$\boldsymbol{d}_{P(s)} = \sum_{j=1}^{n_{low}} \frac{1}{c} \frac{x_{P(s)}}{\mathfrak{D}_{P(s)j}} \boldsymbol{J}_j^N - \frac{1}{c} \left(\sum_{k=1;P(s)\neq k}^{n_{low}} \frac{x_k}{\mathfrak{D}_{P(s)k}} \right) \boldsymbol{J}_{P(s)}. \tag{244}$$

The sum $\sum_{k=1;P(s)\neq k}^{n_{low}} \frac{x_k}{\mathfrak{D}_{P(s)k}}$ is only valid for low molecular species and diffusive fluxes of other polymers does not occur due to the assumption to have no friction between polymer molecules. The equation therefore develops to

$$\boldsymbol{d}_{P(s)} = \sum_{j=1}^{n_{low}} \left(\frac{1}{c} \frac{x_{P(s)}}{\mathfrak{D}_{P(s)j}} \boldsymbol{J}_j^N - \frac{1}{c} \frac{x_j}{\mathfrak{D}_{P(s)j}} \boldsymbol{J}_{P(s)} \right). \tag{245}$$

Multiplication with c^2 and with the diffusion coefficient, it follows a relation for the flux of the polymer moments $\xi^k = \sum_{s=1}^{\infty} s^k c_{P(s)}$

$$\sum_{j=1}^{n_{low}} c^2 \mathfrak{D}_{P(s)j} \boldsymbol{d}_{P(s)} = \sum_{j=1}^{n_{low}} \left(c x_{P(s)} \boldsymbol{J}_j^N - c x_j \, \boldsymbol{J}_{P(s)} \right) = \sum_{j=1}^{n_{low}} \left(c_{P(s)} \boldsymbol{J}_j^N - c_j \, \boldsymbol{J}_{P(s)} \right). \tag{246}$$

After rearranging the equation, an expression for the polymer flux follows

$$\boldsymbol{J}_{P(s)}^{N} = \sum_{j=1}^{n_{low}} \frac{-c^2 \mathfrak{D}_{P(s)j} \boldsymbol{d}_{P(s)} + c_{P(s)} \boldsymbol{J}_j^N}{c_j}. \tag{247}$$

After applying the moment approach, the diffusive flux for moments develops to

$$\begin{aligned} \boldsymbol{J}_{\xi^k}^{N} &= \sum_{s=1}^{\infty} s^k \boldsymbol{J}_{P(s)}^{N} = \sum_{s=1}^{\infty} s^k \sum_{j=1}^{n_{low}} \frac{-c^2 \mathfrak{D}_{P(s)j} \boldsymbol{d}_{P(s)} + c_{P(s)} \boldsymbol{J}_j^N}{c_j} \\ &= \sum_{j=1}^{n_{low}} \frac{\xi^k \boldsymbol{J}_j^N - \sum_{s=1}^{\infty} s^k c^2 \mathfrak{D}_{P(s)j} \boldsymbol{d}_{P(s)}}{c_j} \\ &= \sum_{j=1}^{n_{low}} \frac{\xi^k \boldsymbol{J}_j^N - \mathfrak{D}_{P(s)j} (c \nabla \xi^k - \xi^k \nabla c)}{c_j}. \end{aligned} \tag{248}$$

From equation (112), the diffusive flux of moments depends only on the diffusion of the low molecular species, the moment itself and the total concentration. Thus, the diffusion does not depend on other moments.

A.4.2 Maxwell-Stefan limiting case for highly concentrated polymer solutions

Multiplication of Equation (106) with this diffusion coefficient leads to

$$\mathfrak{D}_{PP} \boldsymbol{d}_{P(s)} = \mathfrak{D}_{PP} \sum_{j=1}^{n_{low}} -\frac{1}{c} B_{P(s)j} \boldsymbol{J}_j^N + \mathfrak{D}_{PP} \sum_{P(r)=1}^{\infty} -\frac{1}{c} B_{P(s)P(r)} \boldsymbol{J}_{P(r)}^N. \tag{249}$$

Further assuming that $\mathfrak{D}_{PP} \to 0$, which implies that the friction between Polymer species approaches infinity, and all polymers are transported with the same diffusive velocity. From Equation (115) follows

$$0 = \mathfrak{D}_{PP} \sum_{P(r)=1}^{\infty} -\frac{1}{c} B_{P(s)P(r)} \boldsymbol{J}_{P(r)}^N \tag{250}$$

and

$$\mathfrak{D}_{PP}B_{P(s)P(s)} = \left(x_{P(s)} \frac{\mathfrak{D}_{PP}}{D_{P(s)J}} + \sum_{k=1;P(s)\neq k}^{J} x_k \frac{\mathfrak{D}_{PP}}{\mathfrak{D}_{P(s)k}} \right) = \sum_{k=1;P(s)\neq k}^{J} x_k$$

$$\mathfrak{D}_{P}B_{P(s)P(r)} = -x_{P(s)} \left(\frac{\mathfrak{D}_{PP}}{\mathfrak{D}_{P(s)P(r)}} - \frac{\mathfrak{D}_{PP}}{\mathfrak{D}_{P(s)J}} \right) = -x_{P(s)}. \tag{251}$$

Inserting Equation (251) into Equation (250) and multiplication with c^2, it follows a relation for the flux of the polymer moments $\xi^k = \sum_{s=1}^{\infty} s^k c_{P(s)}$

$$c x_{P(s)} \sum_{P(r)=1}^{\infty} \boldsymbol{J}_{P(r)}^{N} = \left(\sum_{P(r)=1}^{\infty} c_{P(r)} \right) \boldsymbol{J}_{P(s)}^{N} = \xi^0 \boldsymbol{J}_{P(s)}^{N}\,, \tag{252}$$

respectively

$$\boldsymbol{J}_{P(s)}^{N} = \frac{c_{P(s)}}{\xi^0} \sum_{P(r)=1}^{\infty} \boldsymbol{J}_{P(r)}^{N} = \frac{c_{P(s)}}{\xi^0} \boldsymbol{J}_{P}^{N}. \tag{253}$$

After applying the moment approach, the diffusive flux for moments develops to

$$\boldsymbol{J}_{\xi^k}^{N} = \sum_{s=1}^{\infty} s^k \boldsymbol{J}_{P(s)}^{N} = \frac{\sum_{s=1}^{\infty} s^k c_{P(s)}}{\xi^0} \boldsymbol{J}_{P}^{N} = \frac{\xi^k}{\xi^0} \boldsymbol{J}_{P}^{N} \tag{254}$$

and

$$\boldsymbol{J}_{\xi^0}^{N} = \boldsymbol{J}_{P}^{N}. \tag{255}$$

Finally, the flux of higher polymer moments only depends on the flux of the 0th polymer moment

$$\boldsymbol{J}_{\xi^k}^{N} = \frac{\xi^k}{\xi^0} \boldsymbol{J}_{\xi^0}^{N}\,. \tag{256}$$

In other words, if no polymer molecules are diffusing and thus the polymer remains still in total, diffusion of higher moments is not taking place. This preserves spatial inhomogeneities of the polymer and is a realistic physical behavior for polymer solutions with low solvent content. It is also physically consistent as all polymer moments have the same species velocity, regardless of the polymer moment order.

A.5 CFD Simulations

The equations already presented in Chapter 6 were solved with an algorithm based on the pimpleFOAM solver already available in OpenFOAM® software package, which is suitable for incompressible transient flows. The solver architecture was already presented in [7]. All CFD Simulations were conducted using OpenFOAM® 8 and using the divergence schemes from Table 21.

Table 21: Discretization schemes used in OpenFOAM.

Operator	Variable	Discretization scheme
ddtSchemes $(\partial/\partial t)$	default	"backward"
gradSchemes (∇)	default	"Gauss linear"
divSchemes $(\nabla\cdot)$	default	"Gauss linear MUSCL"
	ρuu	"Gauss linearUpwind grad(U)"
laplacianSchemes	default	"Gauss linear corrected"
interpolationSchemes	default	"linear"
snGradSchemes	default	"corrected"

A.5.1 Mesh study

In order to select a suitable simulation grid for the simulations and especially for the parameter studies, grids with different numbers of cells were tested. Grids with 20000-160000 cells were selected. Figure 158 and Figure 159 show the maximum relative viscosity and polymer weight fraction for the reference case (w_M=20 wt.-% and w_I=0.02 wt.-%) for different calculation grids. The curve for the relative viscosity (Figure 158) is the same for early reaction times (<40 min) for all calculation grids, whereas the results differ for higher times. The same can be observed for the polymer weight content (Figure 161). Since greater fluctuations occur at low cell counts of 20000 and 40000 cells, these grids were not used for the parameter studies. A grid with 80000 cells seems to be a good choice in terms of accuracy of results and calculation time and was therefore used for all investigations in Chapter 6.

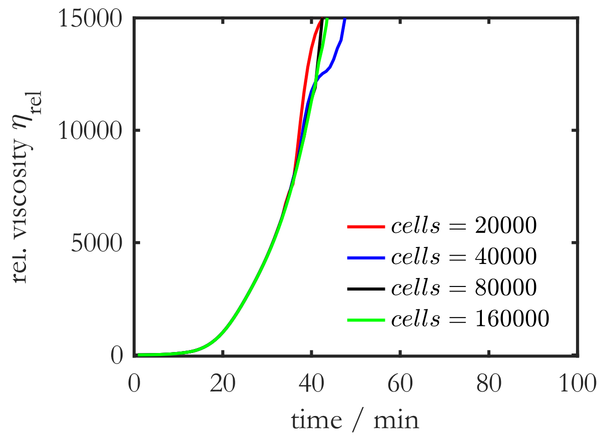

Figure 158: Max. relative viscosity η_{rel} over the reaction time for the reference case of a monomer concentration of w_M=20 wt.-% and an initiator concentration of w_I=0.02 wt.-% conducted for different grids.

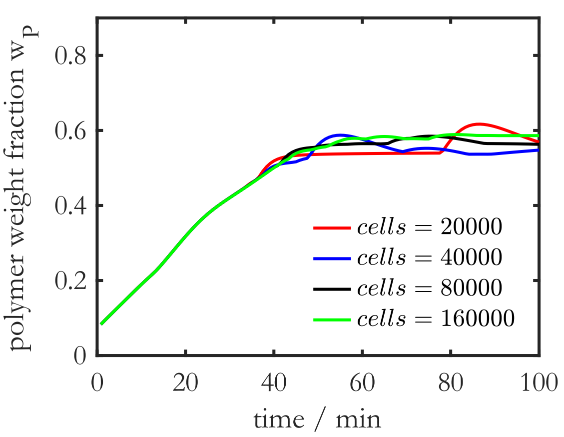

Figure 159: Max. polymer weight fraction w_P over the reaction time for the reference case of a monomer concentration of w_M=20 wt.-% and an initiator concentration of w_I=0.02 wt.-% conducted for different grids.

A.5.2 Residence time distribution simulations

To be able to validate the CFD model, a non-reactive species (Tracer - T) was introduced as described in Chapter 6.3.1. To make a comparison between experiment and simulation, the experimentally measured input signal was used for the simulations. However, the signal had to be normalized

$$E_{in} = \frac{i_{in}}{\int i_{in}\, dt} \tag{257}$$

with the current i_{in} and scaled

$$c_{T,in}^{sim} = N_T^0 E_{in} \tag{258}$$

with the constant N_T^0 beforehand [7].

The constant was then calculated using the experimental and simulative conditions according to

$$N_T^0 = \int c_{T,in}^{sim}\, dt = \frac{n_{T,in}^{exp}}{v_{in} A_{in}} \tag{259}$$

with the inlet velocity v_{in}, the cross-section area of the reactor inlet A_{in} and the amount of tracer used

$$n_{T,in}^{exp} = c_{T,in}^{exp} V_{loop} = 5.5 \cdot 10^{-5}\, mol. \tag{260}$$

The tracer concentration in the sample loop was chosen to $c_{T,in}^{exp}$=1 mol l^{-1} and the volume of the sample loop to V_{loop}=0.055 ml. Therefore, the constant N_T^0 results in different constants due to different reactor cross-sections and velocities.

To select the appropriate diffusion coefficient for the tracer, simulations were carried out with tracer in pure water. These different diffusion coefficients can be compared with the experiment in Figure 160. The dimensionless outlet signal τE_{out} was plotted over time t/τ. A diffusion coefficient of $\mathfrak{D}_T$=7.5e-9 m^2 s^{-1} is therefore a very good choice for describing the diffusion of the tracer at T=85 °C.

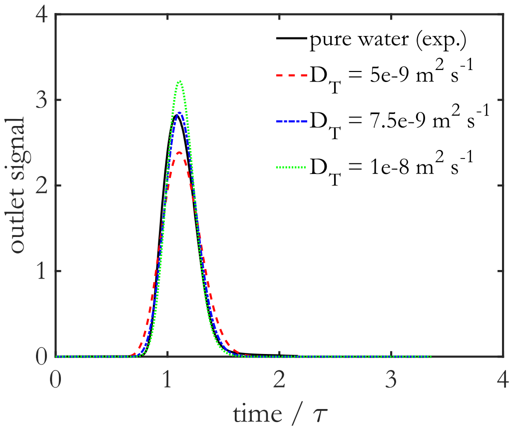

Figure 160: Residence time distributions of different tracer diffusion coefficients compared to the experiment of pure water.

A.5.3 Neural Network for CFD Simulations

The use of neural networks makes it possible in this work to approximate a characteristic field that was generated using the FeOs framework. For this purpose, data was first generated for the activity coefficients of polymer, monomer and solvent depending on the molecular weight of the polymer and the molar mixing fractions in the parameter space that occurs in the CFD simulation. The neural network can then be trained in Matlab®. The number of training data should be a few hundred per parameter in order to obtain a usable network. The number of weights and bias depends on the number of neurons and layers used. In this work, neural networks were trained in advance and then integrated into a specially developed solver. The neural network is integrated into the existing solver as c++ code. Within OpenFOAM®, the molecular weight of the polymer and the molar fractions for each lattice point must therefore be known at the current time step. The mathematical operations for calculating the required quantities are as follows: Normalization of the input variables, calculation of the results of NN with the input variables, weights and bias via activation functions, renormalization of the output variables. The calculated values are then transferred to OpenFOAM® 'ScalarFields'. The calculated fields can then be used to perform mathematical operations such as gradient calculations or Laplacian operations.

A.6 Theory of polymer molecule adhesion/adsorption to surface

Leveraging the acquired knowledge from Chapter 3 and the Appendix A.2, informed assumptions can be made about the processes occurring on or near the surface, as schematically illustrated in Figure 161. This includes a sequence involving rapid polymer diffusion to the interface, swift adsorption, followed by gradual surface rearrangement processes, and ultimately slow desorption.

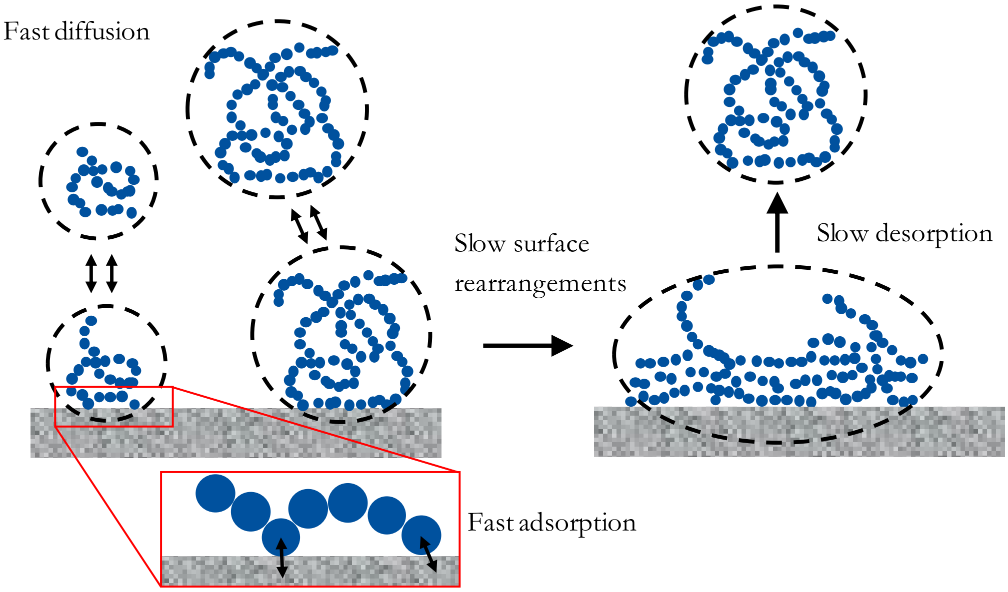

Figure 161: Physical processes of polymers at the interface with different time scales. Adapted from [84].

In addition to these physical processes at the surface, surface reactions of adsorbed polymers at the interface occur according to Figure 162. A polymer with a terminal double bond undergoes an "infinitely" long residence time on the surface and thus side reactions to highly branched or cross-linked polymers are very likely.

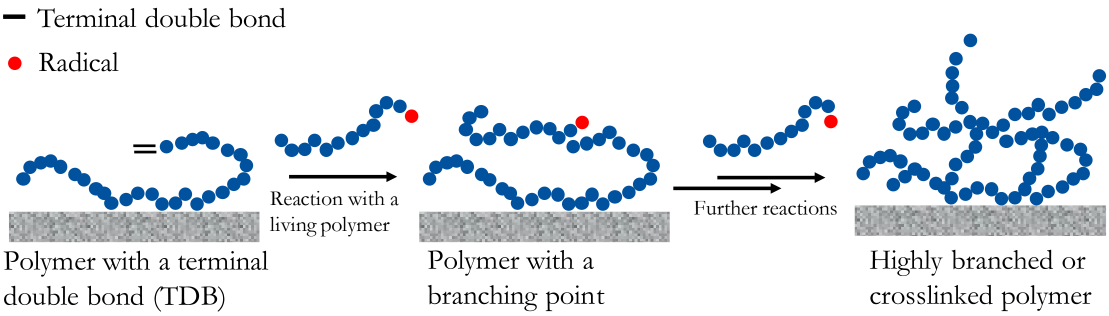

Figure 162: Probable side reactions at the interface leading to very branched and cross-linked polymers up to gel formation.

This theory is supported experimentally by the residence time distributions of unreactive Kollidon K30 in water (Figure 163). After just 15 min, a wall layer is formed, which does not change over a test period of 67 h. After subsequent water rinsing, however, no volume-changing wall layer can be detected in the reactor. This means that unreactive polymer adsorbs on the wall in the same way as a reactive solution and a viscous wall layer subsequently builds up. However, in the case of an unreactive polymer, this viscous wall layer consists of several layers of linear polymer, whereas in the case of a reactive solution, this wall layer continues to polymerize, highly branched polymers are built and cannot be rinsed off as a consequence.

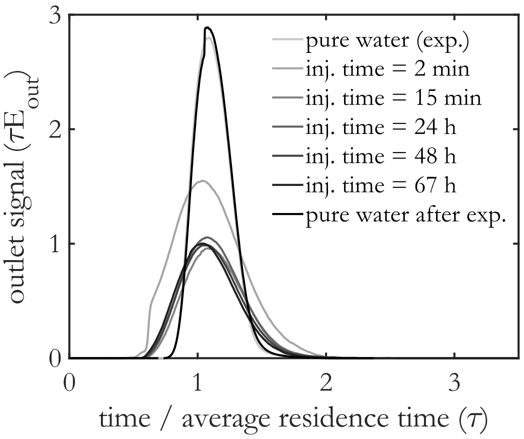

Figure 163: Evolution of the area-normalized response signal Eout at different times for 20 wt.-% Kollidon K30 in water.

To check the extent to which the reactor type plays a role in adhesion to metal surfaces, metal plates were attached at different points inside a CSTR reactor, as in the tube reactor shown in Figure 44E. The residence time of the reaction in the CSTR was set to τ=4.5 h, as such a long residence time also leads to visible gel formation in the reactor [7] and operated for 48 h. Figure 164 shows FTIR spectra of two samples from the CSTR compared with the sample from the tubular reactor. It can be clearly seen that only the intensity of the spectra differs between the tube reactor and the CSTR reactor. There is a large amount of PVP on both surfaces, making it clear that the turbulent energy in the reactor is irrelevant for the adhesion of the molecules, whereby a CSTR reactor is not completely covered with gel but only has deposits on the walls at the end of the run.

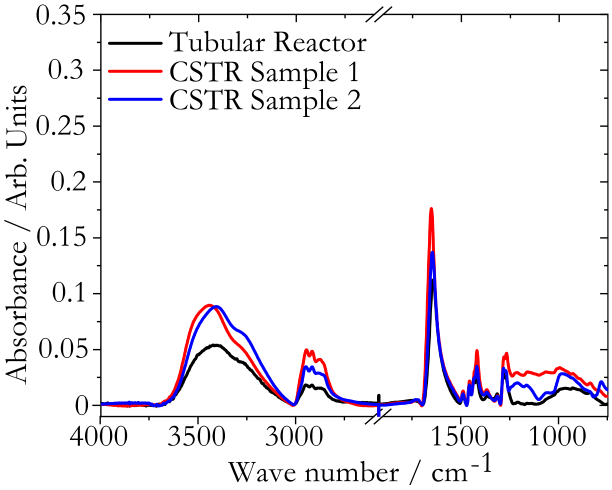

Figure 164: FTIR spectra of the 1.4404 nps surfaces after contact with PVP in the microreactor for one reaction cycle (10 h) and subsequent water cleaning process in comparison to analogously treated bare nps surface in a CSTR reactor (48 h).

At the same time, it could be shown in Appendix A.2.2 that a reactor in an ultrasonic bath does not show any/strong deposit formation. It is therefore particularly important to focus on the introduction of kinetic or turbulent energy from outside in upcoming work. This can be achieved using ultrasound, for example, or by combining a CSTR reactor with a tubular reactor.